

CO₂ Capture Materials For Sorption Enhanced Steam Reforming

Roger Axel Molinder

Submitted in accordance with the requirements for the degree of
Doctor of philosophy

The University of Leeds
School of Process Environmental and Materials Engineering
Energy Research Institute

July 2012

The candidate confirms that the work submitted is his own and that appropriate credit has been given where reference has been made to the work of others.

The right of Roger Axel Molinder to be identified as Author of this work has been asserted by him in accordance with the Copyright, Designs and Patents Act 1988.

Copyright 2012 The University of Leeds and Roger Axel Molinder.

ACKNOWLEDGEMENTS

First of all I want to thank my supervisors Dr Valerie Dupont and Dr Tim Comyn. I also want to thank Dr Amanda Lea-Langton who was my lab supervisor during my first year. Thanks also to Dr Adrian Cuncliffe, Dr Nicole Hondow, Mr Ed Woodhouse, Dr Eric Lewis and Mr Simon Lloid for helpful discussions and guidance.

The RCUK council and the Energy program are gratefully acknowledged for grant EP/G01244X/1 SUPERGEN XIV – Delivery of sustainable hydrogen. Many thanks also to the organisers and partners of SUPERGEN XIV. Special thanks to Linda Jansson for her love and support.

This work is dedicated to the memory of Torgny Axel Molinder (1949-2011)

ABSTRACT

The Ca-looping cycle is a chemical process that alternates capture and release of CO₂ using a Ca-based sorbent which can be applied to hydrogen production by steam reforming. Adding sorbent particles to the reformer achieves nearly pure hydrogen with higher yields via the ‘sorption enhancement’ effect. The major disadvantage is deactivation of the sorbent following multiple cycles and suggested solutions have been incorporation of inert material and regeneration by hydration. This work investigates Ca-based sorbents with a focus on their use for steam reforming of liquid feedstock.

Thermodynamic analysis was used to understand the equilibrium of the steam reforming of three different feedstocks with and without CaO as the sorbent. Addition of sorbent significantly increased the H₂ yield and the H₂ molar fraction for all three feedstocks.

Inert material was incorporated into CaO and CaO derived from Ca-D-gluconate. The resulting sorbents were investigated using thermogravimetric analysis (TGA) and a bench scale reactor in combination with X-ray diffraction (XRD) and N₂ adsorption. Incorporation resulted in a reduction in pores in the 50-100 nm size range and caused self-reactivation behaviour over multiple cycles. The capture capacity and morphology of the sorbent was altered by the CaO precursor but XRD spectra were not.

In situ XRD coupled with Rietveld refinement yielded new insights into the mechanism of Ca-based carbonation and sorbent stability. Agreement between in situ XRD and TGA data was found for carbonation of CaO and Ca(OH)₂, and the mechanism of CO₂ capture in partially hydrated CaO was investigated. Ca(OH)₂ formed CaCO₃ without the CaO intermediate, and anisotropic diffraction peak broadening was observed in the partially hydrated sorbent.

Steam reforming of ethanol and glycerol with and without a Ca-based sorbent was investigated using a novel reactor featuring a nichrome resistance wire with a heating element/catalyst double function. Wire morphology had significant impact on feedstock conversion and the activity of the wire could be increased using a redox pretreatment which caused the formation of chromium oxides on the wire surface. The addition of sorbent by coating resulted in CO₂ capture but not sorption enhancement. The coating also hindered water gas shift and eroded with time on stream.

TABLE OF CONTENTS

ACKNOWLEDGEMENTS	II
ABSTRACT	III
TABLE OF CONTENTS	IV
LIST OF TABLES	IX
LIST OF FIGURES.....	XI
LIST OF ABBREVIATIONS	XX
CHAPTER 1: RESEARCH MOTIVATION AND AIMS	23
1.1 BACKGROUND.....	24
1.2 AIMS AND OBJECTIVES.....	27
CHAPTER 2: MATERIALS AND METHODS	29
2.1 CHEMICALS.....	30
2.2 PREPARATION OF CAO/CA ₁₂ AL ₁₄ O ₃₃	30
2.3 PREPARATION OF CA(OH) ₂	31
2.4 PREPARATION OF CAO DERIVED FROM CA(OH) ₂	31
2.5 PREPARATION OF SORBENT PARTICLES FOR BENCH SCALE REACTOR CARBONATION.....	31
2.6 THERMOGRAVIMETRIC ANALYSIS (TGA).....	32
2.7 SCANNING ELECTRON MICROSCOPY (SEM).....	32
2.8 X-RAY DIFFRACTION (XRD)	33
2.9 IN SITU X-RAY DIFFRACTION	33
2.10 N ₂ ADSORPTION ISOTHERMS.....	34
2.11 BENCH SCALE REACTORS	35
2.11.1 Reactor For Carbonation of Sorbent Pellets	35
2.11.2 Wire Reactor For Steam Reforming Of Liquid Feedstock	37
2.11.3 Equipment Used By Both Reactors	40
2.11.3.1 Gas Cylinders	40
2.11.3.2 Fittings.....	40
2.11.3.3 Mass Flow Controllers.....	40
2.11.3.3.1 Calibration Of Mass Flow Controllers.....	40
2.11.3.4 Gas Cooling And Water Condensation System	42
2.11.3.5 Gas Analyser	42
2.11.3.5.1 Data Logging For Gas Analyser	43
2.12 RAW DATA ANALYSIS	44
2.12.1 Reactor For Carbonation Of Sorbent Pellets	44
2.12.2 Wire Reactor For Steam Reforming Of Liquid Feedstock	45
2.12.2.1 Inputs.....	46
2.12.2.2 Outputs	47

2.12.2.3	Elemental Balances For N, C And H	48
2.13	STATISTICAL ANALYSIS	49
2.14	THERMODYNAMIC ANALYSIS	49
CHAPTER 3: CO₂ SORBENTS FOR MEDIUM AND HIGH TEMPERATURE PROCESSES		51
3.1	INTRODUCTION	52
3.2	POTENTIAL MATERIALS FOR CO ₂ CAPTURE IN MEDIUM AND HIGH TEMPERATURE PROCESSES	
	55	
3.2.1	Lithium Ceramics	55
3.2.2	Hydrotalcites	58
3.2.3	Ca-Based Materials	61
3.2.4	Controlling Sintering	64
3.2.4.1	Doping With Inert Material	65
3.2.4.2	CaO In An Inert Framework	65
3.2.4.3	Pre-Sintering	67
3.2.4.4	Flame Spray Pyrolysis (FSP)	67
3.2.4.5	Hydration	68
3.2.4.6	Introduction Of Oxygen Vacancy Materials	68
3.3	SUMMARY	69
3.4	CONCLUSIONS	70
CHAPTER 4: THERMOCHEMICAL CONVERSION OF GLYCEROL TO HYDROGEN		71
4.1	INTRODUCTION	72
4.2	THERMODYNAMICS OF CONVERSION OF GLYCEROL TO HYDROGEN	75
4.3	GLYCEROL CONVERSION REACTION PATHWAY	80
4.4	STEAM REFORMING (SR)	82
4.4.1	Thermodynamic Equilibrium Analysis	83
4.4.2	Experimental Work	85
4.5	SORPTION ENHANCED STEAM REFORMING (SESR)	95
4.5.1	Thermodynamic Equilibrium Analysis	95
4.5.2	Experimental Work	96
4.6	AUTOTHERMAL REFORMING (ATR)	99
4.6.1	Thermodynamic Equilibrium Analysis	99
4.6.2	Experimental Work	102
4.7	AQUEOUS PHASE REFORMING (APR)	104
4.7.1	Experimental Work	104
4.8	SUPERCRITICAL WATER GASIFICATION (SCWG)	110
4.8.1	Thermodynamic Equilibrium Analysis	110
4.8.2	Experimental Work	111
4.9	THERMAL DECOMPOSITION	116
4.10	CONCLUSIONS	120

CHAPTER 5: THERMODYNAMICS OF SR AND SESR	123
5.1	MOTIVATION FOR WORK 124
5.2	METHODOLOGY AND DEFINITIONS 125
5.3	AIMS AND OBJECTIVES 127
5.4	CHEMICAL PROPERTIES 127
5.5	STEAM REFORMING (SR) 128
5.5.1	Reactions Involved In SR 128
5.5.2	Thermodynamic Analysis Of SR 130
5.5.3	H ₂ Yield 131
5.5.4	Water Conversion 132
5.5.5	Selectivity To Carbon Containing Products 133
5.5.5.1	Methane 133
5.5.5.2	Ethanol And Glycerol 134
5.5.6	Selectivity To Hydrogen Containing Products 136
5.5.7	Dry Molar Composition 137
5.5.7.1	Methane 137
5.5.7.2	Ethanol And Glycerol 138
5.6	SORPTION ENHANCED STEAM REFORMING (SESR) 140
5.6.1	Reactions Involved In SESR 140
5.6.2	Thermodynamics Analysis Of SESR 143
5.6.3	H ₂ Yield 144
5.6.4	Water Conversion 144
5.6.5	Selectivity To Carbon Containing Compounds 145
5.6.5.1	Methane 145
5.6.5.2	Ethanol And Glycerol 146
5.6.6	Selectivity To Hydrogen Containing Products 148
5.6.6.1	Methane 148
5.6.6.2	Ethanol And Glycerol 148
5.6.7	Dry Mole Fraction 149
5.6.7.1	Methane 149
5.6.7.2	Ethanol And Glycerol 150
CHAPTER 6: CO₂ SORBENT CHARACTERISTICS.....	153
6.1	MOTIVATION FOR WORK 154
6.2	AIMS AND OBJECTIVES 156
6.3	SORBENTS INVESTIGATED 156
6.4	CHARACTERISATION 157
6.4.1	CaO Sorbents 157
6.4.1.1	CaO Powder 157
6.4.1.2	Ca(OH) ₂ 159
6.4.1.3	CaO Derived From Ca(OH) ₂ 160
6.4.1.4	CaO Derived From Ca-D-Gluconate 163

6.4.2	Ca ₁₂ Al ₁₄ O ₃₃ Sorbents	167
6.4.2.1	CaO/Ca ₁₂ Al ₁₄ O ₃₃	167
6.4.2.2	CaO-D/Ca ₁₂ Al ₁₄ O ₃₃	169
6.4.2.3	CaO/No Al.....	170
6.5	TGA USING POWDERS	173
6.5.1	TGA Carbonation.....	174
6.5.1.1	Carbonation Of CaO Sorbents	176
6.5.1.2	Carbonation Of Ca ₁₂ Al ₁₄ O ₃₃ Sorbents	179
6.5.2	TGA Cycling	181
6.5.2.1	Cycling Of CaO Sorbents	184
6.5.2.2	Cycling Of Ca ₁₂ Al ₁₄ O ₃₃ Sorbents	186
6.6	REACTOR CARBONATION USING PELLETS.....	187
6.6.1	CaO Sorbents.....	188
6.6.2	Ca ₁₂ Al ₁₄ O ₃₃ Sorbents.....	190
CHAPTER 7: INVESTIGATION OF CO₂ SORBENTS USING IN SITU XRD.....		193
7.1	MOTIVATION FOR WORK	194
7.2	AIMS AND OBJECTIVES	196
7.3	ACCURACY OF THE IN SITU XRD METHOD	197
7.3.1	Atmosphere And Temperature	197
7.3.2	Sample Preparation And Data Collection.....	199
7.3.3	Phase Quantification.....	199
7.4	BENCHMARKING AGAINST TGA	205
7.4.1	Introduction	205
7.4.2	Methodology	206
7.4.2.1	Carbonation Experiment	206
7.4.2.2	Calculations Of Carbonation From TGA Data For Comparison With In Situ XRD.....	206
7.4.2.3	Sample Preparation.....	209
7.4.3	Results And Discussion.....	210
7.4.3.1	Preparation Of CaO	210
7.4.3.2	Carbonation Of CaO.....	210
7.4.3.3	Carbonation Of Ca(OH) ₂	212
7.5	PARTIALLY HYDRATED CAO.....	217
7.5.1	Introduction	217
7.5.2	Methodology	218
7.5.3	Results And Discussion.....	218
7.5.3.1	Sample Preparation.....	218
7.5.3.2	Carbonation	219
7.5.4	High Resolution Synchrotron Diffraction	222
7.6	INVESTIGATION OF CAO/CA ₁₂ AL ₁₄ O ₃₃ CARBONATION	225
7.6.1	Introduction	225
7.6.2	Results and Discussion.....	225

VIII

7.6.2.1	Preparation.....	225
7.6.2.2	Carbonation	227

CHAPTER 8: NICHROME WIRE REACTOR FOR STEAM REFORMING OF LIQUID

FEEDSTOCK.....233

8.1	MOTIVATION FOR WORK.....	234
8.2	METHODOLOGY AND DEFINITIONS.....	235
8.3	AIMS AND OBJECTIVES.....	237
8.4	SELECTING OPTIMUM TEMPERATURE AND MOLAR STEAM TO CARBON RATIO.....	238
8.5	FLOW ADJUSTMENTS FOR ACCURATE QUANTIFICATION	238
8.5.1	Carrier Gas Flow.....	239
8.5.2	Input Mixture Flow.....	240
8.6	ESTABLISHING A STANDARD OPERATING PROCEDURE.....	241
8.6.1	Air Purge Step.....	241
8.6.2	H ₂ Reduction Step.....	242
8.7	TEST OF FEEDSTOCK.....	242
8.7.1	Glycerol (Run 1).....	242
8.7.2	Ethanol (Run 2).....	244
8.8	INTRODUCTION OF AN ALUMINA STACK.....	246
8.9	CATALYTIC ACTIVITY OF THE NICHROME WIRE.....	247
8.9.1	Investigation Of Nichrome Wire Characteristics.....	247
8.9.2	Effect Of Nichrome Wire Morphology On Steam Reforming (Run 3).....	250
8.9.3	Nichrome Wire Pretreatment	252
8.9.4	Effect Of Wire Pretreatment On Steam Reforming (Run 4).....	256
8.10	REPEATABILITY OF THE EXPERIMENTAL PROCEDURE (RUN 5).....	258
8.11	SORPTION ENHANCED STEAM REFORMING (SESR).....	261
8.11.1	Sorbent Pellets (Run 6).....	262
8.11.2	Sorbent Coating.....	267
8.11.2.1	Monolith Coating Using Ca(OH) ₂ Solution (Run7).....	268
8.11.2.2	Nichrome Wire Coating Using Ca(OH) ₂ Solution (Run 8).....	272
8.11.2.3	Alumina Support Coating Using CaCl ₂ Solution (Run 9).....	277

CHAPTER 9: CONCLUSIONS AND FUTURE WORK287

9.1	SUMMARY AND CONCLUSIONS	288
9.2	SUGGESTED FUTURE WORK.....	290

REFERENCES292

LIST OF TABLES

CHAPTER 2

Table 2. 1. Chemicals used for prepare sorbent materials.	30
Table 2. 2. Gases used for the bench scale reactors.	40

CHAPTER 4

Table 4. 1. Summary of thermodynamic equilibrium analysis of steam reforming. Temperatures are given in °C.....	84
Table 4. 2. Enthalpy (Cal °C ⁻¹ mol ⁻¹) for a number of 1, 2 and 3 carbon containing compounds ²⁰⁸	87
Table 4. 3. Summary of experimental work on steam reforming. Temperatures in °C	90
Table 4. 4. Summary of thermodynamic and experimental work on sorption enhanced steam reforming. Temperatures in °C	98
Table 4. 5. Summary of results from thermodynamic and experimental work on autothermal reforming. Temperatures in °C	103
Table 4. 6. Summary of work carried out on aqueous phase reforming. Temperatures in °C, pressures in bar	107
Table 4. 7. Summary of thermodynamic equilibrium analysis and experimental work on supercritical water gasification of glycerol. Temperatures in °C, pressures in bar.....	114
Table 4. 8. Summary of experimental work on thermal decomposition. Temperatures in °C...119	119

CHAPTER 5

Table 5. 1. Species included in the thermodynamic analysis.....	125
Table 5. 2. Selected chemical properties of methane, ethanol and glycerol.	128
Table 5. 3. The input mole fractions used for thermodynamic analysis of steam reforming (SR) of methane, ethanol and glycerol.	131
Table 5. 4. Values of n , m and k (elemental formula C _n H _m O _k) for methane, ethanol and glycerol.	131
Table 5. 5. The input mole fractions used for thermodynamic analysis of sorption enhanced steam reforming of methane, ethanol and glycerol.	144

CHAPTER 7

Table 7. 1. Materials used to determine the actual temperature of a sample for any given temperature setting.....	198
---	-----

Table 7. 2. Derived data from a Williamson Hall plot of high resolution synchrotron data of $\text{Ca}(\text{OH})_2$ in partially hydrated CaO . For comparison, the derived strain, size and stress are also shown for pure $\text{Ca}(\text{OH})_2$, as determined using XRD at Leeds with subsequent Rietveld analysis.	224
Table 7. 3. $\text{Ca}_{12}\text{Al}_{14}\text{O}_{33}$ mass at temperatures between 25 and 800 °C assuming 100 g starting sample mass.....	230

CHAPTER 8

Table 8. 1. Gas concentrations derived from thermodynamic equilibrium analysis of glycerol for input compound compositions corresponding to a S:C of 3 and input mixture flows (ml h^{-1}) between 6 and 48 ml h^{-1} at 597 °C*	240
Table 8. 2. Selectivity to carbon and hydrogen containing species during SR of ethanol with wire 1 and 2.	251
Table 8. 3. The gases used to create oxidizing and reducing atmospheres during the redox pretreatment and the duration for which they were used during a redox cycle.	252
Table 8. 4. Median CO and CO_2 selectivity before and after nichrome wire pretreatment (comparing Run 3, before pretreatment with Run 4, after pretreatment).	258
Table 8. 5. Molar production rates of CO, CH_4 and H_2 at 2500-2600s time on stream and at 7500-7600 s time on steam.....	267
Table 8. 6. Selectivity (C) to CO, CO_2 and CH_4 at steady state to before and after monolith coating.	272
Table 8. 7. Summary of Runs 1-9.....	284

LIST OF FIGURES

CHAPTER 1

Figure 1. 1. Illustration of the Ca-looping cycle.	26
---	----

CHAPTER 2

Figure 2. 1. Setup for preparation of CaO derived from Ca(OH) ₂	31
Figure 2. 2. Schematic of the in situ XRD experimental setup. The equipment on the left hand side was placed outside the XRD powder diffraction unit while the equipment enclosed within the rectangle on the right hand side was placed inside the XRD powder diffraction unit.	34
Figure 2. 3. Schematic of the reactor for carbonation of sorbent pellets.	36
Figure 2. 4. Dimensions of the quartz tube reactor showing the position of the thermocouple.	36
Figure 2. 5. Schematic of the wire reactor for steam reforming of liquid feedstock.	37
Figure 2. 6. Image of the porcelain monolith.	38
Figure 2. 7. Schematic of the inside of the reactor showing the monolith (and dimensions of the wire reactor).	39
Figure 2. 8. Schematic of the mass flow controller calibration setup.	41
Figure 2. 9. Schematic of the data logging set up for the gas analyser.	43
Figure 2. 10. Voltage and analyser readings collected during flows of N ₂ and of CO ₂ calibration gas entered as X and Y values and the resulting curve.	44

CHAPTER 3

Figure 3. 1. Schematic diagram of a faujasite-type zeolite (M ⁺ is a charge balancing cation). Reprinted with permission from Davies (2003). ⁸² Copyright 2003 Elsevier.	53
Figure 3. 2. Structure of a metallic organic framework (MOF-5). Reprinted with permission from Lee et al. (2007). ⁹⁰ Copyright 2007 Elsevier.	53
Figure 3. 3. The amine scrubber process as described in US Patent 1783901. ⁹⁴	54
Figure 3. 4. Double shell model proposed by Ida and Lin (2003). Reprinted with permission from Ida and Lin (2003). ¹⁰⁰ Copyright 2003 American Chemical Society.	56
Figure 3. 5. 3D Structure of a hydrotalcite like compound. M ²⁺ = Mg ²⁺ , Ni ²⁺ et al., M ³⁺ = Al ³⁺ , Fe ³⁺ et al., A ⁿ⁻ = CO ₃ ²⁻ , SO ₄ ²⁻ . Reprinted with permission from Yong et al (2001). ¹¹⁸ Copyright 2001 American Chemical Society.	59
Figure 3. 6. Typical CO ₂ capture curve for a Ca-based material. Reprinted with permission from Alvarez and Abanades (2005). ¹³⁵ Copyright 2005 American Chemical Society.	62

CHAPTER 4

Figure 4. 1. Formation of biodiesel from oils.....	74
Figure 4. 2. Concentrations of products from reactions of glycerol with water at molar steam to carbon ratio (S:C) of 3 at 1 bar.....	76
Figure 4. 3. Hydrogen concentration with temperature from water-glycerol reaction for various S:C at 1 bar.....	77
Figure 4. 4. Free energy diagram of glycerol decomposition intermediates at 210 °C and 1 bar on Pt(111) for all levels of dehydrogenation states of glycerol. Black squares = the adsorption thermochemistry of the most stable dehydration intermediate for a given dehydrogenation state, diamonds = the most stable dehydrogenation transition state for a given dehydrogenation state, triangles = the corresponding energetics for the C-C cleavage transition state for a given dehydrogenation state. Reprinted with permission from Liu and Greeley (2011). ¹⁸⁶ Copyright 2011 American Chemical Society.....	81
Figure 4. 5. H ₂ yield as a function of WGS reactor temperature following steam reforming of glycerol with S:C 2.2 at 804 °C. Reprinted with permission from Douette et al. (2007). ²⁰⁶ Copyright 2007 American Chemical Society.....	86
Figure 4. 6. Carbon compound distribution at temperatures between 427 and 827 °C during sorption enhanced steam reforming of glycerol at S:C of 3. Reprinted with permission from Wang et al. (2010). ¹⁹⁹ Copyright 2010 Elsevier.....	96
Figure 4. 7. Overall heat of reaction as a function of O:C during ATR of glycerol for S:C between ½ and 4 and 627 °C. Reprinted with permission from Wang et al. (2009). ²²⁷ Copyright 2009 Elsevier.....	101
Figure 4. 8. Calculated hydrogen yield at equilibrium of H ₂ , CO ₂ , CO and CH ₄ for a 5 wt% glycerol-water feed solution at 250 bar. Reprinted with permission from van Bennekom et al. (2011). ²⁴¹ Copyright 2011 Elsevier.....	111
Figure 4. 9. Relative yields as a function of pressure at 667 K (394 °C). Reprinted with permission from Buhler et al. (2002). ²⁴⁴ Copyright 2002 Elsevier.....	113

CHAPTER 5

Figure 5. 1. Molecular structure of methane, ethanol and glycerol.....	128
Figure 5. 2. H ₂ yield during SR of methane, ethanol and glycerol with a S:C ratio of 4 at temperatures between 27 and 1007 °C.....	132
Figure 5. 3. Water conversion during SR of methanol, ethanol and glycerol with a S:C ratio of 4 at temperatures between 27 and 1007 °C.....	133
Figure 5. 4. Selectivity to carbon containing products CO and CO ₂ during SR of methane with a S:C ratio of 4 at temperatures between 27 and 1007 °C.....	134

Figure 5. 5. Selectivity to carbon containing products CO, CO ₂ and CH ₄ during SR of ethanol with a S:C ratio of 4 at temperatures between 27 and 1007 °C.....	135
Figure 5. 6. Selectivity to carbon containing products CO, CO ₂ and CH ₄ during SR of glycerol with a S:C ratio of 4 at temperatures between 27 and 1007 °C.....	136
Figure 5. 7. Selectivity to hydrogen containing products H ₂ and CH ₄ during SR of ethanol and glycerol with a S:C ratio of 4 at temperatures between 27 and 1007 °C.....	137
Figure 5. 8. Dry molar composition during SR of methane with a S:C ratio of 4 at temperatures between 27 and 1007 °C.	138
Figure 5. 9. Dry molar composition during SR of ethanol with a S:C ratio of 4 at temperatures between 27 and 1007 °C.	139
Figure 5. 10. Dry molar composition during SR of glycerol with a S:C ratio of 4 at temperatures between 27 and 1007 °C.	140
Figure 5. 11. Dry CO ₂ molar composition during SR of methane, ethanol and glycerol with a S:C ratio of 4 at temperatures between 27 and 1007 °C.	140
Figure 5. 12. The relationship between CO conversion and temperature during sorption enhanced WGS as a function of CO ₂ capture amount. Reprinted with permission from Stevens Jr. et al. ²⁶⁰ Copyright 2010 Elsevier.....	142
Figure 5. 13. H ₂ yield during SESR of methane, ethanol and glycerol with a S:C ratio of 4 at temperatures between 27 and 1007 °C.....	144
Figure 5. 14. Water conversion during SESR of methane, ethanol and glycerol with a S:C ratio of 4 at temperatures between 27 and 1007 °C.....	145
Figure 5. 15. Selectivity to carbon containing products CO, CO ₂ and CaCO ₃ during SESR of methane with a S:C ratio of 4 at temperatures between 27 and 1007 °C.	146
Figure 5. 16. Selectivity to carbon containing products CO, CO ₂ , CH ₄ and CaCO ₃ during SESR of ethanol with a S:C ratio of 4 at temperatures between 27 and 1007 °C.....	147
Figure 5. 17. Selectivity to carbon containing products CO, CO ₂ , CH ₄ and CaCO ₃ during SESR of glycerol with a S:C ratio of 4 at temperatures between 27 and 1007 °C.	147
Figure 5. 18. Selectivity to hydrogen containing products H ₂ and Ca(OH) ₂ during SESR of methane with a S:C ratio of 4 at temperatures between 27 and 1007 °C.	148
Figure 5. 19. Selectivity to hydrogen containing products H ₂ , Ca(OH) ₂ and CH ₄ during SESR of ethanol and glycerol with a S:C ratio of 4 at temperatures between 27 and 1007 °C.....	149
Figure 5. 20. Dry molar composition during SESR of methane with a S:C ratio of 4 at temperatures between 27 and 1007 °C.....	150
Figure 5. 21. Dry molar composition during SESR of ethanol with a S:C ratio of 4 at temperatures between 27 and 1007 °C.....	151
Figure 5. 22. Dry molar composition during SESR of glycerol with a S:C ratio of 4 at temperatures between 27 and 1007 °C.....	151

CHAPTER 6

Figure 6. 1. XRD spectrum between 2θ 15-130 ° of CaO powder. Vertical lines show the expected positions of diffraction peaks for CaO and Ca(OH) ₂ .	158
Figure 6. 2. SEM image of CaO at 50000X magnification.	159
Figure 6. 3. XRD spectrum between 2θ 15-130 ° for Ca(OH) ₂ . Vertical lines show the expected positions of diffraction peaks for CaCO ₃ and Ca(OH) ₂ .	160
Figure 6. 4. SEM image of Ca(OH) ₂ at 50000X magnification.	160
Figure 6. 5. XRD spectrum between 2θ 15-130 ° for CaO derived from Ca(OH) ₂ . Vertical lines show the expected positions of diffraction peaks for CaO and Ca(OH) ₂ .	161
Figure 6. 6. SEM image of CaO derived from Ca(OH) ₂ at 5000X magnification.	162
Figure 6. 7. Pore size distribution of the CaO sorbents.	163
Figure 6. 8. Decomposition of Ca-D-gluconate.	164
Figure 6. 9. XRD spectra of Ca-D-gluconate before decomposition.	165
Figure 6. 10. XRD spectrum of Ca-D-gluconate after decomposition.	165
Figure 6. 11. SEM image of Ca-D-gluconate at 50000X magnification.	166
Figure 6. 12. SEM image CaO derived from decomposition of Ca-D-gluconate at 50000X magnification.	166
Figure 6. 13. Pore size distribution of CaO derived from Ca-D-gluconate and of CaO powder.	167
Figure 6. 14. XRD spectrum between 2θ 15-130 ° C for CaO/Ca ₁₂ Al ₁₄ O ₃₃ . Vertical lines show the expected positions of diffraction peaks for CaO, Ca(OH) ₂ and Ca ₁₂ Al ₁₄ O ₃₃ .	168
Figure 6. 15. SEM image of CaO/Ca ₁₂ Al ₁₄ O ₃₃ at 50000X magnification.	168
Figure 6. 16. XRD spectrum between 2θ 15-130 ° C for CaO-D/Ca ₁₂ Al ₁₄ O ₃₃ . Vertical lines show the expected positions of diffraction peaks for CaO, Ca(OH) ₂ and Ca ₁₂ Al ₁₄ O ₃₃ .	169
Figure 6. 17. SEM image of CaO-D/Ca ₁₂ Al ₁₄ O ₃₃ at 50000X magnification.	170
Figure 6. 18. XRD spectrum between 2θ 15-130 ° C for CaO/No Al. Vertical lines show the expected positions of diffraction peaks for CaO and Ca(OH) ₂ .	171
Figure 6. 19. SEM image of CaO/No Al at 50000X magnification.	172
Figure 6. 20. Pore size distribution of the Ca ₁₂ Al ₁₄ O ₃₃ sorbents.	173
Figure 6. 21. Carbonation TGA temperature program.	175
Figure 6. 22. Data collected during the blank TGA run.	175
Figure 6. 23. Data collected during the decomposition of the Ca(OH) ₂ phase from the CaO powder.	176
Figure 6. 24. Carbonation of CaO powder during TGA.	178
Figure 6. 25. Carbonation of CaO from Ca(OH) ₂ during TGA.	178
Figure 6. 26. Carbonation of CaO derived from Ca-D-gluconate during TGA.	179

Figure 6. 27. Carbonation of CaO/Ca ₁₂ Al ₁₄ O ₃₃ during TGA.	180
Figure 6. 28. Carbonation of CaO-D/Ca ₁₂ Al ₁₄ O ₃₃ during TGA.	180
Figure 6. 29. Carbonation of CaO/No Al during TGA.	181
Figure 6. 30. Cycling TGA temperature program.	182
Figure 6. 31. Equilibrium CO ₂ pressure as a function of temperature. Reprinted with permission from Ortiz and Harrison 2001. ²²¹ Copyright 2001 American Chemical Society.	183
Figure 6. 32. Conversion as a function of cycle number for the CaO sorbents.	185
Figure 6. 33. Conversion as function of cycle number for the Ca ₁₂ Al ₁₄ O ₃₃ sorbents.	186
Figure 6. 34. Carbonation bench scale reactor temperature program.	188
Figure 6. 35. Carbonation of CaO in the bench scale reactor.	189
Figure 6. 36. Carbonation of CaO derived from Ca(OH) ₂ in the bench scale reactor.	190
Figure 6. 37. Carbonation of CaO/Ca ₁₂ Al ₁₄ O ₃₃ and CaO-D/Ca ₁₂ Al ₁₄ O ₃₃ in the bench scale reactor.	191

CHAPTER 7

Figure 7. 1. Example of a phase change due to a change in temperature (derived from BaCO ₃).	198
Figure 7. 2. Sample temperature calibration curve using known materials phase transition temperatures.	199
Figure 7. 3. CaCO ₃ preparation.	200
Figure 7. 4. XRD spectrum of Ca(OH) ₂ . Crosses = raw data, upper solid line = refinement model, lower solid line = residual. Insert showing phase composition (in wt%), residual (R _p) and weighted residual (R _{wp}). Vertical lines show the expected positions of diffraction peaks for Ca(OH) ₂ and CaCO ₃	201
Figure 7. 5. XRD spectrum of CaCO ₃ prepared according to section 7.3.3. As Fig. 7.4. Vertical lines show the expected positions of diffraction peaks for CaCO ₃	202
Figure 7. 6. XRD spectra of a mixture of Ca(OH) ₂ and CaCO ₃ with and intended composition of 75 wt% Ca(OH) ₂ and 25 wt% CaCO ₃ . As Fig. 7.4. Vertical lines show the expected positions of diffraction peaks for Ca(OH) ₂ and CaCO ₃	203
Figure 7. 7. XRD spectra of a mixture of Ca(OH) ₂ and CaCO ₃ with and intended composition of 50 wt% Ca(OH) ₂ and 50 wt% CaCO ₃ . As Fig. 7.4. Vertical lines show the expected positions of diffraction peaks for Ca(OH) ₂ and CaCO ₃	203
Figure 7. 8. XRD spectra of a mixture of Ca(OH) ₂ and CaCO ₃ with and intended composition of 25 wt% Ca(OH) ₂ and 75 wt% CaCO ₃ . As Fig. 7.4. Vertical lines show the expected positions of diffraction peaks for Ca(OH) ₂ and CaCO ₃	204
Figure 7. 9. XRD spectrum of scans nr 1, 6 and 12 collected for CaO at 500 °C in a CO ₂ atmosphere and a close up of the scan range 2θ 46-50 °	205

Figure 7. 10. Conversion of Ca(OH) ₂ to CaO in TGA in an N ₂ atmosphere.....	208
Figure 7. 11. Phase change before and after preparation of CaO from commercially available CaO powder with in situ XRD.	210
Figure 7. 12. XRD spectra of CaO at 25 and 800 °C in a CO ₂ atmosphere. As Fig. 7.4. Vertical lines show the expected positions of diffraction peaks for CaO and CaCO ₃	211
Figure 7. 13. Conversion to CaCO ₃ from CaO in a CO ₂ atmosphere as a function of temperature, using XRD and TGA. Both are calculated as wt% CaCO ₃ . Heating rate 40 °C min ⁻¹ , 2h hold at each temperature.....	212
Figure 7. 14. XRD spectra of Ca(OH) ₂ at 25 and 800 °C in a CO ₂ atmosphere. As Fig. 7.4. Vertical lines show the expected positions of diffraction peaks for Ca(OH) ₂ and CaCO ₃	213
Figure 7. 15. XRD spectra of Ca(OH) ₂ transforming to CaCO ₃ as a function of temperature. The location of CaCO ₃ and Ca(OH) ₂ diffraction peaks are shown via tick marks at the top and bottom respectively. CaO phase was not detected as an intermediate phase (absent peaks at 2θ ~ 32.2 and 37.7 °).....	214
Figure 7. 16. Conversion to CaCO ₃ from Ca(OH) ₂ in a CO ₂ atmosphere as a function of temperature, using XRD and TGA. Both are calculated as wt% CaCO ₃ . Heating rate 40 °C min ⁻¹ , 2h hold at each temperature.	215
Figure 7. 17. Illustration of an X-ray beam reflecting off highly carbonated particle in a sample containing a mixture of highly carbonated particles and uncarbonated particles.....	216
Figure 7. 18. XRD spectrum of Ca(OH) ₂ heated to 800 °C in CO ₂ . As Fig. 7.4. Vertical lines show the expected positions of diffraction peaks for CaCO ₃	216
Figure 7. 19. XRD spectra of the back of the pellet formed during carbonation and of the powder resulting from crushing that pellet. As Figure 7. 4. Vertical lines show the expected positions of diffraction peaks for CaO, Ca(OH) ₂ and CaCO ₃	217
Figure 7. 20. XRD spectrum of partially hydrated CaO. As Fig. 7.4. Vertical lines show the expected positions of diffraction peaks for CaO, Ca(OH) ₂ and CaCO ₃	219
Figure 7. 21. Composition of partially hydrated CaO as a function of temperature in a CO ₂ atmosphere derived from in situ XRD analysis. Heating rate 40 °C min ⁻¹ , 2h hold at each temperature.	220
Figure 7. 22. Wt% CaCO ₃ as a function of temperature for CaO, partially hydrated CaO and Ca(OH) ₂ derived from in situ XRD analysis. Heating rate 40 °C min ⁻¹ , 2h hold at each temperature.....	221
Figure 7. 23. XRD spectra at 2θ 30-36 ° at temperatures of 200-500 °C displaying the broadening of the Ca(OH) ₂ peak at 2θ 34.1 °.	222
Figure 7. 24. High resolution synchrotron spectrum of partial hydration CaO for 2θ 9-19 °. As Fig. 7.4. Vertical lines show the expected positions of diffraction peaks for CaO, Ca(OH) ₂ and CaCO ₃ . Peak labels showing the full width half maximum (FWM).	223

Figure 7. 25. Williamson-Hall plots for the $\text{Ca}(\text{OH})_2$ phase of the partially hydrated CaO from data collected using high resolution synchrotron diffraction.	224
Figure 7. 26. Illustration of a $\text{Ca}(\text{OH})_2$ shell around a CaO core.	224
Figure 7. 27. XRD spectrum of $\text{CaO}/\text{Ca}_{12}\text{Al}_{14}\text{O}_{33}$. As Fig. 7.4. Vertical lines show the expected positions of diffraction peaks for CaO, $\text{Ca}(\text{OH})_2$ and $\text{Ca}_{12}\text{Al}_{14}\text{O}_{33}$	225
Figure 7. 28. Spectrum of $\text{CaO}/\text{Ca}_{12}\text{Al}_{14}\text{O}_{33}$ after removal of the $\text{Ca}(\text{OH})_2$ phase by heating to 700 °C in N_2 . As Fig. 7.4. Vertical lines show the expected positions of diffraction peaks for CaO, and $\text{Ca}_{12}\text{Al}_{14}\text{O}_{33}$	227
Figure 7. 29. Composition of $\text{CaO}/\text{Ca}_{12}\text{Al}_{14}\text{O}_{33}$ as a function of temperature in a CO_2 atmosphere derived from in situ XRD analysis.	228
Figure 7. 30. R_p and R_{wp} values from the in XRD spectra collected during in situ XRD analysis of $\text{CaO}/\text{Ca}_{12}\text{Al}_{14}\text{O}_{33}$	230
Figure 7. 31. XRD spectra of $\text{CaO}/\text{Ca}_{12}\text{Al}_{14}\text{O}_{33}$ at 700 °C in a CO_2 atmosphere. As Fig. 7.4. Vertical lines show the expected positions of diffraction peaks for CaO, CaCO_3 and $\text{Ca}_{12}\text{Al}_{14}\text{O}_{33}$	231

CHAPTER 8

Figure 8. 1. Common experimental setup for SR of glycerol. Reprinted with permission from Cheng et al. ⁵² Copyright 2010 American Chemical Society.	234
Figure 8. 2. Schematic of the setup used to investigate input mixture flow.	239
Figure 8. 3. CO_2 concentration in the reactor off gas with time on stream for a typical air purge step.	242
Figure 8. 4. CO_2 and CH_4 gas analyser readings during SR of glycerol (Run 1) at 600 °C with a S:C ratio of 3:1.	243
Figure 8. 5. Molar production rates of CO, CH_2 , CO_2 and H_2 during SR of glycerol (Run 1) at 600 °C with a S:C ratio of 3:1.	244
Figure 8. 6. CO, CH_4 , CO_2 and H_2 gas analyser readings during SR of ethanol (Run 2) at 600 °C with a S:C ratio of 3:1.	245
Figure 8. 7. Molar production rates of CO, CH_4 , CO_2 and H_2 during SR of ethanol (Run 2) at 600 °C with a S:C ratio of 3:1.	246
Figure 8. 8. Top and side images of Al support pieces used to make the Al stack. The pieces are 20 mm long and 15 mm wide.	247
Figure 8. 9. Photograph (10X magnification) of the nichrome wire supplied by Johnson Matthey (wire 1).	248
Figure 8. 10. Photograph (10X magnification) of the nichrome wire purchased from Omega (wire 2).	248

Figure 8. 11. SEM image (top left) and EDX maps of nickel, oxygen and chromium collected from a cross section of the wire purchased from Omega (wire 2).....	249
Figure 8. 12. EDX peaks derived from a cross section of the wire purchased from Omega (wire 2) showing overlap between a peak derived from oxygen and a peak derived from chromium.	249
Figure 8. 13. Molar production rates of CO, CH ₄ , CO ₂ and H ₂ during SR of ethanol using wire 2 (Run 3) at 600 °C with a S:C ratio of 3:1.	250
Figure 8. 14. Schematic of the setup used to carry out redox pretreatment on 50 mm lengths of nichrome resistance wires.....	252
Figure 8. 15. Photograph (10X magnification) of the nichrome wire purchased from Omega Ltd (wire 2) after 5 redox cycles outlined in Table 8. 3 at a temperature of 700 °C.....	253
Figure 8. 16. Equilibrium gas ratio p _{H₂O} /p _{H₂} as a function of inverse temperature for the reduction of various oxides. ³⁴⁰ Reprinted with permission from Tapir Academic Press, Norway.	254
Figure 8. 17. Photograph (10X magnification) of the nichrome wire purchased from Omega Ltd (wire 2) after 10 repeats of the procedure outlined in Table 8. 3 at a temperature of 700 °C. ..	255
Figure 8. 18. SEM image (top left) and EDX maps of nickel, oxygen and chromium collected from a cross section of the wire purchased from Omega (wire 2) after 5 redox cycles.	256
Figure 8. 19. SEM image (top left) and EDX maps of nickel, oxygen and chromium collected from a cross section of the wire purchased from Omega (wire 2) after 10 redox cycles.	256
Figure 8. 20. Molar production rates of CO, CH ₄ , CO ₂ and H ₂ during SR of ethanol after nichrome wire pretreatment (Run 4) at 600 °C with a S:C ratio of 3:1.	257
Figure 8. 21. Molar production rates of CO, CH ₄ , CO ₂ and H ₂ during a replicate of SR of ethanol (Run 5) at 600 °C with a S:C ratio of 3:1.....	259
Figure 8. 22. The power supplied to the reactor as a function of time during SR of ethanol (Run 5) at 600 °C with a S:C ratio of 3:1.	261
Figure 8. 23. Schematic of the nichrome wire reactor with sorbent particles below the monolith.	263
Figure 8. 24. Comparison of power supply over time for Run 5 (without sorbent pellets) and run 6 (with sorbent pellets).	264
Figure 8. 25. H ₂ concentration and temperature readings from above the monolith recorded during Run 6.	265
Figure 8. 26. Molar production rates of CO, CH ₄ , CO ₂ and H ₂ during Run 6 (with sorbent pellets below the monolith).....	266
Figure 8. 27. Schematic of the monolith submerged in a Ca(OH) ₂ solution.	268
Figure 8. 28. Pictures taken of the monolith before and after monolith coating in a Ca(OH) ₂ solution.	269

Figure 8. 29. Molar production rates of CO, CH ₄ , CO ₂ and H ₂ during Run 7 (monolith coated in a Ca(OH) ₂ solution).	270
Figure 8. 30. Reactor off-gas concentrations of CO, CH ₄ , CO ₂ and H ₂ recorded between 400 and 1000s time on stream during Run 7 (monolith coated in a Ca(OH) ₂ solution).	271
Figure 8. 31. A short length of nichrome resistance wire coated using a Ca(OH) ₂ solution shown next to an uncoated length of wire.	273
Figure 8. 32. Pictures taken of the monolith before and after wire coating using a Ca(OH) ₂ solution.	273
Figure 8. 33. Molar production rates of CO, CH ₄ , CO ₂ and H ₂ during Run 8 (wire coating using a Ca(OH) ₂ solution).	274
Figure 8. 34. Molar production rates of CH ₄ and CO during Run 8 (wire coating using a Ca(OH) ₂ solution).	275
Figure 8. 35. Molar production rates of H ₂ during Run 8 (wire coating using a Ca(OH) ₂ solution).	275
Figure 8. 36. Selectivity to hydrogen containing species (H ₂ and CH ₄) during Run 8 (wire coating using a Ca(OH) ₂ solution).	276
Figure 8. 37. Feedstock and water conversion during Run 8 (wire coating using a Ca(OH) ₂ solution).	277
Figure 8. 38. Pictures taken of the monolith before and after Run 8 (wire coating using a Ca(OH) ₂ solution).	277
Figure 8. 39. Picture of the Al support pieces arranged in a quadrant inserted into the reactor with the nichrome wire (wire 2) threaded through them (as seen from above).	278
Figure 8. 40. Molar production rates of CO, CH ₄ , CO ₂ and H ₂ during Run 9 (Al support impregnation).	279
Figure 8. 41. Molar production rates of CO ₂ and CH ₄ during Run 9 (Al support impregnation).	280
Figure 8. 42. Selectivity to hydrogen containing products (H ₂ and CH ₄) during Run 9 (Al support impregnation).	281
Figure 8. 43. Feedstock and water conversion during Run 9 (Al support impregnation).	282
Figure 8. 44. Temperature readings for the first 2000s of steady state recorded by the thermocouple above the monolith after monolith coating (Run 7) and using impregnated Al support pieces (Run 9).	283

LIST OF ABBREVIATIONS

AC	:	Activated carbon
AFC	:	Alkaline fuel cell
APGTF	:	Advanced power generation technology forum
APR	:	Aqueous phase reforming
ATR	:	Autothermal reforming
BEP	:	Brønsted–Evans-Polanyi (relationship)
BET	:	Brunauer, Emmet, Teller
BP	:	British petroleum
Ca:C	:	Calcium to carbon ratio
CCC	:	Copyright Clearance Center
CCS	:	Carbon capture and storage
DBFC	:	Direct borohydride fuel cell
DFT	:	Density functional theory
DMFC	:	Direct methanol fuel cell
EDS	:	Energy dispersive X-ray spectroscopy
EDX	:	Energy dispersive X-ray spectroscopy
FSP	:	Flame spray pyrolysis
FTIR	:	Fourier transform infrared spectroscopy
FWHM	:	Full width at half maximum
GM	:	General motors
HHV	:	Higher heating value
ICSD	:	Inorganic Crystal Structure Database
IEA	:	International energy agency
IGCC	:	Integrated gasification combined cycle
IPCC	:	Intergovernmental panel on climate change
LHV	:	Lower heating value
MCFC	:	Molten carbonate fuel cell
MCM	:	Mesoporous molecular sieve
MEA	:	Monoethanolamine
MOF	:	Metallic organic framework
MSR	:	Methane steam reforming
MW	:	Molecular weight
NIST	:	National Institute of Standards and Technology

NDIR	:	Nondispersive infrared spectroscopy
O:C	:	Oxygen to carbon ratio
PAA	:	Polyacrylic acid
PAFC	:	Phosphoric acid fuel cell
PEI	:	Polyethyleneimine
PEMFC	:	Proton exchange membrane fuel cell
PI	:	Proportional integral
PID	:	Proportional integral derivative
PWM	:	Pulse width modulation
PROX	:	Preferential oxidation
PSA	:	Pressure swing adsorption
RHA	:	Rice husk ash
RT-XRD	:	Real Time X-ray Diffraction
RWGS	:	Reverse water gas shift
S:C	:	Steam to carbon ratio
SD	:	Superheated dehydration
SEM	:	Scanning Electron Microscopy
SERP	:	Sorption enhanced reaction process
SESR	:	Sorption Enhanced Steam Reforming
SWR	:	Supercritical water reforming
TEM	:	Transmission electron microscopy
TCD	:	Thermal conductivity detector
TR-XRD	:	Time resolved X-ray diffraction
TGA	:	Thermogravimetric Analysis
Toe	:	Tonnes oil equivalent (metric)
TOC	:	Total organic carbon
TPO	:	Temperature programmed oxidation
TPR	:	Temperature programmed reduction
US-DOE	:	United states Department of energy
US-EPA	:	United states environmental protection agency
USR	:	Unmixed Steam Reforming
WGS	:	Water Gas Shift
WHO	:	World health organisation
WtW	:	Well to wheel
XRD	:	X-Ray Diffraction
ZIF	:	Zeolitic imidazolate frameworks

CHAPTER 1: RESEARCH MOTIVATION AND AIMS

“The only fence against the world is a thorough knowledge of it”

John Locke

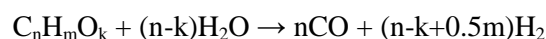
1.1 BACKGROUND

The burning of fossil fuels is the dominant route to heat and power production, especially in the transport sector and results in the release of CO₂ into the earth's atmosphere. Changes in atmospheric CO₂ have been shown to correlate with changes in climate over the last 800 000 years and the amounts of atmospheric CO₂ have increased sharply in the last 200 years to the highest levels ever recorded.¹⁻⁴ This latest increase has been attributed to the burning of fossil fuels and is expected to cause a change in climate just like previous changes in atmospheric CO₂ have done in the past. To date the effects that climate change would have are unclear but there is potential for negative effects such as reduced crop yields and increased frequency of storms.⁵⁻⁸ Other effects are rising sea levels and ocean acidification.^{9,10} Concerns regarding the negative effects of climate change have prompted both global and national policies to reduce CO₂ emissions such as the Kyoto protocol to the UN framework convention on climate change from 1997 and the UK climate change act of 2008. In 2011 during a climate change conference (COP17/CMP7) hosted by the UN in Durban, South Africa, a decision was made to write a legally binding agreement on CO₂ emission reductions by 2015 which will come into force in 2020.

Continued increase in atmospheric CO₂ can be prevented either by switching to renewable energy sources or by preventing release of CO₂ during the burning of fossil fuels. With regard to the transport sector there exist many alternative renewable energy sources such as ethanol or wind and many different energy carriers including biodiesel and electricity. Several endpoint technologies such as internal combustion engine vehicles (ICEVs), electric vehicles (EV) and fuel cell electric vehicles (FCEV) are also available. However, only two alternatives have the potential to achieve zero CO₂ emissions and those involve the use of renewable electricity as the energy source which is then either used directly in an EV or converted to H₂ and used in a FCEV.¹¹ However, using electricity derived from fossil fuels for these applications is a poor choice due to conversion losses involved in electricity production, electrolysis and H₂ compression.¹² When considering renewable electricity as the energy source, FCEVs have three major advantages over EVs. First, electricity has to be used as it is produced which creates the need for energy storage during high energy availability coupled with low demand. However this can be mitigated by optimising the electricity grid and several potential means of energy storage solutions have been put forward, such as pump hydroelectric storage and compressed air energy storage.¹³ Second, the limited storage capacity of onboard EV batteries results in a limited range and finally, onboard EV batteries take hours to charge. Conversion of renewable electricity to H₂ for use in a FCEV solves all three of the above problems. During periods of high energy availability and low demand the excess electricity can be converted into compressed H₂ and stored. The H₂ onboard storage tank of current FCEVs can

be filled in minutes and their storage capacity secures a range which is superior to that of the EV and comparable to those of current fossil fuelled combustion engines.

The most commonly used and best understood route to H₂ production today is steam reforming of natural gas. Thanks to the superior efficiency of the fuel cell over the combustion engine, the well to wheel CO₂ emissions are lower when natural gas is converted to H₂ by steam reforming and used in a FCEV compared to direct use in an ICEV.^{11,14} The well to wheel CO₂ emissions can be reduced further through steam reforming of renewable energy sources.¹⁵ Steam reforming of renewable feedstock such as ethanol and glycerol (Reaction 1. 1) have been demonstrated, making this a viable option.^{16,17} The process involves gasification of the feedstock and reacting it in the presence of steam in a reformer to produce a ‘syngas’ containing H₂ as well as carbon containing compounds, most notably CO but also CO₂ and CH₄.



Reaction 1. 1. Steam reforming of an oxygenated hydrocarbon.

These are removed downstream of the reformer to produce high purity H₂ gas. Commonly a water gas shift (WGS) reactor is used to convert CO to CO₂ with simultaneous production of additional H₂ (Reaction 1. 2).¹⁸ Various alternatives are then available for removal of CO₂ including pressure swing adsorption and amine scrubbing.^{19,20}



Reaction 1. 2. The water gas shift (WGS) reaction.

Sorption enhanced steam reforming (SESR) enables steam reforming, WGS and CO₂ removal in a single step process. This is achieved by introducing a sorbent into the reformer which removes CO₂ from the gas phase and subsequently shifts the WGS reaction and the steam reforming reaction through Le Chatelier’s principle.²¹⁻²³ Ca-based sorbents are well suited for use in SESR due to their abundance, low cost, high capture capacity, fast reaction kinetics and reaction temperature range (Chapter 3). The raw material is limestone or dolomite which is calcined, resulting in CaO as the active component. CO₂ is captured by the oxide via a gas-solid reaction resulting in a carbonate which can then be calcined back to the oxide form in a process referred to as the calcium looping cycle (Figure 1. 1). This is often carried out in practice using a twin fluidised bed system consisting of a carbonator where CaO is reacted with the CO₂ containing gas at around 650 °C and a calciner where the resulting CaCO₃ is regenerated at around 900 °C and the captured CO₂ is released as a pure gas, ready for storage or sequestration if necessary.²⁴⁻²⁶

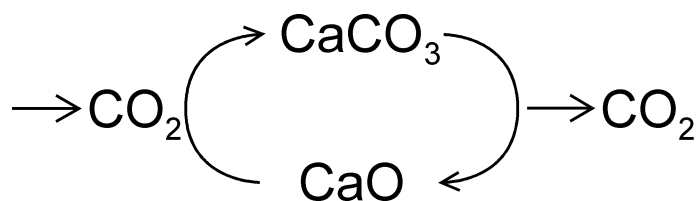


Figure 1. 1. Illustration of the Ca-looping cycle.

Carbon capture and storage (CCS) is a method of preventing release of CO_2 during the burning of fossil fuels. CCS typically involves the capture of CO_2 from a coal or gas-fired power plant, after which it is pressurised to form a liquid which is injected into underground rock formations or saline aquifers for long term storage.²⁷⁻²⁹ The calcium looping cycle is a promising method for CCS as it is a well known technology that uses a cheap and abundant sorbent and that can be retrofitted to existing power plants.³⁰⁻³² There is also a potential synergy between the calcium looping cycle used for CCS and cement production, as spent sorbent could be used to manufacture cement.^{33,34} The technology has been shown to be potentially economically viable (assuming a form of CO_2 emission tax which is a possible outcome of future legally binding agreements) and has moved to the demonstration stage.

The major disadvantage with the calcium looping cycle is that the sorbent is deactivated over multiple cycles, meaning that fresh sorbent has to be continuously added to the process.³⁵ Deactivation is caused by loss of material through attrition³⁶⁻³⁹ and loss of surface area and porosity through sintering⁴⁰⁻⁴² as well as through reaction between the CaO and sulphur species in the gas causing highly stable products which do not readily calcine.⁴³ Attrition is caused by mechanical stresses following the fluidised bed circulation and sintering is a result of the high temperature treatment, mainly during calcination.

A large body of work has aimed to address these issues (Chapter 3). For example, heat treatments have been applied to Ca-based materials to increase mechanical strength and inert material has been incorporated in order to prevent sintering. Hydration has been suggested as a regeneration method for sintered sorbents.⁴⁴⁻⁴⁷ With this method, surface area and porosity can be restored but it also causes a reduction in mechanical strength.^{37,45} Recent work has aimed at understanding the effects of hydration on the whole calcium looping cycle and the presence of steam has been shown to impact the carbonation stage.^{48,49} However this work is made difficult by the limitations of conventional techniques used to study CO_2 sorbent materials (Chapter 7). For example, thermogravimetric analysis (TGA) relies on measuring sample mass and cannot distinguish between a change in sorbent mass derived from CO_2 capture and from hydration/dehydration. The products of reaction can be inferred by measuring TGA off-gases but this is challenging when steam is present.

1.2 AIMS AND OBJECTIVES

This work focussed on Ca-based CO₂ sorbents for use in sorption enhanced steam reforming (SESR) of renewable feedstock. The first aim of the work was to carry out two literature reviews (Chapters 3 and 4). Chapter 3, which was compiled in 2009 compared Ca-based materials with alternative high temperature CO₂ capture materials. It demonstrated that Ca-based sorbents are a suitable option based on high capture capacity, fast reaction kinetics and low cost. Chapter 4 reviewed the alternative thermochemical routes to H₂ production from glycerol which is an opportunity to produce renewable energy from a waste stream. It revealed that SESR of glycerol is a highly viable route to production of high purity H₂ gas in comparison with the alternatives. It also found that laboratory scale SESR is often carried out in a reformer filled with catalyst which is inserted into an electrical furnace.⁵⁰⁻⁵² Such a setup incurs an energy penalty as the heat transfer encounters several thermal resistances from its place of origin (the furnace) to its point of use (the catalyst surface). Based on the background information gathered from the two literature reviews, three additional aims were added. In summary, the aims of this work were:

- To identify a suitable CO₂ sorbent for SESR of renewable liquid feedstock.
- To review the options for thermochemical production of H₂ from a renewable liquid feedstock.
- To understand the equilibrium thermodynamics of steam reforming and sorption enhanced steam reforming.
- To understand the effect on Ca-based materials of hydration and the inclusion of inert material with regards to capture capacity and stability over multiple cycles.
- To develop a method for studying CO₂ sorbents which can address the challenges derived from the limitations of conventional techniques.
- To produce H₂ from renewable liquid feedstock with and without sorbent using a novel reactor technology which can generate heat directly at the catalyst surface.

The objectives were:

- To carry out thermodynamic analysis using minimisation of Gibbs free energy of SR and SESR of methane, ethanol and glycerol.
- To manufacture Ca-based sorbents with incorporated inert material.

- To characterize selected Ca-based sorbents with regards to composition, morphology, surface area and porosity.
- To study the CO₂ capture capacity of selected sorbents using conventional techniques i.e. TGA and a bench scale reactor, as well as the non-conventional technique of in situ XRD coupled with Rietveld refinement.
- To develop the use of a novel wire reactor for steam reforming of liquid feedstock using a nichrome resistance wire functioning both as a heating element and a catalyst.
- To investigate different means of adding CO₂ sorbent to the novel wire reactor.

CHAPTER 2: MATERIALS AND METHODS

“Measure what is measurable, and make measurable what is not so”

Galileo Galilei

2.1 CHEMICALS

The chemicals used for preparation of the sorbent materials are listed in Table 2. 1. The chemicals were stored in ventilated cupboards at room temperature. The $\text{Al}(\text{NO}_3)_3$ granules clumped together so the lumps were broken up using a mortar before weighing to make the material easier to handle, and to facilitate weighing out the correct amount.

Table 2. 1. Chemicals used for prepare sorbent materials.

Chemical	Product name	Purity	Supplier
2-Propanol	2-Propanol Chromasolv Plus, for HPLC	99.9%	Sigma Aldrich, UK
$\text{Al}(\text{NO}_3)_3$	Aluminum nitrate nonahydrate	99+%	VWR international, UK
CaO	Calcium oxide	99.95% (metals basis)	Alfa Aesar, UK

2.2 PREPARATION OF $\text{CaO}/\text{Ca}_{12}\text{Al}_{14}\text{O}_{33}$

The $\text{CaO}/\text{Ca}_{12}\text{Al}_{14}\text{O}_{33}$ material was prepared using a modified version of a method described by Li et al.⁵³ 760 ml of deionised water was heated on a hot plate and agitated with a magnetic stirrer. When 75 °C was reached, 130 ml of 2-propanol was added together with 26.2g CaO and 28.4g $\text{Al}(\text{NO}_3)_3$. The amounts of CaO and $\text{Al}(\text{NO}_3)_3$ were adjusted so that the final material would have a composition of 75 wt% CaO and 25 wt% $\text{Ca}_{12}\text{Al}_{14}\text{O}_{33}$ which is the composition recommended by Li et al.^{53,54} The resulting solution was stirred for 1h at 75 °C. The beaker was put in an oven overnight at 120 °C in order to evaporate the water from the solution. The resulting cake was crushed to a fine powder using a mortar and the powder was heated in a furnace. The temperature was increased at 20 °C min⁻¹ from room temperature to 500 °C and kept at 500 °C for 3h. The resulting cake was crushed to a fine powder using a mortar and the powder was dissolved in deionised water to form a slurry. The slurry was placed in an oven and heated at 120 °C for 2h. The resulting cake was crushed to a fine powder using a mortar and the powder was heated in a furnace at 900 °C for 1.5h. In this case the furnace was preheated to 900 °C before the powder was placed inside it. The resulting powder was stored in a glass container with a screw-capped lid sealed with parafilm.

According to Li et al.⁵³ the addition of CaO powder to the mixture of water and 2-propanol results in the formation of ultrafine $\text{Ca}(\text{OH})_2$ particles. During heating at 500 °C $\text{Al}(\text{NO}_3)_3$ is predicted to form Al_2O_3 and during heating at 900 °C there will be both formation of CaO as well as a reaction between CaO and Al_2O_3 resulting in the formation of $\text{Ca}_{12}\text{Al}_{14}\text{O}_{33}$.

2.3 PREPARATION OF $\text{Ca}(\text{OH})_2$

$\text{Ca}(\text{OH})_2$ was prepared from CaO by carrying out steps 1-3 of the preparation of $\text{CaO}/\text{Ca}_{12}\text{Al}_{14}\text{O}_{33}$ without adding $\text{Al}(\text{NO}_3)_3$. After heating over night at $120\text{ }^\circ\text{C}$, the resulting cake was crushed. This preparation method resulted in a single phase $\text{Ca}(\text{OH})_2$ powder as shown by XRD powder diffraction.

2.4 PREPARATION OF CaO DERIVED FROM $\text{Ca}(\text{OH})_2$

For XRD, SEM and N_2 adsorption experiments, CaO derived from $\text{Ca}(\text{OH})_2$ by heating $\text{Ca}(\text{OH})_2$ (prepared according to section 2.3) to $700\text{ }^\circ\text{C}$ in a pure N_2 atmosphere in a quartz reactor inserted into a tube furnace (Figure 2. 1). CaO derived from $\text{Ca}(\text{OH})_2$ for use in TGA was prepared in the TGA setup (described in detail in Chapter 6, Section 6.5).

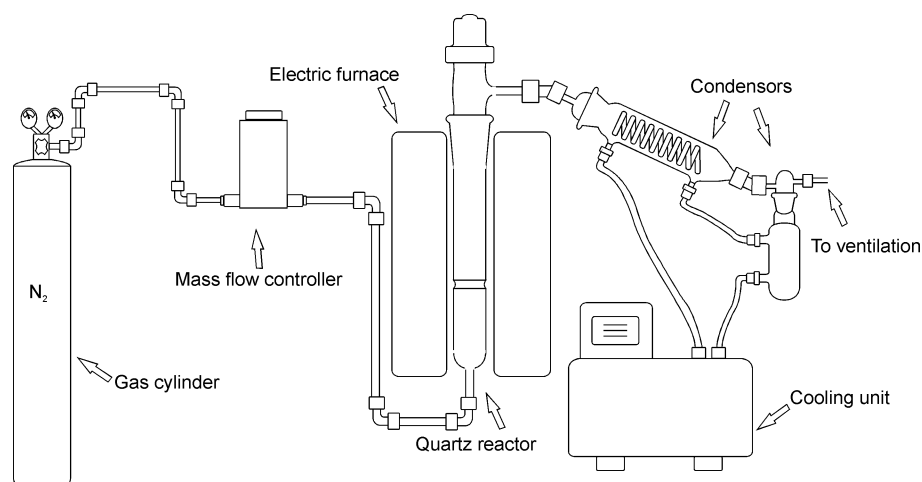


Figure 2. 1. Setup for preparation of CaO derived from $\text{Ca}(\text{OH})_2$.

2.5 PREPARATION OF SORBENT PARTICLES FOR BENCH SCALE REACTOR CARBONATION

Sorbent pellets were prepared and used for bench scale carbonation experiments. Earlier work on rigs with reactors of similar size has been carried out with sorbent particles in the size range of $0.66\text{-}2.0\text{ mm}$.^{23,55} The sorbent particle size range chosen for this work was $1.0\text{-}1.4\text{ mm}$.

The pellets were prepared by pressing the sorbent powders into large pellets, crushing these into smaller pellets with a mortar and separating out the small pellets with a size range of $1.0\text{-}1.4\text{ mm}$ using a set of sieves. The pellets were prepared under 2000 kg of pressure using a Specac 15.011 bench top hydraulic press. Two stainless steel laboratory test sieves (Endecotts ltd, UK) with aperture sizes of 1.0 and 1.4 mm respectively were stacked on top of each other (the sieve with a 1.4 mm aperture size on top and the sieve with a 1.0 mm aperture size underneath). The pellets were poured onto the sieve stack and the stack was shaken to separate

the pellets according to size by allowing pellets with a size lower than the aperture of any given sieve to pass through and by causing pellets with a size larger than the aperture to be retained. The size fraction of pellets left in the 1.0 mm aperture sieve (which had a size range of 1.0-1.4 mm) were collected and used for the bench scale rig sorption experiments.

2.6 THERMOGRAVIMETRIC ANALYSIS (TGA)

TGA involves continuously measuring the mass of a sample over time while changing temperature and environmental composition. This enables study of CO₂ capture as it involves an increase in mass. The sample is placed in a crucible which is suspended from a hang down connected to a balance. The crucible is positioned inside a furnace which controls the temperature. The atmosphere inside the furnace is controlled with gas flows from gas cylinders connected to the furnace with tubing.

The mass readings collected during TGA were used to derive measurements of CO₂ capture which are defined differently in the subsequent chapters depending on the context. CO₂ capture is either defined as the conversion of CaO to CaCO₃ on a molar basis or as the wt% CaCO₃ in the sample. The details of the calculations are given in the relevant chapters.

TGA of carbonation (Chapter 6, Section 6.5.1) was carried out using an air cooled TGA 50 Shimadzu thermogravimetric analyser with an alumina crucible and a TA 60 thermal data acquisition package. This was connected to a PC with TA 60 data collection software. For every run, the crucible was taken out and cleaned, after which the system was tared with the cleaned crucible back in place. A mass of 2 or 10 mg of sample was added to the crucible and the analysis was started. The temperature of the analyser's reactor was allowed to reach below 30 °C before another run was started. A blank run was carried out so that corrections for buoyancy effects could be made. Details of the blank run can be found in Chapter 6, Section 6.5.

TGA of cycling (Chapter 6, Section 6.5.2) was carried out using a Metler Toledo TGA/DSC Star system thermogravimetric analyser with a GC 100 Star system gas controller and an alumina crucible. The crucible was first weighed separately and then 10 mg of sample was added prior to analysis.

2.7 SCANNING ELECTRON MICROSCOPY (SEM)

The morphology of samples can be studied at high magnification using SEM. Changes in materials can be identified such as the formation of pores or smoothening of surfaces. Such changes can be used as evidence of processes such as sintering. In this work, secondary electron imaging was applied which involves sending a beam of electrons at the sample thereby causing secondary electrons from the sample to be emitted. The emitted electrons are then accelerated to

make them emit light which is converted to an electric signal and further converted to a digital image.

SEM images at 50kX magnification were taken with a Leo 1530 Field emission gun scanning electron microscope and saved in digital form using Smartsem v5 software. The samples were sputter coated with a Platinum/Palladium alloy containing 80% Platinum and 20% Palladium. The layer thickness of the coating was 20 nm.

2.8 X-RAY DIFFRACTION (XRD)

XRD can be used to identify phases in a powdered sample. X-rays are aimed at the sample at different diffraction angles and the scatter intensity of the ray is recorded. By displaying scatter intensity as a function of diffraction angle, a pattern of peaks is formed which is referred to as an XRD spectrum. XRD spectra are unique to every phase meaning that a spectrum of a known phase can be compared to the one derived from an unknown sample to investigate its components.

To minimise the error from instrumental peak broadening, a spectrum of a Si standard (NIST, SRM 640b) was first collected using X'Pert Data Collector software. Rietveld refinement was then carried out on the resulting spectrum using X'Pert HighScore Plus software from PANalytical (UK) using reference pattern 04-007-8736 from the International Centre for Diffraction Data (ICSD). The Si phase was subsequently used as a size strain standard. spectra were then collected from 2θ 15.026-130.000 ° using CuK α radiation with a continuous scan, at a scan speed of 0.101280 ° s⁻¹ for a total of 19 min and 19 s. The phases of the samples were identified using spectra of known phases from the International Centre for Diffraction Data (ICDD) data base. Rietveld refinement was carried out on the spectra and the scale factors derived from the refinement was used to calculate the weight fraction of each phase using Equation 2. 1.⁵⁶

$$W_p = \frac{S_p(ZMV)_p}{\sum_i S_i(ZMV)_i}$$

Equation 2. 1. S = Rietveld scale factor, Z = number of formula units per unit cell, M = mass of the formula unit, V = the unit cell volume.

2.9 IN SITU X-RAY DIFFRACTION

In situ XRD was carried out in order to monitor phase changes (e.g. from CaO to CaCO₃) and crystal lattice strain effects of sorbents during CO₂ capture. The sample was placed inside an HTK-1200 high temperature chamber XRD sample stage (Anton Paar, UK) which was connected to a Philips X'Pert XRD powder diffraction unit (Figure 2. 2). The temperature was controlled using X'Pert data collector Software from PANalytical (UK). To control the

atmosphere, gas cylinders were connected to one end of the high temperature chamber and a Dreschel bottle filled with water was connected to the other end using Swagelok® fittings and plastic tubing (Figure 2.8). A gas flow of 50 ml min⁻¹ was maintained using mass flow controllers with a range of 0-500 ml min⁻¹ (MKS, UK). By monitoring the bubbles rising through the water in the Dreschel bottle any loss of gas flow through the high temperature chamber could be detected. Spectra were collected from 2θ 14.993-130.000 ° using CuKα radiation with a continuous scan at a scan speed of 0.190986 ° s⁻¹ for a total of 10 min and 16 s. 12 such scans were carried out back to back for a total scan time of 2h, 3 min and 12s. Phase identification and quantification was carried out as described above. Spectra collected from ICSD with the reference codes 00-037-1497, 04-006-9147 and 04-007-0049 were used to identify the CaO, Ca(OH)₂ and CaCO₃ phases respectively.

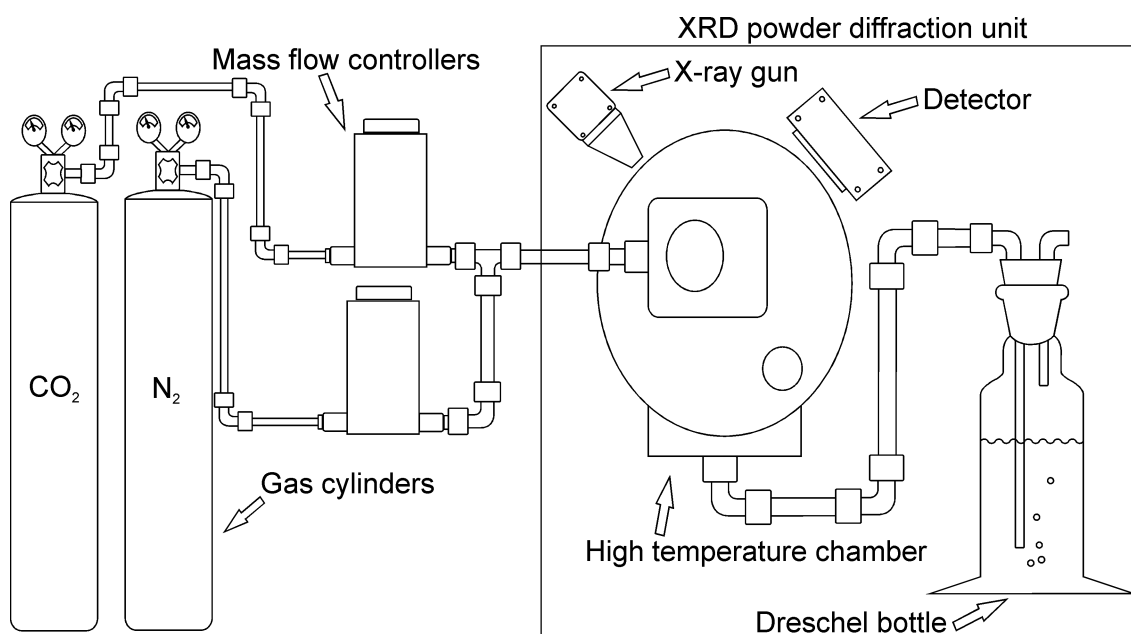


Figure 2. 2. Schematic of the in situ XRD experimental setup. The equipment on the left hand side was placed outside the XRD powder diffraction unit while the equipment enclosed within the rectangle on the right hand side was placed inside the XRD powder diffraction unit.

2.10 N₂ ADSORPTION ISOTHERMS

The surface area and the pore size distribution of a sample can be estimated by measuring the amount of gas molecules that adsorb onto it. First, the sample has to be prepared by removing all moisture and impurities from it. This is done by heating it under either a N₂ gas flow or in a vacuum and is referred to degassing. The degassing temperature and duration needed depends on the characteristics of the sample. When the sample is prepared it is put in the analyser (in this case a Nova® 2200 analyser from Quantachrome instruments, UK) and

subjected to a flow of N₂ under a set of different partial pressures (p/p_0) at -196 °C. The amount of gas molecules adsorbed onto the sample is calculated by the analyser which then derives values for the surface area using the BET method or the pore size distribution using the BJH method.

To measure the surface area and pore size distribution of the sorbents 200-300 mg of sample in pellet form (prepared according to Section 2.5) was degassed at 300 °C for 2h under N₂ flow followed by a 17 point N₂ adsorption isotherm at p/p_0 between 0.05 and 0.98. The p/p_0 was increased in increments of 0.05 between 0.05 and 0.40. The other points were at p/p_0 of 0.475, 0.54, 0.60, 0.68, 0.74, 0.80, 0.88, 0.94 and 0.98. Surface area was determined with NovaWin[®] software using the BET method⁵⁷ with the adsorption points between p/p_0 of 0.05 and 0.3. Pore size distribution was determined using the BJH method with all 17 adsorption points. The degassing conditions were chosen based on the conditions used in earlier work.^{58,59} A six point adsorption is the recommended standard setting for determining surface area using the BET method according to the analyser manufacturer. All surface area measurements are given in m²g⁻¹.

2.11 BENCH SCALE REACTORS

Two bench scale reactors were built, one for the study of carbonation of sorbent pellets (used in Chapter 6) and a wire reactor for steam reforming of liquid feedstock (used in Chapter 8). Both reactors were built using the same gas cylinders, gas tubing and fittings. Gas flows were controlled in the same way and they used the same off-gas cooling and water condensation system as well as the same off-gas composition measurement and data logging system. The systems shared by the reactors are described separately (Section 2.11.3).

2.11.1 REACTOR FOR CARBONATION OF SORBENT PELLETS

The reactor used for carbonation of sorbent pellets consisted of a CO₂ and an N₂ gas cylinder (Section 2.11.3.1) connected to a quartz reactor inserted into a TSV-10-20-85 electric heater (Elite thermal systems, UK) (Figure 2. 3).

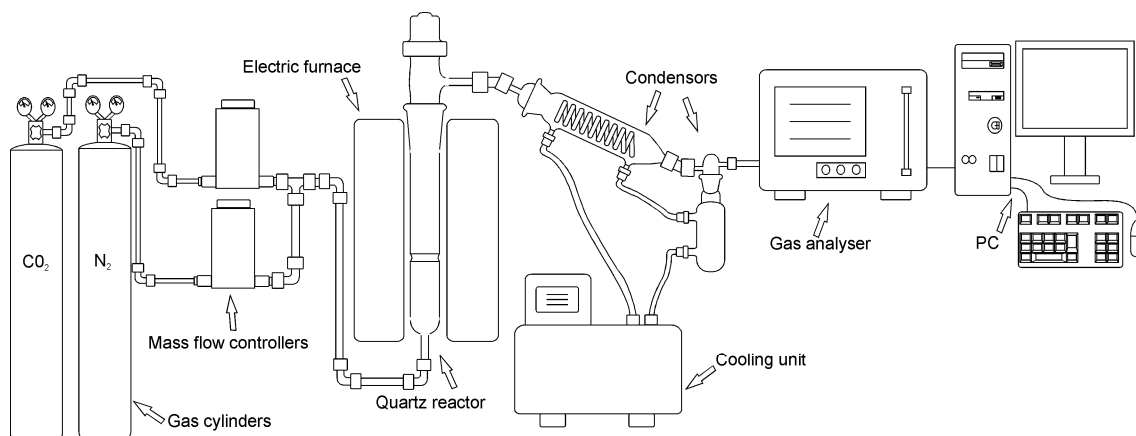


Figure 2. 3. Schematic of the reactor for carbonation of sorbent pellets.

The quartz reactor had two connection points to which plastics Swagelok[®] fittings were attached. It also had a screw cap on the top which contained a septum (Figure 2. 4). The temperature inside the reactor was controlled by the electric heater and the temperature was measured using a K-type thermocouple which was inserted inside the reactor through the septum in the screw cap. The thermocouple tip was placed at the top of the sorbent bed (Figure 2. 4) with the intention to monitor the temperature around the sorbent itself as opposed to the reactor as a whole. Therefore no temperature profile was determined. Note that the temperature control was carried out with a thermocouple that was part of the electric heater. The thermocouple was connected to the temperature and voltage logger for data logging (Section 2.11.3.5.1).

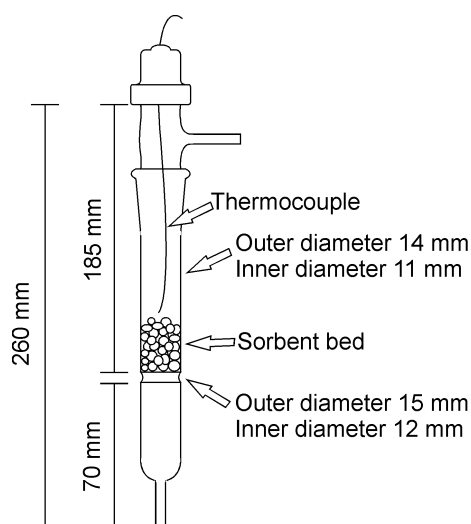


Figure 2. 4. Dimensions of the quartz tube reactor showing the position of the thermocouple.

The gas flows were controlled by mass flow controllers (Section 2.11.3.3). The reactor off gas was passed through an off-gas cooling system (Section 2.11.3.4) and into a gas analyser

(Section 2.11.3.5) and the data was logged on a PC which was connected to the analyser through a temperature and voltage logger (Section 2.11.3.5.1).

CO₂ capture was carried out by adding a known mass of sorbent with a known wt% of CaO into the quartz reactor, placing it inside the electric furnace and passing a gas mixture containing CO₂ and N₂ of known composition at a known flow rate through the reactor while controlling the reactor temperature using the electric furnace to induce CO₂ capture. Conversion of the sorbent was derived from the logged data according to Section 2.12.1.

2.11.2 WIRE REACTOR FOR STEAM REFORMING OF LIQUID FEEDSTOCK

The wire reactor for steam reforming (supplied by Johnson Matthew, UK) was used with glycerol and ethanol as feedstocks and consisted of an N₂ gas cylinder (Section 2.11.3.1) connected to a reactor through a spray injection system (model AL 01-8 from Delavan Spray Technologies, UK) (Figure 2. 5). The gas flow was controlled by a mass flow controller (Section 2.11.3.3). Also connected to the reactor through the spray injection system was a 50 ml glass syringe (SGE, UK) that was filled with a water and feedstock mixture of known composition and placed on a NE-100 syringe pump (New Era Pump Systems, inc., USA).

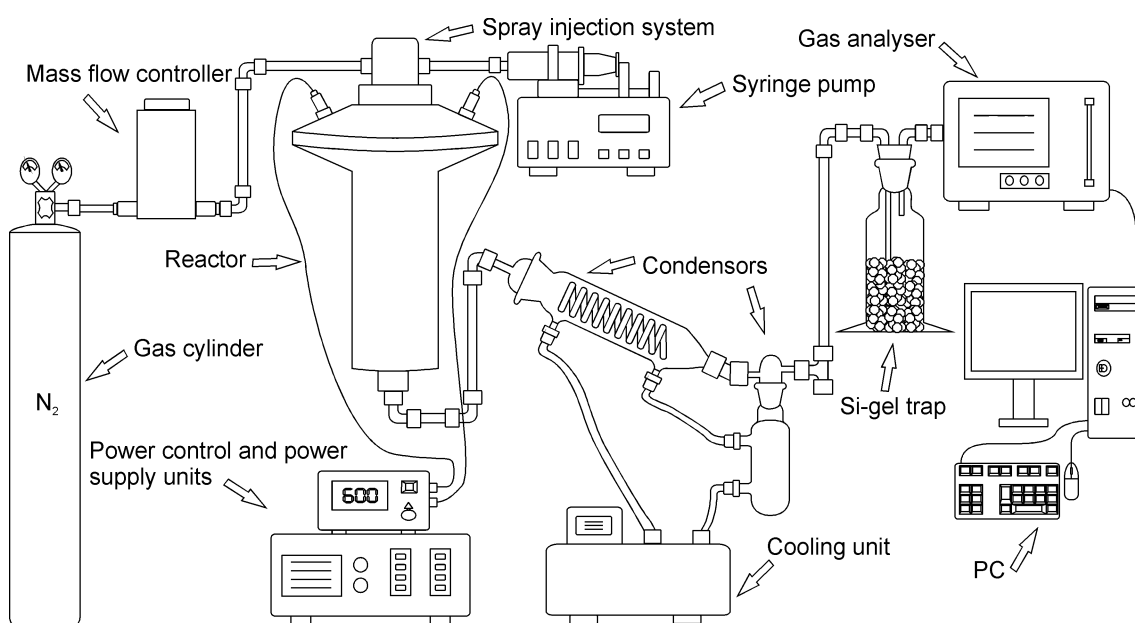


Figure 2. 5. Schematic of the wire reactor for steam reforming of liquid feedstock.

A 4 m length of nichrome resistance wire (80% Ni, 20% Cr) was threaded through a porcelain monolith consisting of 55 cylindrical shaped channels of 3 mm diameter and 80 mm length (Figure 2. 6) which was placed inside the reactor. A few channels were left without a length of wire threaded through them. These were sealed with Pyro Putty[®] (Aremco, USA) to stop input mixture from passing through them. The ends of the wires were then threaded through holes in the reactor top (Figure 2. 7). The lengths of the wires leading from the

monolith to the holes in the reactor top were covered with ceramic beads for heat insulation. The holes were sealed with an Opti-Tec high temperature epoxy adhesive (intertronics, UK). The ends of the nichrome resistance wires were connected to electric wires. The connections were covered with heat shrink for electric insulation. The bottom part of the reactor was wrapped in glass wool for thermal insulation (not shown in Figure 2. 5). The electric wires were connected to an OPX1200 DC power supply unit (TTi, UK) which in turn was connected to a power output unit containing a Eurotherm 2216e temperature controller and a solid state relay. The power output unit supplied a set voltage and allowed for the power control unit to pass an electric current to the nichrome resistance wire. The thermocouple inserted below the monolith (Figure 2. 7) was connected to the power supply unit to provide a feed back to it, thus enabling the power supply unit to adjust the current and achieve the set temperature. A second thermocouple was inserted above the monolith which was used to monitor the temperature above the monolith but was not used for temperature control. Ideally, the thermocouple used for temperature control would be inserted into a monolith channel in order to monitor the temperature in the centre of the reactor. However, this was extremely difficult to achieve in practice, especially since the reactor needed to be dismantled on a regular basis.

The set voltage was 46V and the maximum allowed current (as controlled by the power supply unit) was 9A. These settings were chosen based on information from the manufacturer.



Figure 2. 6. Image of the porcelain monolith.

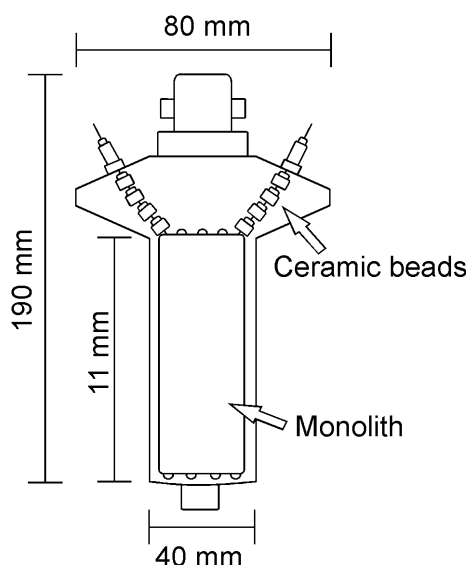


Figure 2. 7. Schematic of the inside of the reactor showing the monolith (and dimensions of the wire reactor).

The power output from the OPX1200 DC power supply unit was logged on a PC in order to monitor the amount of energy used for the steam reforming reaction. The power supply unit was connected to a PC using USB. The voltage and current outputs from the power supply was monitored using Labview software (National Instruments, UK) and logged once every second. The power output (P_{out}) was derived from the voltage (V_{out}) and current (I_{out}) outputs using Equation 2. 2:

$$P_{out} = V_{out} \times I_{out}$$

Equation 2. 2. Calculation of power output from voltage and current outputs.

Two different wires were used and they are described in detail in Chapter 8. The reactor off-gas was passed through a cooling and water condensation system (Section 2.11.3.4). The off-gas stream was then put through a gas analyser (Section 2.11.3.5). The data collected by the gas analyser was logged on a PC which was connected to the gas analyser through a temperature and voltage logger (Section 2.11.3.5.1). The temperature inside the reactor was monitored using two type K thermocouples (not shown in Figure 2. 7) connected to the temperature and voltage logger. One thermocouple measured the temperature above the monolith and the other one measured the temperature below the monolith.

Steam reforming was carried out by passing a N_2 gas through the spray injection system and the reactor while simultaneously injecting a water and feedstock mixture with a known composition into the spray injection system. The reactor was heated using the nichrome wire to induce the steam reforming process. Water was removed from the reactor off-gas using the gas

cooling and water condensation system to produce a dry gas which was passed through the gas analyser. The logged raw data was handled according to Section 2.12.2. The resulting data was investigated using the statistical analysis described in Section 2.13.

2.11.3 EQUIPMENT USED BY BOTH REACTORS

2.11.3.1 GAS CYLINDERS

High purity gases were used for the rigs (Table 2. 2). All gases were purchased from BOC (UK). The cylinders were fitted with regulators in order to safely release the gas from the cylinders. The regulators were used to set a gas pressure of 1bar.

Table 2. 2. Gases used for the bench scale reactors.

Gas	Product	Purity
N ₂	Nitrogen (oxygen free)	99.998 % + minimum
CO ₂	CP grade carbon dioxide	99.995 %

2.11.3.2 FITTINGS

¼ “ Swagelok[®] fittings and plastic tubing were used to transport the gas flow between the different parts of the rig. To avoid damage to the connections, brass fittings were used for brass connectors and stainless steel fittings were used for stainless steel connectors. The fittings used to connect to the glass reactor were made out of plastic so they would not crack the glass. All connections were leak tested using soapy water. The rig was pressurised to 100 bar using the regulators and the mass flow controllers were set at a flow of 100 ml min⁻¹. The connections were tested for leaks by dripping soapy water onto the connections. If there was a leak bubbles would be formed by the gas flow.

2.11.3.3 MASS FLOW CONTROLLERS

The mass flow controllers were purchased from MKS (UK). They were calibrated for CO₂, N₂ and air respectively and had a flow range of 0-500 ml min⁻¹. The flow range was chosen to fit size of the reactor as well as the gas analyser. Earlier steam reforming work on a reactor of similar size used gas flows of 200–600 ml min⁻¹⁶⁰ and the gas flow range permitted by the analyser was 333 ⅓ ml min⁻¹ to 1500 ml min⁻¹. To adjust the gas flow settings of the mass flow controllers they were connected to a four channel digital readout unit.

2.11.3.3.1 CALIBRATION OF MASS FLOW CONTROLLERS

The calibration was carried out using the digital readout unit and a handheld flow meter (Figure 2. 8). Since the mass flow controllers assumes standard temperature and pressure (STP)

when they control the gas flow, the temperature, pressure and gas flow must be measured in order to calculate the gas flow at STP which is produced by the mass flow controller.

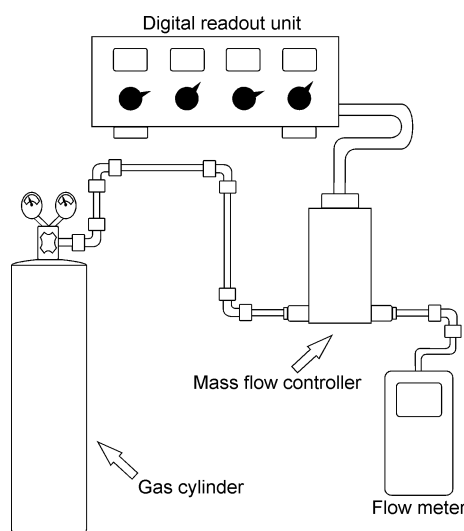


Figure 2. 8. Schematic of the mass flow controller calibration setup.

Gas flow, temperature and pressure can be described as:

$$\frac{PV}{T}$$

Equation 2. 3. P = pressure, V = velocity (or gas flow) and T = temperature

Gas flow under STP can be derived from the temperature, pressure and gas flow accordingly:

$$\frac{P_s V_s}{T_s} = \frac{P_l V_l}{T_l}$$

Equation 2. 4. P_s = standard pressure, V_s = standard velocity, T_s = standard temperature, P_l = pressure in the lab, V_l = velocity in the lab and T_l = temperature in the lab

$$V_s = \frac{P_l V_l T_s}{T_l P_s}$$

Equation 2. 5. As Equation 2. 4.

First T_l and P_l was measured. Then the gas pressure was set at 1 bar using the regulator on the gas cylinder and the digital readout unit was set to between 50 and 200 ml min⁻¹ depending on what gas flow would be used for the particular experiment. The flow reading on the digital

readout unit was noted and V_1 was measured using the handheld flow meter. V_s was then calculated using Equation 2. 4. The reading of the digital readout unit was adjusted so that it matched V_s .

2.11.3.4 GAS COOLING AND WATER CONDENSATION SYSTEM

In order to cool the off-gas coming from the reactors and to remove water from the off-gas it was first passed through a set of condensers cooled with a water/ethylene glycol mixture and then passed through a Si gel trap to remove residual water. Note that the CO₂ capture rig did not use the Silica gel trap (Figure 2. 3). The reason is that no water is used which needs to be removed from the reactor off-gas. In the case of the CO₂ capture rig, the gas only needs to be cooled in order to avoid harming the gas analyser. When the gas passed through the condensers it was cooled down so that it could safely be injected into the gas analyser without harming it. The water in the gas which was in a gas phase was converted to a liquid phase and was subsequently removed from the gas. Silica gel readily reacts with water and will hence remove water in a gas that is being passed through the gel. The condensers were made of borosilicate glass and were purchased from York glass (UK). A water/ethylene glycol mixture (Ethylene glycol from Fisher Scientific, UK) was pumped through the condensers using a 3006S refrigerated circulator (Fisher Scientific, UK). The Silica gel trap consisted of a Dreschel bottle filled to $\frac{2}{3}$ of its total volume with Silica gel (Merck Chemicals, UK).

2.11.3.5 GAS ANALYSER

The gas analyser was an ABB model EL 3020 with a Caldos 27 unit fitted with a thermal conductivity detector (TCD) to measure H₂ and a Uras 26 unit fitted with an IR absorption detector to measure CO, CO₂ and CH₄ through non dispersive infrared spectroscopy (NDIR). The Caldos 27 unit tolerated flows of 166 $\frac{2}{3}$ - 1500 ml min⁻¹ and the Uras 26 unit tolerated flows of 333 $\frac{1}{3}$ - 1666 $\frac{2}{3}$ ml min⁻¹ making the tolerated flow range of the gas analyser 333 $\frac{1}{3}$ - 1500 ml min⁻¹. Calibration was carried out using calibration gases. First, a flow on N₂ gas was put through the analyser to carry out a tare for CO, CO₂, CH₄ and H₂. Next, a flow of calibration gas containing 20% CO, 25% CO₂ and 25% CH₄ with N₂ as a balance was put through the analyser and the readings on the analyser display for each gas were set according to the calibration gas composition using the analyser's software. The same procedure was then carried out with a calibration gas containing 80% H₂ with N₂ as a balance. Note that the calibration with regards to H₂ assumed measurement of H₂ in the presence of N₂ only while the nichrome wire reactor off-gas contained CO, CO₂ and CH₄. These contribute to the total thermal conductivity of the off-gas thereby introducing an error. At 298K the thermal conductivity of H₂ is 0.18 W (mK)⁻¹ while the thermal conductivity of CO, CO₂ and CH₄ is 0.01, 0.02 and 0.04 W (mK)⁻¹ respectively.^{61,62} During most experiments the order of the gas concentrations were H₂ > CO >

$\text{CH}_4 > \text{CO}_2$ hence the majority of the error was derived from the presence of CO which had a thermal conductivity that is one order of magnitude lower than H_2 .

2.11.3.5.1 DATA LOGGING FOR GAS ANALYSER

For continuous logging of the readings from the gas analyser, a PC was connected to the gas analyser using a USB TC-08 temperature and voltage logger. PicoLog data logging software (version 5.20.1 from software and reference CD-ROM R.38) from Pico Technology was installed on the PC. The signal from the gas analyser output was an electric current which could not be measured with the logger. Therefore, a set of resistors were mounted on a circuit board and connected to the gas analyser output. This converted the electric current to a voltage which was in the ± 70 mV recommended range for the pico logger (Figure 2. 9).

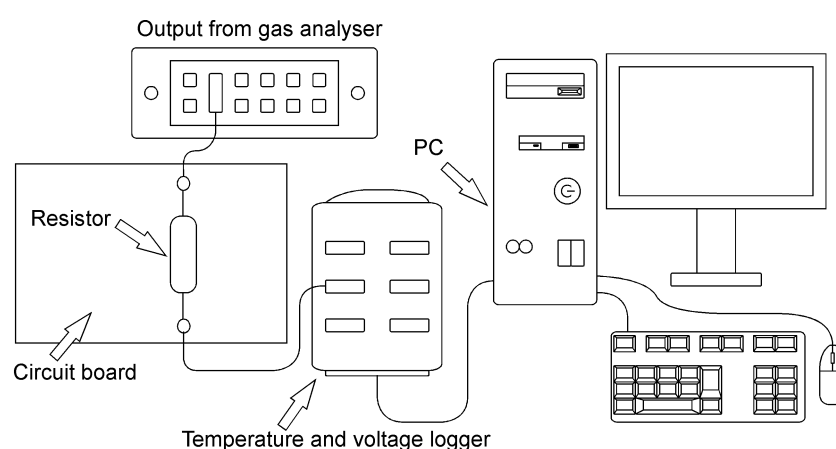


Figure 2. 9. Schematic of the data logging set up for the gas analyser.

To convert the voltage signal from the pico logger to a vol% reading that could be logged, the voltage readings for each gas as displayed by the pico logger software was noted as the N_2 gas and the calibration gases were passed through the analyser. This provided a voltage reading which corresponded to 0% (when N_2 was passed through the analyser) as well as to 20% in the case of CO, 25% in the case of CO_2 and CH_4 and to 80% in the case of H_2 (when the calibration gases were passed through the analyser). The pico logger software allows for adjustment of the voltage reading according to two sets of data points with each set corresponding to an X and a Y value in a graph (Figure 2. 10). The software then uses the slope of the resulting curve to display a corresponding Y value as a reading for each X value. In this case the two sets of data points originate from the voltage readings from the pico logger and the analyser readings when N_2 and calibration gases were used respectively. The voltage readings were entered as X values and the analyser readings as Y values. Figure 2. 10 shows the two sets of data points acquired for the CO_2 gas. In this case the N_2 gas produced a voltage reading of 2.894 mV and an analyser

reading of 0.17% while the calibration gas produced a voltage reading of 12.455 mV and an analyser reading of 25.53%.

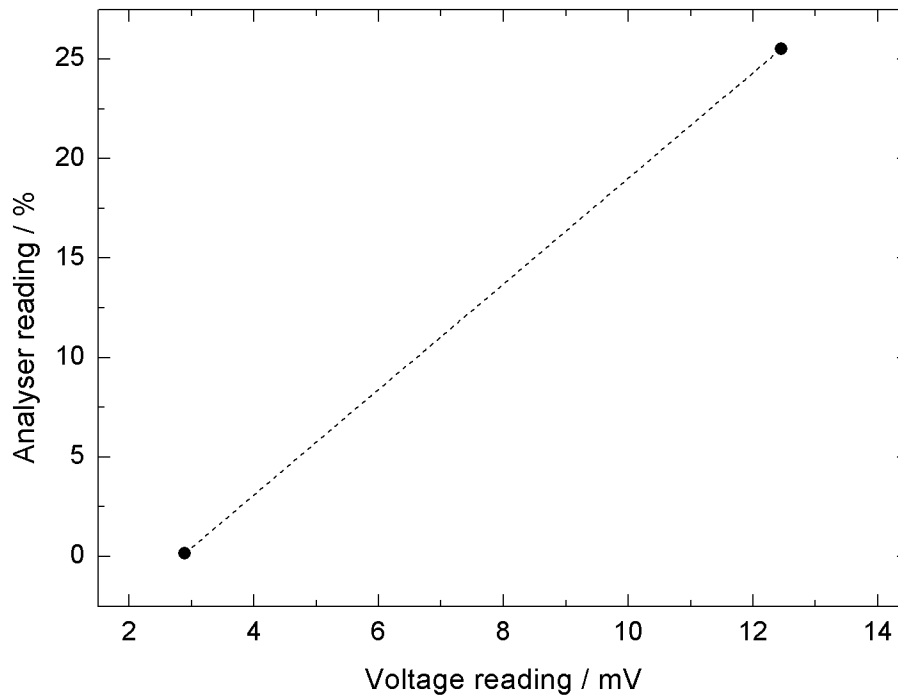


Figure 2. 10. Voltage and analyser readings collected during flows of N₂ and of CO₂ calibration gas entered as X and Y values and the resulting curve.

2.12 RAW DATA ANALYSIS

2.12.1 REACTOR FOR CARBONATION OF SORBENT PELLETS

Conversion of sorbents in the bench scale reactor was calculated by relating the amount of CO₂ leaving the reactor (CO₂ %_{out}) to the known flow (CO₂ flow_{in}) and vol% (CO₂ %_{in}) of CO₂ in the gas entering the reactor together with the known sorbent mass (Mass_{sorbent}) and the amount of CaO in the sorbent (Mass%_{CaO}). The raw data showed a reduced CO₂ concentration in the order of 0.5-2.5%. The amount of CO₂ entering the reactor was 12.5%. First, the CO₂ capture rate was determined. The amount of captured CO₂ was calculated by plotting CO₂ capture rate with time on stream and then integrating the resulting curve over time. Sorbent conversion was then calculated by relating the moles of captured CO₂ the moles of CaO inside the reactor. The CO₂ capture rate was calculated from the raw data accordingly:

Molar rate of CO₂ entering the reactor ($M_{CO_2 in}$) Where P, R and T are standard pressure the gas constant and standard temperature respectively:

$$M_{CO_2 in} = \frac{P CO_2 flow in}{R T}$$

Molar rate of CO₂ leaving the reactor ($M_{CO_2 out}$):

$$M_{CO_2 out} = CO_2 \% out \left(\frac{M_{CO_2 in}}{CO_2 \% in} \right)$$

The CO₂ capture rate ($CO_2 capture rate$) was defined as:

$$CO_2 capture rate = M_{CO_2 out} - M_{CO_2 in}$$

Since every vol% reading was taken every 5 seconds, integration to CO₂ capture ($M_{CO_2 capture, 5s}$) was carried out for each reading accordingly:

$$M_{CO_2 capture, 5s} = CO_2 capture rate \times 5$$

The number of moles of CO₂ captured at any given time t ($M_{CO_2 capture}$) is therefore:

$$M_{CO_2 capture} = \int_0^5 CO_2 capture rate dt$$

A conversion at time t is then given as outlined below where M_{CaO} is the amount of moles of CaO in the sample, M_{CaO} is derived from the sample mass and the wt% CaO in the sample:

$$Conversion (\%) = \left(\frac{M_{CO_2 capture}}{M_{CaO}} \right) \times 100$$

2.12.2 WIRE REACTOR FOR STEAM REFORMING OF LIQUID FEEDSTOCK

Elemental balances of N, C and H were applied to determine molar production rates, feedstock and water conversion as well as selectivity to carbon and hydrogen containing species during the experimental work carried out with the nichrome wire reactor.

Inputs of N, C and H were known from the N₂ carrier gas flow and the input mixture (feedstock and water) flow as well as the composition of the input mixture and the elemental

composition of the feedstock. The outputs were calculated from the gas analyser readings of H₂, CO, CO₂ and CH₄ in the dry reactor off-gas. In the calculations below the composition of the feedstock is referred to as C_nH_mO_k where the values of *n*, *m* and *k* differ depending on what feedstock (glycerol or ethanol) is used.

2.12.2.1 INPUTS

In the equations below, the molar flow rates are in mole s⁻¹ except when specified (i.e. μmole s⁻¹), volume flow rates in m³ s⁻¹, gas molar volumes in m³ mol⁻¹, liquid densities in kg m⁻³ molar masses in kg mol⁻¹ and mass flow rates in kg s⁻¹.

The input of N was derived solely from the N₂ carrier gas, while the input of C was derived solely from the feedstock and the input of H was derived from both feedstock and water.

The input molar flow rate of N (*n_{N,in}*) was calculated from the (volumetric) N₂ carrier gas flow rate (*V_{N2}*) and the molar volume of N₂ at STP:

$$n_{N,in} = \left(\frac{V_{N_2}}{N_2 \text{ molar volume at STP}} \right) \times 2$$

Equation 2. 6. Calculation of input molar flow rate of N (*n_{N,in}*) used in Chapter 8. *V_{N2}* = volumetric N₂ carrier gas flow.

The feedstock input molar flow rate (*n_{C_nH_mO_k,in}*) was defined as the ratio of the input mixture mass flow (*M_{flow C_nH_mO_k}*) and the molar mass of the feedstock (*W_{C_nH_mO_k}*). The input mixture mass flow was in turn calculated from the density (*ρ_{in mix}*) and the volumetric flow rate (*V_{in mix}*) of the input mixture and the mass fraction of feedstock (*M_{Frac C_nH_mO_k}*) in the input mixture.

$$n_{C_nH_mO_k,in} = \frac{M_{flow\ C_nH_mO_k}}{W_{C_nH_mO_k}} = \frac{M_{Frac\ C_nH_mO_k} \times \rho_{in,mix} \times V_{in,mix}}{W_{C_nH_mO_k}}$$

Equation 2. 7. Calculation of feedstock input molar flow rate. *M_{flow C_nH_mO_k}* = input mixture mass flow, *W_{C_nH_mO_k}* = feedstock molar mass, *M_{Frac C_nH_mO_k}* = feedstock mass fraction, *ρ_{in mix}* input mixture density, *V_{in mix}* = input mixture volumetric flow rate.

The water input molar flow rate ($n_{H_2O, in}$) was calculated the same way as feedstock input molar flow rate, i.e.:

$$n_{H_2O, in} = \frac{M_{flow H_2O}}{W_{H_2O}} = \frac{M_{Frac H_2O} \times \rho_{in, mix} \times V_{in, mix}}{W_{H_2O}}$$

Equation 2. 8. Calculation of water input molar flow rate. $M_{flow H_2O}$ = input mixture mass flow, W_{H_2O} = feedstock molar mass, $M_{Frac H_2O}$ = feedstock mass fraction, $\rho_{in mix}$ input mixture density, $V_{in mix}$ = input mixture volumetric flow rate.

$M_{Frac \alpha}$ was defined accordingly were M = mass, = $C_nH_mO_k$ or H_2O :

$$M_{Frac \alpha} = \frac{M_{\alpha}}{M_{C_nH_mO_k} + M_{H_2O}}$$

The density of the input mixture ($\rho_{in mix}$) was defined as:

$$\rho_{in mix} = \frac{M_{C_nH_mO_k} + M_{H_2O}}{Volume\ of\ input\ mixture}$$

2.12.2.2 OUTPUTS

Outputs were calculated from the gas analyser readings. The gas analyser readings (i.e. the raw data collected) were given in vol% and the vol% of N_2 was calculated accordingly:

$$100 - \sum \text{gas analyser readings of } H_2, CO, CO_2 \text{ and } CH_4$$

The vol% readings of H_2 , CO , CO_2 , CH_4 and N_2 were divided by 100 to give their dry output mole fractions (y_{α}) in the reactor off-gas (where α is the relevant species).

2.12.2.3 ELEMENTAL BALANCES FOR N, C AND H

The N balance (Equation 2. 9) was determined based on the N input molar flow rate ($n_{N,in}$) and the dry output N_2 molar fraction (y_{N_2}) determined as described above. The total dry output molar flow rate ($n_{out,dry}$) is unknown.

$$n_{out,dry} = \frac{n_{N,in}}{2 \times y_{N_2}}$$

Equation 2. 9. N balance. $n_{N,in}$ = N input molar flow rate, y_{N_2} = dry output N_2 molar fraction.

Input for the C balance (Equation 2. 10) was determined based on the input feedstock molar flow rate ($n_{C_nH_mO_k,in}$). The output of the C balance was determined based on the dry output molar fractions of CH_4 (y_{CH_4}), CO (y_{CO}) and CO_2 (y_{CO_2}) as calculated from the gas analyser readings (see above). Unknowns were the dry total output molar flow rate ($n_{out,dry}$) and the output feedstock output molar flow rate ($n_{C_nH_mO_k,out}$).

$$(y_{CH_4} + y_{CO} + y_{CO_2} \times n_{out,dry}) + n_{C_nH_mO_k,out} = n_{C_nH_mO_k,in}$$

Equation 2. 10. C balance. y = output molar fraction, $n_{out,dry}$ = the total dry output molar flow rate, $n_{C_nH_mO_k,out}$ = feedstock output molar flow rate, $n_{C_nH_mO_k,in}$ = feedstock input molar flow rate, subscript n = number of C atoms in feedstock.

The input for the H balance (Equation 2. 11) was determined based on the input molar flow rate of feedstock ($n_{C_nH_mO_k,in}$) and water ($n_{H_2O,in}$). The output of the H balance was determined based on the dry output molar fractions of CH_4 (y_{CH_4}) and H_2 (y_{H_2}) as calculated from the gas analyser readings. Unknowns were the dry total output flow rate ($n_{out,dry}$) the water output flow rate ($n_{H_2O,out}$) and the feedstock output molar flow rate ($n_{C_nH_mO_k,out}$).

$$(4y_{CH_4} + 2y_{H_2})n_{out,dry} + 2n_{H_2O,out} + m \times n_{C_nH_mO_k,out} = m(n_{C_nH_mO_k,in}) + 2n_{H_2O,in}$$

Equation 2. 11. H balance. y = output molar fraction, $n_{out,dry}$ = the dry total output molar flow rate, $n_{H_2O,out}$ = water output molar flow rate, $n_{H_2O,in}$ = water input molar flow rate, $n_{C_nH_mO_k,out}$ = feedstock output molar flow rate, $n_{C_nH_mO_k,in}$ = feedstock input molar flow rate, m = value of m in feedstock.

The unknowns, i.e. dry total output molar flow rate ($n_{out,dry}$), water output molar flow rate ($n_{H_2O,out}$) and feedstock output molar flow rate ($n_{C_nH_mO_k,out}$) were determined from the three elemental balances using the determinants method (not shown here for brevity).

2.13 STATISTICAL ANALYSIS

Statistical analysis was carried out on data logged during experimental work with the wire reactor using Minitab software (Minitab inc, USA). The Mann-Whitney non parametric test and the student's t-test was used to determine whether or not two data sets were significantly different. When two data sets were examined the data points from each data set which were at least 1.5x the interquartile range (Q1-Q3) below the first quartile or above the third quartile were considered outliers and were removed. The data sets were tested for normality using the Anderson-Darlin test. If both sets were normal the F-test was used to test homogeneity of variance between the data sets. The student's t-test was then used assuming either homogeneity of variance or not depending on the result of the F-test. If one or both of the data sets were not normal, the Mann-Whitney non parametric test was used. A significance level of 0.05 was used for all statistical analysis. The details of any statistical analysis including information on which test was used, the test statistic, the n-value and the significance level is given in brackets in the text. For example ($T_{(308)} = -45.84, p < 0.05$) means student's t-test, test statistic = -45.84, n-value = 308 and significance level below 0.05. Likewise ($W_{(24)} = 79, p < 0.05$) means Mann-Whitney non parametric test, test statistic = 79, n-value = 24 and significance level below 0.05.

The value of a data set is given as either the mean and the standard deviation or as the median depending on the result of an Anderson-Darling test after the removal of outliers as described above. The value of data sets that follow a normal distribution are given as the mean and the standard deviation while the value of data sets that do not follow a normal distribution are given as the median. The details of the Anderson-Darling test is given in brackets in the text. For example ($AD_{(401)} = 4.84 p > 0.05$) means Anderson-Darling test statistic = 4.84, n-value = 401 and significance level above 0.05. Note that the null hypothesis for the Anderson-Darling test is that the data follows a normal distribution meaning that a significance level above 0.05 means that the data set follows a normal distribution.

2.14 THERMODYNAMIC ANALYSIS

Thermodynamic analysis based on minimisation of Gibbs free energy was carried out using the code EQUIL from the CHEMKIN package.⁶³ Details of the thermodynamic analysis including input and output species and definitions used for H₂ yield etc. are presented and discussed in detail in Chapter 5.

CHAPTER 3: CO₂ SORBENTS FOR MEDIUM AND HIGH TEMPERATURE PROCESSES

“If I have seen further than others, it is by standing upon the shoulders of giants”

Isaac Newton

3.1 INTRODUCTION

CO₂ capture is used in many applications at a wide variety of temperatures. The majority of the low temperature (<200 °C) applications involve the removal of CO₂ from gas streams, for example removal of CO₂ impurities from natural gas.^{64,65} Prevention of CO₂ build up is required for a variety of reasons; such as preventing pressure build up in food packages if CO₂ is produced by vegetable fermentation and avoiding crew suffocation in spacecraft due to the CO₂ from respiration.⁶⁶⁻⁶⁸ Carbon capture and storage (CCS) of CO₂ has been suggested as a technique for reducing CO₂ emissions from the use of fossil fuels.⁶⁹⁻⁷¹ The technique typically involves the capture of CO₂ from a coal or gas-fired power station, after which it is pressurised to form a liquid which is injected into underground rock formations or saline aquifers for storage.²⁷⁻²⁹ Post combustion CO₂ capture can be carried out at 40 °C on flue gas from a conventional coal gasifier.^{19,71} Novel zero emission coal based power generation systems require removal of CO₂ within the coal gasifier where temperatures reach 500-1000 °C.⁷⁰ Another novel technology which requires CO₂ capture at high temperatures is sorption enhanced steam reforming for production of high purity hydrogen.²⁰ The purity of the hydrogen product can be very significantly improved by the addition of a CO₂ capture material which removes CO₂ as it is formed thus shifting the equilibrium of the water gas shift reaction towards hydrogen formation, CO consumption and hence increased fuel conversion according to Le Chatelier's principle. Steam reforming for hydrogen production often uses methane as a feedstock where temperatures of around 800 °C are needed.⁷² However, renewable fuels such as sunflower oil, waste products such as glycerol from biodiesel refineries, or waste cooking oil can also be used as steam reforming feedstocks at temperatures of 600 °C.^{23,72,73}

An ideal CO₂ capture material should exhibit high capture capacity, durability, fast capture/release kinetics and good mechanical strength. Many materials can be used to capture CO₂ but their conditions of carbonation or physisorption of the CO₂ vary from low (T<200 °C), to medium (200 °C<T<500 °C) and high temperatures (T>500 °C). Materials used for low temperature CO₂ capture include zeolites, amines, activated carbon and silica gel. Promising novel materials that have received much attention are zeolitic imidazolate frameworks (ZIFs) and metal organic frameworks (MOFs).⁷⁴⁻⁷⁶

Zeolites are crystalline, porous aluminosilicates with CO₂ capture capacities of 9-31 wt% at temperatures between 0 and 30 °C.^{64,77-79} Increasing the temperature reduces CO₂ capture.^{80,81} Zeolites have shown good selectivity of CO₂ over CH₄ and have therefore been considered for use in natural gas purification.^{64,65} They have also been tested for purification of H₂ from flue gas from steam reforming of CH₄.⁷⁹ However, optimum removal was found to be at 30 °C indicating that the gas first needs to be cooled down before purification can be carried out.

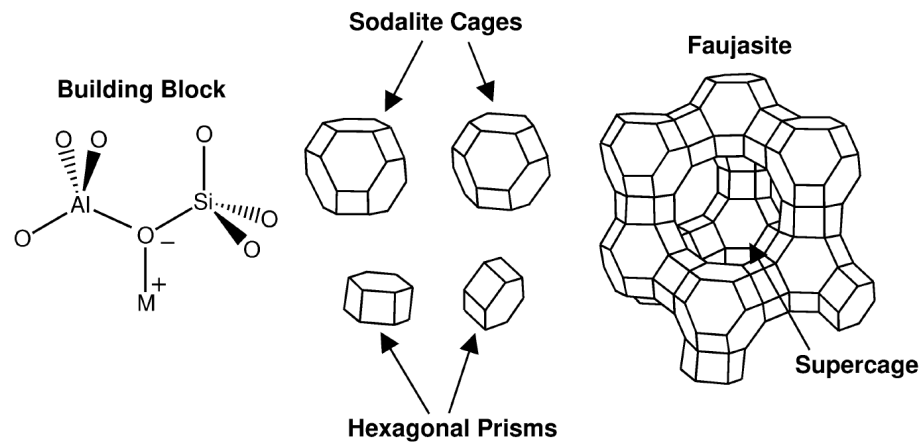


Figure 3. 1. Schematic diagram of a faujasite-type zeolite (M^+ is a charge balancing cation). Reprinted with permission from Davies (2003).⁸² Copyright 2003 Elsevier.

Metallic organic frameworks (MOFs) are a novel group of materials that are suitable for CO₂ capture in the temperature range of 22–31 °C where capture capacities of 13–22 wt% have been reported.^{83–87} MOFs have large molecular structures with cages and channels that can store gas molecules.^{88,89} The sizes of pores on the surface of the MOF structure determine what molecules can enter the cages and channels meaning that MOFs can separate gases according to their molecular size.^{83,89} This makes MOFs promising materials for gas separation applications.

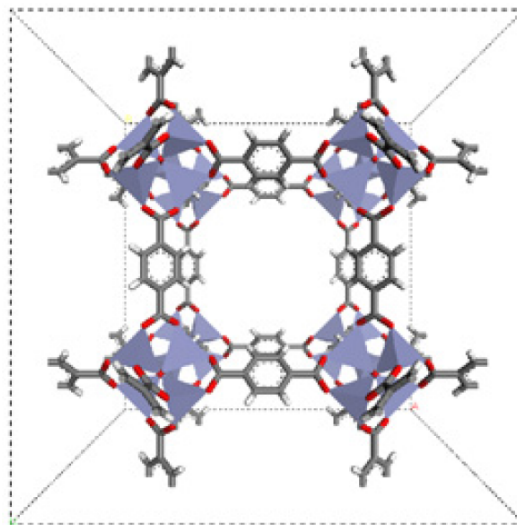


Figure 3. 2. Structure of a metallic organic framework (MOF-5). Reprinted with permission from Lee et al. (2007).⁹⁰ Copyright 2007 Elsevier.

Amines can also be used for CO₂ capture. Amino groups capture CO₂ by the formation of a carbamic salt.⁹¹ Amine scrubbing is a widely used and well understood technology currently used for removal of CO₂ from flue gases. The flue gas is passed through an absorber containing

an amine liquid like Monoethanolamine (MEA), where the CO₂ is removed. The CO₂ is removed from the amine liquid in a stripper. Amine scrubbers can be used for CCS by adding them to existing conventional coal gasification for post combustion CO₂ capture at 40 °C.⁷¹ Monoethanolamine (MEA) is often used for amine scrubbing but other amines such as piperazine and KS-1 are also being considered.¹⁹ Adding polyethyleneimine (PEI) to a polymethyl methacrylate support can be used for CO₂ capture in spacecrafts.⁶⁸ Adding PEI to a mesoporous molecular sieve (MCM-41) results in materials which can capture 13.3 wt% CO₂ at around 75 °C.^{92,93}

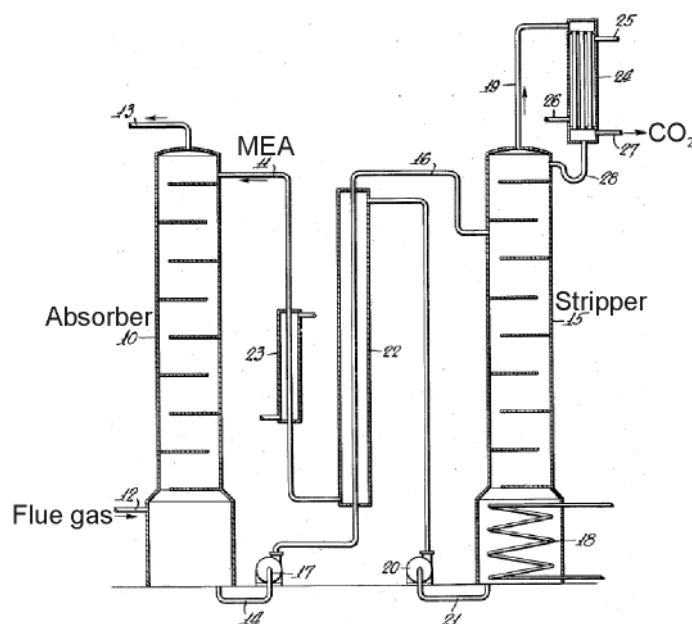


Figure 3. 3. The amine scrubber process as described in US Patent 1783901.⁹⁴

For the novel medium and high temperature applications, three kinds of materials in particular have displayed promising characteristics namely lithium ceramics, hydrotalcites and Ca-based materials.⁹⁵⁻⁹⁷ All of these materials involve capture of CO₂ by the formation of carbonates.⁹⁸⁻¹⁰⁰ CO₂ can be removed from gas mixtures by passing the mixture through a packed or fluidised bed system containing a CO₂ capture material by carrying out a continuous capture/ release cycle. By heating the system to the optimum carbonation temperature, the CO₂ capture material removes CO₂ from the gas mixture.¹⁰¹ When the material reaches its maximum CO₂ capture capacity, it can be regenerated via calcination or desorption which can be induced by either a temperature or pressure change, or a shift in atmospheric composition.

Recently a large body of research has been carried out with the objective of finding suitable materials for capture of CO₂ at medium and high temperatures and cyclic CO₂ capture through repeated carbonation-calcination reactions. This review aims to evaluate existing materials suggested for CO₂ capture in medium and high temperature processes. The scope of

the review is the capture capacity, capture kinetics, operating temperature range and durability of lithium ceramics, hydrotalcites and Ca-based materials in CO₂ capture. These characteristics, together with their cost and availability will be used to evaluate the materials suitability for medium and high temperature CO₂ capture applications.

3.2 POTENTIAL MATERIALS FOR CO₂ CAPTURE IN MEDIUM AND HIGH TEMPERATURE PROCESSES

3.2.1 LITHIUM CERAMICS

Lithium has been proposed as a CO₂ capture material due to its ionic mobility and affinity for CO₂.¹⁰² However, lithium is expensive. In 2008 the world mine production of lithium was 27 400 metric tonnes and in 2007 the price of lithium carbonate was \$6 000-7 000 per metric tonne.^{103,104} The largest market for lithium is for use in rechargeable batteries.¹⁰³ A number of lithium ceramics have been tested for CO₂ capture at high temperatures from the simplest lithium ceramic Li₂O to more complex materials like Li₂ZrO₃, Li₂CuO₂, Li₄SiO₄ and Li₅AlO₄.^{102,105-108} Attempts have also been made to increase the CO₂ capture capacity and uptake kinetics by doping with Y₂O₃ and K₂CO₂.^{100,109} Table 3.1 lists the reactions of carbonation and CO₂ release that each of these materials undergoes.

Table 3.1. CO₂ capture/release mechanisms of lithium ceramics.

Lithium ceramic	CO ₂ capture/release mechanism	Reference
Li ₂ O	Li ₂ O + CO ₂ ↔ Li ₂ CO ₃	102
Li ₂ ZrO ₃	Li ₂ ZrO ₃ + CO ₂ ↔ Li ₂ CO ₃ + ZrO ₂	106
Li ₄ SiO ₄	Li ₄ SiO ₄ + 2 CO ₂ ↔ 2 Li ₂ CO ₃ + SiO ₂	110
Li ₂ CuO ₂	Li ₂ CuO ₂ + CO ₂ ↔ Li ₂ CO ₃ + CuO	107
Li ₅ AlO ₄	2 Li ₅ AlO ₄ + CO ₂ ↔ 5 Li ₂ CO ₃ + Al ₂ O ₃	108

Li₂O displayed a very high CO₂ capture capacity of up to 226 wt% in a pure CO₂ atmosphere at around 700 °C.¹⁰² CO₂ capture investigation was conducted using TGA at 600 °C in a pure CO₂ atmosphere for 2h, after which cracks and fractures were found in the Li₂O particles. These were attributed to the volume expansion following formation of Li₂CO₃. At temperatures around 200-400 °C a layer of Li₂CO₃ formed around the particles through which CO₂ could not diffuse.¹⁰² However, the CO₂ capture capacity of the Li₂CO₃ material increased significantly above 600 °C which was attributed to a sharp increase in the diffusion of Li through the Li₂CO₃ layer allowing additional CO₂ capture.

Li₂ZrO₃ has been extensively studied for CO₂ capture and the general mechanism for capture is the formation of a Li carbonate and a Zr oxide (Table 3.1). Li₂ZrO₃ displayed a CO₂ capture capacity of 11.6-28 wt% at temperatures between 400 and 600 °C.^{95,100,109} CO₂ capture rate was improved by increasing the temperature from 400-600 °C.¹⁰⁹ At 400 °C it took 15 000

min to reach 20 wt% while it took 3 000 min at 500 °C and 1 000 min at 600 °C to reach 20 wt%. At 500 °C Ida and Lin¹⁰⁰ and Fauth et al.⁹⁵ reported CO₂ uptakes of 20 wt% after 7 500 min and 11.6 wt% after 1 500 min respectively. The CO₂ capture decreased with reduced partial pressure of CO₂ in the atmosphere. A threshold of 0.3 bar has been identified below which the CO₂ capture is significantly reduced.^{106,111}

Ida and Lin¹⁰⁰ proposed a double shell model to describe the CO₂ capture and release mechanisms of Li₂ZrO₃ (Figure 3. 4). Their suggested mechanism was the formation of a solid inner ZrO₂ shell preventing the diffusion of CO₂ between an outer Li₂CO₃ shell, and unreacted Li₂ZrO₃ in the centre of the particle.

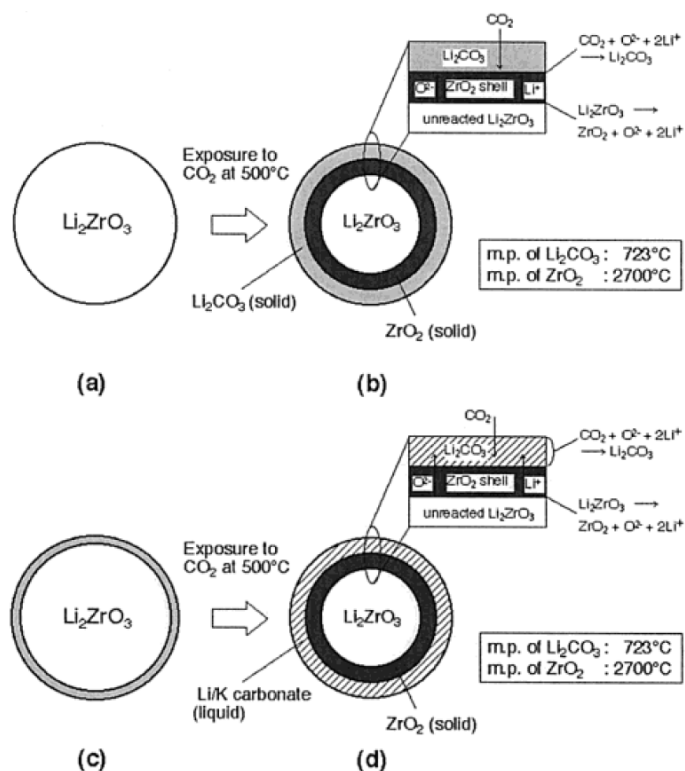


Figure 3. 4. Double shell model proposed by Ida and Lin (2003). Reprinted with permission from Ida and Lin (2003).¹⁰⁰ Copyright 2003 American Chemical Society.

Doping with Y₂O₃ and K₂CO₃ has been observed to improve the CO₂ capture capacity and capture kinetics of Li₂ZrO₃. When K₂CO₃ was added to Li₂ZrO₃ it took 250 min to reach a CO₂ capture of 20 wt% compared to 10 000 min for untreated Li₂ZrO₃ at a temperature of 500 °C.¹⁰⁰ This is equal to a forty-fold improvement in the CO₂ capture rate.

Fauth et al.⁹⁵ tested several compound combinations for doping of lithium ceramics. They reported that at 700 °C in a pure CO₂ atmosphere, a mixture of K₂CO₃, NaF and Na₂CO₃ displayed the best performance with regards to CO₂ capture rate and total CO₂ capture capacity with 17-18 wt% in 60 min. Doping resulted in the formation of eutectic compound mixtures

with a low melting point. Doping with K₂CO₃ resulted in a Li₂CO₃/K₂CO₃ mixture with a melting point of 498 °C, which means that the outer shell of the Li₂ZrO₃ particles were in a liquid state during CO₂ capture at 500 °C.¹⁰⁰ This was suggested to have caused an increased diffusion of CO₂ through the surface layer with a subsequent increase in CO₂ capture.^{95,100} In K₂CO₃ doped Li₂ZrO₃ the rate limiting step above 500 °C was the diffusion of oxygen ions through the ZrO₂ shell.^{109,112} Doping Li₂ZrO₃ with both Y₂O₃ and K₂CO₃ increased the CO₂ capture rate compared to Li₂ZrO₃ doped with K₂CO₃ alone.¹⁰⁹ After 20 min the CO₂ capture for Y₂O₃ and K₂CO₃ doped Li₂ZrO₃ was 17 wt% while the capture for K₂CO₃ doped Li₂ZrO₃ was 12 wt% in at temperature of 650 °C. The results were attributed to oxygen vacancies in the ZrO₂ layer introduced by the Y³⁺ ion.¹¹³ This resulted in enhanced diffusion of lithium and oxygen ions with a subsequent increase in CO₂ capture kinetics.¹⁰⁹ The CO₂ capture capacity was also found to increase from 8 to 23 wt% when 30% steam was added in an atmosphere of 10% CO₂ in N₂ at 500 °C.

Particle size of Li₂ZrO₃ has been reported to influence CO₂ capture characteristics.^{111,112,114} Xiong et al.¹¹² prepared two sets of Li₂ZrO₃ material using ZrO₂ particles with sizes of both 1 and 45 μm as starting material. The resulting materials had average particles sizes of around 10 and 30 μm respectively with the smaller ZrO₂ particles producing the smaller Li₂ZrO₃ particles and vice versa. After 45 min at 650 °C, the 10 μm Li₂ZrO₃ particles showed a CO₂ uptake of 19 wt% while the 45 μm Li₂ZrO₃ particles showed a CO₂ uptake of 7 wt%. Yi and Eriksen¹¹¹ prepared Li₂ZrO₃ using both a liquid phase co-precipitation method resulting in particles with an average size of 40 nm and a high temperature solid-state reaction method resulting in particle with an average size of 2.5 μm. After 10 min in a pure CO₂ atmosphere at 500 °C the 40 nm particles had reached a CO₂ capture of around 23-24 wt% while the 2.5 μm particles had reached 3-4 wt%. The results from both studies were attributed to higher surface area and thinner Li₂CO₃ and ZrO₂ layers with reduced ion diffusion distance in the smaller particles.

Several alternatives to Li₂ZrO₃ have been proposed in which Zr has been replaced with Si, Cu or Al which are all significantly cheaper^{104,115} The CO₂ capture capacities of Li₂SiO₄ and Li₂ZrO₃ were compared by Kato et al.¹⁰⁵ Li₂SiO₄ outperformed Li₂ZrO₃ reaching a CO₂ capture of 25 wt% within 10 min at 500 °C in 2% CO₂ compared to 3-4 wt% for Li₂ZrO₃ in the same period of time. The faster capture kinetics of Li₂SiO₄ was attributed to a larger number of lithium-ion hopping sites available in the crystal structure of Li₂SiO₄, which in turn improved diffusion through the product layer. Palacios-Romero and Pfeiffer¹⁰⁷ tested Li₂CuO₂ as a CO₂ capture material due to its promising Li diffusion properties. The material consisted of dense polyhedral shaped particles with a size of 11 ± 2 μm with a corrugated surface. The CO₂ capture capacity was 13.6 wt% after 150 min at 650 °C. Li₅AlO₄ reached a CO₂ capture capacity of around 54 wt% at 700 °C within the first few minutes and a maximum capacity of 69 wt% after

30 minutes.¹⁰⁸ However, after a heat treatment at 675 °C for 1h the material had a CO₂ capture capacity of 34 wt% after 4h at 675 °C. The reductions in capture capacity and capture kinetics were attributed to sintering. Grain growth which is a typical sign of sintering has also been reported in Li₂ZrO₃ materials as a result of heat treatment.^{114,116,117} Cracks and fractures were found in Li₂O particles after CO₂ capture however, which indicated retarded sintering.^{41,102,117}

3.2.2 HYDROTALCITES

Hydrotalcite like compounds are a large group of basic and anionic clays and are also called double layer hydroxides.¹¹⁸ They have highly porous laminar structures which comprise positively charged brucite-like metal ion layers and interlayers containing water and anions like carbonates or hydroxides (Figure 3. 5).^{119,120} There are several hydrotalcite compounds containing various cations, displaying various anion compositions and varying amounts of water.^{118,121} The composition of a hydrotalcite influences its CO₂ capture capacity. A low amount of water favours CO₂ capture and carbonate anions favour CO₂ capture above hydroxide anions.¹¹⁸ With few exceptions, the metal ions in the structures are Mg and Al ions so a typical synthetic hydrotalcite would therefore be produced using Al(NO₃)₂ and Mg(NO₃)₃ as starting materials.⁹⁹ The 2008 World mine production of Al and Mg was 39 700 000 and 808 000 tonnes respectively. China is the world's largest producer of both metals supplying 34% of the Al the 86% of the Mg in 2008.¹⁰³ The 2007 average annual LME cash price of aluminium ingot was \$2 600 per tonne and the average European free market price for Mg in 2008 was \$4 400 per tonne.^{103,115}

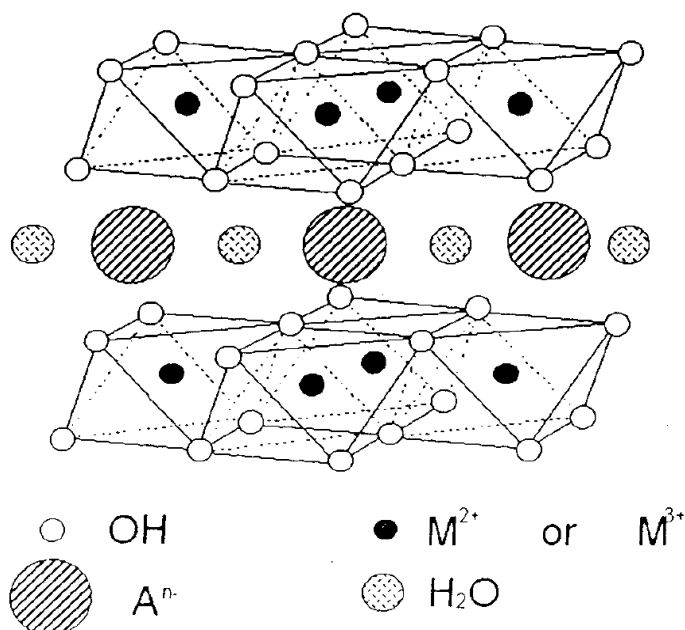


Figure 3. 5. 3D Structure of a hydrotalcite like compound. M²⁺ = Mg²⁺, Ni²⁺ et al., M³⁺ = Al³⁺, Fe³⁺ et al., Aⁿ⁻ = CO₃²⁻, SO₄²⁻. Reprinted with permission from Yong et al (2001).¹¹⁸ Copyright 2001 American Chemical Society.

Hydrotalcites are capable of capturing between 1.9 and 5.2 wt% at temperatures between 200–450 °C.^{96,119,122–126} As such they are more suited to medium temperature CO₂ capture such as the steam reforming of oxygenated hydrocarbons. Only their upper temperature range of carbonation is potentially useful in combustion and some reforming applications.

Ficicilar and Dugo⁹⁶ tested temperatures between 400 and 527 °C. The highest CO₂ capture capacity 5.2 wt% was achieved at 400 °C. Maximum CO₂ capture was reached within 5 min according to a CO₂ breakthrough curve. Lee et al.¹²⁷ tested the CO₂ capture capacity of a K₂CO₃ doped hydrotalcite in temperatures of 400 and 520 °C. They reported superior performance at 400 °C where the CO₂ capture was 3.9 wt% compared to 2.6 wt% at 520 °C. Mass transfer was however found to increase with temperature. By using CO₂ column breakthrough curves and modelling work, a weak function of the mass transfer coefficient with temperature was found. Ding and Alpay¹¹⁹ reported better CO₂ capture at 400 °C than at 480 °C. The capture capacities were 2.8 wt% at 400 °C and 2.3 wt% at 480 °C. Further, Ding and Alpay¹²⁴ reported CO₂ capture capacities of 3.1–4.0 and 2.4–3.5 wt% at 208 and 302 °C respectively for a K₂CO₃ doped hydrotalcite. The CO₂ capture capacities of synthetic Mg–Al–CO₃ hydrotalcites were measured at temperatures between 100 °C and 400 °C using sorption Quantachrome instruments analysers.^{125,128} It was found that 200 °C was the optimum temperature for CO₂ capture where the capture capacity was 2.2–4.0 wt%. Increasing the temperature to 400 °C resulted in a reduction in capture capacity to 0.7 wt% in both studies. By

removing gas from the material without changing the temperature, the CO₂ captured by physisorption was removed leaving the chemically captured CO₂. The capture capacity measurement was repeated and the relative amounts of CO₂ capture via physisorption and chemisorptions were determined from the difference in capture capacity retrieved from the first and the second measurement. It was concluded that 81-88% of the CO₂ was captured by a physisorption mechanism. At 200 °C the hydrotalcite structure becomes unstable due to loss of water and at 400 °C the interlayer spacing is completely collapsed, while the material retains its layered structure.^{118,125,128} At 400 °C a change in the structure to a 3-D network has been proposed based on an observed increase in surface area and pore volume due to an increase in temperature from 120 °C to 400 °C.¹²⁸ The presence of water vapour has been reported to have only a negligible effect on the CO₂ capture capacity of hydrotalcites.^{96,119} However, water vapour has also been reported to enhance the CO₂ capture and release processes of four commercially available Mg-Al hydrotalcites.¹²⁹

CO₂ capture and cyclic stability of hydrotalcites can be increased by doping with K₂CO₃ and Cs₂CO₃ as well as by changing the metals used in the material structure.^{120,126,129} The CO₂ capture mechanism of K₂CO₃ doped hydrotalcite has been described as the combination of three reversible reactions using a nonequilibrium kinetic model.⁹⁹ The proposed mechanism was rapid diffusion and chemisorption of CO₂ followed by slow formation of the carbonates Mg₆Al₂K₂O₉(CO₃) and Mg₆Al₂K₂O₈(CO₃)₂. K₂CO₃ doping reduced the surface area by up to 69 % while increasing the CO₂ capture, indicating that surface area is not a key factor for CO₂ capture in K₂CO₃ doped hydrotalcites.¹²⁰ Addition of K₂CO₃ almost doubled the CO₂ capture of a capacity of a Ga substituted Mg/Al hydrotalcite at 200 °C from 2.5 to 4.9 wt%.¹²⁶ Oliveira et al.¹²⁰ tested both Cs₂CO₃ and K₂CO₃ doping at 200 °C and a CO₂ partial pressure of 0.4 bar. Cs₂CO₃ Doping increased CO₂ capture from 0.4 wt% to 1.8 wt%. However, K₂CO₃ doping proved more efficient resulting in a CO₂ capture of 3.3 wt%. Substituting some of the Al³⁺ with Ga³⁺ in a Mg/Al based hydrotalcite improved CO₂ capture from 1.9 wt% to 2.5 wt% at 200 °C with a CO₂ partial pressure of 0.7 atm.¹²⁶ The CO₂ capture capacity of a K₂CO₃ doped hydrotalcite in pelletised form was subjected to multiple CO₂ capture and release cycles using TGA.¹²² The temperature was kept at 400 °C and the pressure was kept at 1 atm. CO₂ capture was induced by introducing a gas mixture to 30% CO₂ and 70% N₂ for 1h and CO₂ release was induced to switching to pure N₂ for 1h. The CO₂ capture capacity was reduced from 2.3 to 2.0 wt% over 10 CO₂ capture and release cycles and then remained stable for another 50 cycles. A similar pattern was reported by the US-DOE at 550 °C in the presence of steam.¹²³ Each cycle consisted of 0.3 atm CO₂ together with 9.7 atm steam for 2h followed by 1 atm N₂ for another 2h. The CO₂ capture capacity was reduced from 3.5 to 2.2 wt% from the first to the tenth cycle. The capacity then remained stable for another 10 cycles. Oliveira et al.¹²⁰ reported a 7 % loss in CO₂ capture capacity over 75 CO₂ capture and release cycles with a K₂CO₃ doped hydrotalcite.

Needle like structures were found in K₂CO₃ doped hydrotalcites which disappeared after CO₂ capture testing without any loss of potassium, indicating that the structures were rearranged during CO₂ capture.¹²⁰

3.2.3 CA-BASED MATERIALS

Ca-based materials for CO₂ capture and cyclic carbonation and calcinations have been extensively studied due to their high CO₂ capture capacity and fast kinetics. The 2008 world mine production of lime (used in this context as a collective term for a range of Ca containing compounds) was 290 000 thousand tonnes and the price was \$92 per tonne.¹¹⁵ Note that limestone is the raw material used to produce lime. The cost of lime is given here as opposed to the cost of limestone because there is little or no trade in limestone due to its abundance. Compared to the raw materials needed for the production of lithium ceramics and hydrotalcites, limestone is available in far larger quantities and is much cheaper. Limestone deposits are abundant all over the world and future shortages are considered unlikely.^{115,130} The basis for the use of Ca-based materials for chemical looping of CO₂ is the reversible carbonation reaction:



Reaction 3. 1. CaO carbonation.

Microscopic examinations of Ca-based materials have revealed particles with a micrograin structure.^{98,131} Macropores are found between the particles and micropores are visible within the micrograin structure.^{98,131} The micrograins have been described as parallel rods with a network of quasi-cylindrical pores.⁹⁸ The structure can also be described both as nonporous grains surrounded by intergranular pores and a solid pore filled continuum.¹³² Further examination using XRD measurements have revealed crystalline structures in the materials.¹³³

The CO₂ capture process can be divided into an initial fast stage during which micropores within the material are filled (where around 75 % of the total CO₂ uptake occurs) followed by a second, much slower stage controlled by diffusion through a product layer of CaCO₃ (Figure 3. 6).¹³⁴⁻¹³⁶ SEM images of high purity limestone particles after CO₂ capture showed that the micropores were filled with CaCO₃ while a product layer of CaCO₃ had formed inside the surfaces of larger pores.¹³⁵ The initial fast stage was found to be dominated by the filling of the micropores.⁴⁰ It has also been reported that CO₂ capture capacity is determined by the micropore volume.¹³⁶ The switch to the slower stage could be explained by the CaCO₃ product layer reaching a critical thickness above which the capture becomes controlled by the diffusion of CO₂ through the carbonate product layer.¹³⁷ Beruto et al.¹³⁸ attributed the diffusion controlled process more specifically to grain-boundary bulk diffusion. Materials through which diffusion of CO₂ is promoted have displayed improved CO₂ capture capacity.^{58,139} Introducing oxygen

vacancies has also been observed to increase the CO₂ capture capacity in Ca-based materials by improving diffusion of CO₂ through the product layer.¹⁴⁰ The data suggests that CO₂ capture proceeds with the filling of the micropores and simultaneous growth of a product layer on the surface of macropores. When the micropores are filled and the products layer has reached a critical thickness, the CO₂ capture process slows down considerably.

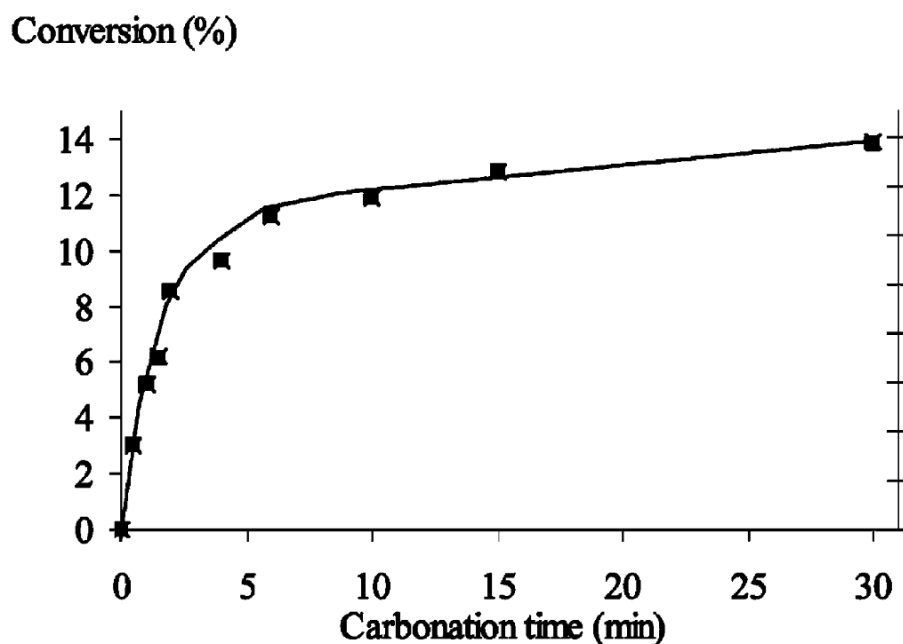


Figure 3. 6. Typical CO₂ capture curve for a Ca-based material. Reprinted with permission from Alvarez and Abanades (2005).¹³⁵ Copyright 2005 American Chemical Society.

CaO derived from crushed limestone has showed CO₂ capture capacity of 31-33 wt% at 650 °C.^{98,131} At temperatures of 800 °C the CO₂ capture can reach up to 35.8 wt%.¹⁴¹ Many different precursors for production of synthetic CaO have been tested including Ca(OH)₂, CaCO₃ and Ca(CH₃COOH)₂.^{58,101,133,142} Synthetic CaO produced from Ca(C₂H₅COO)₂ and Ca(CH₃COO)₂ showed the highest CO₂ capture capacities of 69-70 wt% at 700 °C. CO₂ capture of the synthetic CaO materials was found to be correlated with surface area such that the synthetic CaO with the highest CO₂ capture had the highest surface area.^{101,133} The surface areas of the materials were between 11-20 m² g⁻¹. Synthetic CaO derived from nanosized precursors with surface areas between 40-60 m² g⁻¹ has showed CO₂ capture capacities of 69-71 wt% at temperatures between 650 and 700 °C.^{59,143}

It is well documented that Ca-based materials loses CO₂ capture capacity as a result of multiple carbonation/calcination cycles.^{97,131,135,140,142,144-148} For example, the capture capacity of CaO particles was reduced from 34 to 8 wt% for 40 cycles with carbonation at 650 °C and

calcination at 850 °C.¹³¹ Reductions in the capture capacity of CaO particles from 21 to 6wt% with carbonation at 650 °C and calcination at 920 °C.¹⁴⁹

The capture capacity is reduced quickly over the first set of cycles and then levels out to reach an asymptote.^{97,98,144,146} Florin and Harris¹⁴³ suggested that the asymptotic CO₂ capture capacity is the result of equilibrium between the reduction of surface area and pore volume, and the increase in surface area and pore volume derived from release of CO₂ during calcination. During the calcination process, pores are produced inside the CaO particle.⁵³ Chen et al.¹⁵⁰ tested the CO₂ capture capacity of CaO using TGA. The capture step involved a temperature of 650 °C with 10 vol% CO₂ in N₂ for 10 min while the release step was induced by switching the gas to pure N₂, increasing the temperature by 40 °C min⁻¹ to 850 °C and holding it for 1 min. The temperature was returned to 650 °C at a rate of 60 °C min⁻¹ to complete the cycle. They reported that the CO₂ capture capacity could be increased after 22 CO₂ cycles by increasing the carbonation stage in the 23rd cycle. The same was observed in nanosized CaO particles by Florin and Harris¹⁴³ when they extended the 51st CO₂ capture cycle from 20 min to 24h. They used a TGA setup with CO₂ capture at 650 °C and 14 vol% CO₂ in N₂ and release at 850 °C in pure N₂. The observation was explained by the enhanced effect of CO₂ release with subsequent increase in porosity following the larger amount of CO₂ captured during the extended carbonation.

Reduction of surface area and pore volume has been reported after multiple cycles.^{40,42} The surface area in natural limestone was reduced from 38 m²g⁻¹ to 13 m²g⁻¹ after 30 cycles and from 30-35 m²g⁻¹ to 10-15 m²g⁻¹ after 15 cycles. This has been attributed to sintering which involves the transformation of particles into a solid object through densification and grain growth.^{41,117} The driving force behind sintering is a reduction in surface energy, which is achieved by a reduction in surface area with the formation of interparticle bonds that are controlled by solid state diffusion. The existence of sintering has been confirmed in many studies by the observation of grain growth from scanning electron microscope (SEM) images taken before and after CO₂ capture.^{42,135} For example, Yi et al.¹⁴⁰ reported grain growth from 50 nm to 5 µm in synthetic CaO after 40 cycles with carbonation at 700 °C in 70% CO₂ and calcination at 700 °C in pure He. Sintering occurs at around half of the melting point of the material which is referred to as the Tammann temperature. This makes temperature an important parameter for sintering. Increased temperatures lead to the loss of CO₂ capture capacity over multiple carbonation/calcination cycles.^{97,146} Grasa and Abanades¹⁴⁶ found that temperatures above 950 °C accelerated the decay in CO₂ capture capacity in CaO derived from natural limestone. Lysikov et al.⁹⁷ reported a 50% reduction in CO₂ capture capacity of CaO derived from Ca(NO₃)₂ with an increase in temperature from 750 to 822 °C. Multiple carbonation/calcination cycles also causes smoothing of surfaces in Ca-based materials which is

consistent with the sintering process.^{42,97} Surface energy is reduced by the smoothing of a surface and is known to occur during sintering.^{41,117}

Fennell et al.⁴² found that a reduction of pore volume in pores narrower than 150 nm in diameter was the principal reason for the reduction of CO₂ capture capacity of CaO. Capture of CO₂ by CaO was reported by Beruto et al.¹³⁸ to cause a reduction in the volume of small pores (diameter less than 0.2 μm) as well as an increase in the volume of larger pores. This is in agreement with Sun et al.⁴⁰ who reported reduced pore volume for pores < 220 nm together with an increase in the volume of pores > 220 nm in limestone particles after 6 CO₂ capture and release cycles. Pore size distribution measurements were carried out on samples taken before and after cycling in a fixed bed quartz reactor placed inside a furnace. The temperature was held at 850 °C and CO₂ capture/release cycles were induced by changing the atmosphere between CO₂ and N₂ at atmospheric pressure. The growth of large pores with a reduction in small pores is described in sintering theory and is explained by mass flow through grain boundaries.^{41,117} CO₂ mass flow during calcination has been suggested to enhance this mass transfer process.⁴⁰ After multiple cycles a bimodal pore size distribution forms due to the increase in macropores and the pores formed from the evolution of CO₂ during calcination.¹³⁷ Apart from sintering, pore blockage and collapse of internal structure of the material has also been put forward as causes for loss of CO₂ capture capacity.^{58,137}

Pellets of Ca-based material with high strength can be manufactured using an appropriate binder.^{141,142,151,152} The use of bentonites as binders caused the formation of eutectic melts of calcium-silica compounds with low melting points which contributed to sintering in CaO pellets.^{142,151} Pelletisation using Na₂CO₃ as a binder showed promising results up to 5 cycles but no further testing was carried out since Na₂CO₃ had reduced the performance of natural limestone in earlier studies.^{142,151,153} Calcium aluminate cements were found to be an appropriate binder showing good setting performance and high strength.¹⁵¹

The CO₂ capture was reduced when pellets were manufactured from CaO powder, due to the addition of inert material and loss of surface area.¹⁵¹ However, making pellets out of hydrated lime increased CO₂ capture due to an even dispersion of Ca₁₂Al₁₀O₃₅ which retarded sintering by providing a stable nano-sized network.¹⁵² Over 1000 cycles, pelletisation of hydrated lime increased CO₂ capture by retarding sintering and reducing the loss of pore volume.¹⁴¹

3.2.4 CONTROLLING SINTERING

Reduction in surface areas due to sintering has been identified as the cause of the reduced CO₂ capture capacity over multiple CO₂ capture/release cycles. Apart from this loss in capacity, Ca-based materials have displayed excellent properties in terms of capture capacity, capture kinetics and operating temperature range as well as in terms of cost and availability. This has

created an interest in trying to reduce sintering in Ca-based materials. This includes different techniques for strengthening the materials by doping, adding inert frameworks and by applying high temperature pre-treatments.

3.2.4.1 DOPING WITH INERT MATERIAL

Lu et al.¹⁴² manufactured materials using a flame spray pyrolysis method (described below) doped with Si, Ti, Cr, Co, Zr and Ce. The Zr doped material displayed the highest CO₂ capture capacity after 100 CO₂ capture and release cycles with a molar conversion of CaO of around 50%. This was attributed to the fact that Zr had the highest Tammann temperature of the tested materials in their oxide form. Initial CO₂ capture capacity was reduced with increasing molar ratio of Zr in the material. Over multiple CO₂ capture and release cycles, both the material with a Zr/Ca molar ratio of 1:1 and 3:10 showed no signs of performance decay and retained CaO molar conversions of 15 and 62% respectively. X-ray diffraction revealed the formation of CaZrO₃ during doping with Zr which formed a product layer on the CaO grains at molar ratios of 3:10 and above. It was suggested that the CaZrO₃ hindered sintering by restricting the growth of CaO grains. However, when the Zr doped material was produced using a wet precipitation method it failed to retain its CO₂ capture capacity.¹⁴² Fennell et al.⁴² tested doping CaO with Na₂CO₃. Small amounts of Na₂CO₃ gave marginal improvements in stability while larger amounts resulted in a significantly reduced CO₂ capture capacity.

Adding an inert material has several inherent problems. First, the CO₂ capture capacity by weight is reduced since parts of the material cannot capture CO₂.¹⁵¹ This means that a larger mass of the doped material will be needed to achieve the same initial CO₂ capture capacity.⁵⁸ However, in the case of Li₂ZrO₃ doped with K₂CO₃ for example the CO₂ capture was increased due to changes in chemical properties of the material.¹⁰⁰ There is also a penalty in the amount of energy needed for heating to the correct CO₂ capture temperature since the inert material will also be heated.

3.2.4.2 CAO IN AN INERT FRAMEWORK

The stability of Ca-based materials over multiple cycles was increased by integrating CaO with Ca₁₂Al₁₄O₃₃ as a composite binder.^{53,54,101,136,139,150,154} Through a preparation procedure consisting of a series of hydration and heating processes, Ca₁₂Al₁₄O₃₃ could be uniformly distributed within the CaO micrograin structure thereby retarding CaO particle growth. Li et al.⁵³ reported a stable CO₂ capture capacity of 0.45 g CO₂ g⁻¹_{sorbent} over 13 cycles with carbonation at 690 °C and calcination at 850 °C using TGA. SEM images showed no particle growth or any decrease in pore space before or after the experiment. Pacciani et al.¹³⁶ reported stable CO₂ capture of 0.3 g CO₂ g⁻¹_{sorbent} for 20 cycles at 750 °C in a fluidised bed system. Li et al.⁵⁴ reported a loss of CO₂ capture capacity from 50 wt% to 41 wt% over 50 cycles with carbonation at 700 °C and calcination at 850 °C using TGA. Increasing the calcination

temperature to 980 °C resulted in a capacity loss from 52 wt% to 22 wt% over 56 cycles. This is in agreement with Li et al.⁵³ who reported reduced stability when the calcination temperature was increased to 950 °C. Martavaltzi and Lemonidou¹⁰¹ used both Ca(OH)₂ and Ca(CH₃COOH)₂ as starting materials to produce the CaO/Ca₁₂Al₁₄O₃₃ material. The Ca(OH)₂ derived material displayed a stable CO₂ uptake of 20 wt.% over 45 cycles. The Ca(CH₃COOH)₂ derived material displayed a reduction in CO₂ capture from 35 to 29 wt% over 45 cycles showing lower stability but a higher CO₂ capture capacity even after multiple cycles. Using Ca(CH₃COO)₂ as a precursor for the material resulted in higher stability and lower CO₂ capture capacity over multiple cycles than Ca(OH)₂ due to a more favourable tortuosity in the pore system which was hypothesized to reduce access of CO₂ to un-reacted sites.¹⁰¹ Tortuosity is referred to as the ratio between pore length to the length of the porous medium.¹⁵⁵ Both materials showed increased CO₂ capture over pure CaO derived from Ca(OH)₂ and Ca(CH₃COOH)₂ respectively. This could be explained by the formation of ultrafine CaO particles with high surface area during the preparation procedure.⁵³

Chen et al.¹⁵⁰ used Al[OCH(CH₃)₂]₃ as a precursor. The capacity of the resulting material was 0.22 g CO₂ g⁻¹_{sorbent} which was reduced to 0.15 g CO₂ g⁻¹_{sorbent} after 60 cycles. This was no improvement over untreated CaO which displayed a starting capacity of 0.27 CO₂ g⁻¹_{sorbent} with a capacity of 0.12 CO₂ g⁻¹_{sorbent} after 60 cycles. The influence of CO₂ amount and carbonation time on the CO₂ capture capacity of CaO with Ca₁₂Al₁₄O₃₃ binder was stronger than for dolomite.^{139,154} By increasing the carbonation time from 500s to 15 min and to 30 min after 20 cycles at a temperature of 750 °C, the CO₂ capture capacity of CaO/Ca₁₂Al₁₄O₃₃ could be increased from 0.22 to 0.36 over 25 cycles while the capture capacity of dolomite was steadily reduced from 0.32 to 0.24 CO₂ g⁻¹_{sorbent}.¹⁵⁴ The CO₂ uptake of Ca/Ca₁₂Al₁₄O₃₃ could be increased from 0.16 to 0.44 g CO₂ g⁻¹_{sorbent} within 20 cycles by increasing the amount of CO₂ to 27 % after 40 cycles with a CO₂ amount of 14% at a temperature of 750 °C. Dolomite showed no change in CO₂ capture as a result of the increased amount of CO₂. Modeling work showed that the yield stress needed to disrupt the product layer of the CaO/Ca₁₂Al₁₄O₃₃ material was about an order of magnitude lower than for dolomite which could explain the higher sensitivity to CO₂ amount.

Aihara et al.¹⁵⁶ used CaTiO₃ as an inert framework for CaO to increase capacity upon cyclic carbonations-calcinations. A powder method was applied to produce Ca-based materials with and without CaTiO₃. Carbonation/calcination cycle experiments were carried out in a reactor with a constant temperature of 1000 °C and cycling the gas composition between 20% CO₂, 80% N₂ for carbonation and pure N₂ for calcination. SEM images revealed less particle growth in the material with CaTiO₃ as a result of cycling. The surface area of the material with CaTiO₃ was initially lower than untreated CaO (around 4 and 9 m²g⁻¹ respectively). However, after 10 cycles the surface area of the materials with CaTiO₃ had increased while the untreated CaO surface area had decreased and both materials had a surface area of around 6 m²g⁻¹.

3.2.4.3 PRE-SINTERING

Treatment of material with high temperatures is expected to increase the stability of the material during carbonation/calcination cycles.^{59,97} Lysikov et al.⁹⁷ proposed a model in which the strengthening was explained by the formation of an interconnected CaO network which is unsusceptible to sintering. Pre-sintering of CaO derived from nano-sized CaCO₃ at 900 °C and 1100 °C for 12 hr in air was investigated by Florin and Harris.¹⁴³ Pre-sintering at 900 °C could delay the reduction in CO₂ capture following 100 carbonation/calcination cycles. However after 100 cycles the pre-sintered material reached the same asymptotic CO₂ capture capacity as non pre-sintered material. Pre-sintering at 1100 °C offered no improvement over untreated material. Lysikov et al.⁹⁷ tested pre-sintering at 1100-1300 °C for a variety of Ca-based materials derived from different precursors. They found that high stability could be achieved at the cost of CO₂ capture capacity. For example, CaO derived from crystalline CaCO₃ pre-sintered at 1200 °C remained stable over more than 100 cycles but the CO₂ capture capacity was less than 4%. From the results they concluded that materials derived from smaller elements with a loosely packed structure were more suitable for CO₂ capture but were not strong enough to resist sintering at high temperatures.

Albrecht et al.¹⁴⁸ tested pre-sintering of natural limestone at 900 °C for 3 hours, and at 1100 °C for 2 and 5 hours. Pre-sintering at higher temperature and/or longer sintering time reduced both surface area and pore volume with subsequent reduction in initial CO₂ capture capacity. Pre-sintering at 900 °C for 3h resulted in an initial CO₂ capture capacity of 61 wt%, 1100 °C for 2h of around 39 wt% and 1100 °C for 5h of around 26 wt%. After 80 cycles the two milder treatments resulted in capture capacities of around 31 wt% while the limestone pre treated at 1100 °C for 5h remained stable at 26 wt%. The results represent a trade-off between capture capacity and stability.

3.2.4.4 FLAME SPRAY PYROLYSIS (FSP)

Production of nanosized Ca-based material from liquid solutions using flame spray pyrolysis (FSP) has been tested.^{59,142} The FSP method involves converting precursor droplets into solid nano sized particles in a high temperature flame. Lu et al.⁵⁹ produced a nano-structured Ca-based material using the FSP method and compared it to a Ca-based material produced from a Ca(CH₃COOH)₂ precursor at 700 °C. Both materials had similar initial CO₂ capture capacity of 95% molar conversion. The nano-sized material showed a faster initial capture capacity loss over the first 20 cycles down to 50% which was attributed to the smaller particle size which enhances sintering.^{41,117} The CO₂ capture capacity remained stable at 50% for another 40 cycles while the capacity of the Ca(CH₃COOH)₂ based material was steadily reduced. There was a cross over after 40 cycles at which the two materials had the same capture capacity. The performance of materials produced by the FSP method was significantly increased by doping

with Zr.⁵⁹ Zr doped FSP made material displayed a stable CO₂ capture capacity of around 65% molar conversion at 700 °C over 45 cycles and just above 50% at 850 °C over 20 cycles. TEM images revealed only minor particle growth after the multicycle experiment indicating that the level of sintering was negligible. XRD results showed that the FSP method gave a better incorporation of the Zr dopant into the CaO crystal lattice compared to the conventional wet precipitation method which could explain the higher stability of the material.

3.2.4.5 HYDRATION

Li et al.¹⁵⁷ modified CaO derived from limestone with water and solutions with ethanol and water. Both CO₂ capture capacity and performance over multiple carbonation/calcination cycles were improved by hydration and the effect was increased further by the addition of ethanol. It was reported that hydration shifted the pore size distribution towards smaller pores thereby increased the surface area and pore volume. The increase in pores smaller than 220 nm is of high significance since these pores has been reported to control CO₂ capture capacity.^{40,136} Ethanol was reported to increase the affinity and permeability of the water, increasing the effect on pore size distribution.

3.2.4.6 INTRODUCTION OF OXYGEN VACANCY MATERIALS

Yi et al.¹⁴⁰ showed that the introduction of oxygen vacancy possessing materials could increase the stability over multiple CO₂ capture and release cycles. Oxygen vacancies was expected to facilitate diffusion of CO₂ through the CaCO₃ product layer according to the diffusion process proposed by Bathia and Perlmutter.¹⁵⁸ The material was prepared using CaO and a mixture of Ce and Zr nitrates known for the oxygen vacancies sites in their oxidised crystal forms. The material was compared to CaO prepared without the addition of Ce and Zr nitrates. The conversion of the CaO without Ce and Zr nitrates was reduced from 80% to around 40% over 40 cycles while the conversion of the CaO/CeZr material was initially 40%, increased to 60% over the first 20 cycles was then stable for the next 20 cycles.

An explanation for the results can be found in the work of Barker¹⁵⁹ who attributed the loss of CO₂ capture capacity of CaO to pore closure during carbonation. After carrying out a set of multiple CO₂ capture and release cycles, an increased CO₂ capture phase was introduced. This resulted in an increased CO₂ capture capacity and surface area over subsequent cycles. It was concluded that the release of CO₂ from fully carbonated CaO (i.e. pure CaCO₃) results in the formation of pores which results in an increase in surface area with a subsequent increase in CO₂ capture capacity. This is in agreement with Yu et al.¹⁶⁰ who reported that formation of porosity as a result of CO₂ release only occurred if the carbonation reaction was carried out over an extended time period. Hence when the carbonation reaction is allowed to go to completion, porosity is formed during subsequent CO₂ release, surface area is retained and the CO₂ capture capacity remains unchanged. The stability of the Ca/CeZr material could therefore be attributed

to full conversion of CaO to CaCO₃ made possible by oxygen vacancies in the CaCO₃ layer. It is possible for full conversion of CaO in the Ca/CrZr material to have occurred in the work presented by Yi et al.¹⁴⁰ since they have defined conversion (X) as:

$$X = \frac{\text{moles of } CO_2 \text{ absorbed in sorbent}}{\text{moles of CaO in sorbent}} \times 100$$

Equation 3. 1. Definition of conversion used by Yi et al.¹⁴⁰

Hence if inert substances formed from Ca, Ce and Zr formed during the materials preparation process, then the conversion reported could equal complete conversion of available CaO.

3.3 SUMMARY

Out of the three types of materials suggested for high temperature CO₂ capture, the lithium ceramics are the most expensive, especially Li₂ZrO₃ considering the price of LiCO₃ of around \$6000-7000 per metric tonne in 2007 and the price of ZrO of up to \$12 200 per metric tonne in 2008.^{104,115} The raw materials needed for production of hydrotalcites are lower (\$2 600 per metric tonne for Aluminium ingot in 2007 and \$4 400 per metric tonne for Mg in 2008) but the lime needed for production of Ca-based materials is by far the cheapest with a price of \$92 per metric tonne. Also, lime deposits are plentiful meaning that lime can be mined in many locations worldwide.

With regards to operating temperature range, hydrotalcites appear more suitable for medium temperature applications at 200-400 °C, while lithium ceramics are more useful at medium and high temperatures between 400 and 700 °C and Ca-based materials work best at high temperatures of 650 to 850 °C. All materials capture CO₂ by the formation of carbonates but hydrotalcites seems more effective at lower temperatures where physisorption is the main capture mechanism.

The CO₂ capture capacity the Ca-based materials out-performed both lithium ceramics and hydrotalcites. The capture capacity of Ca-based materials is between 31 and 70 wt% while lithium ceramics have a capture capacity of anything from 7-69 wt% with most materials showing capacities of 12-28 wt%. The exception is Li₂O which displayed a massive 226 wt% capacity. Hydrotalcites have by far the lowest capture capacities of as low as 1.9-5.2 wt%. Hydrotalcites will reach maximum CO₂ capture relatively fast. At 400 °C maximum CO₂ capture of 3.3 wt% has been reached in 8-9 min and 5.9 wt% within 5 min.^{96,120} The uptake rates of lithium ceramics vary significantly from around 7 wt% in 45 min up to 54 wt% within just a few minutes depending on the type of lithium ceramic.^{108,112} It takes around 20 min for most,

Ca-based materials to reach maximum CO₂ capture at 650-850 °C.^{40,131,157} However, the time taken to reach maximum capacity is a limited measure of the viability of a sorbent for steam reforming. Fast reaction rates are of higher significance. Faster reaction rates enable shorter reformer residence time and slow reaction rates results in the need for a large reformer. Ca-based sorbents display the higher reaction rates during the initial fast stage, however the reaction rate then slows down during the diffusion controlled stage

Over multiple carbonation/calcination cycles hydrotalcites lose between 7-13% of their capacity while Ca-based materials can lose up to as much as 66%. The reduced capacity in Ca-based materials has been attributed to sintering. The literature on lithium ceramics reviewed here has no information on the stability over multiple cycles but typical signs of sintering have been reported such as grain growth and loss of capacity due to high temperature pre treatment. Again, Li₂O is the exception showing signs of retarded sintering.

Many attempts have been made to reduce sintering in Ca-based materials. The materials can be strengthened by the addition of inert materials or by high temperature heat treatments and stability can be increased by introducing oxygen vacancies. Doping with inert materials involve a trade-off between capture capacity and durability but inclusion of a composite material through hydration and heat treatment synthesis processes can insure high stability and retained capture capacity. Over multiple cycles, the capture capacity is typically reduced quickly at first and then reaches an asymptotic value after which no more sintering occurs. High temperature heat treatments like pre-sintering will often reduce the capture capacity directly to the asymptotic value. However, high temperature FSP can be used to incorporate an inert material in such a way that high capacity and durability can be combined.

3.4 CONCLUSIONS

Ca-based materials are considered to be the most suitable CO₂ sorbents for SESR. They are superior to hydrotalcites and lithium ceramics in terms of CO₂ capture capacity as well as price and availability. Their main disadvantage is the loss in capacity over multiple CO₂ capture and release cycles and many attempts have been made to correct this problem.

CHAPTER 4: THERMOCHEMICAL CONVERSION OF GLYCEROL TO HYDROGEN

“Employ your time in improving yourself by other men’s writings, so that you shall gain easily what others have laboured hard for”

Socrates

4.1 INTRODUCTION

World energy demand is expected to increase from 11.8 billion tons oil equivalent (toe) in 2010 and reach 16.4-16.8 billion toe in 2030.^{161,162} Our current major sources of energy come from fossil fuels such as coal, oil and gas. The increase of CO₂ in the atmosphere over the last 200 years has been attributed to the burning of fossil fuels and is expected to cause a change in climate just like previous changes in atmospheric CO₂ have done in the past.¹⁻⁴ Negative effects such as reduced crop yields and increased frequency of storms are expected.⁵⁻⁸ G8 leaders proclaimed a target of 50% reductions in CO₂ emissions by 2050 from 2005 levels after their meeting in Lake Toya, Japan, in 2008. In 2009 it was recognized by the G8 leaders and the Major Economies Forum that the concentration of atmospheric greenhouse gases ought not to exceed 450 ppm CO₂ equivalent. At the UN climate change conference (COP17/CMP7) in Durban, South Africa in 2011, a decision was made to write a legally binding agreement by 2015 which will come into force in 2020. Fossil fuel resources are spread unevenly over the planet and their use has made many nations dependent on energy imports. This represents a threat to national security in the case of shortages, high prices and high demand, but also in the case of conflict, both military and diplomatic.

The use of fossil fuel for transportation is achieved mainly through the use of gasoline in internal combustion engine vehicles (ICEV). This results in the release of air pollutants, including particulates which have been linked to respiratory and cardiac disease.¹⁶³ These effects are worsened by increased population density and internal combustion engine vehicles which result in ever growing concentrations of particulates in populated areas. The efficiency of the process from energy source to end use is commonly quantified using the ‘well to wheel’ (WtW) efficiency (η_{WtW}). The latter takes the efficiency of the manufacture, transportation and storage of the energy carrier into account as well as the efficiency of the end use. Efficiency at each step of the WtW calculations is defined according to Equation 4. 1:

$$\eta = \frac{\text{Energy output of process or product}}{\text{Energy input of process or product}}$$

Equation 4. 1. Definition of efficiency used for WtW calculations.

Crude oil as an energy source, gasoline as an energy carrier and ICEV as their end use has a η_{WtW} of 14-15% and results in WtW CO₂ emissions of about 200 g km⁻¹.^{11,14} There are several alternatives to this route which have higher WtW efficiencies and lower WtW CO₂ emissions such as refining the crude oil to diesel instead of gasoline, using ICE-hybrid vehicles, switching to biofuels like biodiesel and ethanol. However, two alternatives stand out as potential long term solutions to achieve near zero CO₂ emissions. The first alternative is to directly use

renewable electricity (e.g. wind, solar, hydro, tidal) in an electric vehicle, the second is to allow a renewable energy source (biomass, surplus wind/solar/hydro) to convert to H₂ and use it to power a fuel cell vehicle.¹¹ Battery electric and fuel cell electric vehicles (BEV and FCEV) using electricity and H₂ as energy carriers respectively are considered the best long term end uses with regard to the reduction of CO₂ emissions.

H₂ as energy carrier can solve the problems of intermittency of renewable electricity by acting as a grid buffer. However this assumes successful compression and storage of H₂ which is challenging. FCEV (as end use) are quickly refilled for a similar range to that of current ICEV, unlike BEV which require frequent and lengthy recharging and are suited only to short journeys. However, a powerful high volt system could reduce recharging time. Also, a recharging infrastructure for BEV is already in place (the electricity grid) and the use of H₂ would require a new infrastructure of refuelling points. Since the only endpoint emissions from a FCEV run on hydrogen is water, the health problems derived from particulate matter are solved through this solution. H₂ can be produced from electricity and water using electrolysis; however it can also be produced from the combination of water and a number of different carbon-containing feedstocks. Therefore, this solution may also solve the problem of national security. The most economical production route of H₂ is currently steam reforming of natural gas. Hekkert et al.¹⁴ reported that producing H₂ from natural gas using steam reforming, compressing the H₂ for transportation and storage and using the H₂ in a fuel cell vehicle was the scenario which had a higher WtW efficiency (21%) and the lower WtW CO₂ emissions (115 g km⁻¹) than directly fuelling a ICEV with compressed natural gas. The results were in agreement with Svensson et al.¹¹. Adding carbon capture and storage (CCS) to the steam reforming process reduced WtW CO₂ emissions further but also reduced η_{WtW} .¹¹ In summary, steam reforming of natural gas was considered a viable route to hydrogen production for the transport sector because the WtW efficiency was higher, and the WtW CO₂ emissions lower than those of the alternative uses of natural gas for the transport sector. However, for a truly sustainable route of hydrogen production, renewable feedstock is needed.

Biodiesel can be produced from vegetable oils and animal fats, either from fresh or waste streams.¹⁶⁴ An emerging energy source is algae. Biodiesel consists of methyl esters and is conventionally produced through direct transesterification of the triglycerides present in the energy source (Figure 4. 1).¹⁶⁵ Another route to biodiesel is through biomass gasification followed by Fischer-Tropsch synthesis.

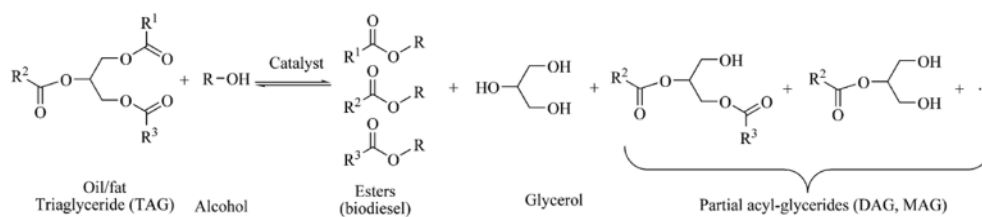


Figure 4. 1. Formation of biodiesel from oils.

A major by-product formed during biodiesel production is crude glycerol, which is a mixture containing glycerol as well as alcohols, soaps, alkali hydroxides salts and ash as well as calcium, magnesium, phosphor and sulphur.¹⁶⁶⁻¹⁶⁹ The composition of the crude glycerol varies depending on what energy source is used.¹⁶⁷ For every 100 kg of vegetable oil that is transesterified, about 10 kg of crude glycerol is formed and this makes it too large a by-product stream to be economically disposed of. The increased production of biodiesel has caused a surplus of crude glycerol as evidenced by the reduced value of glycerol. Biodiesel production increased by 295% between 2000 and 2005 and the value of glycerol was reduced almost tenfold between 2004 and 2006.¹⁷⁰⁻¹⁷² Between 2005 and 2008 world biodiesel production was below capacity, which can be attributed in part by the reduced cost of glycerol.¹⁷³ This provides an economic incentive to find new ways of adding value to crude glycerol from biodiesel production. Biofuel production increased from 0.7 million barrels daily (mb/d) in 2007 to 1.8 mb/d in 2010 and has been predicted to increase further to 2.4 mb/d in 2015 and 6.5 mb/d in 2030.^{161,162,174} Assuming a reference scenario in which the atmospheric level of greenhouse gas emissions were limited to 450 ppm CO₂ equivalent, the use of biofuels would be 275 Mtoe in 2030.¹⁶¹ It has also been reported that in order to meet a target of 50% reduction in CO₂ emissions by 2050 from 2005 levels, biofuel production needs to equal 12 exajoules (EJ, where exa = ×10¹⁸) by 2030 and 32 EJ by 2050.¹⁷⁵ Therefore the incentives to add value to crude glycerol from biodiesel production will be stronger in the future, especially if the goals of CO₂ emission reductions are to be reached.

The glycerol and the alcohols in the crude glycerol can be thermochemically converted to hydrogen. The glycerol can also be purified prior to hydrogen production. This way two transport fuels (biodiesel and hydrogen) can be produced from the same renewable energy source. The yield of hydrogen from glycerol must be maximised as well as the purity of the hydrogen. The inefficiencies of the process must be minimised and any problems that arise such as catalyst deactivation must be addressed.

In order to address all these issues, several thermochemical routes to hydrogen production from glycerol have been investigated. Thermodynamic equilibrium analysis has been performed with the aim of understanding the processes involved and to identify the optimum conditions for maximum hydrogen yield and purity. Experimental work has been carried out building on the

experience from the thermodynamic equilibrium analysis. Catalysts have been manufactured, characterized and used for hydrogen production in order to understand the effects of catalyst characteristics on hydrogen production and to learn how to manufacture catalysts which optimise hydrogen yield and purity.

The aim of this chapter is to review the work carried out on thermochemical conversion of glycerol to H₂. First, the thermodynamics of the process is introduced followed by an introduction of the parameters used when studying glycerol conversion to H₂ and how they are defined (e.g. glycerol conversion and hydrogen yield). The routes to conversion of glycerol to H₂ are then reviewed. These are steam reforming (including sorption enhanced steam reforming), aqueous phase reforming, autothermal reforming, supercritical water gasification and thermal decomposition. Although the term ‘gasification’ is more often applied to solid feedstock, it is also in some cases used instead of ‘reforming’ to gaseous and liquid feedstock in the literature. Each route is first introduced and then the results from thermodynamic equilibrium analysis (if any) are reviewed followed by those from experimental work. The work regarding catalysts is then reviewed. The main focus of this chapter is on the effects of the process parameters of temperature, ratio of water to glycerol and catalyst characteristics on the H₂ concentration and yield for each of the routes of thermochemical conversion of glycerol to H₂.

4.2 THERMODYNAMICS OF CONVERSION OF GLYCEROL TO HYDROGEN

Three main reactions are involved in the thermochemical conversion of glycerol to H₂, namely glycerol decomposition (Reaction 4. 1), CO methanation (and its reverse, methane steam reforming (Reaction 4. 2) and the water gas shift (WGS) reaction (Reaction 1. 2).



Reaction 4. 1. Glycerol decomposition.



Reaction 4. 2. CO methanation.

The dry gas composition at temperatures between 27 and 1007 °C derived from thermodynamic equilibrium analysis of glycerol conversion in the presence of water using minimisation of Gibbs free energy is shown in Figure 4. 2. In this example, the molar ratio of water to glycerol is 9:1 corresponding to a molar water or steam to carbon ratio (S:C) of 3:1 at 1 bar. With this method, glycerol conversion is complete at all temperatures in this range. At lower temperatures CH₄ and CO₂ are formed through the methanation (the reverse of Reaction

4. 2) and WGS (Reaction 1. 2), respectively, from the CO and H₂ produced by the glycerol decomposition reaction (Reaction 4. 1). As the temperature is increased, the balance of Reaction 4. 2 and Reaction 1. 2 shifts further to the left resulting in decreasing concentrations of CH₄ and CO₂ in favour of increased concentrations of CO and H₂. Note that the reverse of the CO methanation reaction is referred to as the methane steam reforming reaction (MSR). When MSR has gone to completion and the concentration of CH₄ is negligible, the H₂ concentration is maximised, and as the temperature is increased further, the H₂ concentration will decrease as the reverse WGS reaction is favoured.

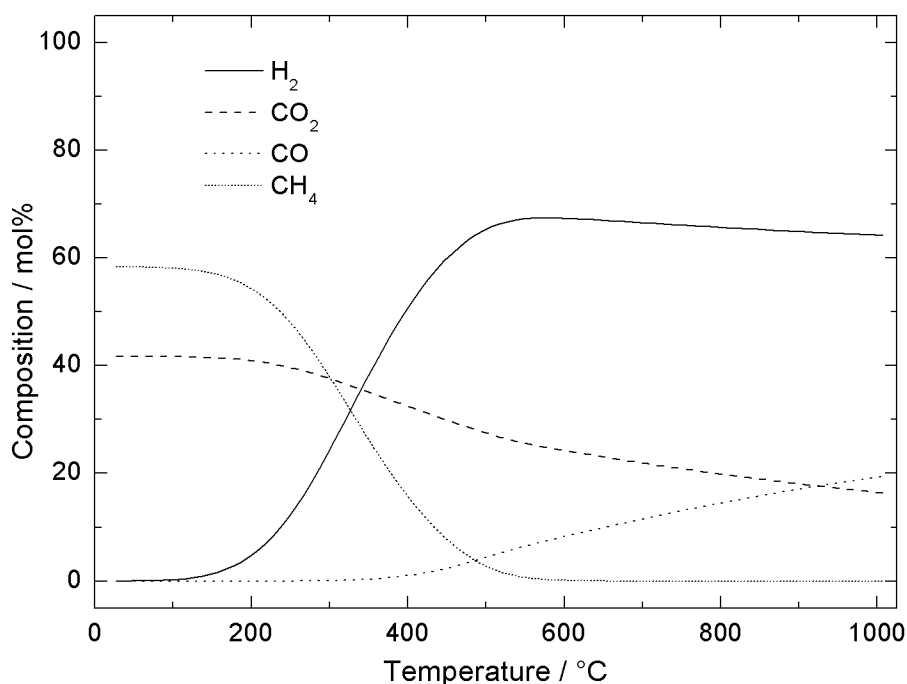


Figure 4. 2. Concentrations of products from reactions of glycerol with water at molar steam to carbon ratio (S:C) of 3 at 1 bar.

With increasing S:C, the H₂ concentration is increased for all temperatures, and maximum H₂ concentration is reached at a decreasing temperature (Figure 4. 3). This is because an increase in water concentration will shift Reaction 4. 2 and Reaction 1. 2 towards more H₂ production.

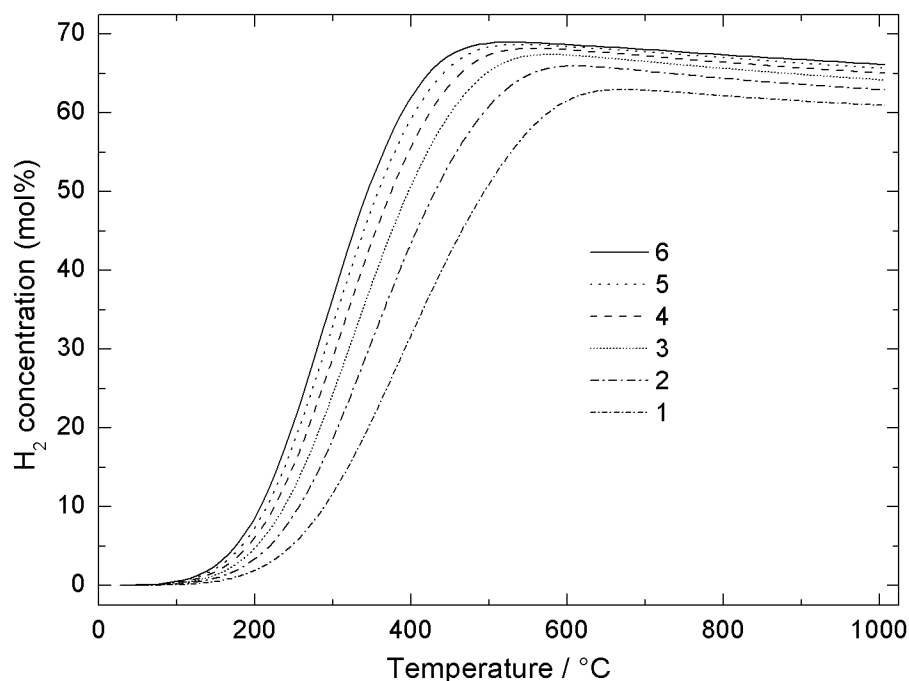


Figure 4. 3. Hydrogen concentration with temperature from water-glycerol reaction for various S:C at 1 bar.

Combining Reactions 1 and 3 gives the ‘complete’ steam reforming reaction of glycerol (Reaction 4. 3).



Reaction 4. 3. Complete glycerol steam reforming

The theoretical maximum H_2 production from reacting glycerol with water is 7 moles of H_2 per mole of glycerol. H_2 yield is a parameter used to measure the amount of H_2 which is derived from glycerol and is commonly defined as either Equation 4. 2^{176,177}, Equation 4. 3^{178,179} or Equation 4. 4^{50,180,181}. However, King et al.¹⁸² refer to Equation 4. 2 as H_2 selectivity while Hu and Lu¹⁸³ and Slinn et al.¹⁸⁴ use Equation 4. 3 for H_2 selectivity. In the tables below their results will be presented as H_2 yields according to Equation 4. 2 and Equation 4. 3.

$$\text{H}_2 \text{ yield (\%)} = 100 \times \left(\frac{\text{moles of H}_2 \text{ produced}}{7 \times (\text{moles of glycerol converted})} \right)$$

Equation 4. 2. H_2 yield definition 1

$$H_2 \text{ yield (\%)} = 100 \times \left(\frac{\text{moles of } H_2 \text{ produced}}{7 \times (\text{moles of glycerol supplied})} \right)$$

Equation 4. 3. H₂ yield definition 2.

$$H_2 \text{ yield} = \frac{\text{moles of } H_2 \text{ produced}}{\text{moles of glycerol supplied}}$$

Equation 4. 4. H₂ yield definition 3.

The difference between Equation 4. 2 and Equations 4. 3 and 4. 4 is the amount of moles of glycerol which are taken into account. Equation 4. 2 only takes the amount of converted glycerol into account hence disregarding unconverted glycerol, while Equations 4. 3 and 4. 4 take all the glycerol which is supplied to the reactor into account. When considering thermodynamic equilibrium analysis using minimization of Gibbs free energy Equation 4. 3 and Equation 4. 4 will provide the same result since thermodynamic equilibrium results in complete conversion of glycerol. However, all work on thermodynamic equilibrium analysis reviewed here used Equation 4. 4 to define the H₂ yield. In the case of Equations 4. 2 and 4. 3, the maximum H₂ yield is 100% while in the case of Equation 4. 4 the maximum H₂ yield is 7.

Another useful parameter is the glycerol conversion. This parameter is used for experimental work and is a measure of how much of the glycerol supplied to the experimental setup was converted. Combined with the H₂ yield, this parameter can provide useful information on the ability of the experimental setup to convert the glycerol to H₂. Glycerol conversion is defined in different ways by different authors, and the definition used is often dictated by the methodology employed to quantify the conversion products. If for example the amount of glycerol in the product condensate (volatile products condensed by cooling) is quantified by measurement, Equation 4. 5 can be applied. If only gaseous products are quantified, then Equation 4. 6 and Equation 4. 7 can be applied. Equation 4. 6 and Equation 4. 7 only differ in the amount of carbonaceous gaseous products that are quantified. However, they are defined here with separate definitions since CO, CO₂ and CH₄ are by far the most common gaseous carbonaceous species to be quantified, but additional species such as C₂H₆ or C₂H₄ are sometimes also measured. Due to the variety of additional species that are reported in the literature, Equation 4. 7 is used to describe the definition of glycerol conversion when species other than just CO, CO₂ and CH₄ are quantified. Equation 4. 8 is used when both liquid and gaseous products are taken into account to calculate glycerol conversion.

$$\text{Glycerol conversion (\%)} = 100 \times \frac{\text{moles of glycerol ((supplied) - (in the products))}}{\text{moles of glycerol supplied}}$$

Equation 4. 5. Glycerol conversion definition 1.

$$\text{Glycerol conversion (\%)} = 100 \times \frac{\text{moles of C in CO, CO}_2 \text{ and CH}_4 \text{ produced}}{3 \times (\text{moles of glycerol supplied})}$$

Equation 4. 6. Glycerol conversion definition 2.

$$\text{Glycerol conversion (\%)} = 100 \times \frac{\text{moles of C in all gas products}}{3 \times (\text{moles of glycerol supplied})}$$

Equation 4. 7. Glycerol conversion definition 3.

$$\text{Glycerol conversion (\%)} = 100 \times \frac{\text{moles of C in gas and liquid products}}{3 \times (\text{moles of glycerol supplied})}$$

Equation 4. 8. Glycerol conversion definition 4.

The final parameter used when describing glycerol conversion to hydrogen which will be considered here is the selectivity to products. Conventional definition for selectivity to a product containing a specific element is the ratio of molar production of this species to the sum of the molar productions of all the products containing the same element. For example, for selectivity to hydrogen gas from the products containing the hydrogen element, all the hydrogen containing products are considered in the ratio (H₂, CH₄, NH₃, hydrocarbons). For selectivity to the carbon containing products CO or CO₂, all the carbon containing products are considered (CH₄, CO, CO₂, carbonaceous deposits, carbonates, hydrocarbons, volatile organic compounds). But other definitions have appeared in the literature such as Equation 4. 9 to Equation 4. 11. Among the non-conventional definitions of selectivity, for H₂ selectivity Equation 4. 9 is by far the most common. It compares the ratio of H₂ in the gas to gaseous carbon containing species to the ratio of H₂ to CO₂ under thermodynamic equilibrium. Note that only H₂ and CO₂ are formed (in the ratio 7/3) under thermodynamic equilibrium according to Reaction 4. 3. In the Tables below, only H₂ selectivity is listed for clarity.

$$\text{H}_2 \text{ selectivity (\%)} = 100 \times \frac{\text{moles of H}_2 \text{ produced}}{\text{moles of C produced in gas phase}} \times \frac{1}{RR}$$

Equation 4. 9. H₂ selectivity definition 1. RR = the reforming ratio (7/3), defined as the ratio of moles of H₂ to CO₂ formed at thermodynamic equilibrium.

$$H_2 \text{ selectivity (\%)} = 100 \times \frac{\text{moles of } H_2 \text{ produced}}{\sum \text{moles of } H_2, CO, CH_4 \text{ and } CO_2 \text{ produced}}$$

Equation 4. 10. H_2 selectivity definition 2.

$$H_2 \text{ selectivity (\%)} = 100 \times \frac{\text{moles of species } \alpha \text{ produced}}{\sum \text{moles of } C \text{ produced in the gas phase}}$$

Equation 4. 11. H_2 selectivity definition 3. $\alpha = CO, CO_2, CH_4$ etc.

Other characteristics which are less common (maybe even specific to one particular reference) are listed in the text. When the characteristics listed above are referred to in the text or in a Table the definition used is given in brackets. Temperatures are given in degrees Celsius ($^{\circ}C$) and pressures are given in bar.

4.3 GLYCEROL CONVERSION REACTION PATHWAY

The reaction pathway for the conversion of glycerol to hydrogen is complex and many reaction intermediates are possible on the route from glycerol through 2- and 3-carbon compounds to CO , CO_2 and CH_4 . Conversion of glycerol is commonly carried out using a catalyst containing a metal on a support material. The metal has the ability to bind to C and O atoms in the glycerol molecule and then break C-C or C-O bonds.¹⁸⁵ By binding to two C atoms in the glycerol molecule, the catalyst can break a C-C bond resulting in the formation of ethylene glycol (ethane-1,2-diol), CO and H_2 and thus promoting glycerol decomposition. By binding to one C and one O atom in the glycerol molecule, the catalyst can break a C-O bond resulting in the formation of 1,2 or 1,3-propanediol and H_2O . This is referred to as dehydrogenation since water is removed from the compound. Further C-C and C-O breakage of the ethylene glycol, 1,2 and 1,3-propanediol by the metal catalyst then follows. Liu and Greeley¹⁸⁶ constructed free energy diagrams for a series of glycerol conversion intermediates on Pt(111) using density functional theory (DFT) calculation correlation schemes for binding energies and Brønsted–Evans–Polanyi (BEP) relationships for transition state energies (Figure 4. 4). They reported that for the first 6 dehydrogenation decomposition intermediates the energy of the dehydrogenation transition state was lower than the C-C bond cleavage transition state. The results showed that decomposition of glycerol is more likely to first proceed through a series of dehydrogenation reactions and then through C-C bond cleavage reactions.

A metal catalyst can also induce the WGS reaction by adsorption of CO and H_2O molecules, followed by dissociation of the H_2O molecules into OH and then O .¹⁸⁷ The CO molecules can then react with adsorbed OH and H to form CO_2 and H_2 with $COOH$ as an intermediate or alternatively the CO molecules can react with O to form CO_2 . In the latter case,

adsorbed H form H_2 without interfering with the reaction between CO and O. Hence a metal catalyst can induce the WGS reaction by dissociating O-H bonds in the H_2O and OH molecules and promote C-O bonds in the CO_2 molecules.

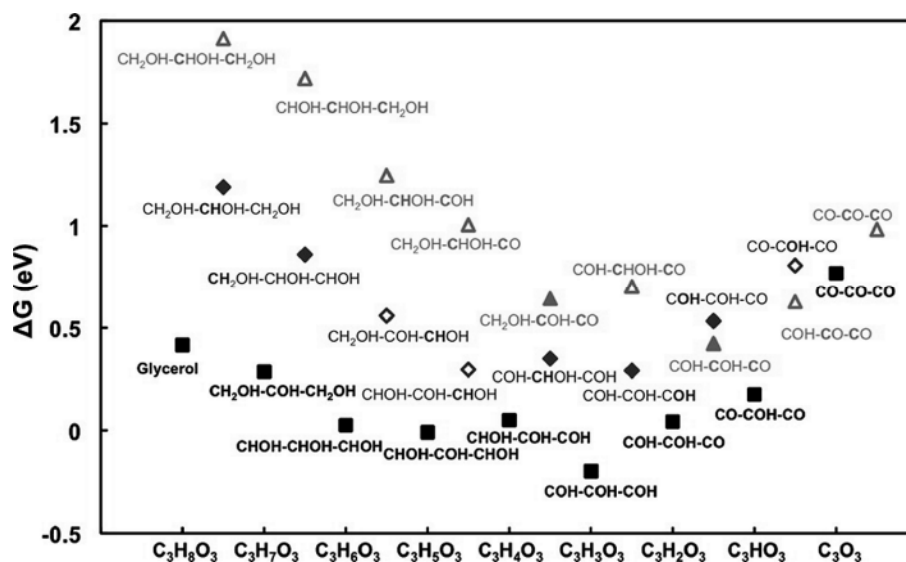


Figure 4. 4. Free energy diagram of glycerol decomposition intermediates at 210 °C and 1 bar on Pt(111) for all levels of dehydrogenation states of glycerol. Black squares = the adsorption thermochemistry of the most stable dehydration intermediate for a given dehydrogenation state, diamonds = the most stable dehydrogenation transition state for a given dehydrogenation state, triangles = the corresponding energetics for the C-C cleavage transition state for a given dehydrogenation state. Reprinted with permission from Liu and Greeley (2011).¹⁸⁶ Copyright 2011 American Chemical Society.

Apart from gaseous and liquids compounds, it is also possible that elemental carbon (or coke) is formed during glycerol conversion. A common route to coke formation is Reaction 4. 4. Coke formation can cause catalyst deactivation and measures are therefore taken to minimise it.



Reaction 4. 4. Formation of coke from CO and H_2 .

By analysing the gaseous products and the liquid products formed during glycerol conversion as well as analysing the coke, the understanding of the reaction pathways can be increased. Dupont et al.¹⁸⁸ for example studied thermal decomposition of glycerol using thermogravimetric analysis (TGA) by heating it with a temperature ramp rate of $5 \text{ }^\circ\text{C min}^{-1}$ in N_2 . Mass loss began at 150 °C and ended at 230 °C. The crude glycerol decomposed into 94 wt% volatiles and 6 wt% residues. The results showed that glycerol will readily decompose at

temperatures below 230 °C in N₂. Thermal decomposition of glycerol at temperatures between 500 and 700 °C produced H₂, CO, CO₂ and CH₄ as well as ethane, ethene, propane, propene, *n*-butane, butane, and significant amounts of coke.¹⁸⁹ In this study, up to 50% of the carbon in the glycerol converted to coke during catalytic cracking at 500 °C with a S:C of 1.7 using a commercial FCC catalyst containing Y-zeolite in a Si/Al matrix. Valliyappan et al.¹⁹⁰ carried out thermal decomposition of glycerol at 650 °C with N₂ as a carrier gas and analysed the off-gas using gas chromatography. The off gas consisted mainly of CO (54.0%) while the second most common species was H₂ (17%). Other species detected in the off gas were CO₂ (0.2 %), CH₄ (14.2 %), C₂H₄ (10.1%), C₂H₆ (2.2%) and C₃H₆ (2.4%).

Chiodo et al.¹⁷⁶ investigated glycerol's thermal decomposition at 800 °C in the presence of steam (S:C of 3) and analysed the reactor off gas and condensate using GC and GS-MS respectively. With regard to the gas phase, CO had the highest selectivity with regards to carbon (50%) followed by C₂H₂ and C₃H₆ (25% in total), CH₄ (13%), H₂ (10%) and CO₂ (1%). The condensate contained acetone, acetaldehyde, ethanol, propanol, acetic acid and 2,3-dihydroxypropanal. Stein et al.¹⁹¹ performed thermal decomposition of glycerol in the presence of steam at temperatures between 650 and 700 °C and analysed both the condensate and the off gas using gas chromatography. At 650 °C only acetaldehyde and acrolein were formed (the moles of acetaldehyde and acrolein formed per mole of converted glycerol were 0.48 and 0.52 respectively).

The absence of any other species could be explained by the short residence time used in the experiment (0.1 s). As the temperature increased, the moles of acetaldehyde and acrolein per mole of converted glycerol decreased while the moles of CO, CO₂, CH₄ and H₂ per mole of converted glycerol increased. The results indicated that glycerol first decomposed to acetaldehyde and acrolein which then reacted further to form CO, CO₂, CH₄ and H₂. Stein et al.¹⁹¹ also carried out thermal decomposition in the presence of steam at 700 °C and (S:C 168.7, 1 bar) with and without the presence of NO₂ gas (which has the ability to inhibit radical initiated reactions). The presence of NO₂ gas had no effect on the yield of acetaldehyde but reduced the yield of acrolein by 71%. They concluded that acetaldehyde was formed by a bond cleavage reaction and acrolein was formed by a radical initiated reaction.

4.4 STEAM REFORMING (SR)

Steam reforming (SR) is the most extensively investigated production route to hydrogen from glycerol. It involves adding glycerol and water to a reactor where the glycerol is gasified and the water is turned into steam. The water can also be turned into steam before it reaches the reactor using a preheating system. A Ni based catalyst is commonly placed inside the reactor. A CO₂ sorbent can also be incorporated to the reactor, which has the ability to capture the CO₂ formed

from the WGS reaction and thus shifting favourably its equilibrium, and as a knock-on effect, also that of the decomposition of glycerol. The SR process with in situ CO₂ capture is referred to as sorption enhanced steam reforming (SESR).

4.4.1 THERMODYNAMIC EQUILIBRIUM ANALYSIS

Thermodynamic equilibrium analysis with reactor temperatures between 77 and 1127 °C, S:C between 1/3:1 and 4 2/3:1 has been undertaken by a number of research groups.¹⁹²⁻²⁰¹

The H₂ concentration increased as the temperature increased and reached a maximum level.^{192-194,197,198,200,201} The maximum H₂ concentration was dependent on the S:C so that the higher the S:C, the lower the temperature of maximum H₂ concentration.^{192-194,197} A higher S:C also resulted in higher H₂ concentrations over a range of temperatures.^{192-194,197-199}

Thermodynamic equilibrium analysis has shown that the optimum temperature for steam reforming of glycerol with regard to maximum H₂ yield was 540-677 °C.^{50,195,198-201}

The maximum H₂ yield (Equation 4. 4) was 6-6.9 (Table 4. 1). S:C affected the H₂ yield such that a higher S:C resulted in a higher H₂ yield,^{195,200,201} as illustrated by Figure 4. 3.

Table 4. 1. Summary of thermodynamic equilibrium analysis of steam reforming. Temperatures are given in °C

Reference	Temperatures	S:C	Best results	Optimum conditions	
				Temperature	S:C
201	350-700	3	Yield (Equation 4. 4) 6.2	580	3
199	427-827	3	Concentration 67% Yield (Equation 4. 4) 6	652 652	3 3
198	277-727	0-4	Yield (Equation 4. 4) 6.2	652	4
195	227-1177	0.5 - 4 $\frac{2}{3}$	Concentration 70% Yield (Equation 4. 4) 6.3	727 667	2 4 $\frac{2}{3}$
50	300-800	6.8 - 15 $\frac{1}{3}$	Yield (Equation 4. 4) 6.9	540	15 $\frac{1}{3}$
194	327-927	0-7	Concentration 65%*	577	4
192	327-727	0.3-3	Yield (Equation 4. 4) 6	627	3
193	327-727	0.3-3	Concentration 65% Yield (Equation 4. 4) 6	627 627	3 3
196	327-927	0.3-3.3	Yield (Equation 4. 4) 6	627	3.3
197	327-727	0.3-3	Selectivity (Equation 4. 9) 78% Yield (Equation 4. 4) 5.8	627 652	3 3

*while allowing a maximum CO concentration of 5%.

4.4.2 EXPERIMENTAL WORK

Many experimental investigations of steam reforming of glycerol with reactor temperatures between 200 and 803 °C and S:C between 0.5 and 15.3 have been carried out (Table 4. 3). Both electrical heating and microwave heating were used.²⁰² H₂ yields of 46-67% (Equation 4. 2), 56.5-95% (Equation 4. 3) and 2.5-6.5 (Equation 4. 4) were achieved (Table 4. 3). High temperatures and high S:C resulted in improved performance. Buffoni et al.²⁰³ for example carried out steam reforming between 450 and 600 °C (S:C 6) and reported that the H₂ concentration increased from 59 to 71% as the temperature was raised from 450 to 600 °C while the concentrations of CO, CO₂ and CH₄ reduced. This is in agreement with Zhang et al.²⁰⁴, Adhikari et al.¹⁹³ and Pompeo et al.²⁰⁵ who all reported increased H₂ concentrations with rising temperature in the 350-650 °C range. The effect of S:C was studied by Slinn et al.¹⁸⁴ who performed steam reforming of crude glycerol at 850 °C and reported an increase in H₂ concentration when the S:C grew from 0.5 to 2.5.

The effects on the steam reforming process of the WGS reaction were demonstrated by Douette et al.²⁰⁶ who carried out steam reforming with a separate WGS reactor. The steam reforming reactor was at 1 bar, 804 °C and S:C of 2.2 while the WGS reactor was between 320 and 420 °C. The H₂ yield (as defined by Equation 4. 4) increased from 4.3 to 5.9 for WGS temperature from 320 to 380°C (Figure 4. 5). As the temperature increased further to 420 °C the H₂ yield (Equation 4. 4) reduced to 5.3. The results demonstrated the ability of the WGS reaction to aid in H₂ production at lower temperatures but also to have the opposite effect when it is reversed as temperature increases, as explained by the thermodynamics of the steam reforming process.

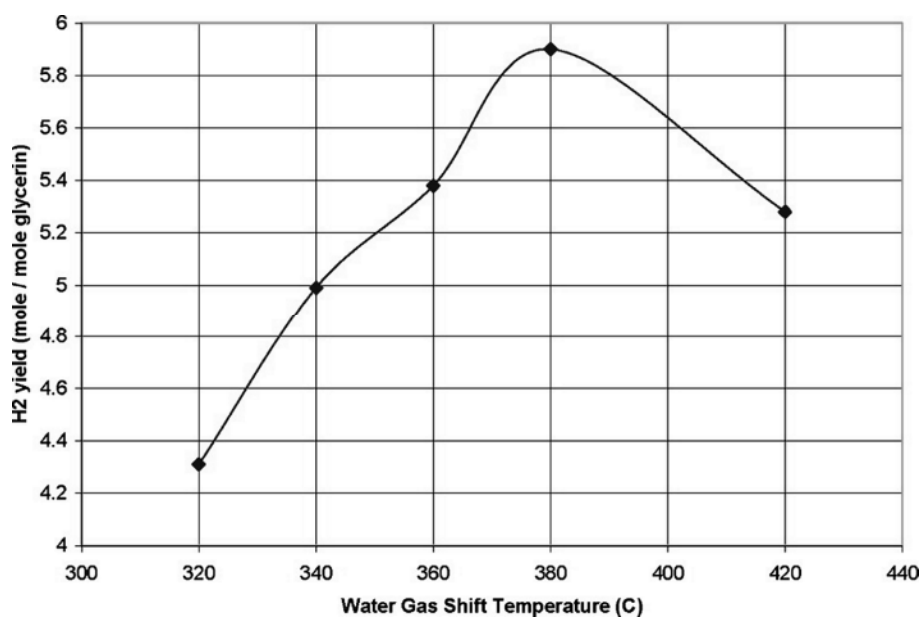


Figure 4. 5. H₂ yield as a function of WGS reactor temperature following steam reforming of glycerol with S:C 2.2 at 804 °C. Reprinted with permission from Douette et al. (2007).²⁰⁶ Copyright 2007 American Chemical Society.

The means of heating the steam reforming reactor can also affect the steam reforming process as demonstrated by Fernandez et al.²⁰², who steam reformed glycerol using an activated carbon (AC) catalyst at 1 bar, 800 °C and S:C between 1 and 9 using both electrical heating and microwave heating. With electrical heating, H₂ in the reactor off gas increased with S:C from 30.9 to 38.2% while the amount of CO reduced from 47.2 to 44.1%. As a result the H₂:CO ratio augmented from 0.7 to 0.9. With microwave heating, H₂ increased from 40.9 to 49.1% as S:C increased while CO reduced from 44.0 to 42.7%, causing the H₂:CO ratio to increase from 0.9 to 1.2. However, the conversion to gaseous products (Equation 4. 7) was lowered from 67.8 to 52.3% under electrical heating and from 70.4 to 62.3% under microwave heating.

The results showed that increased S:C augmented the H₂:CO ratio and that microwave heating produced a higher H₂:CO ratio for a given S:C compared to electrical heating. However, there was a trade off between conversion to gaseous products and H₂:CO ratio. The improved performance of microwave heating compared to electrical heating was discussed by Fernandez et al.²⁰⁷ (reviewed in the section on thermal decomposition).

During analysis of the gaseous products from glycerol steam reforming, only the concentrations of H₂, CH₄, CO and CO₂ are normally measured since the formation of other compounds with higher numbers of carbon atoms that can form is negligible.^{199-201,208} The reason for this is that the enthalpy of formation for carbon containing compounds is increased with the number of carbon atoms (Table 4. 2).²⁰⁸ This subsequently increases the Gibbs free energy of formation with the number of carbon atoms, making it less likely for compounds

containing more carbon atoms to form compared to compounds containing less carbon atoms. In fact, thermodynamic analyses using minimisation of Gibbs free energy have shown that the compounds methanal, methanol, formaldehyde, ethanal, ethanol, ethane, ethene, ethylene, propanal, propane, propene, propanone, propionaldehyde, acetone, acetic acid, acrolein, allyl alcohol and acetaldehyde either exist in negligible concentrations (molar fractions $<10^{-6}$) or not at all at equilibrium.^{195,199-201} However, equilibrium is hard to reach under experimental conditions and higher carbon containing compounds have been found. Gas chromatography-mass spectrometry (GC-MS) analysis of condensate produced during steam reforming at temperatures up to 650 °C has shown the presence of unreacted glycerol as well as pyrolysis products.^{184,203,209} This shows that high carbon containing compounds can indeed form but they collect in the condensate, which is expected since volatility is reduced with increased number of carbon atoms.

Table 4. 2. Enthalpy (Cal °C⁻¹ mol⁻¹) for a number of 1, 2 and 3 carbon containing compounds²⁰⁸

Compound	Temperature (°C)		
	427	627	827
Methane	43.86	46.47	48.78
Ethane	55.25	59.24	62.90
Propane	65.90	71.47	76.63
Methanol	56.41	59.66	-
Ethanol	67.22	72.31	76.88
Propanol	85.59	92.57	-

Catalysts were manufactured using a range of metals and supports. The metal particle size and the metal dispersion on the catalyst can be altered by using different metals²⁰⁵, different metal loadings²¹⁰ and different supports.^{209,211} It is also possible to alter the metal dispersion through the manufacturing process such as using different calcination atmospheres during the catalyst synthesis process.¹⁷⁹ A small metal particle size and a high metal dispersion should be favourable to a high H₂ yield, H₂ selectivity and H₂ concentration. However, this is not always the case and factors other than particle size and dispersion such as what metal is used can have a larger impact on the catalyst properties.^{203,204} In other words, one metal can outperform another even if it displays a larger particle size and lower dispersion.

With increased time on stream, catalyst deactivation is commonly reported and this has been linked to coke formation of the catalyst surface which limits the contact between the catalyst and the glycerol. Choi et al.¹⁷⁹ for example undertook steam reforming at 600 °C with S:C of 8, achieving a H₂ yield (Equation 4. 3) of 90-95% and a glycerol conversion (Equation 4. 7) between 95 and 100% for 200 min. This then reduced to 80% after 350 min. The results were in agreement with Araque et al.¹⁸⁰, who reported a reduction in H₂ yield (Equation 4. 3) from 85.7 to 50% after 3 h at 650 °C and S:C ratio of 3. Chiodo et al.'s experiments at 700 °C and S:C of 3 for 100 h produced a stable H₂ yield (Equation 4. 2) at 4.7% for 8 h, which then

reduced to 2.5% after 100 h.¹⁷⁶ Chiodo et al.¹⁷⁶, Choi et al.¹⁷⁹ and Araque et al.¹⁸⁰ all reported coke formation on the catalyst which was used to explain the reduction in H₂ yield with increased time on stream. Coke formation has been shown to reduce the surface area and pore volume of catalysts.^{201,203,205} The extent of coke formation has also been shown to correlate with reduced formation of gaseous products, reduced H₂ production and increased formation of liquid products.^{180,183,203} Doping the catalyst with an additional metal or using different supports can reduce coke formation of the catalyst.^{180,203,209} CeO₂ as a support has been particularly useful for this while simultaneously reducing metal particle size and dispersion. The effect of the CeO₂ can be attributed to the formation of strong bonds between the CeO₂ support and the metal. Farmer and Campbell²¹² have reported on strong chemical bonding between Ni and Ce which subsequently reduces the driving force for particle growth. Strong bonding between metal and support has also been reported to reduce the catalyst metals susceptibility to oxidation²¹³, another notorious deactivation process of nickel based catalysts during steam reforming.

During the steam reforming process coke can form through Reaction 4. 4, Reaction 4. 5 (Boudouard) and thermal decomposition of glycerol or CH₄ (Reaction 4. 6 and Reaction 4. 7).



Reaction 4. 5. Boudouard reaction.



Reaction 4. 6. Coke formation by thermal decomposition of glycerol.



Reaction 4. 7. Coke formation by thermal decomposition of CH₄.

Since all reactions leading to the formation of coke apart from the decomposition of CH₄ are exothermic, coke is not expected to form with regard to the thermodynamics of the steam reforming process at high temperatures. As H₂O is formed together with coke in three out of the five reactions listed above, a higher S:C reduces the amount of coke. In fact, thermodynamic analyses of glycerol steam reforming using minimisation of Gibbs free energy and the stoichiometric method have shown that coke formation is thermodynamically inhibited with S:C between 1.5-4 between 277-927 °C.^{192-196,198,200}

Therefore, high temperatures and high S:C will reduce catalyst deactivation by coking. This was confirmed by Sanchez et al.²¹⁴ who carried out steam reforming at 600, 650 and 700 °C for 4 and 8 h and determined the glycerol conversion. For steam reforming at 600 and 650 °C

they reported significantly lower conversion after 8h compared to after 4h. However the conversion at 700 °C was similar after 8 h and after 4h.

Temperature programmed reduction and oxidation (TPR/TPO) have revealed that the coke formed on catalysts consists of two types of carbon containing species while SEM imaging has shown coke deposits with filamentous form.^{17,52,180,215}

Cheng et al.^{17,52,215} analysed the characteristics of carbon deposits formed on a bimetallic Co-Ni/Al₂O₃ catalyst and on a Co/Al₂O₃ catalyst. TGA-MS was used to carry out temperature programmed reduction (TPR) in a mixture of H₂ and Ar followed directly by temperature controlled oxidation (TPO). TPO was carried out in air in the case of the Co/Al₂O₃ catalyst and in both air⁵² and pure O₂²¹⁵ in the case of the bimetallic Co-Ni/Al₂O₃ catalyst. During TPR, the catalysts displayed a mass loss and subsequent release of CH₄. During TPO the catalysts displayed further mass loss and subsequent release of CH₄, CO and CO₂. Based on mass change of the bimetallic Co-Ni/Al₂O₃ catalyst it was concluded that the carbon deposits removed during TPR and TPO had molar C:H ratios of 1 and 6 respectively. The results indicated the presence of two types of carbon containing species in the carbon deposits. Cheng et al.⁵² carried out a second set of TPR and TPO. This resulted in a mass loss during TPR subsequently regained during the TPO, which indicated that the changes in mass were due to reduction and oxidation of the Co-Ni species. Since the net mass change was zero after the second set of TPR and TPO it was concluded that the first set of TPR and TPO removed all carbon deposits.

Using different supports can result in catalysts with different acidity (i.e. with different electron acceptor capability) which has an impact on the gas and condensate composition. Pompeo et al.⁵¹ manufactured catalysts using supports with different acidity. The catalyst with the highest acidity (with the highest electron donor capacity) caused lower conversion to gaseous products, and dehydration products were found in the liquid phase. This suggested that the acidic support initiated dehydration reactions which led to a reaction pathway resulting in liquid instead of gaseous products. Different supports can also lead to differences in selectivity to CO₂ and CO selectivity.²¹³ High selectivity to CO₂ correlated with high selectivity to H₂ and this was explained by the ability to promote the WGS reaction. As discussed by Nichele et al.²¹³ the reason why the WGS reaction was promoted was that CO attached to the catalyst where it was subjected to the WGS reaction. No correlation between catalyst surface area and H₂ concentration or H₂ yield has been reported.^{179,181,216}

Table 4. 3. Summary of experimental work on steam reforming. Temperatures in °C

Reference	Temperature	S:C range	Catalyst	Best results	Optimum conditions	
					Temperature	S:C
178	550-650	2	Ni/MgO	Conversion (Equation 4. 5) 100%	650	2
				Selectivity (Equation 4. 9) 65.6%	650	2
				Conversion (Equation 4. 5) 97.7%	600	2
			Ni/CeO ₂	Selectivity (Equation 4. 9) 66.7%	550	2
				Yield (Equation 4. 3) 43.6%	600	2
				Conversion (Equation 4. 5) 98%	650	2
			Ni/TiO ₂	Selectivity (Equation 4. 9) 62.2%	650	2
				Yield (Equation 4. 3) 47.0	650	2
180	450-650	3	Ce ₂ Zr _{1.5} Co _{0.5} O _{8-δ}	Conversion (Equation 4. 5) 100%	650	3
				Yield (Equation 4. 4) 5.7	650	3
			Ce ₂ Zr _{1.5} Co _{0.47} Rh _{0.07} O _{8-δ}	Conversion (Equation 4. 5) 100%	650	3
				Yield (Equation 4. 4) 6.7	650	3
50	600-700	6.8-15.3	Ni/CeO ₂	Conversion (Equation 4. 5) 94.1%	700	15.3
				Selectivity (Equation 4. 9) 59.8	700	15.3
				Yield (Equation 4. 4) 3.4	700	15.3
			Ni-ZrO ₂ /CeO ₂	Conversion (Equation 4. 5) 100%	700	15.3
				Selectivity (Equation 4. 9) 62.5%	700	15.3
				Yield (Equation 4. 4) 3.9	700	15.3

Table 4.3 (Continued)

Reference	Temperature	S:C range	Catalyst	Best results	Optimum conditions	
					Temperature	S:C
181	700	2	Ni	Conversion (Equation 4. 5) 65%	700	2
				Concentration 60%	700	2
				Yield (Equation 4. 4) 2.2	700	2
			NiIr	Conversion (Equation 4. 5) 99%	700	2
				Concentration 60%	700	2
				Yield (Equation 4. 4) 4.5	700	2
			NiPd	Conversion (Equation 4. 5) 99%	700	2
				Yield (Equation 4. 4) 3.7	700	2
			NiPt	Conversion (Equation 4. 5) 98%	700	2
				Yield (Equation 4. 4) 4.8	700	2
			NiRu	Conversion (Equation 4. 5) 89%	700	2
				Yield (Equation 4. 4) 2.4	700	2
216	500-600	3.3	Ru/Y ₂ O ₃	Conversion (Equation 4. 6) 100%	600	3.3
				Yield (Equation 4. 3) 82.2%	600	3.3
			Ru/ZrO ₂	Conversion (Equation 4. 6) 98.5%	600	3.3
				Yield (Equation 4. 3) 81.6%	600	3.3
			Ru/CeO ₂	Conversion (Equation 4. 6) 82%	600	3.3
				Yield (Equation 4. 3) 73.1%	600	3.3
			Ru/La ₂ O ₃	Conversion (Equation 4. 6) 87.9%	600	3.3
				Yield (Equation 4. 3) 71.8%	600	3.3
			Ru/SiO ₂	Conversion (Equation 4. 6) 32.7%	600	3.3
				Yield (Equation 4. 3) 18.3%	600	3.3

Table 4. 3 (Continued)

Reference	Temperature	S:C range	Catalyst	Best results	Optimum conditions	
					Temperature	S:C
			Ru/MgO	Conversion (Equation 4. 6) 31.3%	600	3.3
			Ru/Al ₂ O ₃	Yield (Equation 4. 3) 12.3%	600	3.3
				Conversion (Equation 4. 6) 28.5%	600	3.3
				Yield (Equation 4. 3) 6.4%	600	3.3
217	500-600	15.3	Ni/Al	Conversion (Equation 4. 6) 100%	600	15.3
				Yield (Equation 4. 4) 6.5	600	15.3
			Ni/Ce	Conversion (Equation 4. 6) 55%	600	15.3
				Yield (Equation 4. 4) 0.3	600	15.3
179	600	8	Ni/Al calcined in air	Conversion (Equation 4. 7) 85%	600	8
				Yield (Equation 4. 3) 80%	600	8
			Ni/Al calcined in N ₂ O	Conversion (Equation 4. 7) 99%	600	8
				Yield (Equation 4. 3) 95%	600	8
176	500-800	3	Rh/Al ₂ O ₃	Conversion (Equation 4. 7) 95%	700	3
				Yield (Equation 4. 2) 67%	700	3
210	650	15.3	Ru/Mg(Al)O	Conversion (Equation 4. 8) 90%	650	15.3
				Yield (Equation 4. 3) 85%	650	15.3
			Ru-Sn/Mg(Al)O*	Conversion (Equation 4. 8) 90%	650	15.3
				Yield (Equation 4. 3) 60%	650	15.3
204	400-550	3	Ir/CeO ₂	Concentration 68.7%	550	3
				Selectivity (Equation 4. 9) 94.1%	550	3
			Co/CeO ₂	Concentration 68.5%	550	3
				Selectivity (Equation 4. 9) 93.4%	550	3
			Ni/CeO ₂	Concentration 67.9%	550	3

Table 4. 3 (Continued)

Reference	Temperature	S:C range	Catalyst	Best results	Optimum conditions	
					Temperature	S:C
				Selectivity (Equation 4. 9) 90.8%	550	3
209	550-650	4	Ni/CeO	Conversion (Equation 4. 5) 100%	600	4
			Ni/TiO ₂	Selectivity (Equation 4. 9) 75%	600	4
				Conversion (Equation 4. 5) 80%	650	2
			Ni/MgO	Selectivity (Equation 4. 9) 40%	650	2
				Conversion (Equation 4. 5) 100%	650	2
				Selectivity (Equation 4. 9) 45%	650	2
213	500-650	15.3	Ni/TiO ₂ **	Conversion (Equation 4. 6) 10%	650	15.3
				Yield (Equation 4. 3) 5%	650	15.3
			Ni/SBA-15**	Conversion (Equation 4. 6) 85%	500	15.3
				Yield (Equation 4. 3) 75%	500	15.3
			Ni/ZrO ₂ **	Conversion (Equation 4. 6) 90%	500	15.3
				Yield (Equation 4. 3) 81%	500	15.3
214	600-700	5.3	Ni/Al ₂ O ₃	Conversion (Equation 4. 7) 99.4%	700	5.3
				Selectivity (Equation 4. 9) 99.7%	650	5.3
183	200-600	2	Ni/Al ₂ O ₃	Conversion (Equation 4. 8) 95%	600	2
				Yield (Equation 4. 3) 65%	600	2
205	350-450	15.3	Pt/SiO ₂	Conversion (Equation 4. 7) 100%	450	15.3
				Concentration 70%	450	15.3
			Ni/SiO ₂	Conversion (Equation 4. 7) 80%	450	15.3
				Concentration 70%	450	15.3
17	497-550	1.1-4	Co/Al ₂ O ₃	Conversion (Equation 4. 7) 50%	550	4

Table 4. 3 (Continued)

Reference	Temperature	S:C range	Catalyst	Best results	Optimum conditions	
					Temperature	S:C
206	804	2.2	Ni based commercial catalyst	Concentration 35%	804	2.2
51	350	15.3	Pt/SiO ₂	Conversion (Equation 4. 7) 100%	350	15.3
				Selectivity (Equation 4. 10) 69%	350	15.3
			Pt/Ce ₄ Zr _{1α}	Conversion (Equation 4. 7) 78%	350	15.3
				Selectivity (Equation 4. 10) 72.5%	350	15.3
			Pt/ZrO ₂	Conversion (Equation 4. 7) 15.5%	350	15.3
				Selectivity (Equation 4. 10) 62.2%	350	15.3
Pt/γ-Al ₂ O ₃	Conversion (Equation 4. 7) 7.5%	350	15.3			
	Selectivity (Equation 4. 10) 61.1%	350	15.3			
203	450-600	2	Ni/CeAl ₂ O ₃ ***	Conversion (Equation 4. 7) 100%	600	2
				Concentration 70.6%	600	2
			Ni/ZrAl ₂ O ₃ ***	Conversion (Equation 4. 7) 100%	600	2
				Concentration 71.1%	600	2
			Ni/Al ₂ O ₃ ***	Conversion (Equation 4. 7) 100%	600	2
Concentration 69.9%	600	2				
193	550-650	2	Ni/MgO	Yield (Equation 4. 4) 4	650	2

*displaying only the Ru-Sn/Mg(Al)O catalyst which gave the best result.

**Results listed are after 5h time on stream.

***Results listed are after 1h time on stream.

4.5 SORPTION ENHANCED STEAM REFORMING (SESR)

Thermodynamic equilibrium analysis has shown that the presence of a CO₂ sorbent will improve the steam reforming process by increasing the concentration of H₂ while reducing the concentrations of CO, CO₂ and CH₄ as well as increasing the H₂ yield (Table 4. 4).^{23,195,199,200,218,219} Both thermodynamic equilibrium analysis and experimental work have demonstrated these improvements using CaO and dolomite as CO₂ sorbents.^{195,200,218,219} The presence of a CO₂ sorbent has also been shown to reduce the temperature and S:C at which maximum H₂ concentration and H₂ yield was reached.^{23,195,199,218,220} However, the CO₂ sorbent will become saturated as sorption proceeds with time, causing a loss of CO₂ capture capacity with subsequent loss of the improvement on the steam reforming process.^{23,218,220,221} Regeneration of the sorbent by desorption of the captured CO₂ is then required when the same sorbent is to be used again.

4.5.1 THERMODYNAMIC EQUILIBRIUM ANALYSIS

Chen et al.²⁰⁰ carried out thermodynamic equilibrium analysis with S:C of 1:3 at 527 °C and 1 bar while varying CO₂ capture fraction from 0-100%. As the fraction of CO₂ removed from the system increased, the H₂ concentration increased and the concentrations of CO and CH₄ reduced. Wang et al.¹⁹⁹, da Silva and Müller¹⁹⁵ and He et al.²²⁰ carried out thermodynamic equilibrium analysis with S:C from 0.5:1 to 4²/₃:1 at temperatures between 227 and 1177 °C with and without CaO as the CO₂ sorbent. Without CaO, the highest H₂ concentration (67-68%) and the highest H₂ yield (≈80%, Equation 4. 3) were reached at 612-652 °C and S:C of 3:1-4²/₃:1. In the presence of CaO the highest H₂ concentration (95-99%) and the highest H₂ yield (≈100%) was reached at temperatures between 427 and 600 °C. Li et al.²¹⁹ carried out thermodynamic equilibrium analysis with CaO as the CO₂ sorbent with S:C of 1¹/₃:1 at 627 °C while varying the CaO:Glycerol ratio from 0:1 to 20:1. When the ratio of CaO to glycerol increased, the concentration of H₂ in the reactor off-gas increased from 60% to above 96% while those of CO and CH₄ reduced from 15 and 4% to below 1 and 2%, respectively.

The improvements in the steam reforming process are attributed to the removal of CO₂ from the gas phase by CaO, resulting in the equilibrium of the WGS reaction and the steam reforming reactions (complete glycerol steam reforming and methane steam reforming (MSR)) to shift according to Le Chatelier's principle, with subsequent reduction of the concentrations and yields of CO and CH₄, glycerol, as well as CO₂. When only carbon containing species were considered, the only remaining compound below 577 °C was CaCO₃, which resulted from CaO carbonation (Reaction 3. 1) (Figure 4. 6).¹⁹⁹

With temperature increased above 577 °C, the concentration of CaCO₃ reduced while those of CO₂ and CO increased. The reduction of CaCO₃ with simultaneous increase in CO₂ was

attributed to decomposition of CaCO_3 through the reverse of CaO carbonation leading to release of CO_2 . The increase in CO was attributed to the reverse WGS reaction.

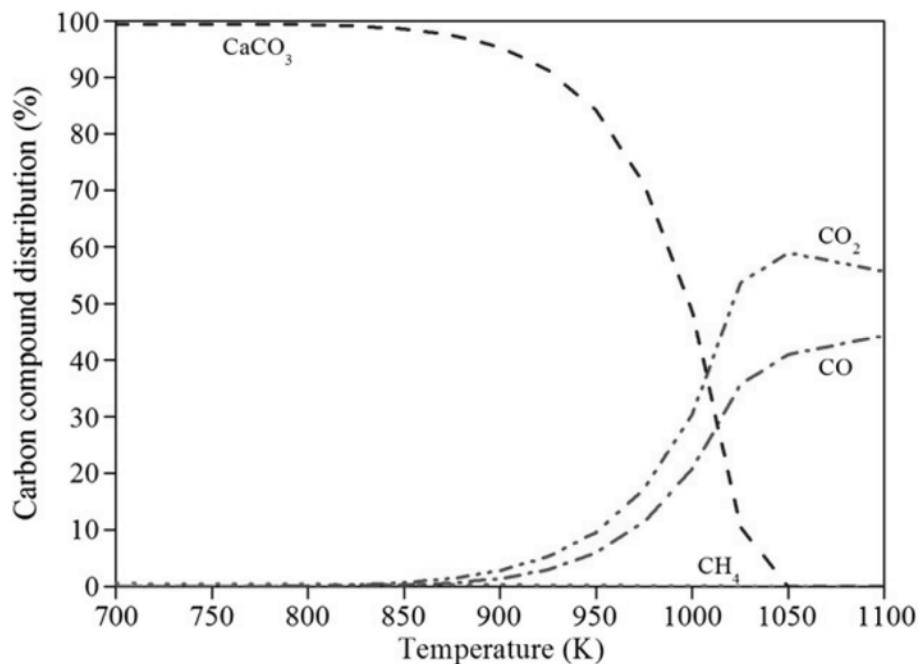


Figure 4. 6. Carbon compound distribution at temperatures between 427 and 827 °C during sorption enhanced steam reforming of glycerol at S:C of 3. Reprinted with permission from Wang et al. (2010).¹⁹⁹ Copyright 2010 Elsevier.

4.5.2 EXPERIMENTAL WORK

The addition of a CaO based CO_2 sorbent has been shown experimentally to increase the H_2 concentration and the H_2 yield (Table 4. 4), however the effect of the Ca -based sorbent is gradually eroded at temperatures above 700 °C due to the decomposition of CaCO_3 .^{23,199,218} He et al.²²⁰ carried out steam reforming of glycerol at temperatures between 500 and 850 °C and S:C of 3 with and without dolomite (a natural mineral consisting of equimolar calcium and magnesium carbonates) as a CO_2 sorbent. Without dolomite, the highest H_2 off gas composition was 70 mol%, reached between 580-600 °C. With dolomite, the highest H_2 concentration was close to 100% and was achieved between 520 and 530 °C. This is in agreement with Dou et al.^{23,218} who carried out steam reforming of pure and crude glycerol in a fixed bed reactor at temperatures between 400 and 850 °C and a S:C of 3 with and without dolomite used as a CO_2 sorbent. Without the dolomite the highest H_2 concentration was 66.7-68.0% and it was achieved at 600-700 °C. With the dolomite the highest H_2 concentration was 88.2-97.0% which was achieved at 500 °C. However, when the temperature increased to 700 °C, the H_2 concentration was lowered to 73.2-77%. The reduced performance of the dolomite at temperatures above 700 °C reported by Dou et al.^{23,218} can be attributed to decomposition of CaCO_3 by the reverse of CaO carbonation.¹⁹⁹

Even under optimised conditions, the effect of CaO is lost after a given time on stream.^{23,218,220} This loss of sorbent effect has been reported earlier and has been attributed to saturation of the CO₂ sorbent.^{221,222}

He et al.²²⁰ achieved >99% H₂ purity with CO, CO₂ and CH₄ levels <1% during steam reforming of glycerol at 575 °C, 1 bar and a S:C of 3 for 200 min, after which the H₂ concentration reduced and the concentrations of CO, CO₂ and CH₄ increased. This was in agreement with Dou et al.²³ who maintained maximum H₂ purity for 3 min at 500 °C and Dou et al.²¹⁸ who reported a 10% drop in H₂ concentration within 10 minutes of operation.

It is possible to regenerate the Ca-based CO₂ sorbents and reuse them in a steam reforming process, however this involves a high energy penalty since temperatures of 800-900 °C are needed to calcine (thermally decompose) the CaCO₃ back to CaO.^{223,224} The CO₂ capture capacity of the sorbent is also reduced for every regeneration step due to sintering, which means that fresh sorbent needs to be continuously added to the steam reforming reactor.^{42,97} However, advances have been made towards solving these issues. CaO based sorbent materials with a low susceptibility towards sintering have been manufactured and methods for reversing the effects of sintering have been proposed.^{45,47}

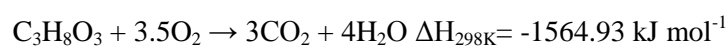
Table 4. 4. Summary of thermodynamic and experimental work on sorption enhanced steam reforming. Temperatures in °C

Reference	Temperature	S:C range	Best results without	Optimum conditions		Best results with	Optimum conditions	
			sorbent	Temperature	S:C	sorbent	Temperature	S:C
Thermodynamic equilibrium analysis								
195	227-1127	1-4.7	Concentration 70%	727	2	Concentration 100%	427	1.2
199	427-827	1-3	Concentration 67%	652	3	Concentration 100%	427	3
220	500-900	1-3	Concentration 60%	620	1.3	Concentration 97%	500	1.3
200	327-727	1-4	Yield (Equation 4. 4) 6	677	3	Yield (Equation 4. 4) 7	327	3
219	227-1227	0-3.3	Concentration 65%	875	3.3	Concentration 100%	477	3.3
Experimental								
220	500-650	1-3	Concentration 70%	600	1.3	Concentration 95%	530	1.3
23	400-700	3	Concentration 68%	600	3	Concentration 97%	500	3
218	500-700	3	Concentration 66.7%	700	3	Concentration 88.2%	500	3

4.6 AUTOTHERMAL REFORMING (ATR)

Autothermal reforming involves carrying out steam reforming in the presence of oxygen. The presence of oxygen results in the exothermic combustion of glycerol (Reaction 4. 8). The heat released by this reaction can be used to sustain the steam reforming reaction (endothermic). If enough oxygen is present the heat released by the exothermic reactions is cancelled out by the heat requirement of the endothermic reforming reactions. This is called a thermoneutral condition and it is an important factor in ATR because no external heating is needed at thermoneutrality and less energy is subsequently needed to heat the reformer. The temperature at which the thermoneutral condition is reached under a given set of conditions is referred to as the thermoneutral temperature. Much attention is given to determine how to maximise hydrogen production while at the same time maintaining thermoneutrality.

In the presence of oxygen, combustion of glycerol (Reaction 4. 8) occurs alongside the glycerol decomposition (Reaction 4. 1) and the WGS (Reaction 1. 2).



Reaction 4. 8. Combustion of glycerol.

By using molar ratios of O_2 to glycerol and of steam to glycerol of 0.269 and 2.770 respectively, the balance of enthalpies of the three reactions at 298 K (25 °C) is zero, realising the thermoneutral condition. This condition corresponds to requiring 7.7% of the glycerol to burn to sustain the steam reforming of the remaining 92.3%.

An increased amount of oxygen relative to the amount of glycerol results in more addition of heat to the process. CO_2 formation is also favoured over CO formation with an increased amount of oxygen (see Reaction 4. 8). Note that the molar amount of H_2 formed for each mole of glycerol during autothermal reforming is lower than the amount of H_2 formed for each mole of glycerol during complete glycerol steam reforming according to Reaction 4. 3. This result in a trade-off between the energy savings from the presence of oxygen and the amount of H_2 produced. Furthermore, the source of O_2 used to carry out ATR introduces additional costs. If air is used, the reformat is significantly diluted with N_2 gas and requires more purification steps. If pure O_2 is used to avoid N_2 dilution of the reformat, an air separation unit is necessary.

4.6.1 THERMODYNAMIC EQUILIBRIUM ANALYSIS

Thermodynamic equilibrium analysis of ATR has been performed at temperatures between 327-927 °C, S:C between 1/3:1 and 4:1 and O:C between 0:1 and 8:1 (Table 4. 5). Note that thermodynamic equilibrium will result in complete conversion of both the glycerol and the O_2 .

High temperature and high S:C improved conditions for hydrogen production. Authayanun et al.²²⁵ reported that the H₂ concentration increased from 15 to 45% as the temperature increased from 427 to 677 °C (S:C 1:1, O:C 0.2:1). This is in agreement with Yang et al.²²⁶ who found that the H₂ selectivity (Equation 4. 9) increased from 20 to 80% as the temperature increased from 400 to 650 °C (SC 1:1, O:C 0.8:1). Wang et al.²²⁷ reported an increase in the H₂ yield (Equation 4. 4) from 2.5 to 5 with an increase from 427 to 727°C (S:C 4:1, O:C 0.2:1). Wang et al.²²⁷ also found that the H₂ yield (Equation 4. 4) increased from 1.5 to 4.5 as S:C increased from 2/3:1 to 4:1 (O:C 0.2:1, 527 °C).

As the O:C increased, conditions for conversion to hydrogen were made less favourable. Authayanun et al.²²⁵ found that the H₂ concentration was reduced from 45 to 40% as the O:C rose from 0.03:1 to 0.27:1 (S:C 1, 727 °C) while Wang et al.²²⁷ reported that the H₂ yield (Equation 4. 4) reduced from 5 to less than 1 when they increased the O:C from 0:1 to 3:1 (S:C 4:1, 727 °C). The hydrogen selectivity (Equation 4. 9) was also reduced as shown by Yang et al.²²⁶ who reported a shift in hydrogen selectivity from 90 to 20% as the O:C was increased from 1/3:1 to 2:1 (S:C 1:1, 600 °C). The concentration, yield and selectivity of CO also reduced while the selectivity of CO₂ increased.

The impact of increased O:C can be attributed to the increased amount of oxygen which favour the combustion reaction over the steam reforming reaction hence reducing the amount of H₂ formed.

Authayanun et al.²²⁵ studied the effect of glycerol concentration in crude glycerol using thermodynamic equilibrium analysis. For this study, the results from thermodynamic equilibrium analysis of pure glycerol were compared to results from analysis of mixtures containing glycerol and methanol with glycerol concentrations of 40-80%. Methanol is the most common contaminant of crude glycerol. The H₂ concentration increased with glycerol concentration at and above 680 °C. This was attributed to the higher amount of H₂ produced per mole of glycerol compared to methanol during steam reforming. Steam reforming of glycerol produces 7 moles of H₂ while methanol steam reforming produces 3 moles of H₂ (Reaction 4. 9).



Reaction 4. 9. Methanol steam reforming.

The thermoneutral temperature increased with the concentration of oxygen.²²⁵⁻²²⁷ Also, the thermoneutral temperature was lowered with increasing S:C for a given O:C.^{225,226}

The overall heat of reaction reduced with increasing O:C (Figure 4. 7).²²⁷ For 627 °C and S:C of 4:1 the overall heat of reaction switched from positive (endothermic) to negative

(exothermic) at O:C of 0.12:1, indicating thermoneutrality. The O:C needed to achieve thermoneutral ATR increased with S:C (Figure 4. 7).

The thermoneutral temperature increased with O:C for a given S:C. Authayanun et al.²²⁵ showed how the thermoneutral temperature increased from 427 to 627 °C as the O:C increased from 0.03:1 to 0.27:1 at S:C of 3:1. This is in agreement with Yang et al.²²⁶ who reported an increase in the thermoneutral temperature from 600 °C to 700 °C as the O:C was raised from 0.7:1 to 0.8:1 when the S:C was kept at 1:1. The addition of oxygen brought heat to the ATR and subsequently the ATR became autothermal at higher temperatures with increasing amounts of oxygen.

The thermoneutral temperature dropped as S:C increased. It was shown that the thermoneutral temperature reduced from 627 to 477 °C when S:C changed from 1/3:1 to 3:1 (O:C 0.13:1) and as the S:C increased from 2.0:1 to 3.4:1 (O:C 1.25:1) it was reduced from 800 °C to 500 °C.^{225,226} This was due to the larger amount of H₂O needing to be heated and the results show that thermal neutral conditions will be reached at higher temperatures with low S:C and low C:O.

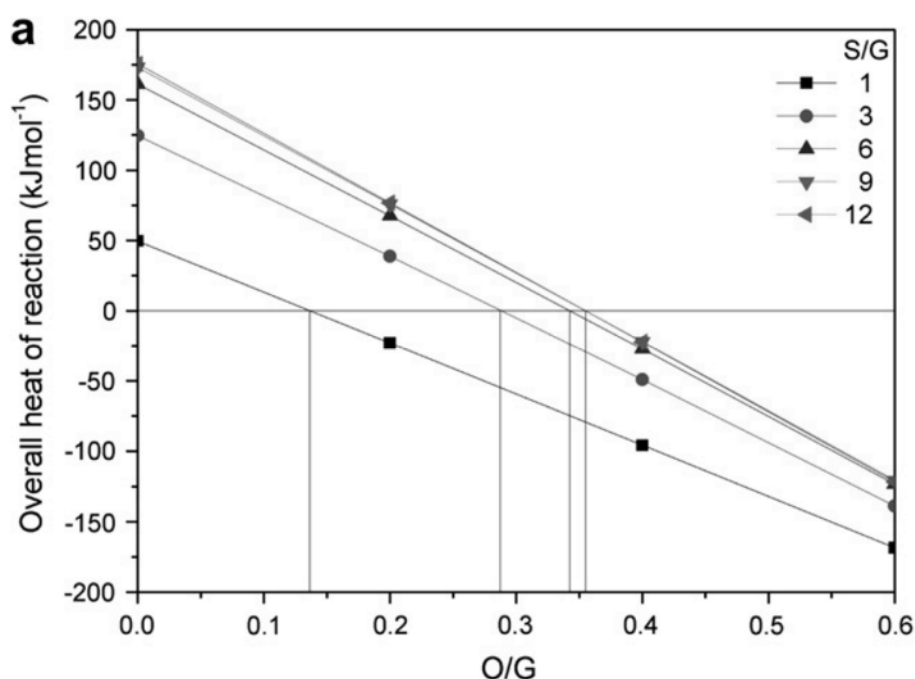


Figure 4. 7. Overall heat of reaction as a function of O:C during ATR of glycerol for S:C between 1/3 and 4 and 627 °C. Reprinted with permission from Wang et al. (2009).²²⁷ Copyright 2009 Elsevier.

Carbon formation was inhibited by high temperatures, high S:C and low O:C. Yang et al.²²⁶ studied the effect of temperature, S:C and O:C on carbon formation between 300 and 800 °C, S:C between 0:1 and 1.2:1 and O:C between 0.7:1 and 1.2.:1 They showed that an increased

temperature resulted in reduced carbon formation for any given S:C and O:C. Increased S:C reduced carbon formation for any given temperature and O:C. Increased O:C increased carbon formation for any given temperature and S:C. The analysis showed that high temperatures, high S:C and high O:C reduced the amount of carbon formation. Wang et al.²²⁷ reported that at 727 °C carbon formation was thermodynamically inhibited in the S:C range of 1/3:1-4:1 and the O:C range of 0:1-1:1. At temperatures between 427 and 627 °C carbon was only formed at S:C below 1 1/3:1 and O:C above 0.6:1.

4.6.2 EXPERIMENTAL WORK

Experiments of ATR have been performed between 375 and 850 °C, S:C between 2:1 and 3:1 and O:C between 0.3:1 and 1.1:1 (Table 4. 5).^{206,228,229} High temperatures favoured the H₂ yield as shown by Swami and Abraham.²²⁹ They reported an increased H₂ yield (Equation 4. 3) from below 5 to ca. 57% as the temperature rose from 500 to 850 °C (S:C 3:1, O:C 0.3:1). The results were in agreement with Douette et al.²⁰⁶, who reported a maximum H₂ yield (Equation 4. 3) of 3.5 ± 0.3 at 850 °C (S:C 2.7:1, O:C 0.8:1). Keeping the temperature at 850 °C and S:C at 2.7:1 while increasing O:C to 1.4:1 reduced the H₂ yield (Equation 4. 4) to 1.2±0.1 showing the negative effect of high O:C. Pereira et al.²²⁸ carried out ATR using a glycerol/ethanol mixture containing 4.2 wt% glycerol and reported an H₂ concentration of 45%.

Table 4. 5. Summary of results from thermodynamic and experimental work on autothermal reforming. Temperatures in °C

Reference	Temperature	S:C	O:C	Catalyst	Best results	Optimum conditions		
						Temperature	S:C	O:C
Thermodynamic equilibrium analysis								
225	327-927	1/3-3	0.03-0.3	n/a	Concentration: 61.6%	594	3	0.23
227	427-727	1/3-4	0-1	n/a	Yield (Equation 4. 4): 6.5	627	4	0
226	400-850	1/2-1	1/3-2	n/a	Selectivity (Equation 4. 9) 110%	650	3 1/3	1
Experimental								
228	375	2	1	Co-Ru(Na)*	Concentration 45%	375	2	1
229	550-850	3	0.3	Pd/Cu/Ni/K- γ -Al ₂ O ₃	Yield (Equation 4. 3) 57%	850	3	0.3
206	770-850	2-2.7	0.8-1.1	Ni	Concentration 31%	807	2.3	0.3
					Yield (Equation 4. 4) 3.5±0.3	850	2.7	0.8

*work carried on a glycerol/ethanol mixture.

4.7 AQUEOUS PHASE REFORMING (APR)

Glycerol can be converted in aqueous phase to hydrogen, for which both batch reactors and continuous flow can be utilised. When the pressure is the same as the saturation pressure of water (water in vapor phase in bubbles inside the reactor) then the WGS reaction is enhanced. This is discussed by Luo et al.²³⁰ and Menezes et al.²³¹. Aqueous phase reforming can be carried out at lower temperatures than for example autothermal reforming but require medium pressures to maintain water mainly as a liquid. As discussed by Ozgur and Uysal²³² the temperature employed for APR is more suitable for the WGS reaction which results in lower CO levels in the reactor off-gas and higher H₂ yield.

4.7.1 EXPERIMENTAL WORK

Experimental work on APR has been carried out between 160 and 280 °C, 4 and 75 bar, and S:C between 0.4:1 and 168.7:1 (Table 4. 6). Note that most experiments were performed in batch reactors, which dictated that the pressure increased as the temperature increased following constant volume transformations. Glycerol conversion increased with temperature and pressure while the H₂ concentration reduced.^{232,233} The decrease in H₂ concentration was attributed to cracking reactions based on the fact that the concentrations of CO₂ as well as the amount of hydrocarbons such as CH₄ and ethylene in the reactor off gas also increased with increasing temperature.²³²

The H₂ yield increased as the temperature increased in the temperature range 225-240 °C²¹¹ and 180-220 °C.²³⁰ An increased S:C was shown to increase the reactor off gas production, the H₂ concentration and the H₂ selectivity.²³¹⁻²³³ Higher pressure had a negative impact on the APR process. Shabaker et al.²³⁴ reported that increasing the pressure resulted in lower H₂ selectivity (Equation 4. 9) and higher alkane selectivity (Equation 4. 11). This was in agreement with Wawrzetz et al.²³⁵ who reported that the H₂ production dropped while the production of C₂ and C₃ oxygenated products increased as the pressure changed from 25 to 45 bar (225 °C, S:C 6.8). As discussed by Barelli et al.²³⁶ the reforming reaction is favoured by low pressure since the reaction involves an increase in gas molecules. This explains the results reported by Shabaker et al.²³⁴ and Wawrzetz et al.²³⁵ since a reduced formation of H₂ and an increased formation of alkanes and C₂ and C₃ oxygenated products result in a lower amount of gas molecules. When using a continuous flow reactor design, a higher residence time had a positive impact on the the reactor off gas flow rate.²³²

Catalyst metal particle size was found to have a positive impact on H₂ selectivity and glycerol conversion but a negative impact on the turnover frequency (TOF, or number of molecules reacting per active site in unit time) of H₂.^{235,237} The impact of metal particle size on the ability of the catalyst to carry out C-C bond cleavage and dehydration reactions is however unclear. When using a metal such as Cu, which is known to have a low ability for C-C bond

cleavage and a high ability of dehydrogenation, the resulting glycerol conversion is low and the H₂ concentration is high.²³⁸ Large pore volume and pore size was found to increase glycerol conversion and H₂ conversion rate (mole min⁻¹g_{catalyst}⁻¹).²³⁷ Pt/Al₂O₃ catalysts were prepared using different supports which resulted in different average pore sizes (between 3.5 and 33.6 nm) and pore volumes (between 0.43 and 1.00 cm³ g⁻¹). The glycerol conversion and the H₂ conversion rate (mole min⁻¹g_{catalyst}⁻¹) increased as the pore size and volume increased. The results were attributed to reduced transport limitations due to pore diffusion in the catalysts with larger pore sizes and volumes.

Doping the catalysts with additional metals can impact the APR process in many ways. Addition of Sn to a Ni catalyst increased H₂ selectivity and reduced alkane selectivity.²³⁴ The results were attributed to the formation of Ni-Sn alloys which reduced the amount of Ni defect sites. As discussed by Shabaker et al.²³⁴, Ni defect sites may facilitate dissociation of CO leading to CH₄ formation. Also, the ability of Sn to weaken adsorption of carbide fragments as well as to decrease the number of adjacent Ni atoms were discussed as being reasons for the results. King et al.¹⁸² manufactured Pt based catalysts supported on activated carbon with and without the addition of Re. The addition of Re increased the glycerol conversion from 5.3 to 88.7% but simultaneously reduced the H₂ yield (Equation 4. 2) from 56.5 to 24.5%. The addition of Re also increased the amounts of compounds found in the condensate. Without Re addition, only ethylene glycol and propylene glycol were identified in the condensate, but with Re addition, 1-propanol, 2-propanol, ethanol, methanol and a number of acids were found as well. The results were attributed to the acidity of oxides of rhenium (ReOx) which catalyzed dehydration reactions. This in turn increased glycerol conversion but also led to a reaction pathway that ended in the formation of additional compounds in the condensate instead of gas phase compounds such as H₂.

Menezes et al.²³¹ made Pt catalyst with different supports (Al₂O₃, CeO₂, ZrO₂ and MgO). The amount of basic and acid surface sites on the catalysts were determined using temperature controlled desorption of CO₂ and *n*-butyl-amine where the moles of adsorbed/chemisorbed CO₂ and *n*-butyl-amine was used to quantify the amounts of basic and acid sites respectively. The ZrO₂ supported catalyst showed the highest conversion and reaction rates while the MgO supported catalyst resulted in the highest H₂ purity. The differences between the ZrO₂ and the MgO supported catalysts were attributed to a higher abundance of basic sites on the MgO catalyst and a higher abundance of acid sites in the ZrO₂ supported catalyst. As discussed by Menezes et al.²³¹ basic oxides (i.e. electron donors) promote the WGS reaction and suppress the formation of CH₄, which explained the higher H₂ purity of the reactor off gas during reforming with the MgO catalyst. Acid sites (i.e. electron acceptors) promoted dehydrogenation reactions which in the case of glycerol favoured the formation of 2 and 3 carbon species over that of H₂. This explained the higher conversion and reaction rate during reforming using the ZrO₂ catalyst

and the lower H₂ purity reactor off gas which contained more than 3 times the amount of C₁+ species than the case of the MgO catalyst.

With time on stream the catalyst can be either deactivated or activated depending on its properties. Deactivation has for example been linked to carbon formation on the catalyst.²³⁰ Phase changes in the catalyst support with time on stream can have both positive and negative effects. Wen et al.²³⁸ recorded changes in catalytic activity with time on stream in Pt catalysts with active carbon and HUSY zeolite and SAPO-11 zeolite supports. The two catalysts were analysed with XRD before and after APR at 230 °C 32 bar and S:C of 15.3 for 220 min time on stream. The rate of H₂ production ($\mu\text{mole min}^{-1} \text{g}_{\text{catalyst}}^{-1}$) increased over time for the active carbon and HUSY zeolite supported catalysts, but decreased for the SAPO-11 zeolite supported catalyst. XRD analysis of the catalysts after reforming showed that new crystal phases had formed.

The changes in catalytic activity with time on stream were attributed to the new crystal phases which either increased or suppressed the exposure of metal sites. Loss of catalyst activity has been attributed to oxidation of the metal of the catalyst.²³⁸ H₂ temperature programmed oxidation (TPO) was carried out on Ni and Co catalysts supported on Al₂O₃ before and after APR of glycerol. After reforming for 230 min, the activity of the catalysts had reduced significantly. H₂-TPO after reforming displayed H₂ consumption peaks at lower temperature than before reforming, indicating oxidation of the catalysts which explained the reduced activity during reforming. However, oxidation can be avoided by reforming at higher temperatures and pressures. Manfro et al.²³³ carried out APR at 250 °C and 37.5 bar and at 270 °C and 52.7 bar using a Ni catalyst supported on CeO₂ and examined the catalyst before and after reforming using XRD. The catalyst performed better at the higher temperature and pressure. Glycerol conversion increased from 10 to 30% after 12h when the temperature and pressure increased. The XRD analysis of the catalyst after reforming showed the formation of a NiO phase during reforming at the lower temperature and pressure. Formation of NiO could be avoided with subsequent increase in glycerol conversion by increasing the temperature and pressure during reforming.

Table 4. 6 (Continued)

Reference	Temperature	S:C range	Pressure	Catalyst	Best results	Optimum conditions		
						Temperature	S:C	Pressure
231	225	168.7	23	Pt/Al ₂ O ₃	Conversion (Equation 4. 7) 23%	225	168.7	23
					Concentration 63.3%	225	168.7	23
				Pt/CeO ₂	Conversion (Equation 4. 7) 13%	225	168.7	23
					Concentration 64.3%	225	168.7	23
				Pt/ZrO ₂	Conversion (Equation 4. 7) 26%	225	168.7	23
					Concentration 62.7%	225	168.7	23
				Pt/MgO	Conversion (Equation 4. 7) 20%	225	168.7	23
					Concentration 71.9%	225	168.7	23

*showing only the catalyst which gave the best result.

**Showing only results from the PtRe/C catalyst which gave the best result.

4.8 SUPERCRITICAL WATER GASIFICATION (SCWG)

Supercritical water gasification, also referred as supercritical water reforming, is carried out in the same way as APR with the difference that the pressure is increased to the point where the water is at a near critical or a supercritical state. When water moves towards a supercritical state, the ionic product (K_w) of the water increases, i.e. the concentrations of H_3O^+ and OH^- ions are increased (Equation 4. 12).

$$K_w = [H_3O^+] \times [OH^-]$$

Equation 4. 12. Definition of ionic product (K_w). $[H_3O^+]$ and $[OH^-]$ are molar concentrations of H_3O^+ and OH^- respectively.

4.8.1 THERMODYNAMIC EQUILIBRIUM ANALYSIS

Thermodynamic equilibrium analysis of supercritical water gasification/reforming has been carried out between 400 and 1000 °C, 241 and 250 bar and S:C between 1.8 and 32.4 (Table 4. 7).²³⁹⁻²⁴² High temperatures and S:C were beneficial for conversion to hydrogen. van Bennekom et al.²⁴¹ reported an increase in H_2 yield (Equation 4. 4) from 1.0 to 5.0 as the temperature increased from 450 to 650 °C (S:C 32.4, 250 bar) (Figure 4. 8). Simultaneously, the yield of CO_2 increased slightly from 1.5 to 2.0 and the yield of CH_4 reduced from 1.5 to 0.5 over the same temperature range. The CO yield was below 0.2 over the whole temperature range. Yields of CO_2 , CH_4 and CO were calculated by replacing H_2 with CO_2 , CH_4 or CO in Equation 4. 4. The results are in agreement with Chakinala et al.²⁴² who reported an increase in H_2 yield (Equation 4. 4) from 1.5 to 3.1 as temperature rose from 500 to 650 °C (S:C of 15.3:1, 250 bar). Even higher H_2 yields were possible at higher temperatures as shown by Byrd et al.²⁴³ and Voll et al.²³⁹ who studied the temperature range 700-800 °C, at 241 bar and S:C of 32.4:1. The H_2 yield (Equation 4. 4) increased slightly from 6 to 6.5 as the temperature was raised from 700 to 800 °C. The highest H_2 yield was reported by Ortiz et al.²⁴⁰ who investigated temperatures up to 1000 °C and reported a H_2 yield (Equation 4. 3) of 100% at 850-900 °C (S:C 33:1, 235 bar).

Ortiz et al.²⁴⁰ also investigated the effects of temperature on selectivity as well as the effects of S:C and pressure on H_2 concentration. The selectivity to H_2 , CO_2 and CO increased with temperature while the selectivity to CH_4 reduced (selectivity to H_2 and to carbon products defined according to Equations. 4. 9 and 4. 11 respectively). The selectivity to CH_4 reduced to zero at 900 °C while the selectivity to CO was below 10% over the whole temperature range. A maximum selectivity to H_2 of 95% was reached at 850 °C. When the temperature and pressure were kept at 800 °C and 235 bar respectively, the H_2 concentration grew from 30 to 67% as the S:C increased from 1.8:1 to 33:1. No change in H_2 concentration was reported as the pressure increased from 202.7 to 304 bar.

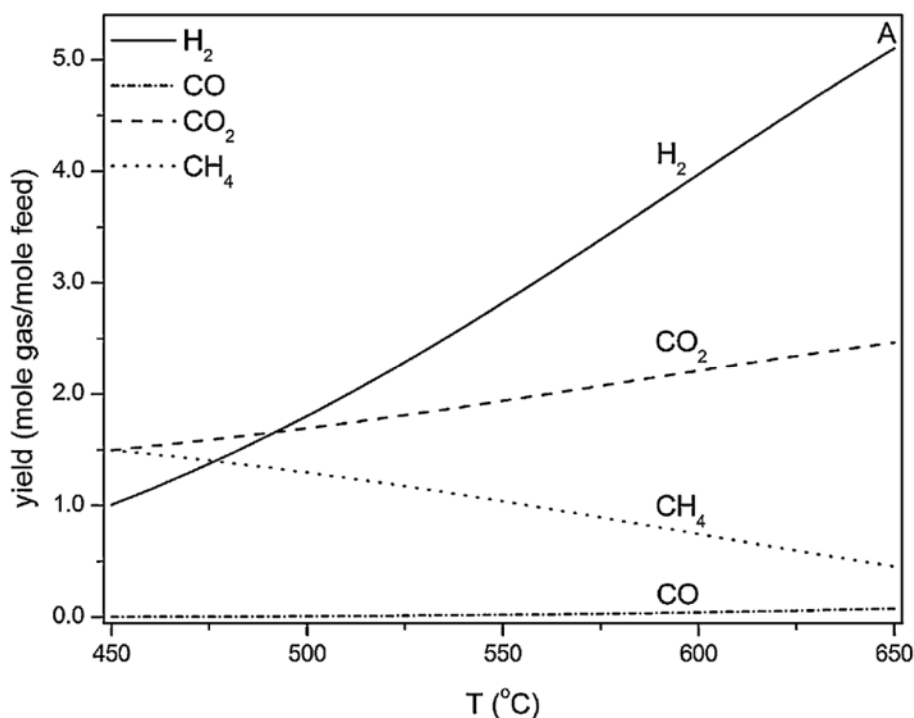


Figure 4. 8. Calculated hydrogen yield at equilibrium of H₂, CO₂, CO and CH₄ for a 5 wt% glycerol-water feed solution at 250 bar. Reprinted with permission from van Bennekom et al. (2011).²⁴¹ Copyright 2011 Elsevier.

4.8.2 EXPERIMENTAL WORK

Supercritical water gasification/reforming has been investigated experimentally between 300 and 800 °C, 85 and 450 bar, and for S:C between 9.3 and 168.7 (Table 4. 7).²⁴²⁻²⁴⁸ Both batch reactors and continuous flow reactors were used.

High temperature and high S:C were beneficial. Xu et al.²⁴⁵ for example showed that the H₂ concentration increased from 45 to 60% and the H₂ yield (Equation 4. 4) increased from 1.5 to 5.1 as the temperature rose from 380 to 500 °C. Chakinala et al.²⁴² found that the H₂ yield (Equation 4. 4) increased from 1.0 to 2.6 from 550 to 650 °C (S:C 15.3:1, 250 bar). Byrd et al.²⁴³ reported that the H₂ yield (Equation 4. 4) increased from 5.1 to 6.5 between 700 and 800 °C (S:C 32.4:1, 241 bar). Byrd et al.²⁴³ also investigated the effect of S:C at 800 °C and 241 bar. As the S:C increased from 2.6:1 to 32.4:1 the H₂ yield (Equation 4. 4) grew from 2.5 to 6.5.

Chakinala et al.²⁴² reported that the CO and CO₂ yield was higher and lower respectively than expected from the thermodynamic equilibrium analysis in the temperature range 550-650 °C. This could be attributed to the WGS reaction not reaching thermodynamic equilibrium during the experiment. However, Chakinala et al.²⁴² also carried out supercritical water reforming in the presence of a K₂CO₃ reagent under the same conditions and found that the H₂ yield increased slightly while significantly reducing the yield of CO and increasing the yield of

CO₂ thus improving the agreement between the experimental results and the thermodynamic equilibrium analysis. Onwudili and Williams²⁴⁸ carried out aqueous reforming at 380 °C and 215 bar with the addition of the reagent NaOH in concentrations between 0.5 and 3.0 mole L⁻¹. As the concentration of NaOH increased the gas production and the H₂ concentration increased. The H₂ concentration reached a maximum of 90% compared to 8.89% without the addition of NaOH. The results were attributed to the formation of NaCO₃ which removed CO₂ and shifted the WGS reaction towards the formation of H₂ through Chatelier's principle. This subsequently increased glycerol decomposition. Xu et al.²⁴⁵ tried adding NaCO₃ in their glycerol/water solution but this had a negative impact.

Similarly differing results have been reported with regard to the effect of catalysts. May et al.²⁴⁷ investigated the gasification of glycerol in supercritical water with and without a Ru/ZrO₂ catalyst with 350 bar, S:C of 32.4:1 at 510 and 550 °C. Without catalyst, the highest H₂ yield (Equation 4. 3) was 30 at 550 °C.

With catalyst, the highest H₂ selectivity was 55 at 510 °C. The results showed that the catalyst could increase the H₂ selectivity and a lower temperature could be used to reach maximum H₂ yield. However Xu et al.²⁴⁶ found no effect on the reactor on the H₂ yield when adding a catalyst. They carried out gasification at 600 °C, 345 bar and S:C 9.3:1 with and without an activated carbon catalyst. The H₂ yield (Equation 4. 4) was 3.15-3.51 in both conditions.

The effect of pressure was shown by Buhler et al.²⁴⁴ who kept the temperature at 394 °C and changed the pressure from 250 to 450 bar while quantifying the resulting liquid products using gas chromatography. The yield (as defined by Equation 4. 13) of acetaldehyde and formaldehyde increased with pressure while the yield of methanol and allyl alcohol reduced (Figure 4. 9). This was attributed to the increased ionic product of the water caused by the increased pressure. A higher ionic product results in a higher level of ionic intermediates which promote ionic reactions. Acetaldehyde and formaldehyde are formed from ionic reactions while methanol and allyl alcohol are formed from free radical reactions which are inhibited at lower pressures as a result of the cage effect.

$$Yield\ of\ \alpha = \frac{moles\ of\ \alpha\ produced}{\sum\ moles\ of\ all\ compounds\ produced}$$

Equation 4. 13. Definition of yield used by Buhler et al.²⁴⁴

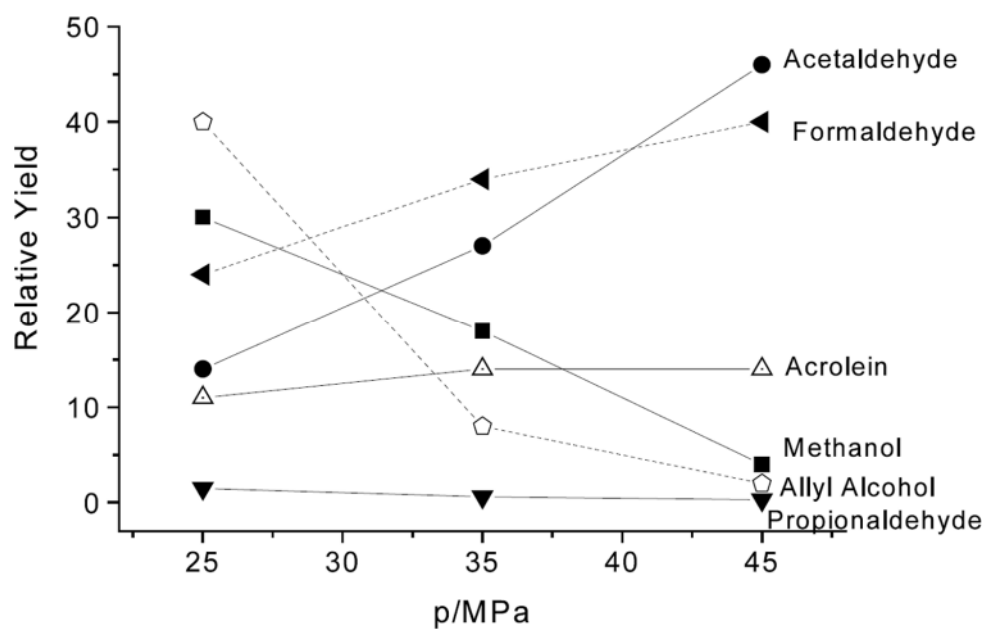


Figure 4. 9. Relative yields as a function of pressure at 667 K (394 °C). Reprinted with permission from Buhler et al. (2002).²⁴⁴ Copyright 2002 Elsevier.

Table 4. 7. Summary of thermodynamic equilibrium analysis and experimental work on supercritical water gasification of glycerol. Temperatures in °C, pressures in bar

Reference	Temperature	S:C	Pressures	Catalyst	Best result	Optimum conditions		
						Temperature	S:C	Pressure
Thermodynamic equilibrium analysis								
239	702-802	2.6-41	241	n/a	Yield (Equation 4. 4) 6.5	802	41	241
241	450-650	6.8-32.4	250	n/a	Yield (Equation 4. 4) 5.0	650	32.4	250
240	400-1000	1.8-33	202.7-304	n/a	Concentration 70%	800	33	235
					Yield (Equation 4. 3) 100%	850	33	235
					Selectivity(Equation 4. 9) 95%	850	33	235
242	550-650	15.3	250	n/a	Yield (Equation 4. 4) 3.1	650	15.3	250
Experimental								
245	380-500	168.7	250	None NaCO ₃	Concentration 60%	500	168.7	250
					Yield (Equation 4. 4) 5.1	500	168.7	250
					Concentration 65%	410	168.7	250
					Yield (Equation 4. 4) 3	410	168.7	250
242	550-650	15.3	250	K ₂ CO ₃	Concentration 55%	600	15.3	250
					Yield (Equation 4. 4) 2.69	600	15.3	250
243	700-800	2.6-32.4	241	Ru/Al ₂ O ₃	Concentration 70%	800	32.4	241
					Yield (Equation 4. 4) 6.5	800	32.4	241

Table 4. 7 (Continued)

Reference	Temperature	S:C	Pressures	Catalyst	Best result	Optimum conditions		
						Temperature	S:C	Pressure
Experimental								
247	510-550	32.4	350	Ru/ZrO ₂	Conversion (Equation 4. 5) 100% Concentration 45% Yield (Equation 4. 3) 55%	550 510 510	32.4 32.4 32.4	350 350 350
246	600	9.3	345	None AC	Yield (Equation 4. 3) 3.51 Yield (Equation 4. 3) 3.15	600 600	9.3 9.3	345 345
248	380-450	2.3	81-310	NaOH	Concentration 90%	380	2.3	215

4.9 THERMAL DECOMPOSITION

Thermal decomposition of glycerol (also called gasification) involves heating glycerol with a gasification agent in order to produce a syngas (a mixture of H_2 and CO as the main components). The aim of gasification is commonly to create a syngas that can be used for the manufacture of other synthetic fuels such as methanol or dimethyl ether (DME). The manufacture of these products is made possible by the different $H_2:CO$ ratios required for different products. Therefore, the $H_2:CO$ ratio is an important factor in thermal decomposition and will be considered here instead of the amount of H_2 in the reactor off gas or the H_2 yield. Air and oxygen can be used as gasification agents, as the input of O_2 achieves oxidation exothermically and can help sustain the endothermic reactions of thermal decomposition. The moisture content of crude glycerol has also been used as a gasification agent. During thermal decomposition both cracking and combustion reactions are possible as well as decomposition and partial oxidation reactions.

Glycerol thermal decomposition has been found to increase with temperature and with growing amounts of gasification agent.²⁴⁹⁻²⁵¹ Yoon et al.²⁴⁹ for example carried out thermal decomposition of crude glycerol (60% glycerol) at 1 bar using air as well as oxygen as gasification agents and changed the excess air ratio from 0.17:1 to 0.7:1. The excess air ratio was defined as “the ratio of the amount of oxygen supplied to the stoichiometric amount of oxygen required for complete combustion of fuel”. Note that the temperature increased as the excess air ratio increased and consequently the temperature increased from 950 to 1050 °C in the case of air and from 1200 to 1500 °C in the case of oxygen, as the excess air ratio increased from 0.17:1 to 0.32:1 and from 0.4:1 to 0.7:1, respectively. Using air the reactor off gas contained around 24% H_2 , and 19% CO over the whole excess air ratio range. The conversion (Equation 4. 7) increased from 57 to 80%. The results showed that a higher conversion of the crude glycerol was achieved when more air was added, but since the air diluted the reactor off gas, the concentrations of H_2 and CO did not change. Using oxygen the concentrations of H_2 and CO were both around 40% while the amount of CO_2 was around 10%. As the excess air ratio increased above 0.6:1 (and the temperature reached above 1400 °C) the H_2 and O_2 concentrations reduced and increased, respectively. The results were attributed to a switch from thermal decomposition to combustion which results in the formation of CO_2 and H_2O from glycerol. This explained the reduction in H_2 and the increase in CO_2 .

Atong et al.^{250,251} carried out thermal decomposition of crude glycerol (moisture content 13.6%) at 1 bar using the moisture in the crude as a gasification agent at temperatures between 500 and 800 °C using a $LaNiO_3$ perovskite catalyst²⁵⁰ and a Ni catalyst supported on olivine.²⁵¹ As temperature increased the gas yield (Equation 4. 14) improved and reached a maximum of 78 (perovskite catalyss and 90% (Ni/Olivine catalyts) at 700 °C. However in both cases the

H₂:CO reduced as the temperature increased and was 1 or below at temperatures above 700 °C. There was a trade off between high H₂:CO ratio and gas yield (i.e. amount of gas reactor off gas produced).

$$\text{Gas yield} = \frac{\text{volume of gas (Nm}^3\text{)}}{\text{mass of crude glycerol supplied (kg)}}$$

Equation 4. 14. Definition of gas yield used by Atong et al.^{250,251}

The H₂:CO ratio increased with increasing temperature between 500 and 600 °C but reduced with a further increase in temperature (Table 4. 8). This meant that at higher temperatures there is a trade off between gasification and H₂:CO ratio.

Fernandez et al.²⁰⁷, Fernandez and Menendez²⁵² and Fernandez et al.²⁰² carried out thermal decomposition of glycerol using activated carbon (AC) as a catalyst using both electrical and microwave heating. Fernandez et al.²⁰⁷ investigated the effect of AC by comparing the results from experiments carried out with and without AC at 1 bar and 800 °C. Without AC the H₂ concentration was 22.6% but by adding AC the concentration increased to 28.9-30.1%. The CO concentration reduced from 51.7% without AC to 43.5-48.7% in the presence of AC causing the H₂:CO ratio to increase from 0.4:1 to 0.6:1-0.7:1. The results were in agreement with Fernandez et al.²⁰² who reported H₂ and CO concentrations of 28.9 and 48.8% respectively with a H₂:CO ratio of 0.6:1 under the same conditions in the presence of AC. The results were attributed to the ability of the AC to catalyse the formation of H₂ and C from C_xH_y hydrocarbon such as CH₄ (e.g. the reverse of Reaction 4. 2).

Fernandez et al.²⁰⁷ also carried out gasification at 1 bar and 800 °C using AC with microwave heating. The results were compared to gasification carried out under the same conditions using electrical heating. The H₂ concentration increased from 28.9-30.1% to 33.2 - 34.6% with microwave heating compared to electrical heating. The results were in agreement with Fernandez and Menendez²⁵² who performed gasification using both electrical and microwave heating at 1 bar and temperatures between 600 and 800 °C using AC. As the temperature increased from 600 to 800 °C, the H₂:CO ratio rose from 0.2:1 to 0.6:1 with electrical heating and from 0.4:1 to 0.8:1 with microwave heating. The results were attributed to the difference in the temperature gradient inside the reactor between the microwave heated and the electrically heated setups. Microwave heating causes the AC to transfer heat from the centre of the reactor outwards while electrical heating transfers heat from outside the reactor inwards toward the AC.

Fernandez and Menendez²⁵² measured the power needed to keep the activated carbon (AC) at temperatures of 700-900 °C using electrical and microwave heating. They found that

less power was needed when microwave heating was used. For example, to keep the temperature at 700 °C, the power needed with electrical heating was 10 W g_{AC}⁻¹ but 5 W g_{AC}⁻¹ with microwave heating. This is in agreement with Hawangchu et al.²⁵³ who reported that 5.5 W g_{SiC}⁻¹ was needed to heat a bed of SiC to 700 °C in a microwave heated quartz reactor.

Table 4. 8. Summary of experimental work on thermal decomposition. Temperatures in °C

Reference	Temperature	Catalyst	Gasification agent	Highest H ₂ :CO	Temperature for highest H ₂ :CO
249	950-1500	none	Air oxygen	1.25 1	950 1200
250	500-800	LaNiO ₃ perovskite	moisture	4.5	500
251	500-800	Ni/Olivine	moisture	8	600
207	800	AC	moisture	0.7	800
202	800	AC	moisture	0.6	800
252	600-800	AC	moisture	0.8	800

4.10 CONCLUSIONS

Steam reforming (SR) is a well understood method and is the most common route to H₂ production today using natural gas and naphtha as the main feedstock. Steam reforming of glycerol is therefore likely to be used initially for H₂ production from glycerol on a large scale. However, steam reforming is limited with regard to the H₂ concentration it can achieve, which is 70% under thermodynamic equilibrium (Table 4. 1). This means that downstream processing systems such as WGS reactors to enhance conversion, and pressure swing adsorption to achieve a product of high purity, are needed to achieve a H₂ gas for use in a fuel cell electric vehicle (FCEV).

Sorption enhanced steam reforming (SESR) can produce high purity H₂ gas which means that the number of process steps are reduced compared to conventional steam reforming, but the process can only be carried out for a limited amount of time before the CO₂ sorbent is saturated and regenerating the sorbent involves an energy penalty.^{23,218,220} One possible solution is to couple sorption enhanced steam reforming with chemical looping, which uses an air flow to oxidise an oxygen transfer material, and uses the heat from the oxidation to regenerate the sorbent as well as providing the heat for the steam reforming reaction.²⁵⁴ Advantages of coupling with chemical looping include avoiding reliance on external burners as the heat generators for either the reformer or the sorbent calciner, allowing the use of cheaper and longer lived reactor materials, and thus become economical at smaller scales, generating H₂ closer to the point of use. The loss in sorbent capture capacity due to sintering presents another energy penalty. CO₂ sorbent materials with low susceptibility towards sintering would reduce the need to continuously add fresh sorbent to the reformer and work has been carried out in this field.⁴⁷ Means of reversing the effects of sintering have also been proposed.⁴⁵

Autothermal reforming (ATR) reduces the energy need of the H₂ production process by allowing for the thermoneutral condition.²²⁷ However, this reduced penalty is offset by both reduced H₂ yield and concentration during ATR. With ATR, in addition to requiring expensive pure oxygen as reactant, downstream purification systems would still be needed.²²⁵

Aqueous phase reforming (APR) allows H₂ to be produced at lower temperatures than SR and hence also presents an alternative with a reduced energy need. However the process requires large amounts of clean water which is evident from the high S:C used (Table 4. 6). The process also requires a higher pressure than SR, SESR and ATR which results in an energy penalty and reduced H₂ production. Reforming in aqueous phase also favour the formation of water soluble 2 and 3 carbon species, which reduces selectivity to H₂ and presents optimisation and purification challenges.

Supercritical water gasification (SCWG) of glycerol operates at high temperatures and pressures and involves a highly reactive environment. The high pressures involved present

challenges regarding safety. Note that the best result with regard to H₂ purity was achieved when a batch process was used (Table 4. 7).²⁴⁸ The reactive environment created during SCWG causes corrosion on reactors and other equipment which could be addressed through improvements in reactor materials development unlikely to be low-cost. SCWG is the most novel of the conversion methods for H₂ production reviewed in this chapter and at presents it is far from commercialisation.

Thermal decomposition is not aimed at producing a high purity H₂ gas for use in FCEV but rather at producing a syngas with a favourable H₂:CO ratio. It presents an alternative use for glycerol as a raw material for other chemicals such as methanol, DME, and non-oxygenated biofuels through further processing. The work on thermal decomposition using microwave heating suggests that the energy penalty for heating can be reduced with alternative heating methods.^{202,207,252} Little explored areas of research include the effects of non glycerol compounds from the crude glycerol waste from biodiesel production plants on the processes reviewed and the degree and type of pretreatment of crude glycerol required for an efficient and economical process of conversion to hydrogen.

CHAPTER 5: THERMODYNAMICS OF SR AND SESR

“Knowing the answer means nothing, testing your knowledge means everything”

Lawrence Krauss

5.1 MOTIVATION FOR WORK

Steam reforming (SR) can be used for thermochemical conversion of gaseous or liquid fuels to hydrogen.^{178,255,256} It involves mixing the fuel with steam in a reformer together with a catalyst which results in the formation of synthesis gas ('syngas') containing mainly H₂ and carbon oxides (CO and CO₂) but also smaller amounts of organics and hydrocarbon gases, most notably CH₄. If the H₂ gas is to be used in a proton exchange fuel cell (PEMFC) then it needs to be of as high purity as possible. The CO content of the H₂ gas is of particular importance as CO poisons the fuel cell catalyst by blocking adsorption sites. This occurs at all concentrations and so tolerance to CO in the H₂ gas can only be measured in acceptable degradation rates for performance of the fuel cell.²⁵⁷ Therefore it is important to maximise H₂ yield as well as the fuel and water conversion to produce a high purity syngas. Addition of a CO₂ sorbent changes the thermodynamics of the system and allows for higher H₂ yields.^{20,200} This is referred to as sorption enhanced steam reforming (SESR).

Steam reforming of natural gas is currently the most common route for hydrogen production in industry and recently the possibility of using other feedstocks has been investigated.^{178,255,256} As outlined in Chapter 4 (Section 4.1) the use of a renewable feedstock for H₂ production using SR or SESR is a potential long term solution to achieve near zero CO₂ emissions for transport. Therefore the viability of SR and SESR of potential feedstocks for hydrogen production needs to be investigated. In order to produce a high purity H₂ gas for use in transport, an understanding of the thermodynamics of the process is needed. To achieve maximum benefit from the addition of a CO₂ sorbent, the effect of the sorbent on the thermodynamics also needs to be understood. This chapter will compare the thermodynamics of the steam reforming systems of three feedstocks, methane (CH₄), ethanol (C₂H₆O) and glycerol (C₃H₈O₃) as well as the effect of sorption enhancement by in situ CO₂ capture by Ca-based sorbents on these systems. Methane was chosen for study due to its ubiquitous use in industrial steam reforming and ethanol was chosen as it was the dominant biofuel for transport with regard to annual global production as of 2010.¹⁷⁵ Glycerol was studied due to its potential as feedstock for hydrogen production as reviewed in Chapter 4. Many sorbent materials can be used for sorption enhanced steam reforming. The most commonly used materials from the literature are compared in Chapter 3 with regards to CO₂ capture capacity, reaction kinetics and cost. It was concluded that Ca-based materials, with CaO as the chemically active part of the material for the carbonation reaction, were most suitable due to their high capture capacity, fast reaction kinetics and low cost. Therefore, CaO is studied here as the CO₂ sorbent.

First, the physical and chemical properties of the three feedstocks are compared and discussed with regards to steam reforming. Second, the thermodynamics of the feedstock/H₂O/CaO system are compared and discussed.

5.2 METHODOLOGY AND DEFINITIONS

Thermodynamic analysis based on minimization of Gibbs free energy was carried out using the code EQUIL from the CHEMKIN package.⁶³ Input mole fractions of water and feedstock corresponding to different ratios of steam and carbon (S:C ratios) were entered and the mole fractions resulting from minimization of Gibbs free energy were used to calculate H₂ yield, selectivity to C and H, water conversion as well as the dry molar fraction at thermodynamic equilibrium for temperatures between 27 and 1027 °C. The modeling relies on the species listed in Table 5. 1. The species were included as they are known to form during thermochemical conversion of the investigated feedstock. Note that the Ca containing species are only relevant during analysis of sorption enhanced steam reforming where CaO is added as an input species. The Ca containing species are solid phase while the other species are gas phase.

Table 5. 1. Species included in the thermodynamic analysis.

C	CO	CO ₂	C ₂ H ₆
C ₂ H ₂	C ₂ H ₄	C ₂ H ₅	C ₂ H ₆ O
C ₃ H ₆	C ₃ H ₈	CH ₄	H ₂
CaO	CaCO ₃	Ca(OH) ₂	O ₂
H ₂ O			

The equilibrium species considered for the methane/H₂O system were H₂, H₂O, CO, CO₂, CaCO₃ and Ca(OH)₂. For the analysis of ethanol and glycerol, CH₄ was also considered as an equilibrium product. This could not be done in the case of methane because minimization of Gibbs free energy returns complete feedstock conversion at all temperatures. Note that not all the possible carbon and hydrogen containing species were included (such as C₂H₆ or C₃H₈ for example). This was due to their extremely low mole fractions under thermodynamic equilibrium. The output species considered displays by far the highest mole fractions by virtue of their low energy of formation. For more information see Chapter 4, Section 4.2. EQUIL uses 1 mole as mixture molar amount, the equilibrium molar amount is called N_{eq} in the following equations. To obtain the equilibrium molar amount of an individual species, it is then necessary to multiply its equilibrium mole fraction by N_{eq}, whereas the input molar amount of a species is the product of its input mole fraction and 1.

The H₂ yield is defined according to Equation 5. 1 and is calculated from the feedstock molar input, the H₂ equilibrium molar amount and the molar masses of the feedstock (methane, ethanol or glycerol) and the H₂ product. H₂ yield refers to the units of H₂ produced for each unit of feedstock and can therefore be defined on either a molar or weight basis. H₂ yield is defined here on a weight basis to enable direct comparison between the different feedstocks which are investigated. Other definitions of H₂ yield have been applied in the literature and those are

presented and discussed in Chapter 4, Section 4.2. Selectivity to carbon and hydrogen containing species are defined according to Equation 5. 2 and Equation 5. 3. Note that selectivity to hydrogen containing species does not include water (i.e. it is calculated on a dry basis). Using minimisation of Gibbs free energy feedstock conversion is complete at all temperatures and is subsequently not included in the results but water conversion is included and is defined according to Equation 5. 4. Dry molar composition corresponds to the reformer off-gas under thermodynamic equilibrium. It is defined according to Equation 5. 5 and is calculated from the mole fractions of H₂, CO or CO₂ in the case of methane steam reforming and to the composition of H₂, CO, CO₂ of CH₄ minus CaCO₃, Ca(OH)₂ and H₂O in the case of ethanol and glycerol. Hence, the mole fractions of CaCO₃ and Ca(OH)₂ are disregarded as they are solids and H₂O is disregarded as steam is removed from a reformer off-gas during H₂ production. The dry molar composition is given in percentage (%).

$$H_2 \text{ yield (wt\%)} = \left(\frac{\text{mass of } H_2}{\text{mass of fuel}} \right) \times 100 = \left(\frac{W_{H_2} \times y_{H_2,eq} \times N_{eq}}{W_{fuel} \times y_{fuel,in} \times 1} \right) \times 100$$

Equation 5. 1. Definition of H₂ yield used in this chapter. y = the relevant mole fractions, W = relevant molar masses.

$$\begin{aligned} & \text{Selectivity to C – containing species } \alpha \text{ (\%)} \\ & = \left(\frac{y_{\alpha,eq} \times N_{eq}}{N_{eq} \times \sum y_{CO,eq}, y_{CO_2,eq}, y_{CH_4,eq} \text{ and } y_{CaCO_3,eq}} \right) \times 100 \end{aligned}$$

Equation 5. 2. Definition of selectivity to carbon containing species used in this chapter where α is CO, CO₂, CH₄ or CaCO₃.

$$\begin{aligned} & \text{Selectivity to H – containing species } \alpha \text{ (\%)} \\ & = \left(\frac{y_{\alpha,eq} \times N_{eq}}{N_{eq} \times \sum y_{H_2,eq}, y_{CH_4,eq} \text{ and } y_{Ca(OH)_2,eq}} \right) \times 100 \end{aligned}$$

Equation 5. 3. Definition of selectivity to hydrogen containing species used in this chapter where α is H₂, CH₄ or Ca(OH)₂.

$$\text{Water conversion (\%)} = \left(\frac{y_{H_2O,in} \times 1 - y_{H_2O,eq} \times N_{eq}}{y_{H_2O,in} \times 1} \right) \times 100$$

Equation 5. 4. Definition of water conversion.

$$\text{Dry molar composition (\%)} = \left(\frac{y_{\alpha,eq}}{\sum (1 - y_{H_2O,eq} - \sum y_{solids,eq})} \right) \times 100$$

Equation 5. 5. Definition of dry molar composition.

When α is H_2 , CO , CO_2 or CH_4 , the dry molar composition at equilibrium can be directly compared to the compositions measured by the gas analyzers with time on stream during the experiments of SR and SESR of the different feedstocks investigated, and thus provide a measure of the different SR reactions' activity by their closeness to equilibrium conditions.

5.3 AIMS AND OBJECTIVES

The aims of this chapter are:

- To understand how the physical and chemical properties of methane, ethanol and glycerol impact on the steam reforming reaction.
- To understand the thermodynamics of the steam reforming systems of methane, ethanol and glycerol and the differences between them.
- To understand the effect of a CaO sorbent on the thermodynamics of the steam reforming of methane, ethanol and glycerol.
- Comment on the viability of SESR of the selected feedstocks as a method for high purity H_2 production.

The objectives are:

- To carry out thermodynamic analysis of steam reforming of methane, ethanol and glycerol at a range of temperatures using input mole fractions of feedstock and water which correspond to a range of S:C ratios both with and without CaO .
- To compare the different feedstocks with regards to H_2 yield, selectivity and water conversion.
- To compare steam reforming with sorption enhanced steam reforming.

5.4 CHEMICAL PROPERTIES

Ethanol and glycerol carry more H molecules per mole than methane but also more C and while methane comprises just C and H atoms, ethanol and glycerol also contain O (Figure 5. 1). Methane features C-H bonds only while ethanol and glycerol are constructed from C-H, C-C, C-O and O-H bonds (Table 5. 2).

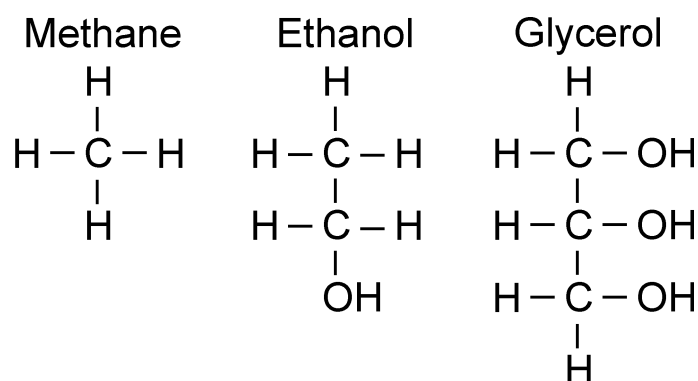


Figure 5. 1. Molecular structure of methane, ethanol and glycerol.

Table 5. 2. Selected chemical properties of methane, ethanol and glycerol.

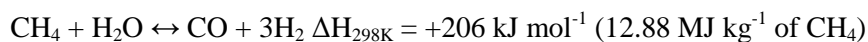
Name	Methane	Ethanol	Glycerol
Composition	CH ₄	C ₂ H ₆ O	C ₃ H ₈ O ₃
Molecular weight (g mol ⁻¹)	16	46	92
ΔH ₂₉₈ Of formation (kJ mol ⁻¹)	-74.5	-235	-582.8
H:C ratio	4:1	3:1	2 ² / ₃ :1
H:O ratio	n/a	6:1	2 ² / ₃ :1
C:O ratio	n/a	2:1	1:1
C-C bonds	n/a	1	2
C-H bonds	4	5	1
C-O bonds	n/a	1	3
O-H bonds	n/a	1	3

At room temperature and atmospheric pressure, methane is a gas while both ethanol and glycerol are liquids. This has practical impacts on the steam reforming process. In the case of methane steam reforming, water has to be evaporated separately and then mixed with the feedstock upstream of the reformer, while in the case of ethanol and glycerol, liquid water can be mixed with the feedstock. Water and feedstock can then be vapourised together either upstream of the reformer or inside the reformer itself. Crude glycerol is a waste stream from biodiesel production and may have some water added to it to decrease its viscosity and ease its handling when pumped.²⁵⁸ Similarly, ethanol is typically sold with some water content and pure ethanol is very expensive. Both crude glycerol and ethanol would require topping up with water to achieve the desired steam to carbon ratio for the steam reforming process.

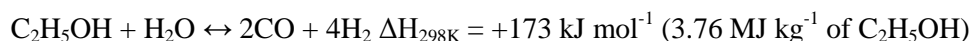
5.5 STEAM REFORMING (SR)

5.5.1 REACTIONS INVOLVED IN SR

In the presence of steam, methane and ethanol undergo their respective steam reforming reactions resulting in the formation of H₂ and CO (Reaction 5. 1 and Reaction 5. 2):



Reaction 5. 1. Methane steam reforming (MSR).



Reaction 5. 2. Ethanol steam reforming.

Note that methane requires oxygen from the water to produce one mole of CO from one mole of CH₄ while 2 moles of CO are produced from one mole of ethanol alone (Reaction 4. 1). Glycerol has the ability to produce CO without steam addition because the glycerol molecule has a C:O of 1:1. This reaction is referred to as glycerol decomposition (Reaction 4. 1).

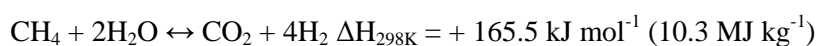
Steam reforming reactions typically require temperatures in excess of 500 °C and at these temperatures, the equilibrium of (Reaction 5. 1) and its reverse; CO methanation (Reaction 4. 2) needs to be considered. Since Gibbs free energy minimisation results in complete conversion of the feedstock, CH₄ itself is not regarded as a product during thermodynamic analysis of methane while during analysis of ethanol and glycerol, it is, via CO methanation (Reaction 4. 2)

The water gas shift (WGS) and its reverse (RWGS) are also predominant features of steam reforming (Reaction 1. 2). WGS converts the CO formed by the steam reforming of methane and ethanol or from the decomposition of glycerol into CO₂ and more H₂. The methane steam reforming (MSR, Reaction 5. 1), ethanol steam reforming (Reaction 5. 2) and the decomposition of glycerol (Reaction 4. 1) are endothermic reactions. Their equilibria will shift towards the right with increased temperature. CO methanation (Reaction 4. 2) and WGS (Reaction 1. 2) are exothermic and will shift to the left with increased temperature. Hence, there exists a temperature above which H₂ production through the WGS reaction stops, and hydrogen consumption takes place via reverse WGS. When the aim is to maximise H₂ yield then steam reforming, decomposition and WGS are preferred reactions while CO methanation and reverse WGS are undesirable. During steam reforming of the investigated feedstock, H₂ yield is optimised at temperatures between 600 and 700 °C.^{18,196,199,259} A temperature range of 27-1027 °C was used for the analysis carried out here to ensure investigation over a wide range of temperatures incorporation the range of optimum H₂ yield.

As discussed by Barelli et al.²³⁶ methane steam reforming (MSR, Reaction 5. 1) is favoured by low pressure since the reaction involves an increase in gas molecules. This applies to ethanol and glycerol steam reforming also (Reaction 5. 2, Reaction 4. 3). From this follows that as the pressure is increased, steam reforming and glycerol decomposition are hindered and CO methanation (Reaction 4. 2) is favoured. WGS (Reaction 1. 2) however is not affected by pressure since it does not change the amount of gas molecules. Due to the more favourable equilibria at low pressure, a pressure of 1 bar is used for the analysis carried out here.

Apart from temperature and pressure, the ratio of feedstock to water also impacts the thermodynamics of steam reforming. This ratio is often normalized to the amount of carbon in the feedstock and defined as the molar steam to carbon ratio (S:C). This definition is also applied here due to its common use in industrial steam reforming operations and because the feedstocks under investigation contain varying amounts of carbon (Figure 5. 1) thus enabling a straightforward comparison. As the S:C ratio is increased methane and ethanol steam reforming and WGS shift towards the right according to Le Chatelier's principle. This in turn shift glycerol decomposition towards the left as CO is removed from the gas phase via WGS. Hence, for a given temperature the H₂ yield is increased as the S:C ratio is increased and consequently there exist no S:C ratio at which H₂ yield is maximised. However, the H₂ yield increases asymptotically with S:C ratio and at ratios around 3-5 the increase becomes small as shown in Figure 4. 3 using glycerol as the feedstock. Also, a high S:C incurs an energy penalty in practice due to the heat needed to raise steam and so a trade-off has to be made between H₂ yield and energy efficiency. Therefore a S:C ratio of 4:1 is used for the analysis carried out here.

When the WGS reaction is coupled with either methanol or ethanol steam reforming or with glycerol decomposition, a complete SR reaction for each of the feedstocks can be compiled (Reaction 4. 3, Reaction 5. 3, Reaction 5. 4), which achieve the maximum H₂ yield from the conversion of the feedstock with steam. Note that the maximum H₂ yield in the case of complete glycerol steam reforming is 15.2 wt% of C₃H₈O₃ feed.



Reaction 5. 3. Complete methane steam reforming (max H₂ yield= 50 wt% of CH₄ feed).



Reaction 5. 4. Complete ethanol steam reforming (max H₂ yield=26.1 wt% of C₂H₆O feed).

The reactions involved in SR as well as the effect of temperature on them are well known and documented hence, all results in Section 5.5 were in agreement with the literature as expected. The work presented in Section 5.5 on SR was carried out solely to enable direct comparison with the work carried out on SESR. A comparison with the literature was therefore not included in the section.

5.5.2 THERMODYNAMIC ANALYSIS OF SR

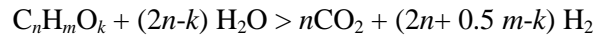
Thermodynamic analysis was carried out with input mole fractions of feedstock and water corresponding to a S:C ratio of 4 (Table 5. 3). The H₂ yield, selectivity to C- and H-containing products, water conversion and dry mole composition for temperatures between 27 and 1007 °C were then plotted. The results are presented and discussed.

Table 5. 3. The input mole fractions used for thermodynamic analysis of steam reforming (SR) of methane, ethanol and glycerol.

Input mole fraction	methane	ethanol	Glycerol
Feedstock	0.2000	0.8571	0.0769
water	0.8000	0.1429	0.9231

5.5.3 H₂ YIELD

Per unit mass of feedstock, CH₄ is expected to produce the highest H₂ yield, followed by ethanol and glycerol (Figure 5. 2). This was due to the differences in molecular weight of the compounds (Table 5. 2) as well as their oxygen content, as illustrated below by the overall reaction of steam reforming for a feedstock of elemental formula C_nH_mO_k:



Reaction 5. 5. Overall steam reforming reaction for a feedstock of elemental formula C_nH_mO_k.

Since the H₂ yield (wt%) is given by the equation:

$$100 \times 2.02 \times (2n+0.5m-k)/(12.01n+m+16k)$$

The values for *n*, *m* and *k* for methane, ethanol and glycerol are given in Table 5. 4.

Table 5. 4. Values of *n*, *m* and *k* (elemental formula C_nH_mO_k) for methane, ethanol and glycerol.

C _n H _m O _k	Methane	Ethanol	glycerol
<i>n</i>	1	2	3
<i>m</i>	4	6	8
<i>k</i>	0	1	3

It is clear that each mole of O in the feedstock becomes a penalty in H₂ yield, as well as adding to the overall molar mass of the feedstock resulting in a substantial decrease. The H₂ yield increased with temperature for all feedstocks reaching a maximum between 600 and 700 °C which was attributed to the shift in the steam reforming reactions and the decomposition reaction with increased temperature.

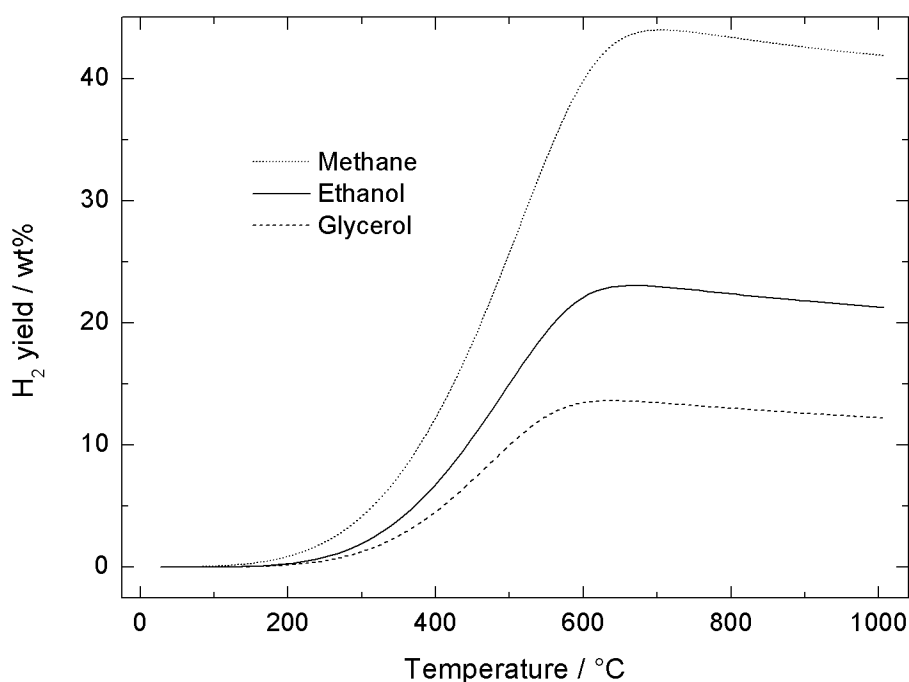


Figure 5. 2. H₂ yield during SR of methane, ethanol and glycerol with a S:C ratio of 4 at temperatures between 27 and 1007 °C.

5.5.4 WATER CONVERSION

Water conversion is promoted by the steam reforming reactions and the WGS reaction, and hindered by the CO methanation reaction (which produces water). Hence, water conversion is increased with increased temperature (because the steam reforming reactions are shifted to the right and the methanation reaction is shifted to the left) until the CH₄ fraction is zero (Figure 5. 3). Water conversion is then reduced with increased temperature as the WGS reaction is shifted towards the left (RWGS). In the case of glycerol the water conversion is negative for temperatures below 300 °C. This is because glycerol can be decomposed without water and the resulting CO and H₂ is converted to water by the methanation reaction resulting in a net increase in the water fraction at equilibrium compared to the input water fraction. Above 300 °C the water conversion is highest for methane, followed by ethanol and then glycerol which is related to the oxygen content of the feedstock. Methane does not contain any oxygen while the C:O of ethanol and glycerol are 2:1 and 1:1 respectively (Table 5. 2). In the methane steam reforming reaction, one mole of water is needed to produce one mole of CO, while in the ethanol steam reforming reaction two moles of CO are produced from one mole of water. The glycerol decomposition reaction produces three moles of CO without any water at all. Subsequently, 2 moles of water is needed for each mole of carbon to balance the complete steam reforming of methane while 1.5 and 1 mole of water is needed to balance the complete steam reforming reaction of ethanol and glycerol respectively. Note that the S:C is 4:1 for all feedstocks.

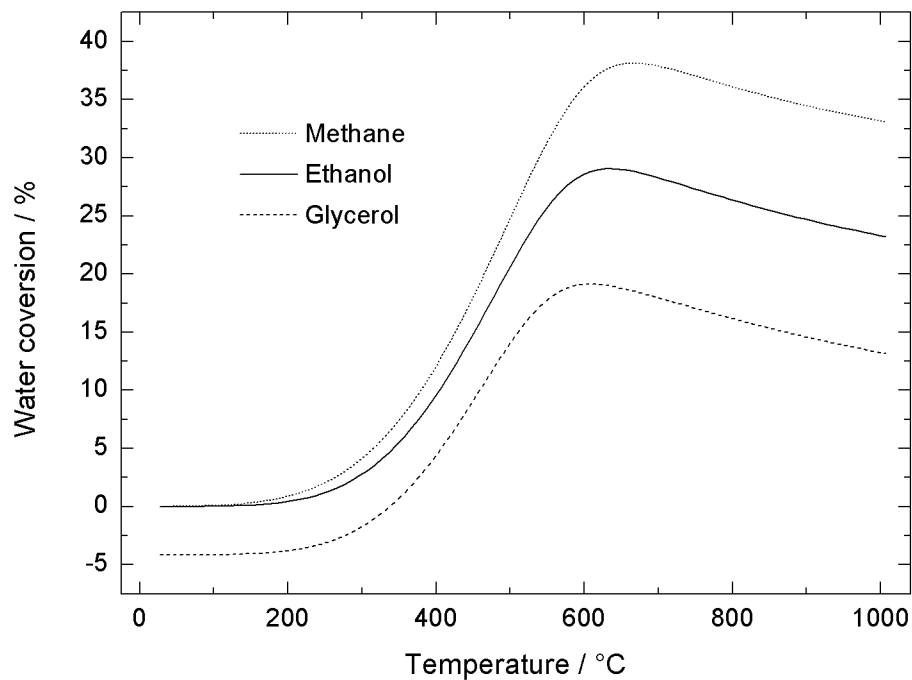


Figure 5. 3. Water conversion during SR of methanol, ethanol and glycerol with a S:C ratio of 4 at temperatures between 27 and 1007 °C.

5.5.5 SELECTIVITY TO CARBON CONTAINING PRODUCTS

5.5.5.1 METHANE

For thermodynamic equilibrium analysis of methane steam reforming and in the absence of coking, CO_2 and CO are the only significant carbon containing products (Figure 5. 4). At temperatures below 400 °C the selectivity to CO_2 was 100%. With increased temperature the selectivity to CO_2 was reduced while the selectivity to CO was simultaneously increased. The results showed the effect of a shift in the WGS reaction towards the right with increased temperature due to its endothermicity. The selectivity to CO and CO_2 switch over at around 700 °C making CO the main carbon product as opposed to CO_2 . Note how this corresponds to a reduction in H_2 yield (Figure 5. 2).

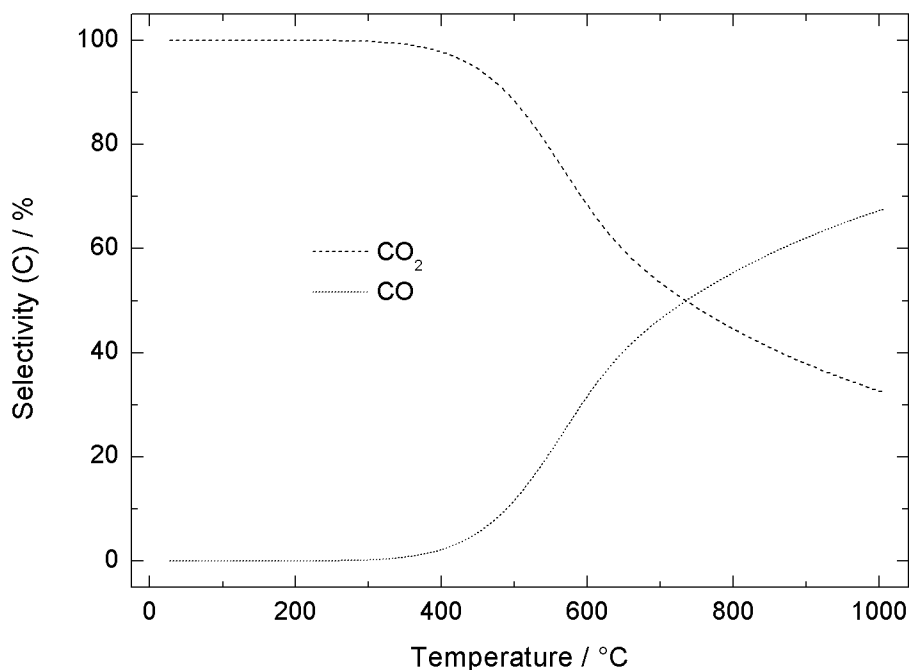


Figure 5. 4. Selectivity to carbon containing products CO and CO₂ during SR of methane with a S:C ratio of 4 at temperatures between 27 and 1007 °C.

5.5.5.2 ETHANOL AND GLYCEROL

In the thermodynamic equilibrium analysis of ethanol and glycerol steam reforming, CH₄ was considered as a potential carbon containing product. Below 400 °C the selectivity to CH₄ was highest because the methanation reaction was more thermodynamically favourable due to its lower free Gibbs energy change (ΔG) than that of the WGS reaction (Figure 5. 5). The selectivity to CO was zero because the thermodynamics favoured formation of CO₂ over CO as shown by the exothermicity of the WGS reaction. With increased temperature the selectivity of CH₄ was reduced in favour of CO and CO₂. The CH₄ selectivity will reach zero as the methane steam reforming reaction goes to completion and the CH₄ fraction reaches zero. At temperatures above this point, the selectivity to CO₂ is reduced and the selectivity to CO is increased due to a shift in the WGS reaction. Note that the H₂ yield is maximised at the temperature at which the CH₄ selectivity (and hence also the dry molar composition of CH₄) reaches zero. At temperatures above this point, the H₂ yield is reduced as a result of the shift in WGS.

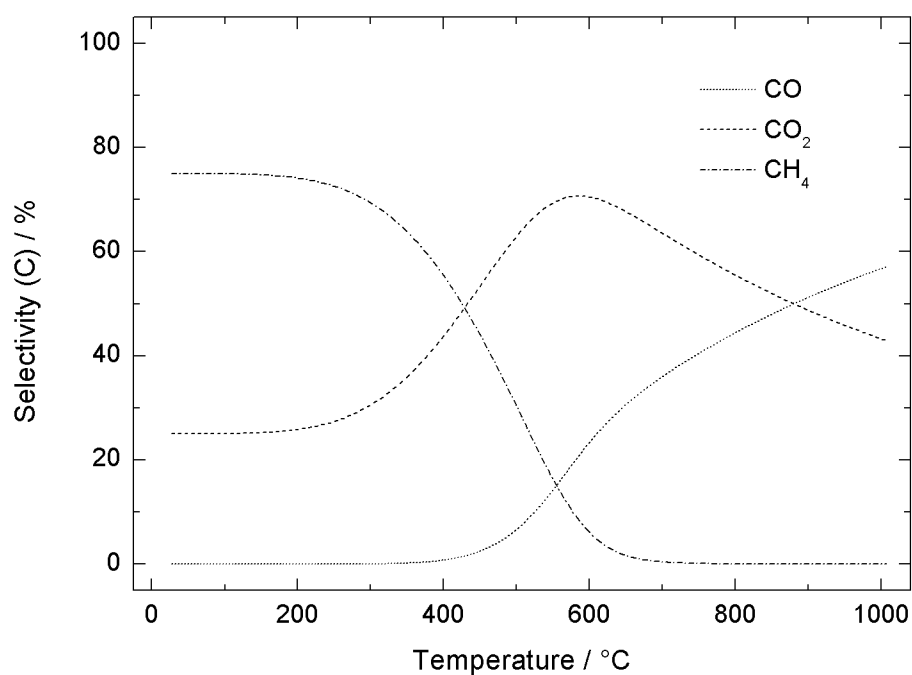


Figure 5. 5. Selectivity to carbon containing products CO, CO₂ and CH₄ during SR of ethanol with a S:C ratio of 4 at temperatures between 27 and 1007 °C.

At temperatures below 300 °C, the order in the selectivity to the carbon containing products during SR of glycerol was the same as for ethanol, but the selectivity to CO₂ was higher and that to CH₄ was lower (Figure 5. 6). This was attributed to the glycerol decomposition reaction. Due to the C:O ratio of the glycerol molecule, it can form CO and H₂ without converting water, hence a higher water fraction remains after minimisation of Gibbs free energy with regards to glycerol. A higher water fraction will shift the WGS reaction towards the right while shifting the CO methanation reaction to the left, thus favoring the selectivity to CO₂ over CH₄.

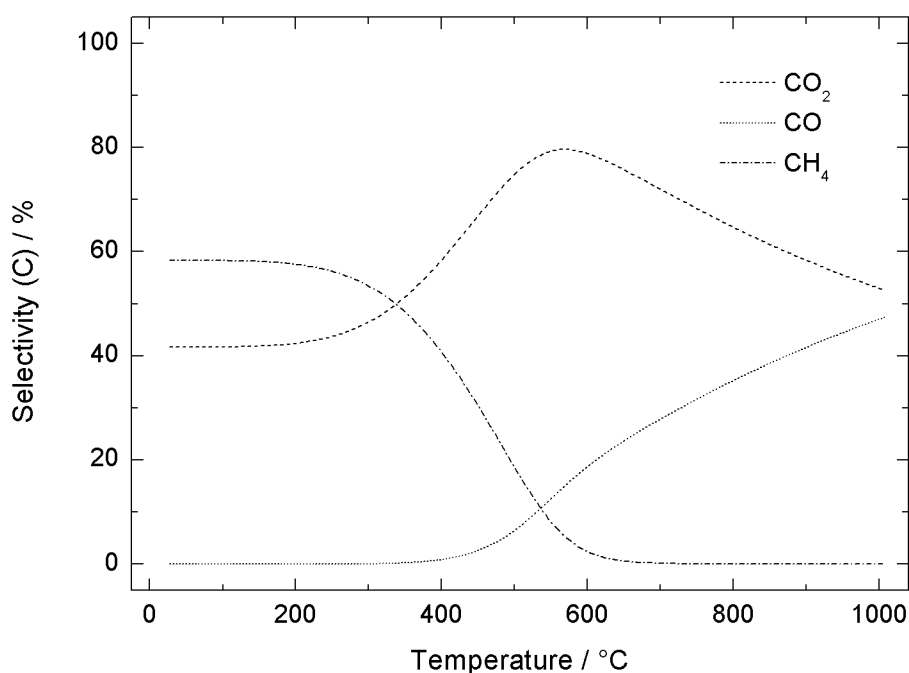


Figure 5. 6. Selectivity to carbon containing products CO, CO₂ and CH₄ during SR of glycerol with a S:C ratio of 4 at temperatures between 27 and 1007 °C.

5.5.6 SELECTIVITY TO HYDROGEN CONTAINING PRODUCTS

Under thermodynamic equilibrium in the SR system, the hydrogen containing species are H₂, H₂O and CH₄. Given that CH₄ is not considered as a product for SR of methane, and that selectivity to hydrogen containing species is calculated on a dry basis it is not discussed for SR of methane. The trends of selectivity to hydrogen containing species are the same for SR of ethanol and glycerol just like in the case of the selectivity to the carbon containing species (Figure 5. 7). With increased temperature, the selectivity to CH₄ is reduced in favour of H₂ which can be attributed to a shift in the CO methanation reaction alone. In the case of glycerol, selectivity as a function of temperature changed faster (the lines in the graph were steeper), hence for any given temperature the selectivity to H₂ was higher and the selectivity to CH₄ was lower in the case of glycerol compared to ethanol. This was attributed to the glycerol decomposition reaction. As it favours the selectivity to CO₂ over CH₄ with regards to the selectivity to carbon containing species, it also favours the selectivity to H₂ over CH₄ with regards to selectivity to hydrogen containing species because H₂ is formed together with CO₂ in the WGS reaction.

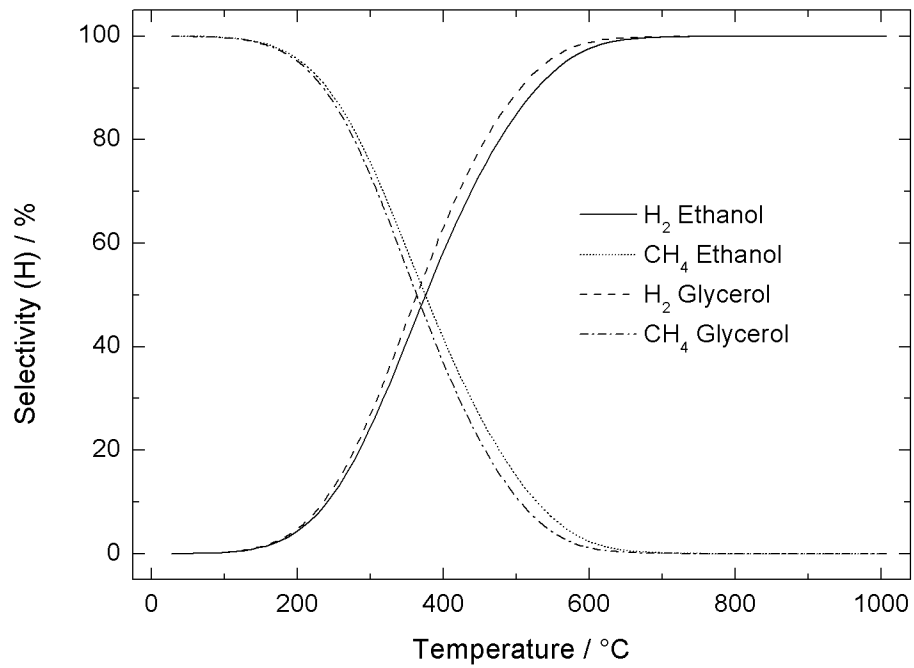


Figure 5. 7. Selectivity to hydrogen containing products H₂ and CH₄ during SR of ethanol and glycerol with a S:C ratio of 4 at temperatures between 27 and 1007 °C.

5.5.7 DRY MOLAR COMPOSITION

5.5.7.1 METHANE

The dry molar composition of H₂ increased with increasing temperature and reached a maximum of 78% in the temperature range 650-800 °C (Figure 5. 8). In the same temperature range the dry molar fraction of CO and CO₂ were 9-12% and 10-13% respectively. Hence syngas purification is needed downstream of the steam reformer during production of high purity hydrogen gas.

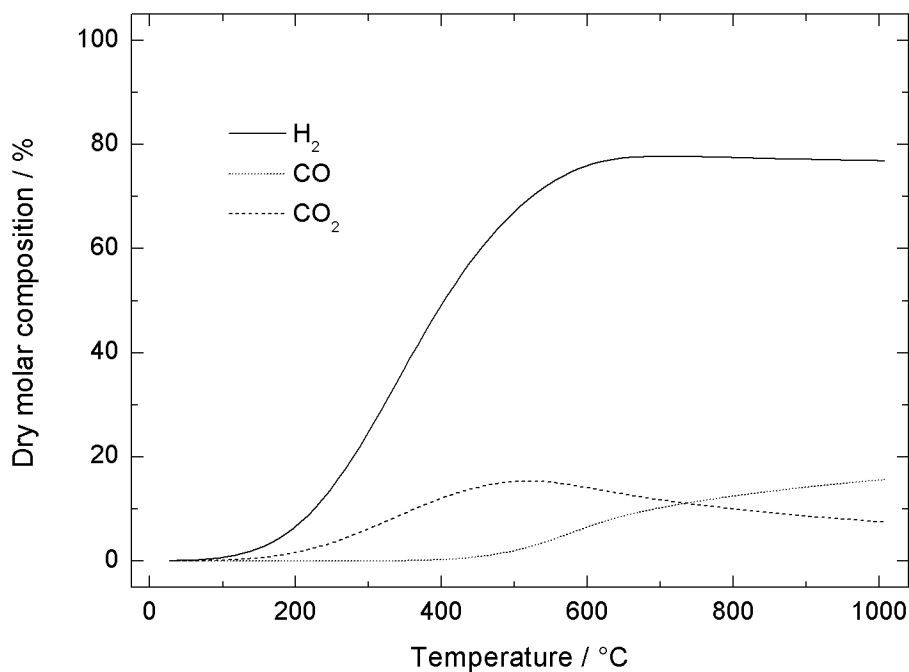


Figure 5. 8. Dry molar composition during SR of methane with a S:C ratio of 4 at temperatures between 27 and 1007 °C.

5.5.7.2 ETHANOL AND GLYCEROL

In the case of ethanol, the dry molar composition of H₂ reached a maximum in the same temperature range as in the case of methane but the maximum fraction was lower, i.e. 72% (Figure 5. 9). At temperatures above 650 °C the dry molar composition of CH₄ is removed from the dry syngas such that all carbon exists bound to oxygen in either CO₂ or CO. The lower composition of H₂ compared to methane is caused by the higher amount of carbon in the ethanol molecule (Figure 5. 1). The H:C ratio of methane and ethanol is 4:1 and 3:1 respectively (Table 5. 2).

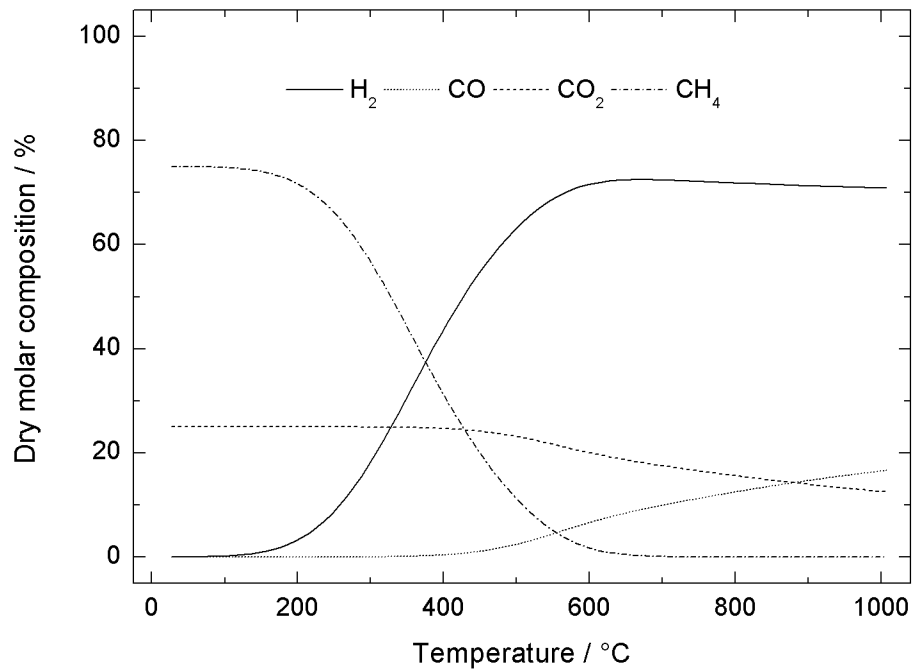


Figure 5. 9. Dry molar composition during SR of ethanol with a S:C ratio of 4 at temperatures between 27 and 1007 °C.

The trends in the dry molar compositions of H_2 , CH_4 , CO_2 and CO with temperature were the same for glycerol and ethanol (Figure 5. 10). The maximum dry H_2 composition was 67% which was lower than both methane and ethanol and was caused by the larger amounts of carbon in the glycerol molecule compared to methane and ethanol (Figure 5. 1). The H:C of glycerol is $2\frac{2}{3}:1$ (Table 5. 2).

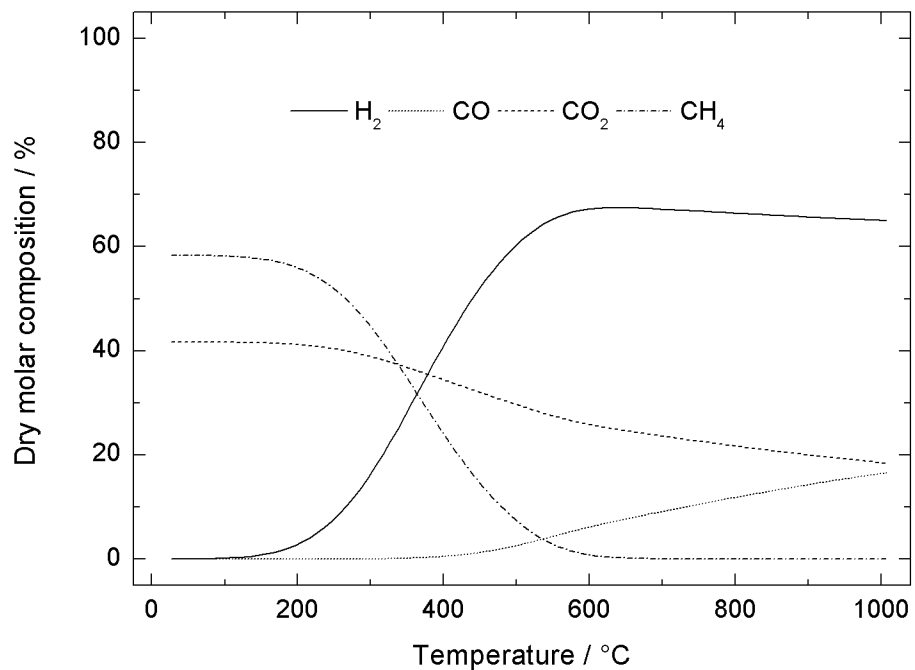


Figure 5. 10. Dry molar composition during SR of glycerol with a S:C ratio of 4 at temperatures between 27 and 1007 °C.

While the dry CO composition was similar for all three SR systems, the CO₂ fraction was highest for glycerol at all temperatures while the CO₂ composition for methane was the lowest (Figure 5. 11). This was explained by the differences in the amounts of oxygen in the different feedstocks (Figure 5. 1). While methane does not contain any oxygen at all the H:O of ethanol and glycerol is 6:1 and 2²/₃:1 respectively (Table 5. 2). Note that the CO₂ curve for methane is different from those of ethanol and glycerol because CH₄ is not considered as a product in the case of methane.

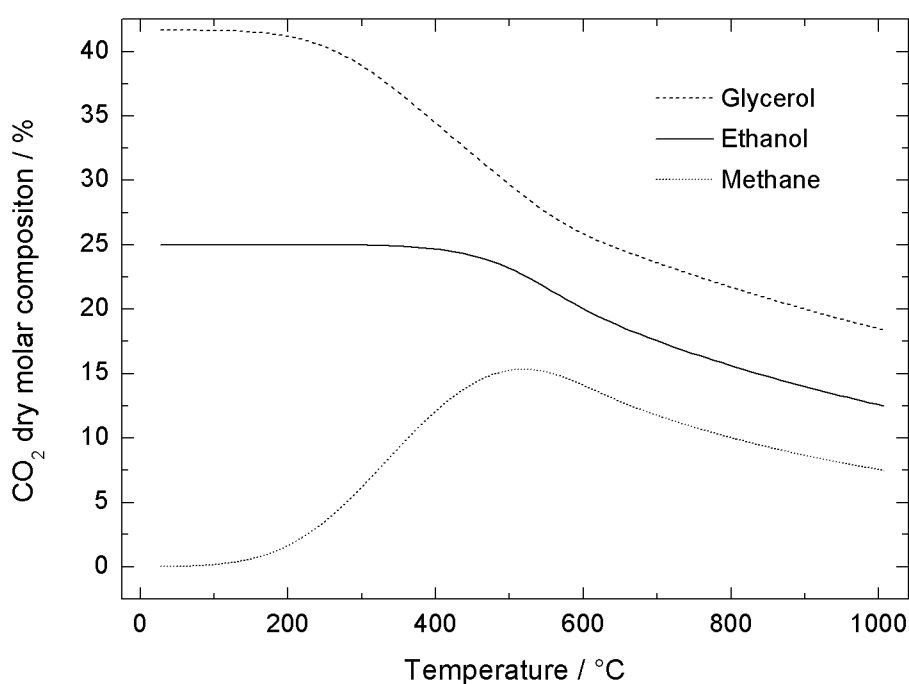
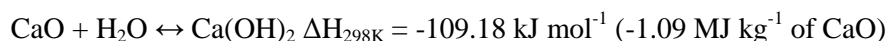


Figure 5. 11. Dry CO₂ molar composition during SR of methane, ethanol and glycerol with a S:C ratio of 4 at temperatures between 27 and 1007 °C.

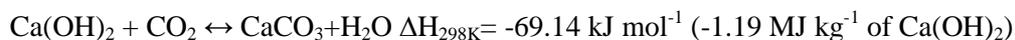
5.6 SORPTION ENHANCED STEAM REFORMING (SESR)

5.6.1 REACTIONS INVOLVED IN SESR

The introduction of CaO enables three potential additional reactions i.e. formation of CaCO₃ through a reaction between CaO and CO₂ (CaO carbonation, Reaction 3. 1), formation of Ca(OH)₂ via a reaction between CaO and H₂O (CaO hydration, Reaction 5. 6), and formation of CaCO₃ through direct reaction of Ca(OH)₂ with CO₂ (Ca(OH)₂ carbonation, Reaction 5. 7). Note that the ΔH_{298K} in the case of CaO carbonation is -1.79 MJ kg⁻¹ of CaO.



Reaction 5. 6. CaO hydration.



Reaction 5. 7. Ca(OH)₂ carbonation.

CaO is highly hygroscopic, hence Ca(OH)₂ will readily form at temperature below 400 °C. Therefore below 400 °C, carbonation can occur via CaO carbonation or via consecutive CaO hydration and Ca(OH)₂ carbonation. Above 400 °C, the CaO hydration reaction shifts fast towards the left. The removal of CO₂ from the gas phase via carbonation of CaO and Ca(OH)₂ shifts the WGS reaction to the right through Le Chatelier's principle which in turn will shift the CO methanation reaction to the left. The steam reforming reactions and the glycerol decomposition reaction will consequently be shifted to the right. The effect of CaO on the WGS reaction has been demonstrated both with thermodynamic analysis and with experimental work.²⁶⁰⁻²⁶⁴ Aspen Plus[®] software has been used to calculate the conversion of CO to CO₂ via the WGS reaction as a function of temperature between 100 and 800 °C at different levels of CO₂ capture (Figure 5. 12).²⁶⁰ CO conversion is increased with a higher level of CO₂ capture regardless of temperature which can be explained with Le Chatelier's principle. At temperatures below 200 °C, no CO₂ capture is needed for complete CO conversion but as the temperature is increased, CO conversion is reduced for all levels of CO₂ capture.

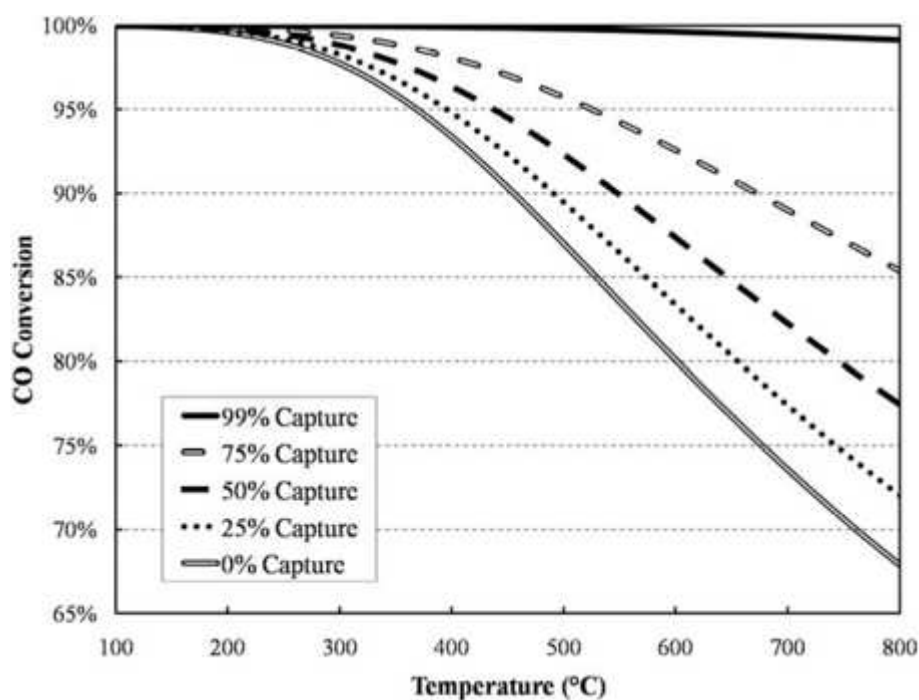


Figure 5. 12. The relationship between CO conversion and temperature during sorption enhanced WGS as a function of CO₂ capture amount. Reprinted with permission from Stevens Jr. et al.²⁶⁰ Copyright 2010 Elsevier.

Han and Harrison²⁶¹ showed that WGS could be carried out at 500-600 °C and 15 bar in the presence of limestone. They reported fractional conversions of CO into CO₂ of 98-100%. This is in agreement with Ramkumar and Fan²⁶² who reported 100% conversion of CO to CO₂ at 650 °C and 21 bar with 10.3% CO in the presence of CaO. Calculated fractional conversions without a CO₂ sorbent were 55-65% at 500-600 °C.²⁶¹ Müller et al.²⁶³ carried out WGS with dolomite as the sorbent at temperatures between 505 and 650 °C with a pressure of 1 bar in an atmosphere of 7 mol% CO and 33 mol% H₂O (N₂ balance). Note that once calcined, dolomite's active sorbent species has been shown to be CaO despite also containing MgO in roughly equimolar amounts. They found that the amount of H₂ in the off-gas more than doubled from <0.02 moles to >0.04 moles as the temperature was increased from 505 to 650°C. The amount of CO₂ simultaneously quadrupled from 4 to 16 mmol. Bretado et al.²⁶⁴ carried out WGS in a quartz fixed bed reactor at a temperature of 600 °C, a pressure of 1 bar in an atmosphere of 5% CO and 15% H₂O (N₂/He balance) using dolomite as a sorbent. Off-gas composition (only regarding CO, CO₂ and H₂) was presented. The CO composition was reduced from 100% to <1% within 30 min while the CO₂ and H₂ compositions were increased from 0 to ≈15 and ≈80% respectively. The results can be attributed to a shift in the water gas shift reaction due to CO₂ capture by the dolomite.

The complete SESR reactions for methane, ethanol and glycerol in the presence of CaO are:



Reaction 5. 8. Complete methane SESR.



Reaction 5. 9. Complete ethanol SESR.



Reaction 5. 10. Complete glycerol SESR.

The $\Delta H_{298\text{K}}$ for all three steam reforming systems are reduced as a result of the addition of CaO due to the exothermicity of the CaO carbonation reaction. Consequently, optimum H_2 yield for a given S:C ratio is reached at a lower temperature following addition of CaO. This means that SESR can be run at a lower temperature than SR which has been demonstrated experimentally.^{218,220}

5.6.2 THERMODYNAMICS ANALYSIS OF SESR

Thermodynamic analysis was carried out with input mole fractions of feedstock and water corresponding to a S:C ratio of 4 and a Ca:C ratio of 2 (Table 5. 5). The S:C ratio was chosen to allow direct comparison with the SR results (Section 5.5.2). When the complete SESR reactions are balanced the Ca:C ratio is 1, hence a Ca:C ratio of 2 ensures excess of CaO and allow potential complete CO_2 capture. Given the molar mass of CaO (56.1 g mol^{-1}) the theoretical amount CaO needed to achieve the a Ca:C ratio of 2 on a weight basis is $7.0 \text{ g}_{\text{CaO}} \text{ g}^{-1}_{\text{feedstock}}$ in the case of methane while the corresponding amounts for ethanol and glycerol are 4.8 and $3.6 \text{ g}_{\text{CaO}} \text{ g}^{-1}_{\text{feedstock}}$ respectively. However, this assumes complete conversion of the CaO to CaCO_3 which is difficult to achieve in practice.

Analysis of SESR under 1 bar of pressure in the temperature range 27-1027 °C was performed to also allow direct comparison with SR. H_2 yield, selectivity and dry molar composition were calculated and plotted as for SR, and plotted in the same format. Note that selectivity to carbon containing species will feature CaCO_3 and selectivity to hydrogen containing species will feature Ca(OH)_2 in addition to the previous species identified for SR.

Table 5. 5. The input mole fractions used for thermodynamic analysis of sorption enhanced steam reforming of methane, ethanol and glycerol.

Input mole fraction	Methane	Ethanol	Glycerol
Feedstock	0.1429	0.0769	0.0526
Water	0.5714	0.6154	0.6316
CaO	0.2857	0.3077	0.3158

5.6.3 H₂ YIELD

The introduction of CaO significantly increased the hydrogen yield (Figure 5. 13). Obviously, the differences in molar mass and oxygen content of the feedstocks persist when CaO is added and therefore methane showed the highest yield followed by ethanol and glycerol just like during SR. As expected from the exothermicity of the CaO carbonation reaction, maximum yield was reached at 400-600 °C meaning that maximum yield was reached at a lower temperature and over a wider temperature range than during SR (500-600 °C). Maximum H₂ yield was 49.9, 26.1 and 15.3 for methane, ethanol and glycerol respectively which was 12-13% higher than during SR (44.0, 23.1 and 13.6 for methane, ethanol and glycerol respectively).

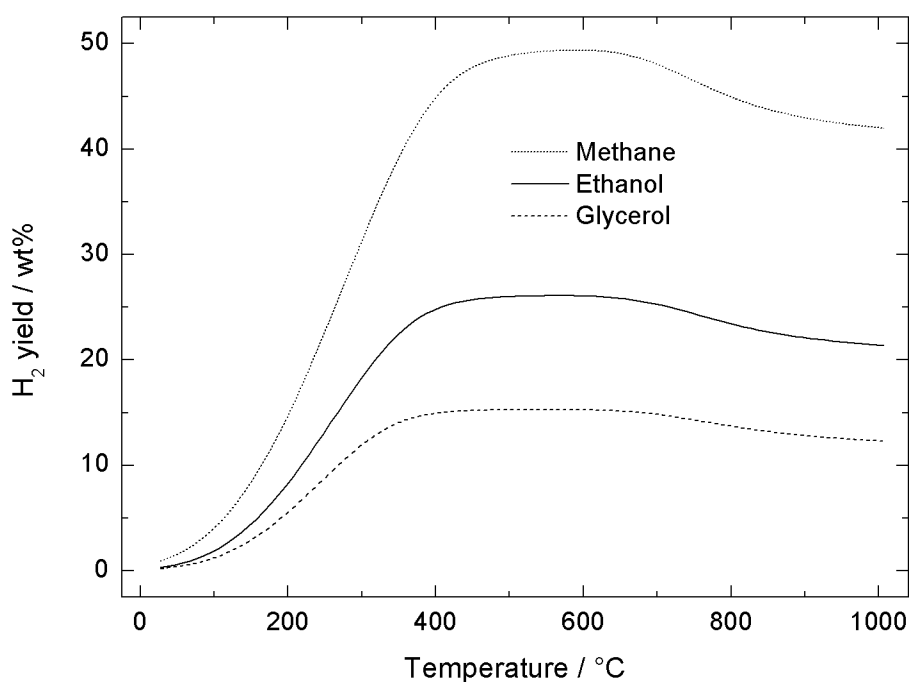


Figure 5. 13. H₂ yield during SESR of methane, ethanol and glycerol with a S:C ratio of 4 at temperatures between 27 and 1007 °C.

5.6.4 WATER CONVERSION

Water conversion reached a maximum at around 300 °C (much earlier than for SR) for all feedstocks and was then reduced (Figure 5. 14). The maximum conversion was higher than for

SR. The shift in the point of maximum conversion was attributed to the shift in the WGS reaction caused by the removal of CO_2 . With increased temperature, the water conversion was reduced as a result of the WGS reaction being shifted to the left. The effect on water conversion due to the introduction of CaO explained the shift in temperature for maximum H_2 yield as H_2 is formed in the WGS reaction.

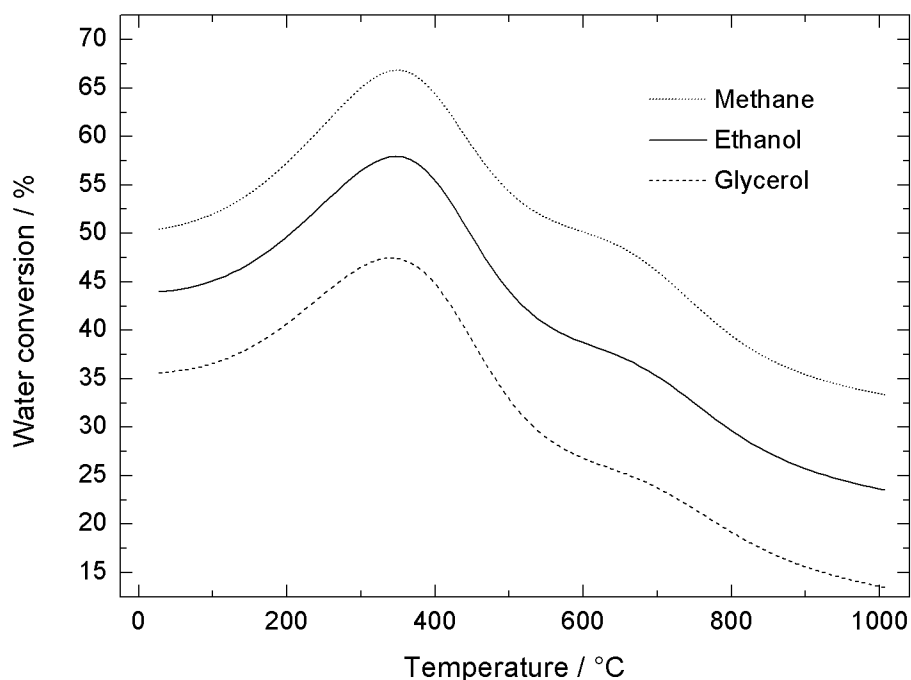


Figure 5. 14. Water conversion during SESR of methane, ethanol and glycerol with a S:C ratio of 4 at temperatures between 27 and 1007 °C.

5.6.5 SELECTIVITY TO CARBON CONTAINING COMPOUNDS

5.6.5.1 METHANE

In the case of methane, the selectivity to CaCO_3 was 100% at temperatures up to 500 °C and consequently, no carbon containing species existed in the gas phase at equilibrium at temperature below 500 °C (Figure 5. 15). Above 500 °C the selectivity to CaCO_3 was reduced in favour of CO and CO_2 because of a shift in the CaO and Ca(OH)_2 carbonation reactions towards the left. This effect has been shown previously by Wang et al.¹⁹⁹ who plotted species concentration over temperature for SESR with glycerol (Figure 4. 6). It has also been shown experimentally^{23,218} which highlights a trade-off between the steam reforming reactions and glycerol decomposition on one hand and CaO and Ca(OH)_2 carbonation and WGS on the other.

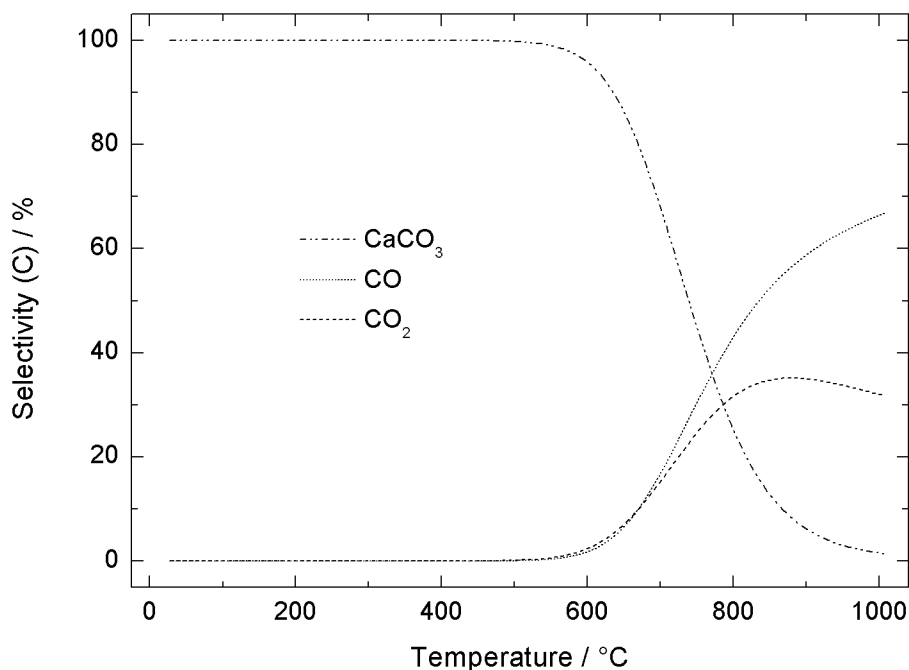


Figure 5. 15. Selectivity to carbon containing products CO, CO₂ and CaCO₃ during SESR of methane with a S:C ratio of 4 at temperatures between 27 and 1007 °C.

5.6.5.2 ETHANOL AND GLYCEROL

For the ethanol and glycerol SESR systems, the selectivity to CaCO₃ and CH₄ dominated at temperatures below 550 °C and with increased temperature the selectivity to CaCO₃ increased while the selectivity to CH₄ reduced (Figure 5. 16, Figure 5. 17). Hence, CH₄ and CaCO₃ competed for carbon in the gas phase. At temperature below 200 °C the glycerol system displayed a higher selectivity to CaCO₃ which can be attributed to the higher selectivity to CO₂ during SR of glycerol compared to ethanol (discussed in Section 5.5.5.2). This in turn meant that the maximum selectivity to CaCO₃ was reached at a slightly lower temperature. Note that the H₂ yield (Figure 5. 13) reached its maximum level in the same temperature range during which selectivity to CaCO₃ was maximised.

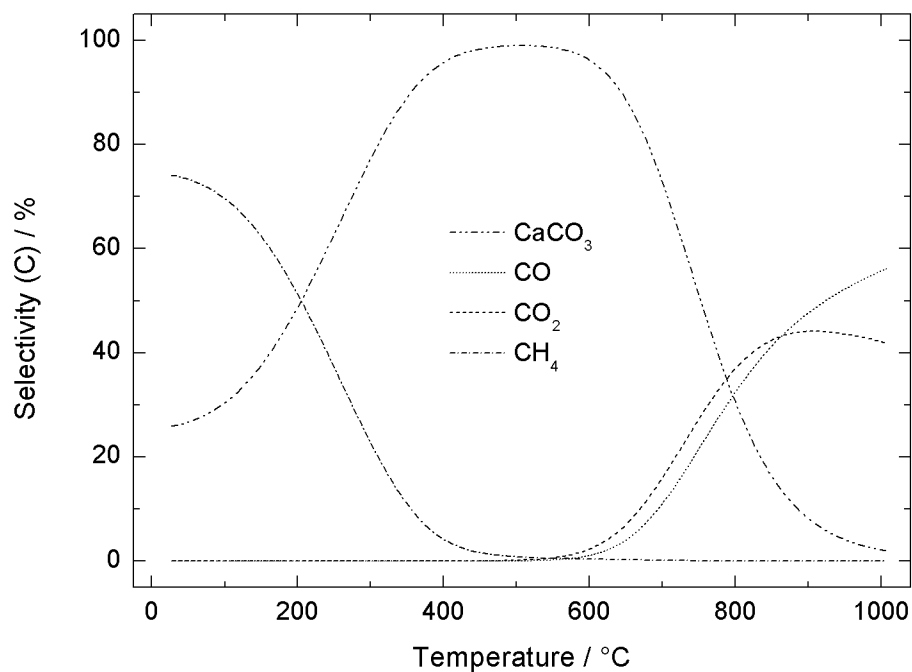


Figure 5. 16. Selectivity to carbon containing products CO, CO₂, CH₄ and CaCO₃ during SESR of ethanol with a S:C ratio of 4 at temperatures between 27 and 1007 °C.

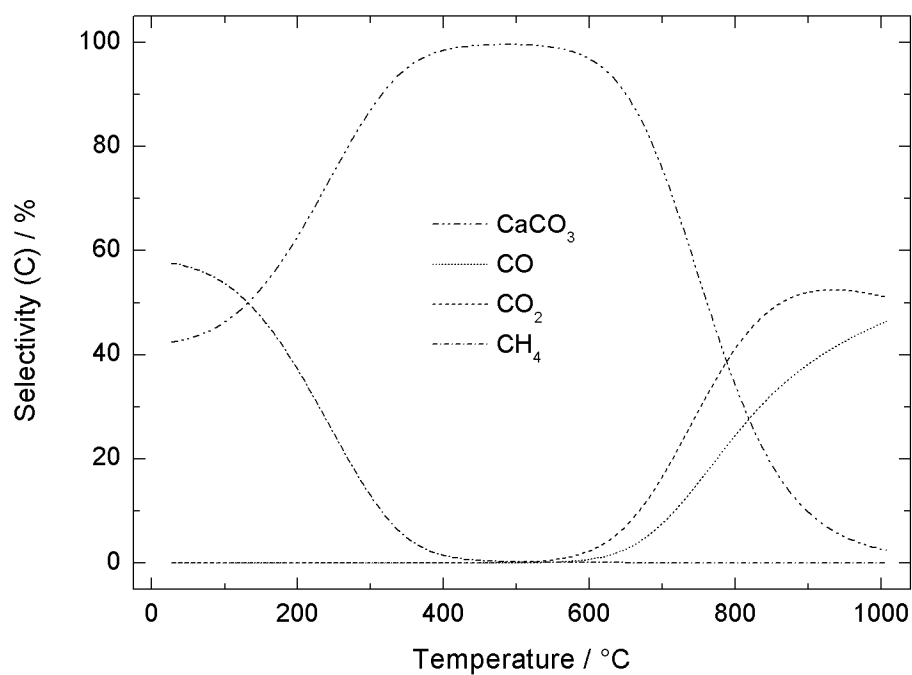


Figure 5. 17. Selectivity to carbon containing products CO, CO₂, CH₄ and CaCO₃ during SESR of glycerol with a S:C ratio of 4 at temperatures between 27 and 1007 °C.

5.6.6 SELECTIVITY TO HYDROGEN CONTAINING PRODUCTS

5.6.6.1 METHANE

During SESR the formation of Ca(OH)_2 through the CaO hydration reaction was considered. In the methane SESR system, the selectivity to Ca(OH)_2 was 96% at 27 °C (Figure 5. 18) which means that CaO removes water from the gas phase thus lowering the S:C ratio for the methane steam reforming reaction. With increased temperature the selectivity to Ca(OH)_2 decreased while the selectivity to H_2 increased. The selectivity to H_2 reached 99% at 627 °C and then the increase as function of temperature significantly reduced.

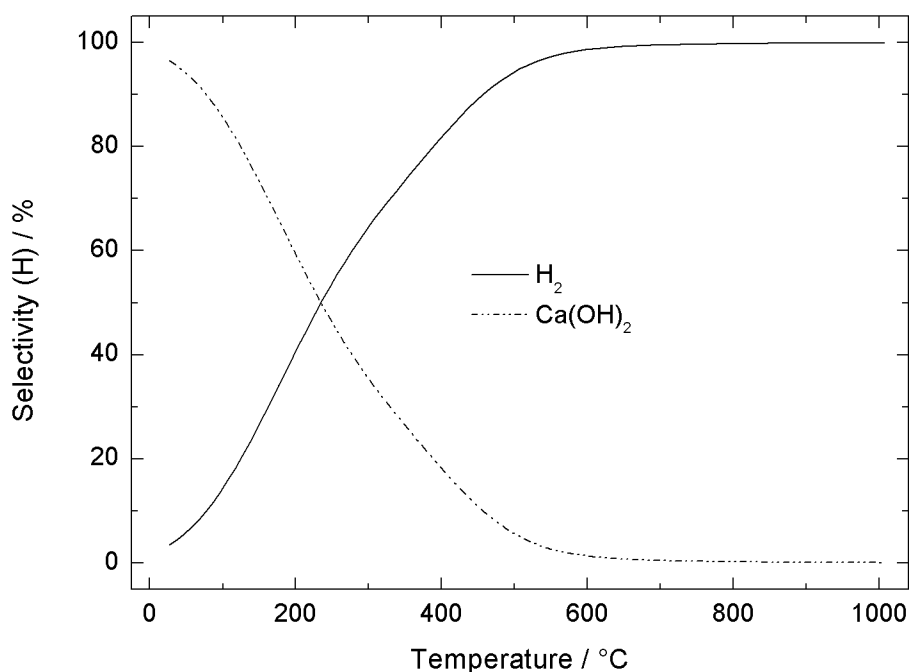


Figure 5. 18. Selectivity to hydrogen containing products H_2 and Ca(OH)_2 during SESR of methane with a S:C ratio of 4 at temperatures between 27 and 1007 °C.

5.6.6.2 ETHANOL AND GLYCEROL

The trends of selectivity to hydrogen containing species was the same for SESR of ethanol and glycerol. Note that the selectivity to Ca(OH)_2 was higher than to CH_4 . The selectivity to CH_4 was significantly lower in the SESR system compared to the SR system because it competes with CaO for water and Ca(OH)_2 is very stable at temperature below 400 °C. Recall that CaO also competed with CH_4 for carbon.

The stability of Ca(OH)_2 below 400 °C means that a significant amount of water is removed from the gas phase thus lowering the S:C ratio with subsequent effects on all water related reactions. With increased temperature, this effect is weakened as water is released back to the gas phase via a shift towards the left of the CaO hydration reaction. The selectivity to CH_4

was lower for glycerol than for ethanol which was attributed the glycerol decomposition reaction which leaves more water in the gas phase than the ethanol steam reforming reaction as discussed previously.. This in turn increased the selectivity to $\text{Ca}(\text{OH})_2$ in the case of SESR. When CH_4 no longer exists in the gas phase (temperature above 400 °C) this results in a slightly lower selectivity to H_2 for glycerol compared to ethanol. Hence the formation of $\text{Ca}(\text{OH})_2$ had a more detrimental effect on SESR of glycerol than on ethanol due to the ability of glycerol to decompose to H_2 and CO without water via the glycerol decomposition reaction.

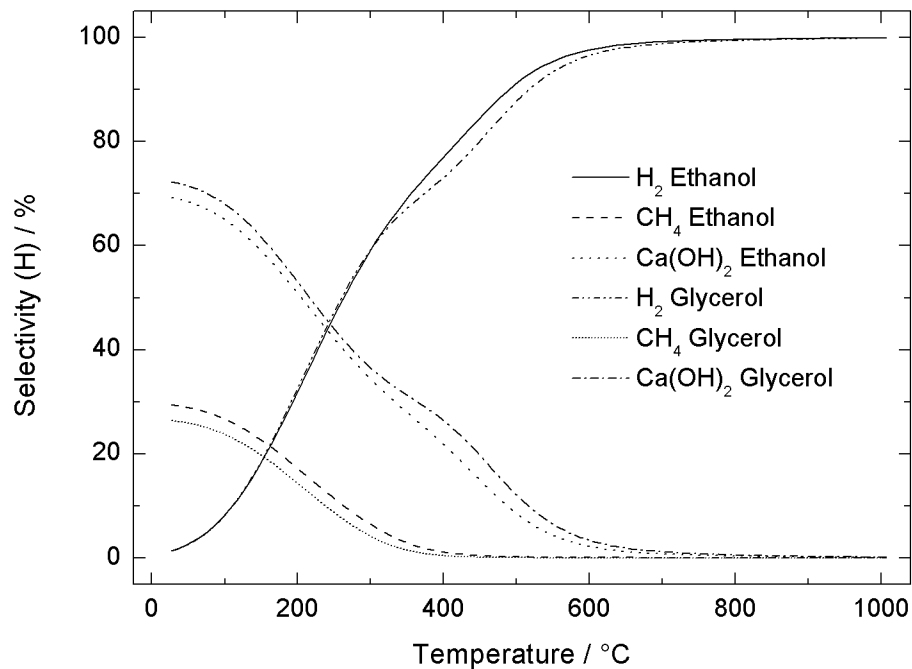


Figure 5. 19. Selectivity to hydrogen containing products H_2 , $\text{Ca}(\text{OH})_2$ and CH_4 during SESR of ethanol and glycerol with a S:C ratio of 4 at temperatures between 27 and 1007 °C.

5.6.7 DRY MOLE FRACTION

5.6.7.1 METHANE

In the presence of CaO the mole fraction of H_2 was 99% for temperatures between 450 and 600 °C (Figure 5. 20) which is a significant improvement over conventional SR. Such a high mole fraction is made possible by the removal of carbon and oxygen from the gas phase via the carbonation reaction. If these conditions could be reached in practice there would only be need for minimal downstream purification of the reformer off-gas. In fact reformer off gas H_2 concentrations of 96.0-96.4% has been reported at temperatures of 450-460 °C during experimental SESR of methane using CaO as the sorbent.^{60,122} At temperatures above 450-600 °C the dry H_2 mole fraction is reduced while the CO and CO_2 mole fractions increase (Figure 5. 20). This effect has been observed during experimental work on SESR of glycerol.^{23,218} As the

reformer temperature was increased from 500 to 700 °C, the hydrogen concentration in the reactor off-gas was reduced. The effect was attributed to a reversal of the CaO carbonation reaction. This is supported by the selectivity to CaCO₃ presented here (Figure 5. 15) which showed a reduction in selectivity in the same temperature range as the H₂ fraction was reduced.

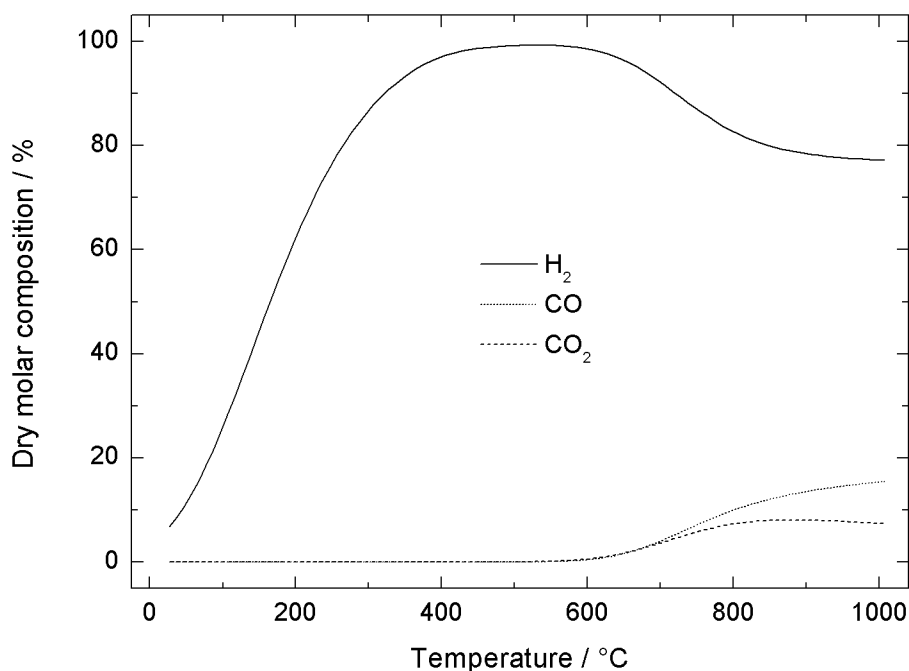


Figure 5. 20. Dry molar composition during SESR of methane with a S:C ratio of 4 at temperatures between 27 and 1007 °C.

5.6.7.2 ETHANOL AND GLYCEROL

A dry H₂ mole fraction of 99% was also reached during SESR of ethanol and glycerol at temperatures between 400-600 °C (Figure 5. 21, Figure 5. 22). Again, the results for ethanol and glycerol were displayed the same trends. The data showed that a high purity reformer off-gas is possible during SR under thermodynamic equilibrium of ethanol and glycerol when CaO is added as a sorbent. Experimental work on SESR of ethanol and glycerol has resulted in reformer off-gas H₂ concentrations of 99 and 95-97% at temperatures of 550 and 500-530 °C respectively.^{23,220,265} The dry H₂ mole fraction was maximised in the same temperature range as when the selectivity to CaCO₃ was maximised (Figure 5. 16, Figure 5. 17). As with methane, the dry H₂ mole fraction reduced at higher temperatures. The CO mole fraction was significantly lower than during SR which is important as CO is a major source of proton exchange membrane fuel cell poisoning.²⁶⁶ At temperature above 600 °C the dry molar concentration of CO₂ relative to that of CO was higher in the case of glycerol indicating a more pronounced WGS which was attributed to the effect of the glycerol decomposition reaction as discussed previously.

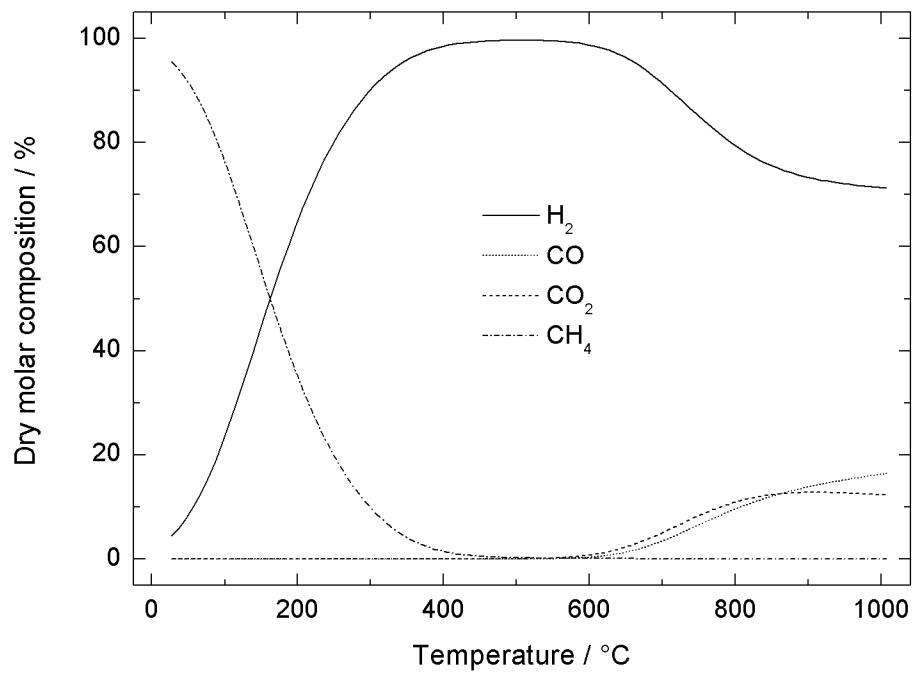


Figure 5. 21. Dry molar composition during SESR of ethanol with a S:C ratio of 4 at temperatures between 27 and 1007 °C.

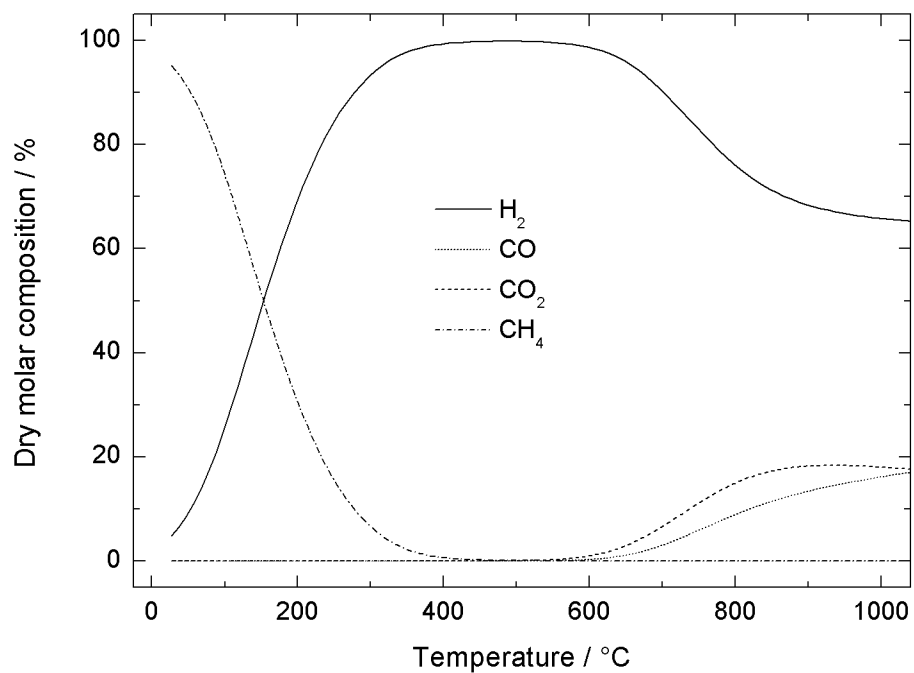


Figure 5. 22. Dry molar composition during SESR of glycerol with a S:C ratio of 4 at temperatures between 27 and 1007 °C.

CHAPTER 6: CO₂ SORBENT CHARACTERISTICS

“Whenever a theory appears to you as the only possible one, take this a sign that you have neither understood the theory nor the problem which it was intended to solve”

Karl Popper

6.1 MOTIVATION FOR WORK

In Chapter 3 it was concluded that Ca-based sorbents are well suited for use in sorption enhanced steam reforming (SESR) as well as post combustion CO₂ capture due to their abundance, low cost, high capture capacity, fast reaction kinetics and reaction temperature range. Chapter 4 reviewed the successful use of Ca-based sorbents for SESR of glycerol and Chapter 5 outlined the thermodynamic equilibrium effects of CaO on the steam reforming process through sorption enhancement. The calcium looping cycle has been demonstrated to be an economically viable option for post combustion CO₂ capture and the technology has advanced to the pilot scale.^{30,31}

As outlined in Chapter 3 (Section 3.2.3) the main disadvantage of Ca-based sorbents is the loss in capacity after multiple cycles due to loss of surface area and porosity through sintering. Other causes for capacity loss are attrition³⁶⁻³⁹ and sulphation.^{43,267,268} Circulation in and between fluidised carbonators and calciners results in particle breakage. Sulphur dioxide impurities in the post combustion flue gas readily react with CaO to form highly stable CaSO₄ which is difficult to calcine. Hence sulphation results in chemical deactivation of the sorbent.⁴³ For large scale post combustion CO₂ capture, CaO itself is the single-most expensive plant component.²⁶⁹ Also, the cost of CaO and its deactivation rate are the parameters which have the highest sensitivities towards the total cost of CO₂ capture.²⁶⁹

The focus of this work is the use of sorbents for steam reforming of the liquid feedstocks ethanol and glycerol which is commonly carried out in packed bed systems and where carbonation and calcination are carried out in the same reactor.^{23,73,254} Consequently, attrition is less of a priority for steam reforming of liquid feedstock in packed bed systems compared to post combustion CO₂ capture from coal combustion. The sulphur content of coal varies heavily and can be anything from less than 400 ppm up to around 11000 ppm.²⁷⁰ The sulphur content of crude glycerol is 14-128 ppm¹⁶⁹ and ethanol is sulphur free meaning that capacity loss due to sulphation is also less of a priority for steam reforming of ethanol and glycerol. Other liquid feedstocks which can be used for steam reforming such as pine oil are also low in sulphur.²⁷¹ Therefore, the work presented here will focus on loss of capacity which is due to sintering.

Sintering can be retarded through the incorporation a Ca₁₂Al₁₄O₃₃ phase through a series of wet mixing and heating steps which prevent densification and grain growth (Chapter 3, Section 3.2.4.2). CaO prepared from specific precursors have also shown sintering resistant behaviour both on their own and with incorporated inert material.^{101,272-274}

Hydration can be used as a regeneration method of sintered sorbents since it can restore surface area and porosity.⁴⁴⁻⁴⁷ A major drawback of hydration as a regeneration method is the reduced mechanical strength of the regenerated sorbent.^{36,37,39,45} It is therefore important to understand the effects of hydration. In addition, steam influences both carbonation and

calcination of Ca-based sorbents which further shows the importance of understanding the interaction between CaO/CaCO₃ and water.

The study of Ca-based sorbents using TGA as well as reactors at both bench scale and pilot scale often involves crushing and sieving of limestone from larger pieces of rock into particles. Synthetic sorbents are manufactured from commercially available chemicals in powder form. Small CaO/Ca₁₂Al₁₄O₃₃ particles have many times been prepared by crushing and sieving the cake formed during the final heating stage of the preparation. Smaller particles (10-350 μm^{53,54,275,276}) have been prepared for TGA analysis and larger particles (500-700 μm¹³⁹) have been prepared for bench scale reactor experiments. Small Ca-based sorbent particles can also be converted into pellets either through granulation⁴⁹ or through the preparation of a paste which has then been sieved and dried.^{151,152,277}

This chapter will study a commercially available CaO powder and the effects of hydration and on subsequent decomposition as well as incorporation of a Ca₁₂Al₁₄O₃₃ phase into the powder. Commercially available CaO powder (99.95% metal basis, Alfa Aesar, UK) was chosen instead of CaO derived from natural limestone to allow comparison with the literature with regards to CaO/Ca₁₂Al₁₄O₃₃ materials. It was also chosen for its high purity (99.95% on a metal basis). This makes it more expensive than CaO derived from natural limestone. Its powder form also means that it is expected to have lower surface area and porosity than CaO derived from limestone. CaO derived from a Ca-D-gluconate precursor was also investigated because this sorbent had shown promising results in previous work²⁷² and a Ca₁₂Al₁₄O₃₃ phase was incorporated in to this sorbent also. The first section of the chapter will be aimed at characterizing a number of Ca-based sorbents using XRD, N₂ adsorption and SEM in order to gauge their composition, surface area, porosity and morphology. The differences between the sorbents will be discussed. All techniques used below are presented in detail in Chapter 2. Next, the sorbents will be investigated using TGA to study their behaviour during carbonation and over multiple cycles.

Finally, sorbent pellets will be prepared from selected Ca-based sorbents using a compression method (outlined in Chapter 2, Section 2.5) and investigated using a bench scale reactor. The bench scale reactor environment is more similar to large scale CO₂ capture setups than the environment inside a TGA setup which makes the results more relevant to the intended application. One major reason for capacity loss in Ca-based sorbents when used for the intended application is attrition and the preparation of pellets from small fines is a possible means of recovering sorbent which has been lost through sintering. The work will compare TGA and reactor results and investigate the effect of pelletisation of CO₂ capture capacity.

6.2 AIMS AND OBJECTIVES

The aims of this chapter are to:

- Characterize selected sorbents to understand the effect of hydration, decomposition and the inclusion of $\text{Ca}_{12}\text{Al}_4\text{O}_{33}$.
- Understand the mechanisms of carbonation in the chosen sorbents.
- Compare the stability of the characterized sorbents over multiple cycles.
- Investigate the effects of pelletisation.

The objectives are to

- Manufacture the chosen sorbents and characterize them in terms of composition, morphology, surface area and porosity.
- Carry out carbonation experiments using TGA with the sorbents in powder form.
- Compress selected sorbents into pellets and carry out carbonation in a bench scale reactor.

6.3 SORBENTS INVESTIGATED

Commercially available CaO powder (99.95% purity, metal basis, from Alfa Aesar, UK) was investigated as received and referred to as 'CaO powder'. Given the importance of understanding the effects of hydration on Ca-based CO_2 sorbents, the CaO powder was hydrated to prepare $\text{Ca}(\text{OH})_2$. The preparation of the $\text{CaO}/\text{Ca}_{12}\text{Al}_4\text{O}_{33}$ sorbent involves wet mixing during which hydration and subsequent formation of $\text{Ca}(\text{OH})_2$ occur. In order to enable investigation into the effects of the wet mixing phase of the $\text{CaO}/\text{Ca}_{12}\text{Al}_4\text{O}_{33}$ preparation (Chapter 2, Section 2.2), the hydration was carried out using the same wet mixing method as during the $\text{CaO}/\text{Ca}_{12}\text{Al}_4\text{O}_{33}$ preparation. This involved dissolving CaO powder in water and 2-propanol for 1h at 75 °C (Chapter 2, Section 2.2). This sorbent is henceforth referred to as ' $\text{Ca}(\text{OH})_2$ '. Hydration followed by decomposition has been suggested as a regeneration method for Ca-based sorbents.^{46,47} The preparation of $\text{Ca}_{12}\text{Al}_4\text{O}_{33}$ sorbents also involves hydration steps followed by calcination. Therefore, $\text{Ca}(\text{OH})_2$ was decomposed at 700 °C in N_2 (either using the bench scale reactor described in Chapter 2, Section 2.11.1 or in the TGA setup) to prepare CaO derived from $\text{Ca}(\text{OH})_2$ which was also investigated. This sorbent is referred to as 'CaO derived from $\text{Ca}(\text{OH})_2$ '.

$\text{CaO}/\text{Ca}_{12}\text{Al}_4\text{O}_{33}$ was prepared using the CaO powder and AlNO_3 using a series of mixing and heating steps described in Chapter 2 (Section 2.2) and originally presented by Li et al.⁵³ This sorbent is referred to as ' $\text{CaO}/\text{Ca}_{12}\text{Al}_4\text{O}_{33}$ '. To investigate the effects of the

Ca₁₂Al₁₄O₃₃ phase, the preparation process was carried out without the addition of AlNO₃. The purpose was to benchmark the properties of the CaO/Ca₁₂Al₁₄O₃₃ sorbent with a sorbent lacking the Ca₁₂Al₁₄O₃₃ phase with everything else being equal. This sorbent will be referred to as 'CaO/No Al'.

CaO was derived from a Ca-D-gluconate precursor (Ca[HOCH₂(CHOH)₄CO₂]₂) by decomposition because this sorbent had shown promising results in previous work.²⁷² This sorbent is referred to as 'CaO derived from Ca-D-gluconate' and it was subsequently used to produce a Ca₁₂Al₁₄O₃₃ containing sorbent prepared as the CaO/Ca₁₂Al₁₄O₃₃ sorbent described above. This sorbent will henceforth be referred to as 'CaO-D/Ca₁₂Al₁₄O₃₃'. The above sorbents were categorized as CaO sorbents and Ca₁₂Al₁₄O₃₃ sorbents and presented separately below.

6.4 CHARACTERISATION

6.4.1 CAO SORBENTS

6.4.1.1 CAO POWDER

XRD analysis showed that apart from a CaO phase, the CaO powder also contained a Ca(OH)₂ phase (Figure 6. 1). This was expected due to the high reactivity of CaO towards water.^{278,279} The Ca(OH)₂ phase appeared to have formed as a result of contact with air. A more thorough XRD analysis of the CaO powder (and of the Ca(OH)₂ and CaO/Ca₁₂Al₁₄O₃₃ sorbents) including phase quantification is presented in Chapter 7.

The BET surface area of the CaO powder was 2.9 m²g⁻¹ which is in agreement with published data^{280,281} as well as being consistent with the characteristics of a non porous material in a powder form. Note that the amount of Ca(OH)₂ could differ between multiple samples used for N₂ adsorption experiments, thus introducing an error. Efforts were made to protect the sample from the surrounding atmosphere after degassing to keep the sample as dry as possible but it was not possible to completely remove the risk of Ca(OH)₂ formation or to quantify the amount of formed Ca(OH)₂.

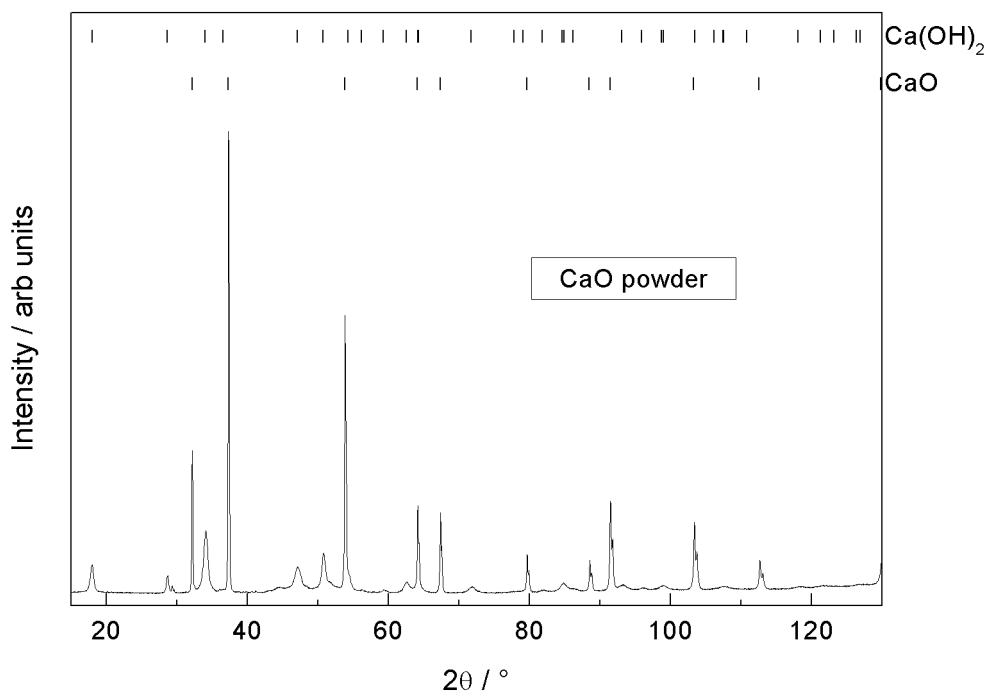


Figure 6. 1. XRD spectrum between 2θ 15-130 ° of CaO powder. Vertical lines show the expected positions of diffraction peaks for CaO and Ca(OH)₂.

SEM imaging showed that the CaO powder particles comprised mostly flat surfaces with sharp edges (Figure 6. 2). The appearance of the CaO powder particles is similar to previously reported SEM results.⁵³ At a magnification of 50000X the surface of the particles appeared smooth without the pores that have been reported in CaO which has been derived from decomposition of CaCO₃.^{98,131} The porosity in CaO from decomposed CaCO₃ is likely to be derived from CO₂ molecules as they leave the sorbent.¹⁶⁰ The CaO powder tested here was therefore not expected to display the same porosity as calcined limestone studied elsewhere.

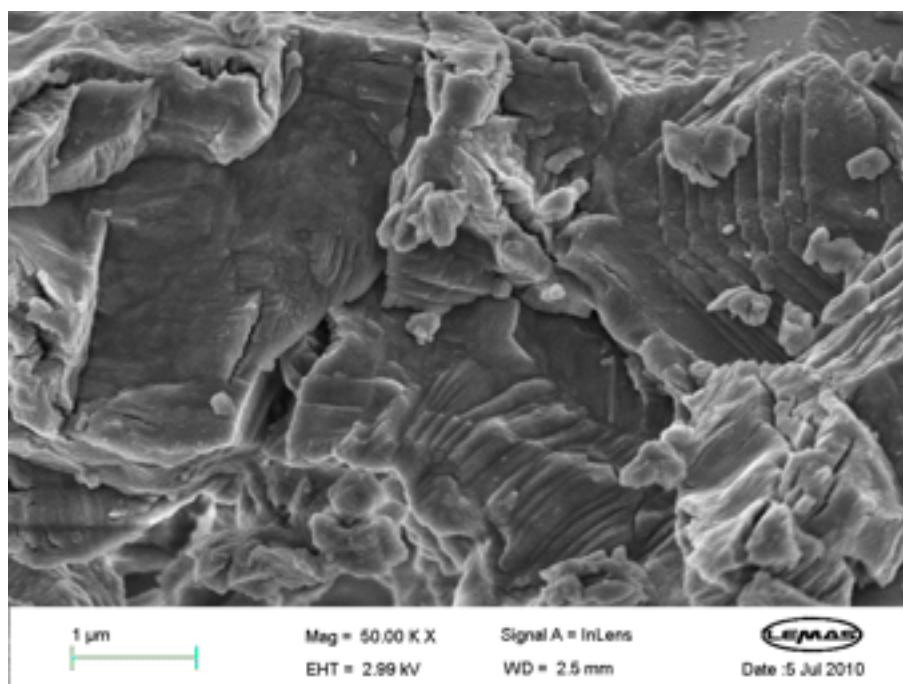


Figure 6. 2. SEM image of CaO at 50000X magnification.

6.4.1.2 Ca(OH)₂

Hydration of the CaO powder resulted in conversion to Ca(OH)₂ as evidenced by the XRD analysis (Figure 6. 3). The sorbent also contained a small amount of CaCO₃ which can be attributed to the high reactivity of Ca(OH)₂ to CO₂. It is possible that CaCO₃ formed during the preparation due to the presence of dissolved CO₂ in the water/2-propanol mixture. SEM imaging showed that hydration caused an increase in porosity (Figure 6. 4). The formation of pores can be explained by the difference in molar volume between CaO (16.9 cm³g⁻¹) and Ca(OH)₂ (33.1 cm³g⁻¹). The difference in molar volume can also explain the cracks which has been observed in hydrated Ca-based sorbents.²⁸² The BET surface area of the Ca(OH)₂ was 24.9 m²g⁻¹. This is higher than the surface area of reagent grade Ca(OH)₂ (9.5-10 m²g⁻¹) which has been reported previously.^{272,283} The result is however in good agreement with that reported by Chew et al.²⁷⁸ on Ca(OH)₂ (28.5. m²g⁻¹). The hydration had increased the surface area 10 times and the increase in surface area and porosity due to hydration is in agreement with the literature.^{42,46,47}

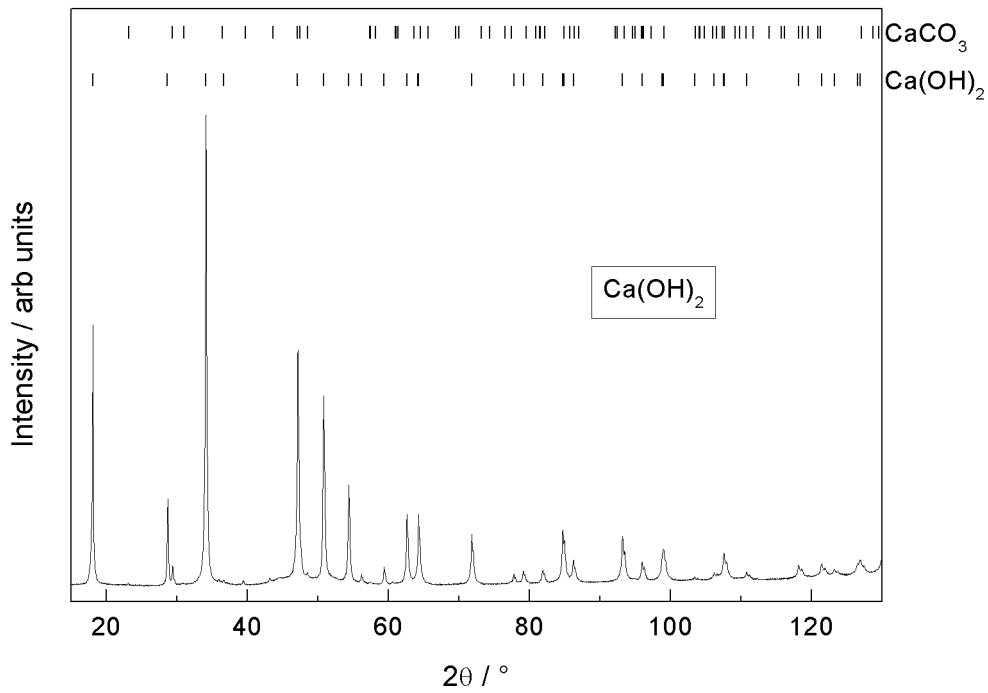


Figure 6. 3. XRD spectrum between 2θ 15-130 ° for $\text{Ca}(\text{OH})_2$. Vertical lines show the expected positions of diffraction peaks for CaCO_3 and $\text{Ca}(\text{OH})_2$.

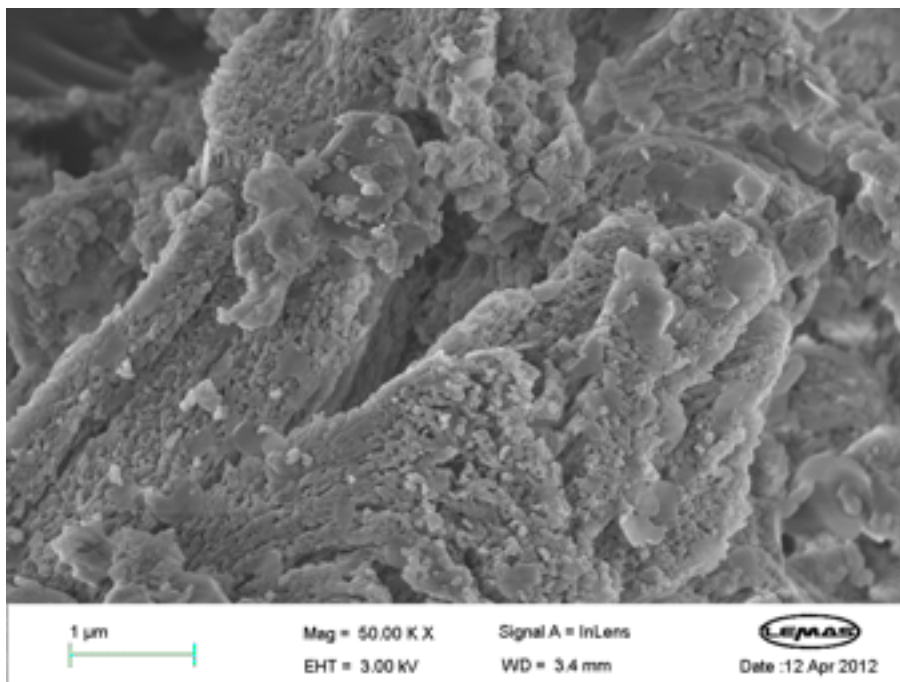


Figure 6. 4. SEM image of $\text{Ca}(\text{OH})_2$ at 50000X magnification.

6.4.1.3 CAO DERIVED FROM $\text{Ca}(\text{OH})_2$

Decomposition of the $\text{Ca}(\text{OH})_2$ (at 700 °C in N_2 according to Section 2.4) recreated the CaO phase and simultaneously decomposed the CaCO_3 phase such that the sorbent regained its

original composition, i.e. it contained a CaO phase and a Ca(OH)₂ as a result of the CaO being hygroscopic (Figure 6. 5). The surface area had increased further to 61.1 m²g⁻¹. Hydration followed by decomposition has previously been shown to increase surface area of Ca-based sorbents and so the results are in agreement with the literature.^{46,47} the morphology became more irregular due to the decomposition and many small grains were visible at 50K X magnification (Figure 6. 6).

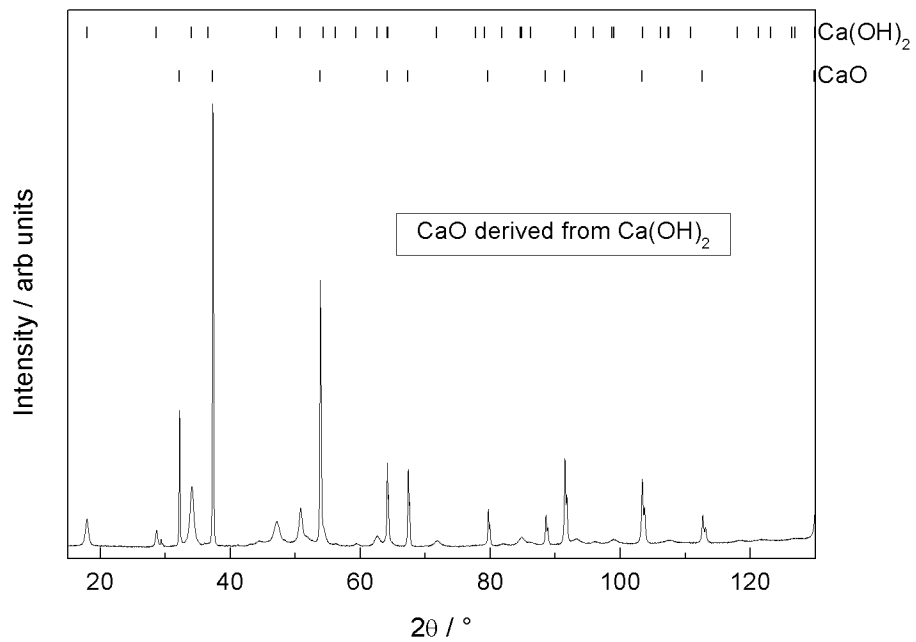


Figure 6. 5. XRD spectrum between 2θ 15-130 ° for CaO derived from Ca(OH)₂. Vertical lines show the expected positions of diffraction peaks for CaO and Ca(OH)₂.

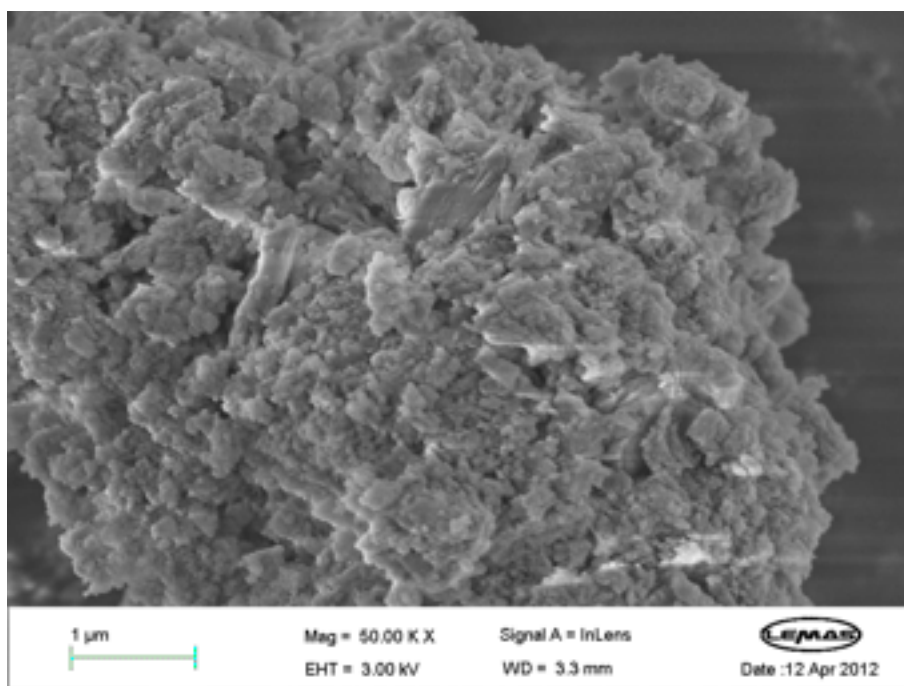


Figure 6. 6. SEM image of CaO derived from $\text{Ca}(\text{OH})_2$ at 5000X magnification.

The CaO powder had insignificant porosity and hydration (formation of $\text{Ca}(\text{OH})_2$) caused an increase in pore volume with the largest volume to be found in pores with a diameter of 30 nm (Figure 6. 7). This was expected on the same grounds as the increase in surface area was expected and the increased porosity was attributed to the difference in molar volume between CaO and $\text{Ca}(\text{OH})_2$ (see Section 6.11.1.2). Reduction in pore volume in pores with a diameter below 100 nm has been reported to correlate with capacity loss over multiple cycles¹³⁵ and so the regeneration of capture capacity from hydration can be attributed to creation of pores. Decomposition of the $\text{Ca}(\text{OH})_2$ back to CaO (at 700 °C in N_2 according to Section 2.4) increased the pore volume further as well as creating a bimodal pore size distribution through a significant increase in the volume of pores with a diameter of about 10 nm. The largest volume after decomposition was in pores with a diameter of 50 nm. Donat et al.⁴⁸ reported that calcination of CaCO_3 in the presence of steam promotes the formation of pores with a diameter of 50 nm which remains over multiple carbonation and calcination cycles. Hence the results presented here pointed to a similarity between the behaviour of hydrated Ca-based sorbents ($\text{Ca}(\text{OH})_2$) and Ca-based sorbents in the presence of steam. One explanation for this could be formation of $\text{Ca}(\text{OH})_2$ but Donat et al. carried out calcination at 900 °C with 20% steam and under these conditions $\text{Ca}(\text{OH})_2$ is not thermodynamically stable.²⁶² Donat et al. did not report the formation of pores with a diameter of 10 nm as was observed here. This was attributed to a higher degree of sintering as Donat et al. used both a higher temperature and steam, both of which promote sintering. Note that only pores with a diameter of up to 100 nm was investigated here, thus

limiting the discussion. Hg porosimetry allows for investigation of larger pores but this was not carried out due to limitations in access to laboratory equipment.

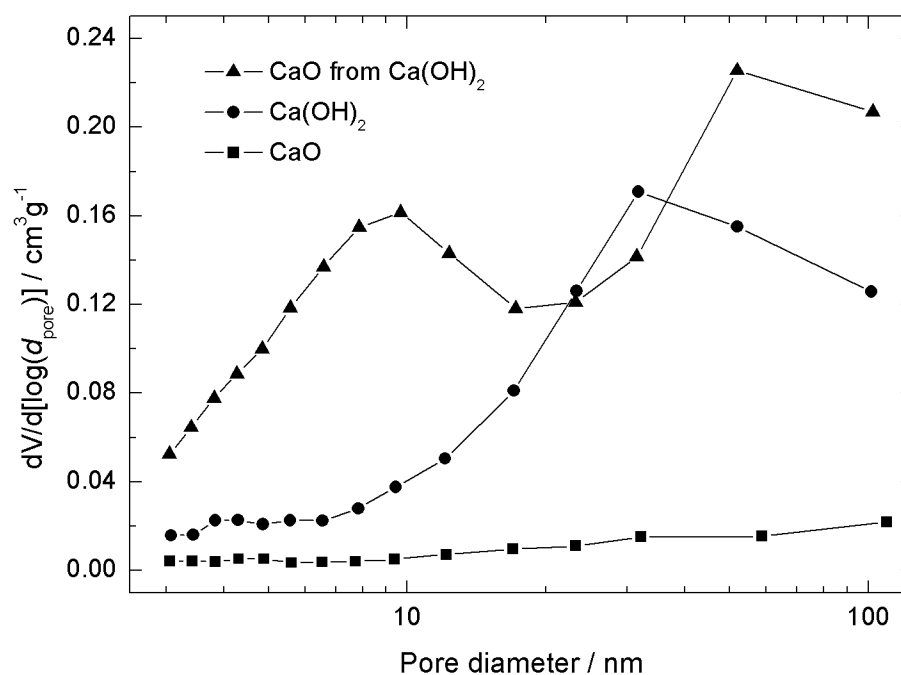


Figure 6. 7. Pore size distribution of the CaO sorbents.

6.4.1.4 CAO DERIVED FROM CA-D-GLUCONATE

Liu et al.²⁷² decomposed Ca-D-gluconate ($\text{Ca}[\text{HOCH}_2(\text{CHOH})_4\text{CO}_2]_2$) by heating at 900 °C for 30 min after a temperature ramp of 30 °C min⁻¹. TGA analysis was carried out using the same temperature program as used to Liu et al.²⁷² to study the decomposition mechanism. The results are given in mass% of the sample mass at the start (Figure 6. 8). Complete decomposition to CaO would result in a mass loss of 87%. A dotted line in Figure 6. 8 marks 13 mass%, thus indicating complete decomposition. The Ca-D-gluconate decomposed completely well within the 30 min hold. The decomposition proceeded via 3 distinct steps. The large mass loss was accompanied by a large reduction in sample volume. Therefore the volume of evolved gases during the decomposition was also high. Therefore, the same temperature ramp could not be applied when CaO from Ca-D-gluconate was prepared for further experiments. Instead a temperature ramp of 10 °C min⁻¹ up to 900 °C was used after which the temperature was held for 30 min. A Carbolite AAF 1100 furnace was used. XRD and SEM imaging was used to study the Ca-D-gluconate before decomposition as well the resulting CaO. The BET surface area of the resulting CaO was also measured.

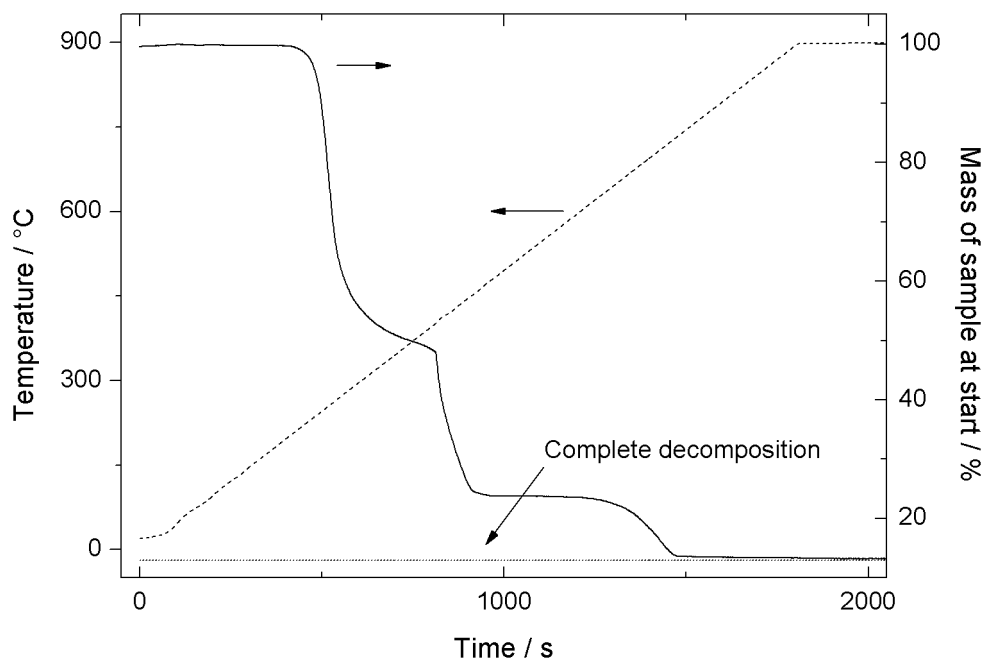


Figure 6. 8. Decomposition of Ca-D-gluconate.

Ca-D-gluconate consisted of multiple phases with the majority of the peaks in the 2θ 15-70 ° range and only a few, low intensity peaks at 2θ angles above 70 ° (Figure 6. 9). Therefore only the 2θ 15-70 ° range is shown in Figure 6. 9. There was no crystallographic information on Ca-D-gluconate on the ICDD data base which the data could be related to. Identification of separate phases of the Ca-D-gluconate was possible by combining crystallographic data from other materials. However, since the identity of the material was known such identification was deemed unnecessary as well as out of the scope of the work. Decomposition caused a significant change in the XRD spectrum (Figure 6. 10). The XRD data of the CaO derived from Ca-D-gluconate is shown here with 2θ 15-70 ° to enable direct comparison with Ca-D-gluconate prior to decomposition. The resulting sorbent contained a CaO phase and a $\text{Ca}(\text{OH})_2$ which could be identified as above. It could be concluded that the decomposition had resulted in complete conversion to CaO as the $\text{Ca}(\text{OH})_2$ phase could be explained by the hygroscopic nature of CaO.

Morphologically, the Ca-D-gluconate comprised large particles with smooth and flat surfaces prior to decomposition (Figure 6. 11). Decomposition caused the morphology to change and the resulting morphology of the CaO derived from Ca-D-gluconate could be described as smaller clusters of pointed plates with flat surfaces and sharp edges (Figure 6. 12).

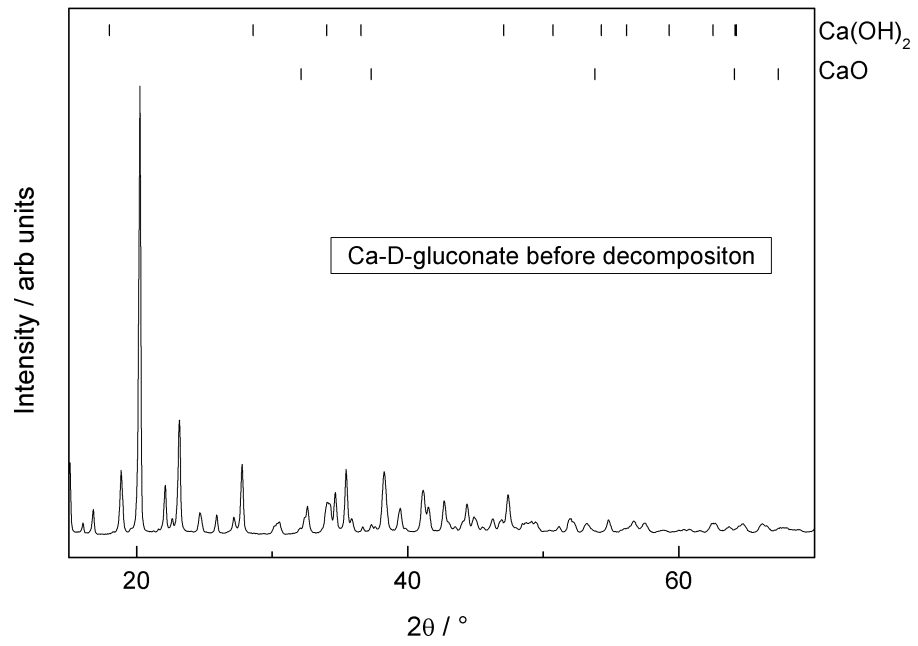


Figure 6. 9. XRD spectra of Ca-D-gluconate before decomposition.

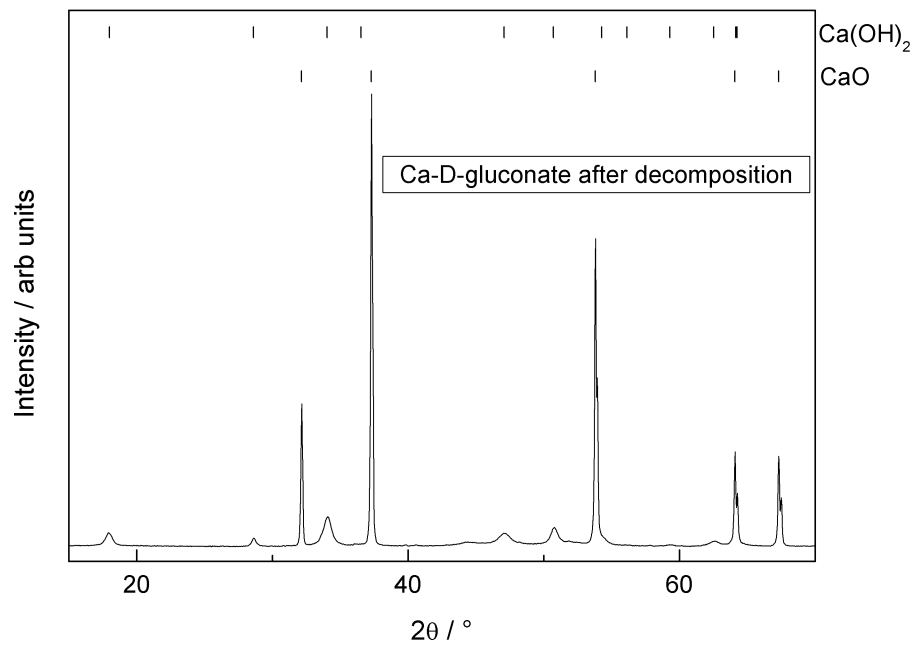


Figure 6. 10. XRD spectrum of Ca-D-gluconate after decomposition.

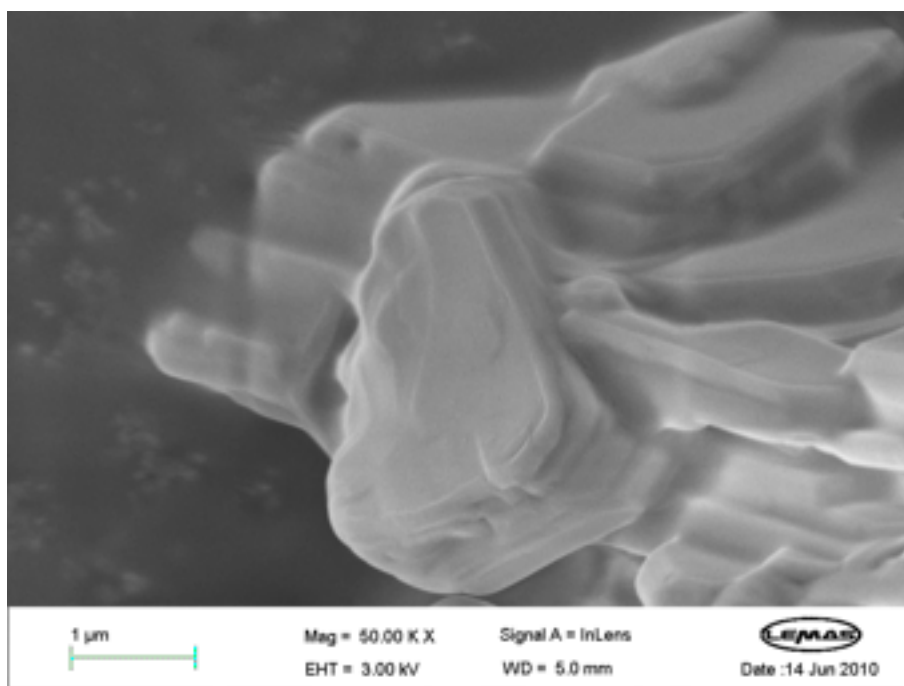


Figure 6. 11. SEM image of Ca-D-gluconate at 50000X magnification.

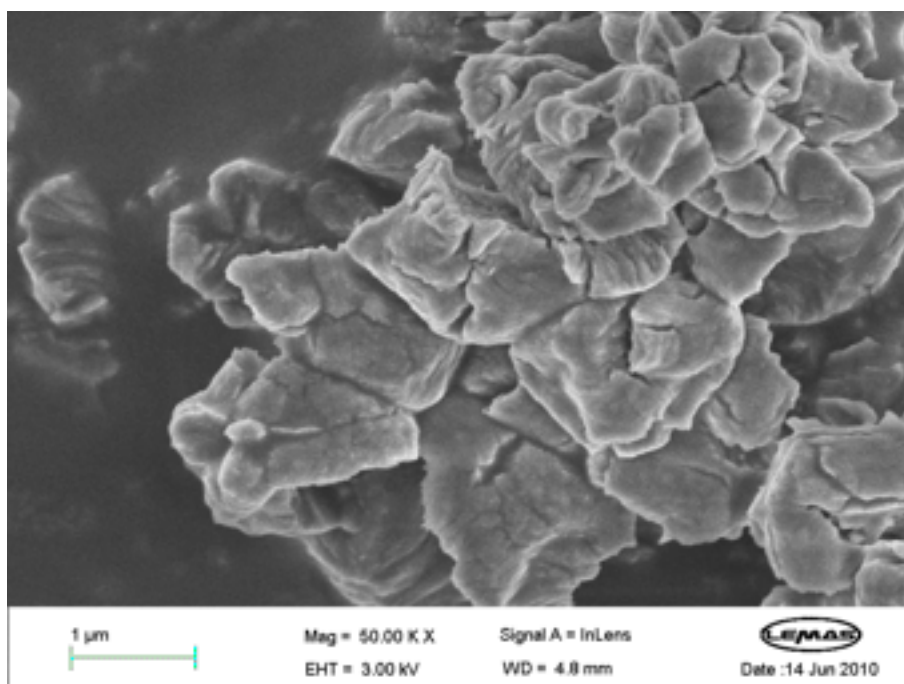


Figure 6. 12. SEM image CaO derived from decomposition of Ca-D-gluconate at 50000X magnification.

The BET surface area of the CaO derived from Ca-D-gluconate was $2.5 \text{ m}^2\text{g}^{-1}$ and hence very similar to the BET surface area of the CaO powder ($2.9 \text{ m}^2\text{g}^{-1}$). Like its surface area, the

porosity (with regards to pores smaller than 100 nm) of the CaO derived from Ca-D-gluconate was very low (Figure 6. 13). In fact its porosity was lower than that of the CaO powder (shown in Figure 6. 13 for comparison). This was in agreement with the SEM data which did not reveal any porosity (Figure 6. 12).

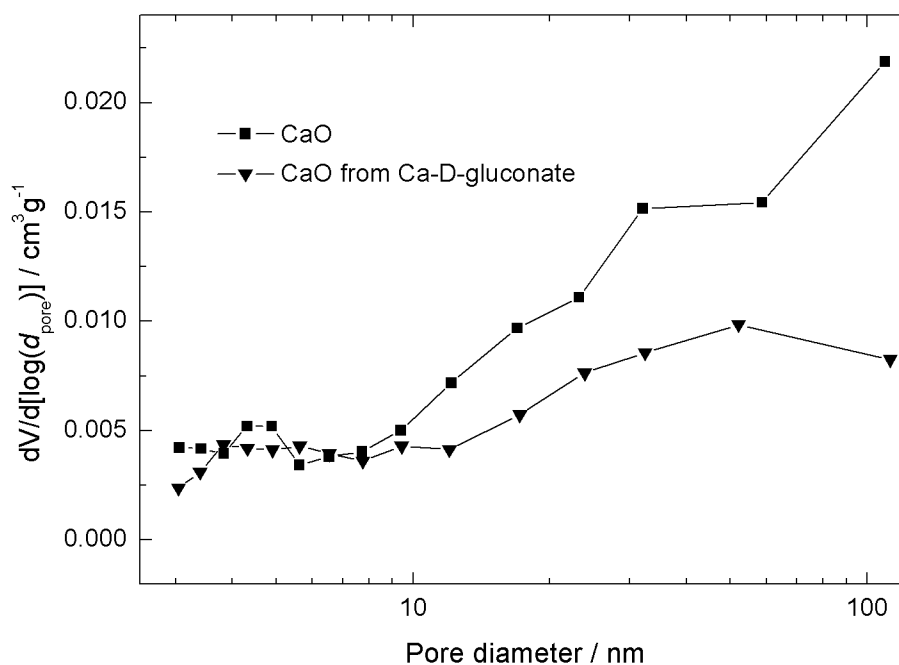


Figure 6. 13. Pore size distribution of CaO derived from Ca-D-gluconate and of CaO powder.

6.4.2 CA₁₂AL₁₄O₃₃ SORBENTS

6.4.2.1 CAO/CA₁₂AL₁₄O₃₃

The CaO/CA₁₂AL₁₄O₃₃ sorbent contained CaO, Ca(OH)₂ and CA₁₂AL₁₄O₃₃ (Figure 6. 14). It could therefore be confirmed that a CA₁₂AL₁₄O₃₃ phase had formed during the sorbent manufacturing process which is in agreement with previous work.^{53,54} Many of the peaks were irregular which was attributed to peak overlap. The CA₁₂AL₁₄O₃₃ phase produces 144 peaks in the 2θ range 15-130 ° which results in a high risk of peak overlap in the CaO/CA₁₂AL₁₄O₃₃ sorbent. A longer scanning time would improve the quality of the XRD data. Removal of the Ca(OH)₂ phase through decomposition at high temperature would also be beneficial. Improvement of the XRD data is pursued in Chapter 7. The sorbent consisted of clusters of irregular grains of varying sizes without the clearly visible pores which were observed in Ca(OH)₂ (Figure 6. 15). This was attributed to sintering during the heating phases of the sorbent preparation (in particular the final heating phase at 900 °C). A similar change in morphology from CaO starting material to finished CaO/ CA₁₂AL₁₄O₃₃ sorbent was observed by Li et al.⁵³

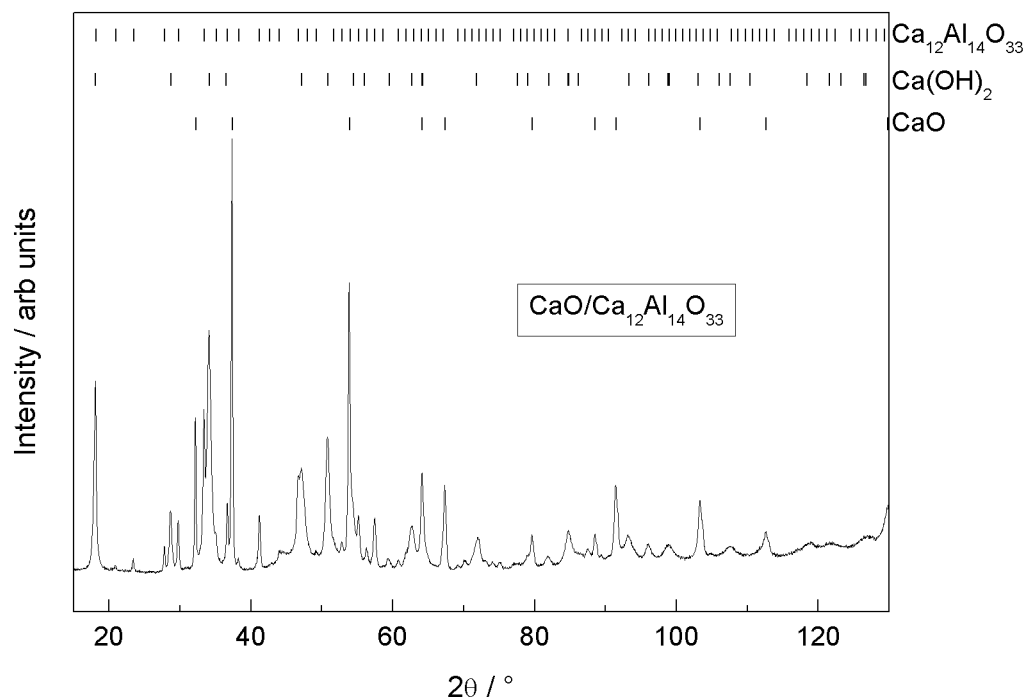


Figure 6. 14. XRD spectrum between 2θ 15-130 °C for $\text{CaO}/\text{Ca}_{12}\text{Al}_{14}\text{O}_{33}$. Vertical lines show the expected positions of diffraction peaks for CaO , $\text{Ca}(\text{OH})_2$ and $\text{Ca}_{12}\text{Al}_{14}\text{O}_{33}$.

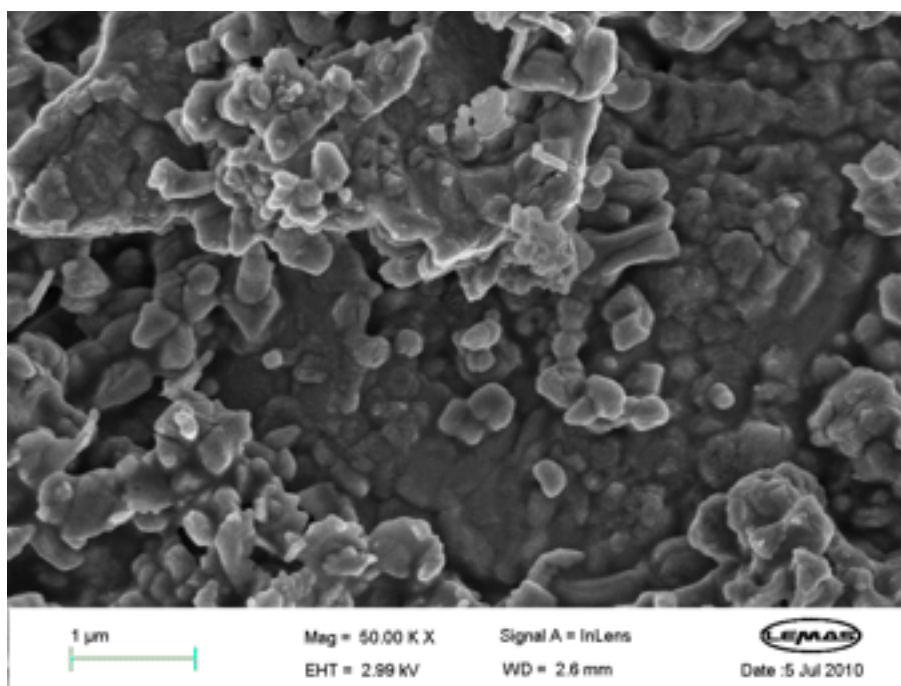


Figure 6. 15. SEM image of $\text{CaO}/\text{Ca}_{12}\text{Al}_{14}\text{O}_{33}$ at 50000X magnification.

The BET surface area was $9.1 \text{ m}^2\text{g}^{-1}$. A wide range of surface area from $2.0\text{-}18.5 \text{ m}^2\text{g}^{-1}$ has been reported for $\text{CaO}/\text{Ca}_{12}\text{Al}_{14}\text{O}_{33}$ sorbents.^{54,136,275} The surface area is dependent on the

content of CaO and Ca₁₂Al₁₄O₃₃ as well as on the temperature used for the final heating step of the preparation procedure.^{54,136} A low content of Ca₁₂Al₁₄O₃₃ and a low heating temperature resulted in a high surface area. However, a low content of Ca₁₂Al₁₄O₃₃ has also been shown to reduce mechanical strength and increase CO₂ capture capacity.^{136,275}

6.4.2.2 CaO-D/Ca₁₂Al₁₄O₃₃

The XRD data of the CaO-D/Ca₁₂Al₁₄O₃₃ sorbent was very similar to the XRD data which was collected from the CaO/Ca₁₂Al₁₄O₃₃ sorbent (Figure 6. 16). Three major phases were identified, namely CaO, Ca(OH)₂ and Ca₁₂Al₁₄O₃₃, hence a Ca₁₂Al₁₄O₃₃ phase had been created during the sorbent preparation just like in the case of the CaO/Ca₁₂Al₁₄O₃₃ sorbent. It was concluded that the use of CaO powder or CaO derived from Ca-D-gluconate made no difference to the XRD spectra of the resulting sorbent. The BET surface area of the CaO-D/Ca₁₂Al₁₄O₃₃ sorbent was 7.3 m²g⁻¹ which was close to the surface area of the CaO/Ca₁₂Al₁₄O₃₃ sorbent (9.1 m²g⁻¹). This was expected as the CaO powder and the CaO derived from Ca-D-gluconate had similar BET surface area. The morphology of the CaO-D/Ca₁₂Al₁₄O₃₃ was however separate from that of the corresponding sorbent based on CaO powder (Figure 6. 17). Most notably the edges and surfaces of the sorbent was smoother which could be related back to the differences in morphology between the CaO powder and the CaO derived from Ca-D-gluconate.

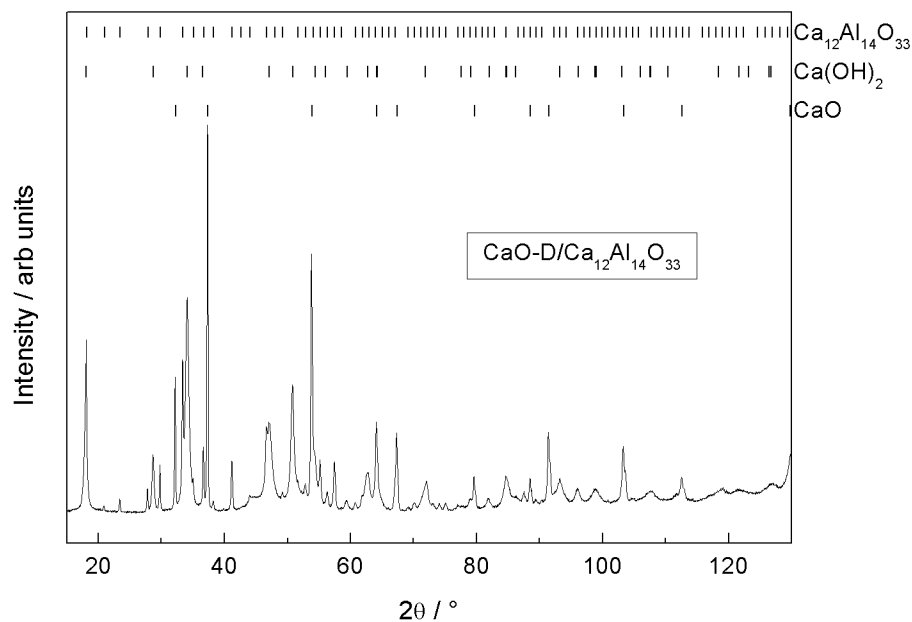


Figure 6. 16. XRD spectrum between 2θ 15-130 °C for CaO-D/Ca₁₂Al₁₄O₃₃. Vertical lines show the expected positions of diffraction peaks for CaO, Ca(OH)₂ and Ca₁₂Al₁₄O₃₃.

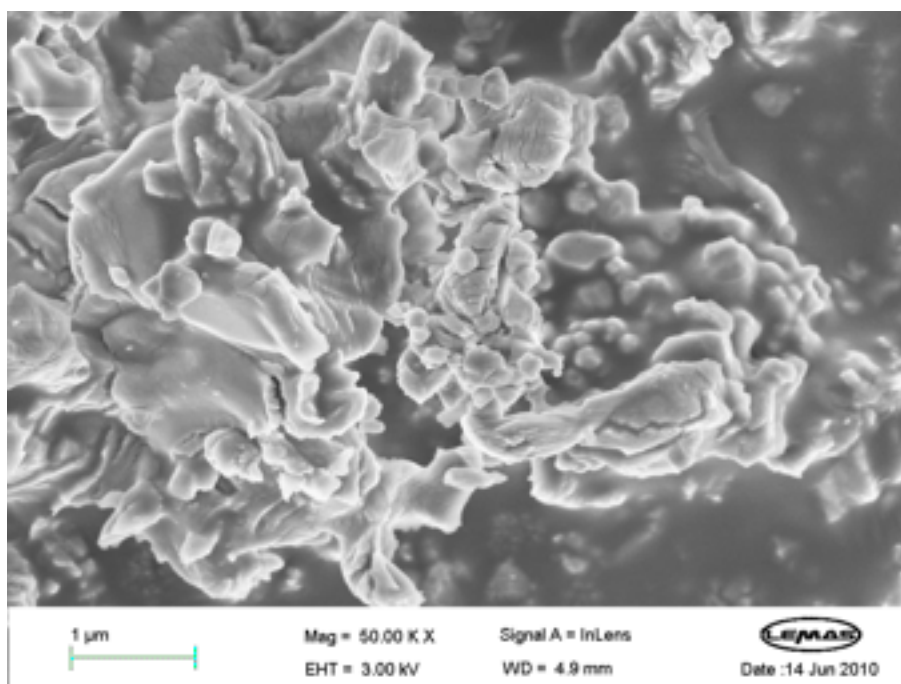


Figure 6. 17. SEM image of CaO-D/Ca₁₂Al₁₄O₃₃ at 50000X magnification.

6.4.2.3 CAO/NO AL

CaO/No Al consisted of a CaO phase and a Ca(OH)₂ phase (Figure 6. 18). This was expected as no other elements had been added in the process. The final step of the sorbent preparation procedure was a high temperature calcination step where all Ca(OH)₂ formed during the previous hydrations steps was calcined to CaO. As noted earlier, Ca(OH)₂ forms when CaO is in contact with air. The BET surface area of the sorbent was 12.8 m²g⁻¹ i.e. 40% higher than the CaO/Ca₁₂Al₁₄O₃₃ sorbent. One reasonable explanation for the difference could be the large size of Ca₁₂Al₁₄O₃₃ compared to CaO and Ca(OH)₂. The higher surface area compared to the CaO powder can be attributed to the hydration processes involved in the preparation of CaO/Ca₁₂Al₁₄O₃₃. However, the surface area of the final sorbent is lower than that which had only been subjected to the initial mixing phase, i.e. the Ca(OH)₂ sorbent investigated here (Section 6.4.1.2). This can be attributed to sintering during the high temperature treatments involved in the final stage of the preparation.

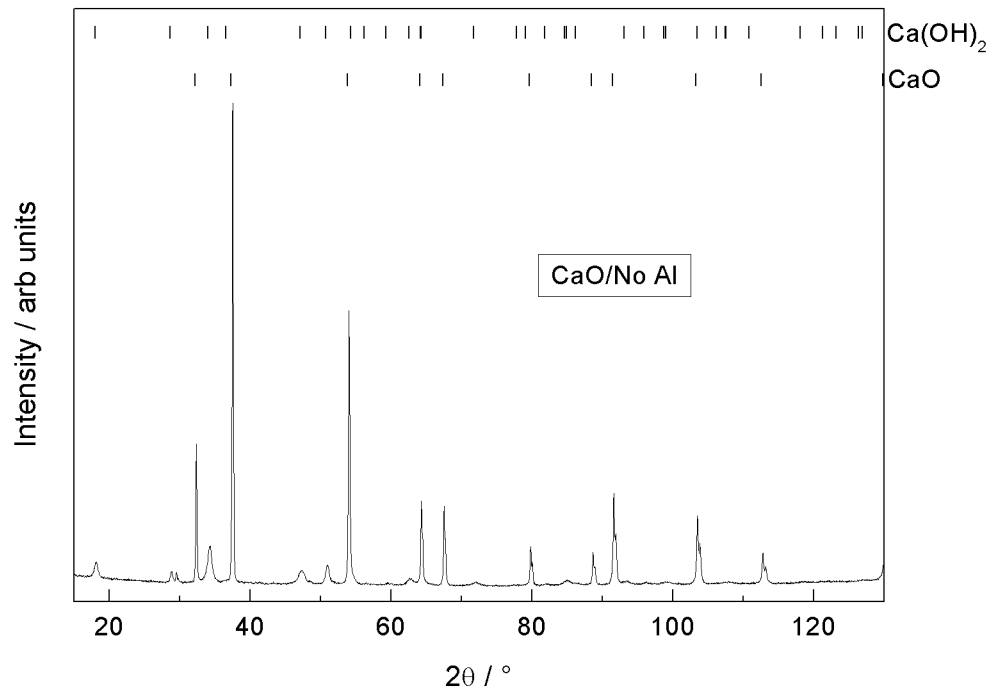


Figure 6. 18. XRD spectrum between 2 15-130 °C for CaO/No Al. Vertical lines show the expected positions of diffraction peaks for CaO and Ca(OH)₂.

The morphology comprised clusters of spherical particles which were both smoother and smaller than those observed for the CaO/Ca₁₂Al₁₄O₃₃ and CaO-D/Ca₁₂Al₁₄O₃₃ sorbents (Figure 6. 19). The differences in morphology explained the differences in surface area as small particles have a larger surface area than large ones (assuming all else being equal). The differences also supported the suggestion that the higher surface area of the CaO/No Al sorbent could be explained by smaller crystallite sizes.

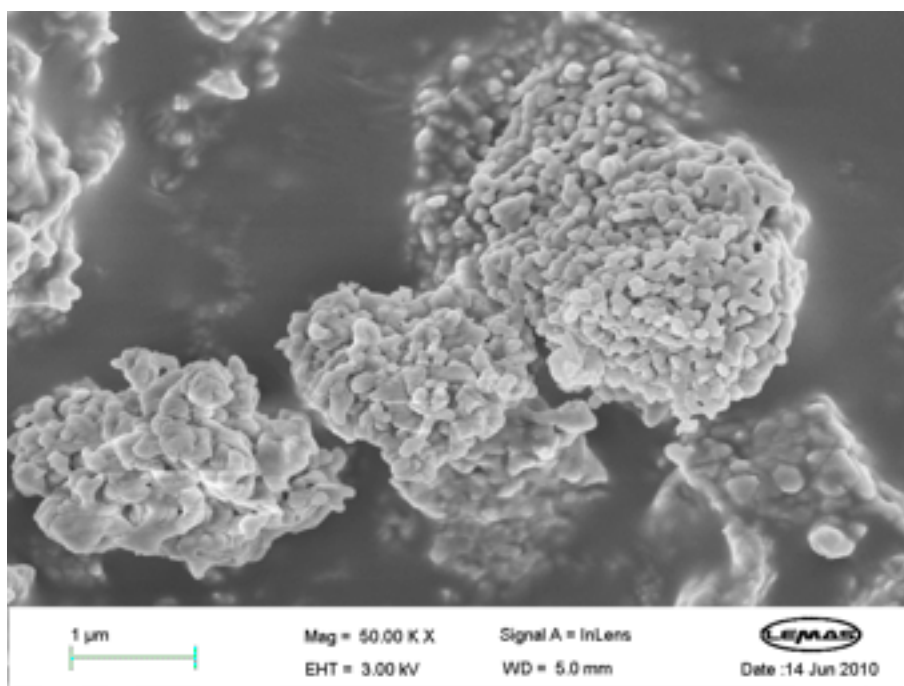


Figure 6. 19. SEM image of CaO/No Al at 50000X magnification.

The $\text{CaO}/\text{Ca}_{12}\text{Al}_{14}\text{O}_{33}$ and $\text{CaO-D}/\text{Ca}_{12}\text{Al}_{14}\text{O}_{33}$ sorbents consist mainly of pores in the upper mesopore range and above, which is in agreement with the literature (Figure 6. 20).^{136,139} The formation of a $\text{Ca}_{12}\text{Al}_{14}\text{O}_{33}$ phase reduced the amount of pores with diameters of 50-100 nm range. Based on the pore size distribution data, it was concluded that the additional surface area of the CaO/No Al sorbent could be attributed to a larger number of pores in the 50-100 nm size range. Note that the additional surface area could also be due to a larger number of pores in size ranges above 100 nm, but this could not be confirmed from that data presented here. The data porosity data was in agreement with the SEM images which showed some porosity in the CaO/No Al sorbent but not in the $\text{Ca}_{12}\text{Al}_{14}\text{O}_{33}$ containing sorbents.

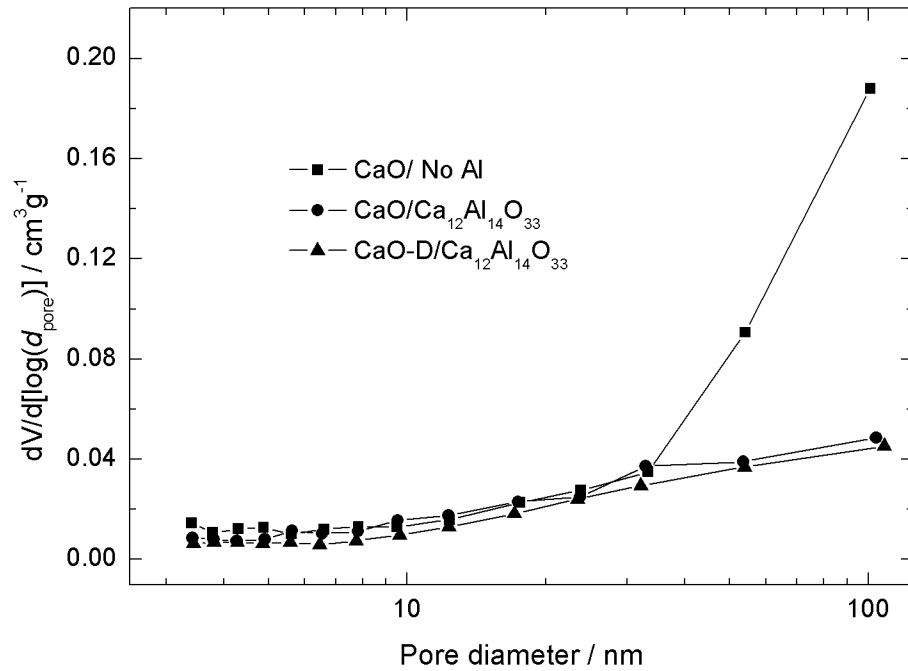


Figure 6. 20.Pore size distribution of the Ca₁₂Al₁₄O₃₃ sorbents.

6.5 TGA USING POWDERS

TGA analysis was carried out using the equipment described in Chapter 2, Section 2.6. First, the carbonation reaction was investigated and then the behaviour of the different sorbents over multiple cycles of carbonation and calcination. For calculation of the conversion of CaO to CaCO₃ during carbonation, it was assumed that any difference in mass at a given time from the starting mass was due solely to the formation of CaCO₃ via the CaO carbonation reaction (Reaction 3. 1).

TGA data is presented in percentage conversion from CaO to CaCO₃ on a molar basis (X) which is common in the literature.^{40,144,146} The percentage conversion at any given time (t) was calculated from the TGA data according to Equation 6. 1. Note that the stoichiometric ratio of CO₂ and CaCO₃ in Reaction 3. 1 is 1:1 Also note that for CaO, CaO/No Al and CaO from CaD, m_i and m_{CaO_i} are the same because the sample contained pure CaO at the start of the experiment.

$$X (\%) = \left(\frac{\frac{m_t - m_i}{W_{CO_2}}}{\frac{m_{CaO_i}}{W_{CaO}}} \right) \times 100$$

Equation 6. 1. Definition of carbonation (X). m_i = initial sample mass, m_t mass at time t, W = molar mass and m_{CaO_i} = initial mass of CaO in the sample.

During carbonation of Ca(OH)_2 , three reactions are possible, direct conversion to CaCO_3 (Reaction 5. 7), or decomposition of Ca(OH)_2 to CaO (Reaction 6. 1) (i.e. the reverse of CaO hydration (Reaction 5. 6)) followed by conversion of that CaO to CaCO_3 via Reaction 3. 1. All three reactions result in changes in sample mass but with the TGA system used here, a change in mass from 25 °C could not be used to accurately determine conversion at any given time during the carbonation experiment. This is discussed in further detail in Chapter 7 where an attempt to accurately determine conversion in a Ca(OH)_2 sample is carried out using a different temperature program. However for this chapter TGA investigation of Ca(OH)_2 is not carried out. Instead CaO was derived from Ca(OH)_2 by decomposition in the TGA setup prior to the carbonation and cycling experiments and the results were compared to those of CaO powder and CaO derived from Ca-D-gluconate . This enabled investigation of the effect of hydration followed by decomposition which has been suggested as a regeneration method for Ca -based sorbents.^{46,47}



Reaction 6. 1. Decomposition of Ca(OH)_2 to CaO .

6.5.1 TGA CARBONATION

Carbonation was carried out in pure CO_2 . The temperature was increased at $10 \text{ }^\circ\text{C min}^{-1}$ to $650 \text{ }^\circ\text{C}$ and was kept for 30 min (Figure 6. 21). The carbonation temperature was chosen as it is in the middle of the carbonation temperature range for CaO and because it has been suggested for post combustion CO_2 capture.^{31,284} $650 \text{ }^\circ\text{C}$ is also a useful temperature for SESR of glycerol and methane.^{22,23,199,218,275} Previous TGA work has been carried out with carbonation at $650 \text{ }^\circ\text{C}$ for 5-30 min in 10-15% CO_2 .^{43,143,150,272,274,285} Hence in relation to the literature the carbonation time used here is long and the CO_2 partial pressure is very high. The aim of this was to achieve a carbonation as close to the maximum capacity as possible. Using conditions less suited for CO_2 capture risks having some sorbents reaching capture capacities that are far from their maximum capacity while others are close to their maximum capacity. Therefore pure CO_2 was used to attempt to enable a fair comparison between samples. A blank run was carried out to account for buoyancy effects. The results of the blank run revealed an increase in mass reading with increased temperature which highlighted the importance of the practice of carrying out a blank run (Figure 6. 22).

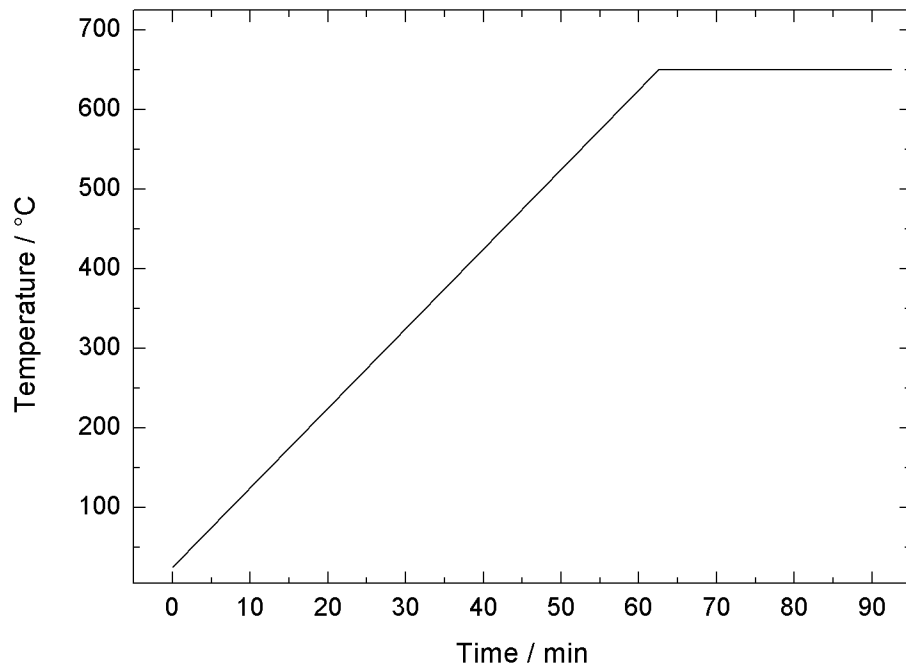


Figure 6. 21. Carbonation TGA temperature program.

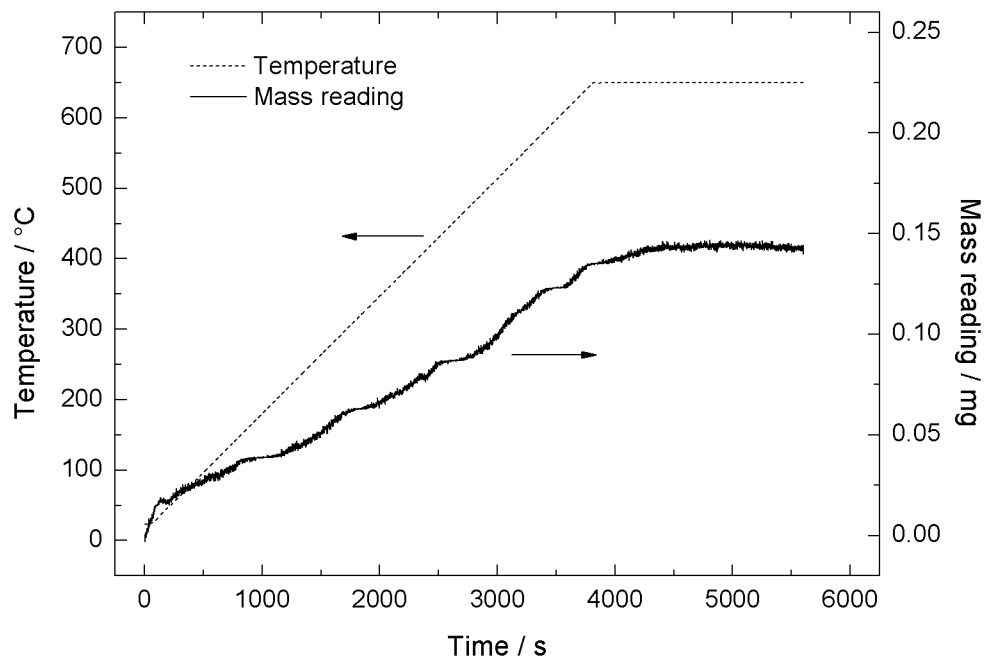


Figure 6. 22. Data collected during the blank TGA run.

A Ca(OH)₂ phase had been identified in all sorbents (Section 6.4) which would prevent accurate measurement of the conversion due to the occurrence of Reaction 5. 7, Reaction 6. 1 and Reaction 3. 1. Therefore the Ca(OH)₂ phase was removed in the TGA setup via decomposition directly prior to the carbonation experiment decomposition by heating the sample to 650 °C in pure N₂. A ramp rate of 25 °C min⁻¹ and a hold time of 10 min at 650 °C

were used. The results from the decomposition of the CaO powder (known to contain hydroxide as per XRD analysis) are shown in Figure 6. 23, as representative of the pretreatment undergone by all the Ca-based sorbents tested. Decomposition as evidenced by a loss in sample mass commenced at around 400 °C. Ca(OH)₂ has previously been shown to readily decompose at 500 °C.²⁸⁶ When 650 °C was reached, decomposition was complete. Assuming all mass loss was due to the removal of water, the amount of Ca(OH)₂ in the sample prior to decomposition was calculated to be 39 wt%. However, a second mass loss observed at 500 °C indicated the presence of CaCO₃. It is possible that small amounts of CaCO₃ had formed from the Ca(OH)₂ in the sample during handling.

The CaO derived from Ca(OH)₂ was prepared in the TGA setup directly prior to carbonation by heating Ca(OH)₂ to 700 °C in N₂ until weight loss was no longer observed. The sample was then cooled to room temperature before the start of the carbonation experiment. N₂ was used to ensure decomposition of the Ca(OH)₂. The use of air for example would risk reformation of Ca(OH)₂ impurities as the temperature was returned to room temperature prior to carbonation.

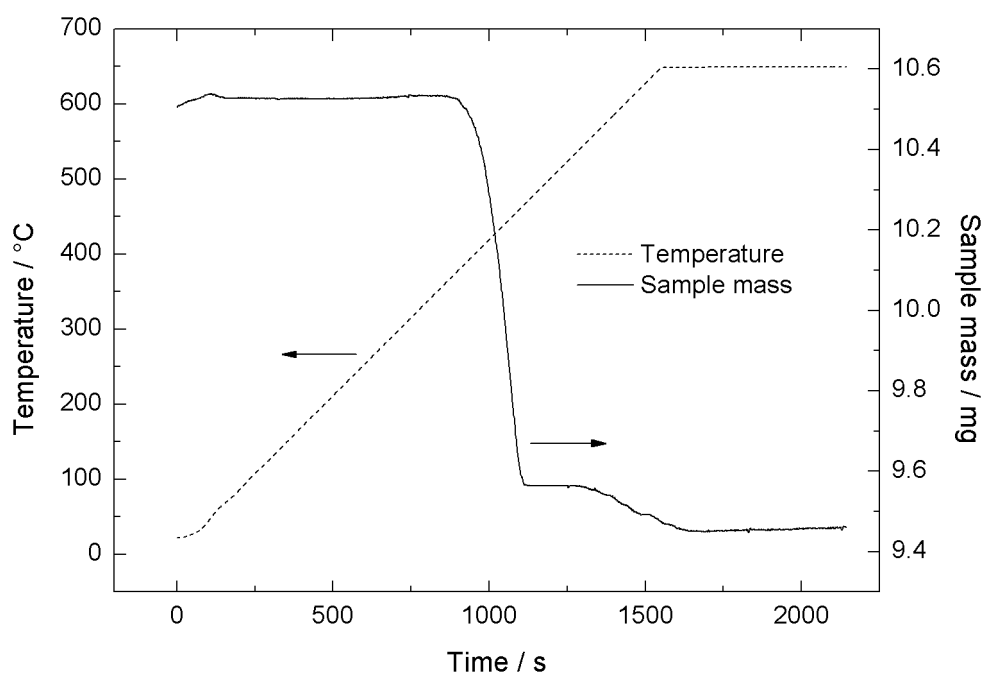


Figure 6. 23. Data collected during the decomposition of the Ca(OH)₂ phase from the CaO powder.

6.5.1.1 CARBONATION OF CAO SORBENTS

The sorbents containing only CaO were investigated first, i.e. the CaO powder, the CaO derived from Ca-D-glutamate and CaO derived from Ca(OH)₂. As the temperature was

increased, the rate of conversion over time was increased (Figure 6. 24, Figure 6. 25, Figure 6. 26). Therefore, the commonly observed carbonation curve with an initial high rate followed by a slow rate¹³⁴⁻¹³⁶ was not observed here. Instead an s-shaped curve was observed where the conversion rate was first increased and then decreased. The main reason for this was the fact that the temperature program used here began at a low temperature (during which carbonation occurs at a lower rate). The final conversion was lowest for the CaO powder and highest for the CaO derived from Ca(OH)₂. This was attributed to the differences in surface area between the samples, where CaO derived from Ca(OH)₂ had the highest surface area and the CaO powder the lowest surface area. The correlation between surface area and conversion to CaCO₃ in Ca-based sorbents has been well established.^{133,275} In the temperature range 300-350 °C all data sets displayed an abrupt reduction in conversion rate, which was most pronounced for the CaO powder and least pronounced in the CaO derived from Ca(OH)₂. This could be attributed to small amounts of Ca(OH)₂ formed when the sample was cooled down after decomposition. Ca(OH)₂ is more reactive towards CO₂ than CaO^{49,287} and the abrupt reduction in conversion rate is likely to be due to complete conversion of the existing Ca(OH)₂ leaving less reactive CaO.

The CaO derived from Ca(OH)₂ displayed a clear reduction in conversion rate beginning at around 600 °C (Figure 6. 25). There was a reduction in the conversion rate in the other sorbents as well but it was less pronounced. The reaction between CaO and CO₂ (Reaction 3. 1) is characterized as an initial fast reaction controlled mechanism which is then switched to a slower diffusion controlled mechanism.¹³⁴⁻¹³⁶ Hence the observations were consistent with a faster shift between reaction and diffusion controlled conversion in the CaO derived from Ca(OH)₂ than the other CaO sorbents. It is also consistent with a longer diffusion dominated phase in CaO than in Ca(OH)₂. This indicated a mechanism in the CaO powder and in the CaO derived from Ca-D-glutamate which was diffusion dominated. This could be expected from their low surface area which reduces the time to complete surface coverage by a continuous CaCO₃ layer. The CaO derived from Ca(OH)₂ displayed the highest final conversion of 77.2% at the end of the 30 min hold at 650 °C. The corresponding conversion for the CaO powder and the CaO derived from Ca-D-gluconate were 21.4 and 27.4%. Hence there was a correlation between conversion and surface area which is in agreement with the literature.²⁷⁵

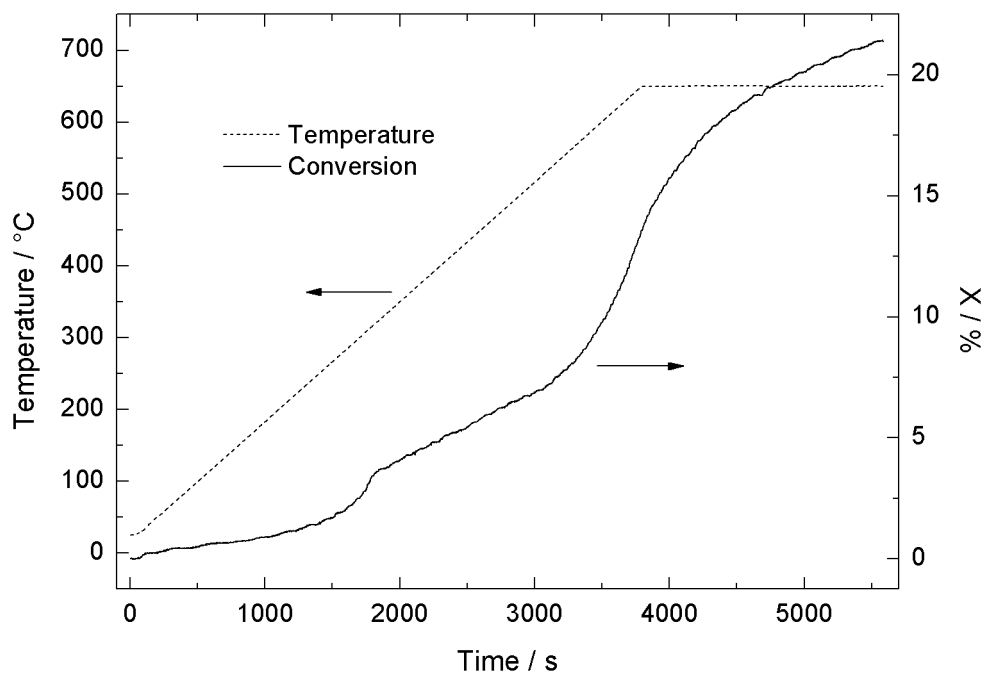


Figure 6. 24. Carbonation of CaO powder during TGA.

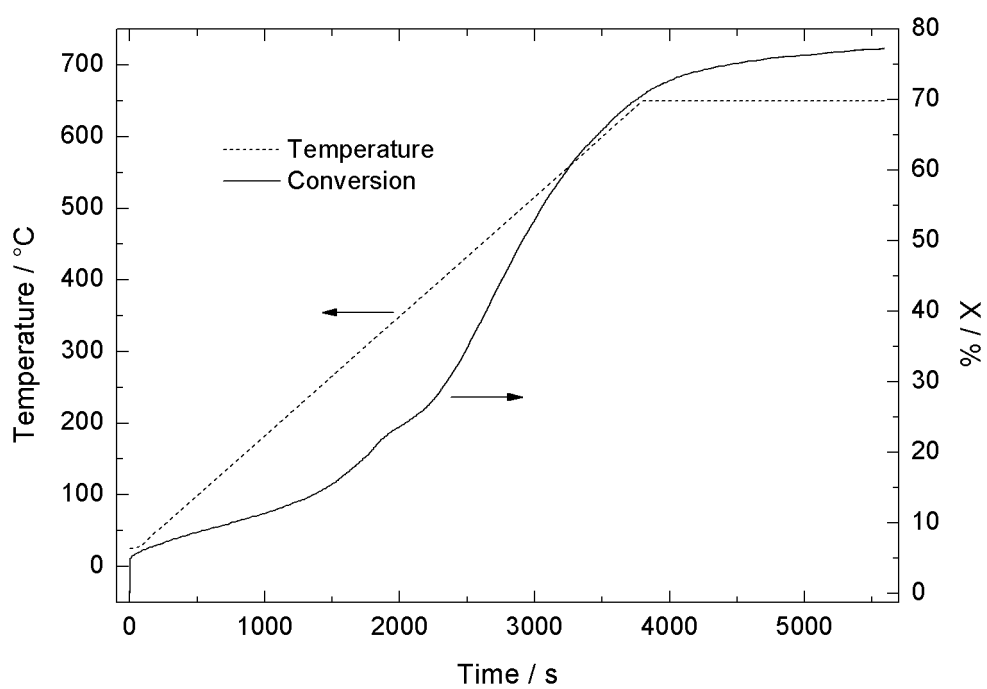


Figure 6. 25. Carbonation of CaO from Ca(OH)₂ during TGA.

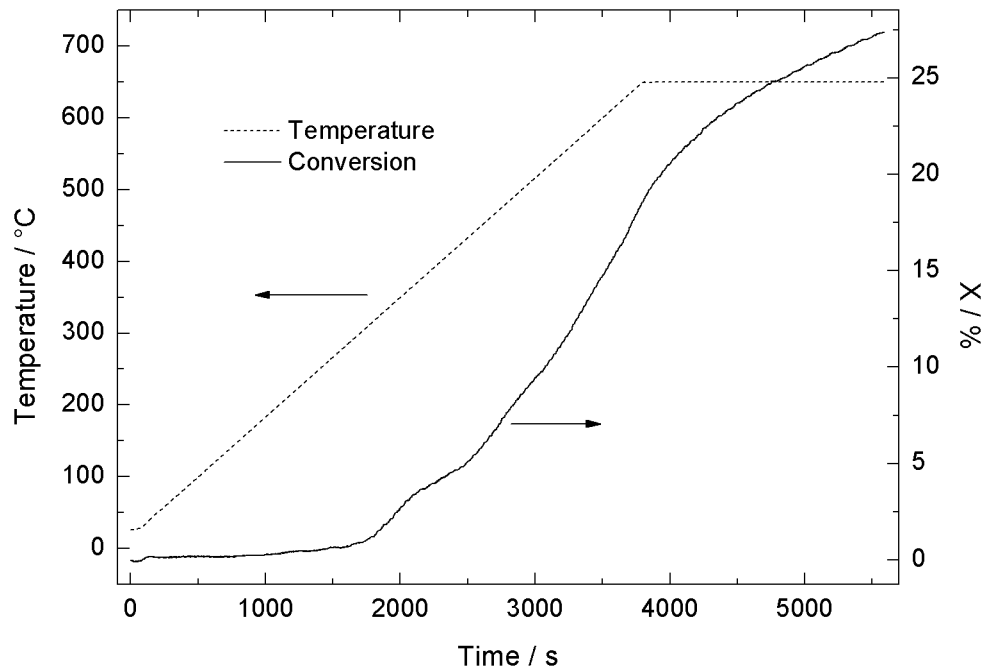


Figure 6. 26. Carbonation of CaO derived from Ca-D-gluconate during TGA.

6.5.1.2 CARBONATION OF $\text{Ca}_{12}\text{Al}_{14}\text{O}_{33}$ SORBENTS

The conversion curve for the $\text{CaO}/\text{Ca}_{12}\text{Al}_{14}\text{O}_{33}$ sorbent displayed the same s-shape as the CaO sorbents (Figure 6. 27). The final conversion was 59.9%, which was higher than the CaO precursor (i.e. the CaO powder) (21.4%). This was in agreement with Li et al.⁵³ The shape of the conversion curve showed that the inclusion of the $\text{Ca}_{12}\text{Al}_{14}\text{O}_{33}$ phase did not affect the mechanism of the reaction between CaO and CO₂. The CaO-D/ $\text{Ca}_{12}\text{Al}_{14}\text{O}_{33}$ sorbent displayed a very similar behaviour with only a slightly higher conversion (64.8%) (Figure 6. 28) just like the CaO derived from Ca-D-gluconate had displayed a slightly higher conversion than the CaO powder.

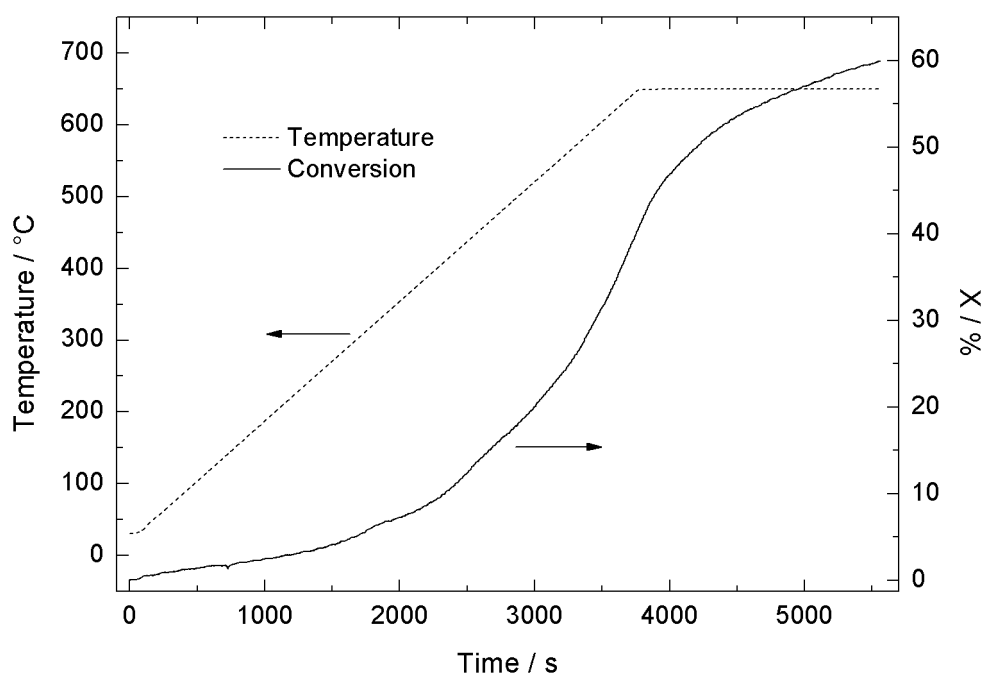


Figure 6. 27. Carbonation of $\text{CaO}/\text{Ca}_{12}\text{Al}_{14}\text{O}_{33}$ during TGA.

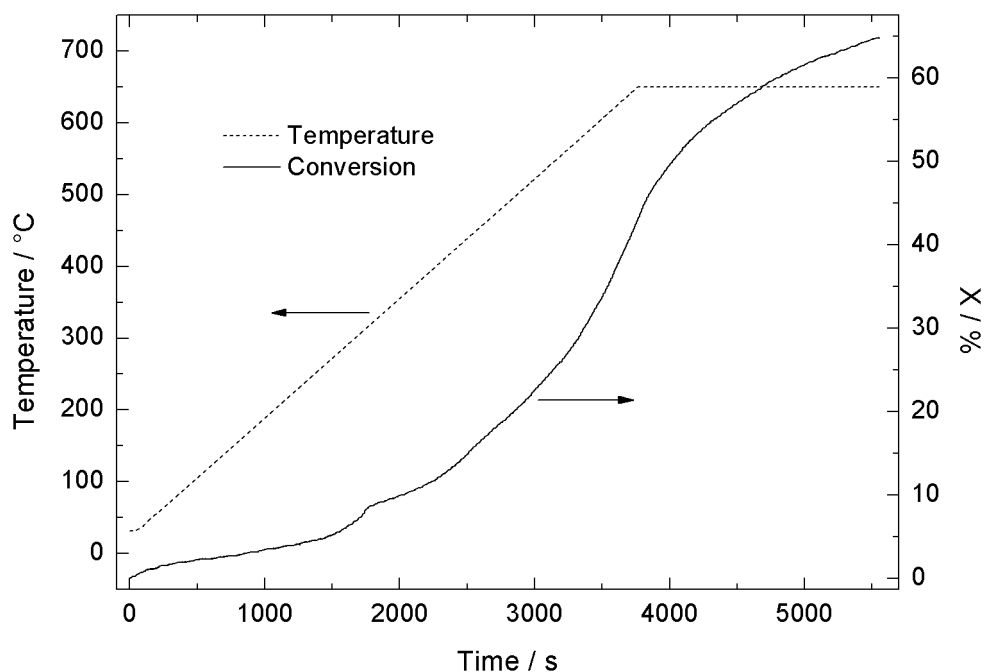


Figure 6. 28. Carbonation of $\text{CaO-D}/\text{Ca}_{12}\text{Al}_{14}\text{O}_{33}$ during TGA.

$\text{CaO}/\text{No Al}$ displayed a lower conversion than the corresponding sorbents containing a $\text{Ca}_{12}\text{Al}_{14}\text{O}_{33}$ phase (Figure 6. 29). Note that $\text{CaO}/\text{No Al}$ had a higher surface area than $\text{CaO}/\text{Ca}_{12}\text{Al}_{14}\text{O}_{33}$ and would be expected to reach a higher conversion, not lower. However, the $\text{CaO}/\text{No Al}$ sorbent consisted of pure CaO while the $\text{Ca}_{12}\text{Al}_{14}\text{O}_{33}$ sorbents consisted of 75 wt% CaO and so the capture capacity of the $\text{CaO}/\text{No Al}$ sorbent was higher (8.6 mmole g^{-1} compared

to 8.0 mmole g⁻¹ for CaO/Ca₁₂Al₁₄O₃₃). The introduction of Ca₁₂Al₁₄O₃₃ creates an inert framework with separated CaO grains.^{54,275,288} This can be expected to facilitate conversion. Hence it was concluded that the formation of Ca₁₂Al₁₄O₃₃ allowed for a high conversion despite low surface area through the formation of separated CaO grains. Note that surface area was measured on samples prior to the carbonation and hence also before decomposition (carried out to remove Ca(OH)₂ phase, directly prior to TGA carbonation) which created a sintering environment. The Ca₁₂Al₁₄O₃₃ phase is known to retard sintering and so it is possible that a significant amount of surface area was lost in the CaO/No Al sorbent during the decomposition while this was not the case for the CaO/Ca₁₂Al₁₄O₃₃ sorbent.

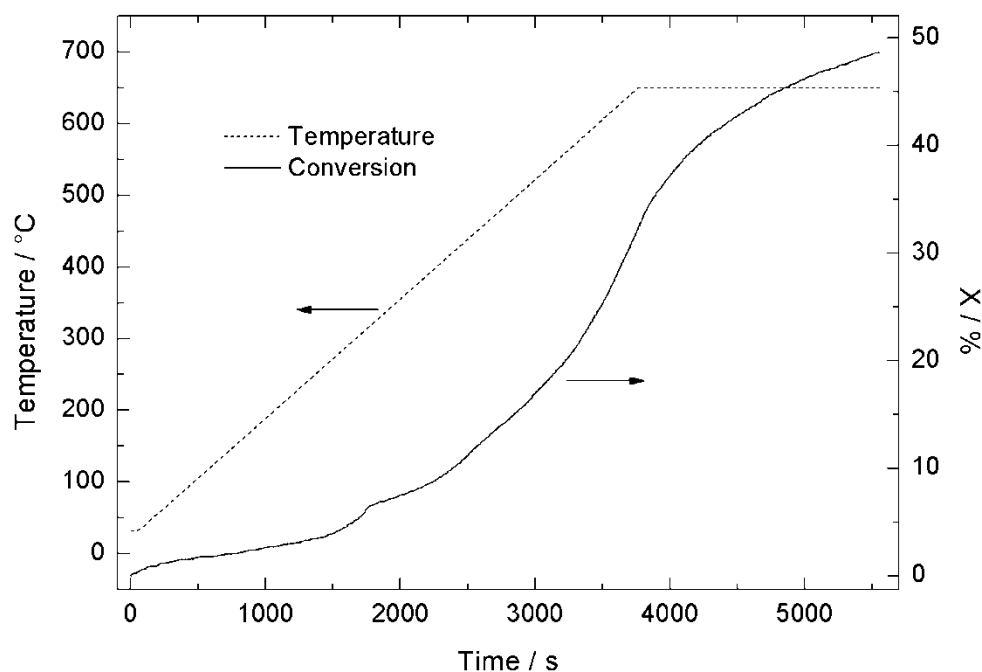


Figure 6. 29. Carbonation of CaO/No Al during TGA.

6.5.2 TGA CYCLING

CO₂ capture and release cycles were carried out with carbonation at 650 °C for 30 min in pure CO₂ and calcination at 900 °C for 10 min in pure N₂ (Figure 6. 30). A temperature ramp of 25 °C min⁻¹ was used.

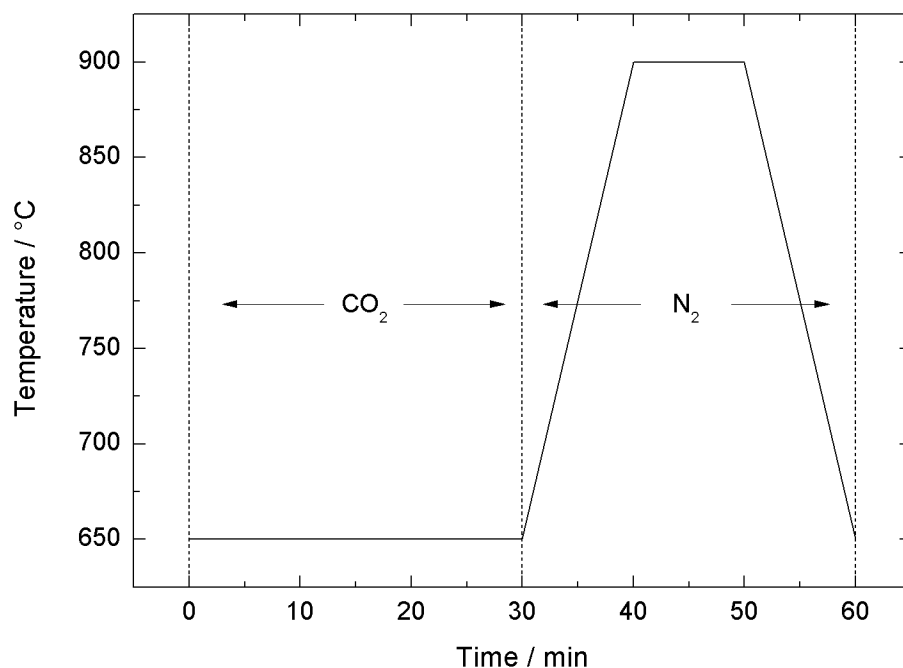


Figure 6. 30. Cycling TGA temperature program.

Note that an even longer carbonation time would ensure higher carbonation but commonly looping has been carried out for 20-50 cycles^{47,54,101,140,223,275} and so to ensure that the expected steady state would be reached it was decided to carry out 20 cycles. The carbonation time was therefore limited to 30 min so that 20 cycles could be carried out over a reasonable amount of time. The disadvantage of using a long carbonation time and a high CO₂ partial pressure is the limited ability to relate the results to large scale post combustion applications where carbonator residence time is only a few minutes and the CO₂ partial pressure is around 10%.²⁸⁴ However, given the aim of the work this disadvantage was considered acceptable.

The purpose of the calcination stage was to ensure complete calcination. The extent of calcination is determined by temperature and CO₂ partial pressure such that high temperatures and low partial pressures favour calcination (Figure 6. 31).^{221,264} The calcination conditions were chosen so as to be well within the conditions needed for calcination. Calcination has been carried out at temperatures of 850-950 °C for 10 min in pure N₂ in previous work.^{53,101,143,272,274}

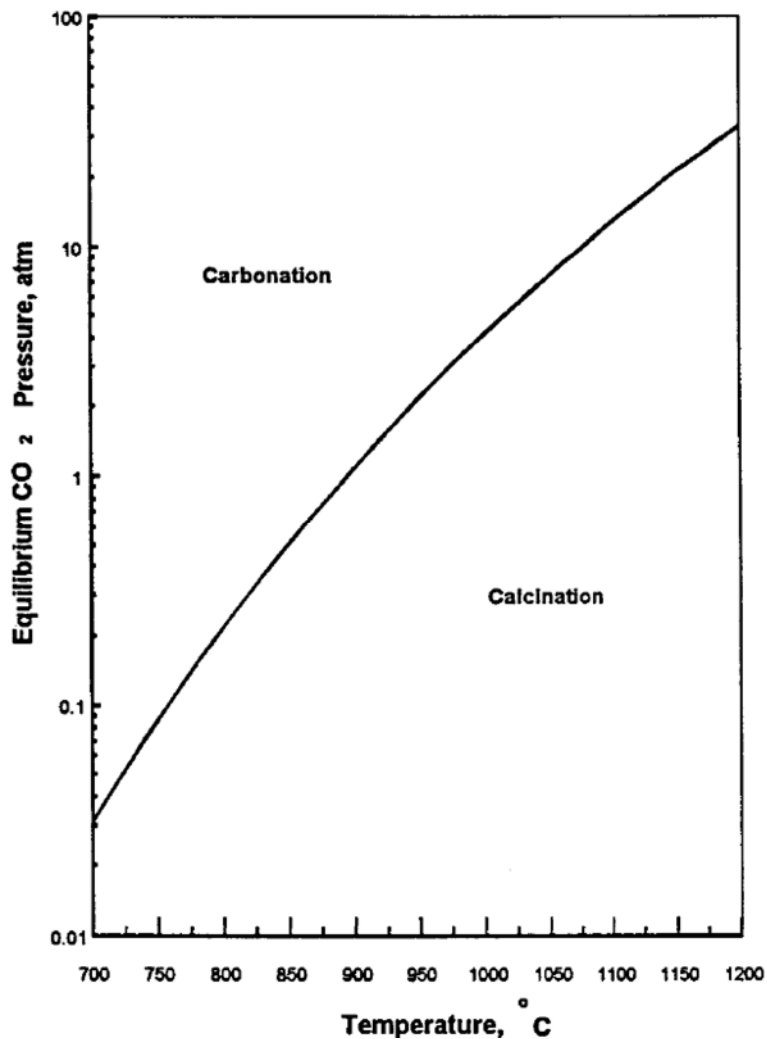


Figure 6. 31. Equilibrium CO₂ pressure as a function of temperature. Reprinted with permission from Ortiz and Harrison 2001.²²¹ Copyright 2001 American Chemical Society.

The conditions used here for calcination are different from those of large scale post combustion applications, where for example the residence time in a calciner is about 2 min.²⁸⁹ Also, one objective in the large scale calcination process is the production of a pure CO₂ stream, ready for compression, liquefaction and storage. One solution would be to calcine in a CO₂ stream but this would require high temperatures and long calcination times. Wang et al.²⁹⁰ for example needed a temperature of 1020 °C and a calcination time of 70 min to reach 95% calcination in limestone in pure CO₂. It is possible to carry out calcination in a mixture of CO₂ and steam as these can be readily separated.³⁰ Adding steam both increases calcination rate as well as the extent of calcination for a given calcination time and temperature.^{291,292} Hence the addition of steam could potentially reduce the temperature needed for calcination.³⁰ However, the presence of steam during calcination promotes sintering as evidenced by the formation of larger pores compared to the pores formed without steam.⁴⁸

As discussed by both Blamey et al.³⁰ in an extensive review of the calcium looping cycle and by Martínez et al.²⁸⁹ in a recent paper on the kinetics of CaCO₃ calcination it has proven difficult to collect reliable information on the calcination reaction mechanism. An example of this is the effect of particle size. Hu and Scaroni²⁹³ reported that there exist a risk of reduced heat and mass transfer in particles as small as 63 μm resulting in reduced temperatures and increased CO₂ partial pressures at the reaction front. However, Martínez et al.²⁸⁹ found that mass transfer was negligible in particles up to 300 μm. For this work, fine sorbent powders were used and so any particle size dependent effect was expected to be minimised.

The temperature program began with a ramp up to 650 °C in pure N₂, followed by a first cycle (30 min at 650 °C in CO₂ followed by calcination at 900 °C in N₂ according to Figure 6. 30). Another 20 cycles were carried out and the results from these 20 cycles are plotted in the figures below. This was to ensure that all cycles were carried out under the same conditions. The first cycle was ignored as it by necessity was carried out under a different condition than the following 20 cycles, i.e. it began with a ramp to 650 °C from room temperature instead of a ramp from 900 °C.

The conversion at each cycle was calculated from a change in sample mass. The change in sample mass was determined by calculating the difference between the mass at the end of the 30 min carbonation phase (in CO₂) and the mass at the end of the ramp back to 650 °C (before the atmosphere was switched back to CO₂, see Figure 6. 30).

Note that the Ca(OH)₂ impurities were removed during the first cycles (which was not included in the analysis). Hence the first cycle of the temperature program filled the function of the Ca(OH)₂ decomposition applied prior to the carbonation experiment. CaO derived from Ca(OH)₂ was prepared by adding Ca(OH)₂ to the TGA and carrying out the same temperature program as for the other sorbents. The Ca(OH)₂ decomposed to CaO during the calcination step of the first cycle, thereby producing CaO derived from Ca(OH)₂.

6.5.2.1 CYCLING OF CAO SORBENTS

The conversion of the CaO powder and the CaO derived from Ca(OH)₂ decreased over multiple cycles in a agreement with the literature (Figure 6. 32).^{97,98,144,146} It is common that the conversion levels out after 20-30 cycles but the conversion of the CaO powder and the CaO derived from Ca(OH)₂ still decreased by the end of the 20th cycle. The conversion of the CaO derived from Ca(OH)₂ decreased by 31% while the conversion of the CaO powder was reduced by 8%. The CaO derived from Ca(OH)₂ displayed a higher extent of capacity. This highlighted a typical feature of the investigation of Ca-based sorbents, which is the trade-off between stability and capture capacity. This trade-off has been evident in previous studies of Ca-based sorbents which have been doped with varying amounts of inert material such as MgO, KMnO₄ and MgAl₂O₄.^{273,294,295} These studies showed that a larger amount of inert material increases the

stability but reduces the capture capacity. In the case of the sorbents investigated here, the lower capture capacity is caused by a lower surface area and lower porosity as opposed to the inclusion of inert material. As the surface area and porosity was low at the start of the experiment, there was little room for a reduction. As a result, there was little room for a reduction in capture capacity.

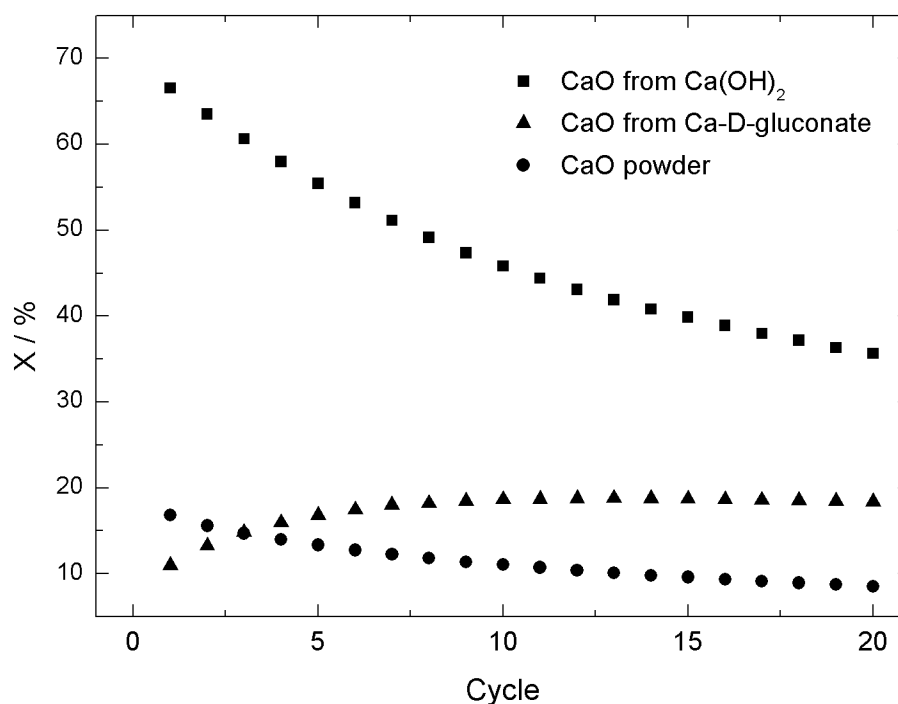


Figure 6. 32. Conversion as a function of cycle number for the CaO sorbents.

The CaO from Ca-D-gluconate showed an initial increase in conversion which then levelled out (Figure 6. 32). Such behaviour over multiple cycles was first reported by Manovic and Anthony who investigated preheated limestone.²⁹⁶ They proposed a pore-skeleton model to explain the behaviour which they called self-reactivation. The model describes how preheating results in formation of a stable material through which ion diffusion is made difficult which subsequently reduces capture capacity. With multiple carbonation/calcination cycles the material is softened and ion diffusion is made easier which increases capture capacity. Simultaneously the stable part of the material delays sintering leading to a net increase in capture capacity with multiple cycles. Self-reactivation has since been observed several times in other preheated Ca-based sorbents.^{143,153,297,298} The pore-skeleton model could explain the behaviour of the CaO derived from Ca-D-gluconate over multiple cycles as it has been subjected to preheating in the form the Ca-D-gluconate decomposition.

6.5.2.2 CYCLING OF $\text{Ca}_{12}\text{Al}_{14}\text{O}_{33}$ SORBENTS

Both the $\text{CaO}/\text{Ca}_{12}\text{Al}_{14}\text{O}_{33}$ and the $\text{CaO-D}/\text{Ca}_{12}\text{Al}_{14}\text{O}_{33}$ sorbent displayed self-reactivation (Figure 6. 33). The conversion increased over the first 5-7 cycles and then reduced for the remaining cycles. The $\text{CaO-D}/\text{Ca}_{12}\text{Al}_{14}\text{O}_{33}$ sorbent showed both a higher extent of conversion and a higher stability over the 13-15 remaining cycles. $\text{CaO}/\text{Ca}_{12}\text{Al}_{14}\text{O}_{33}$ sorbents have displayed self-reactivation in the past.^{54,139,275} The behaviour of the $\text{CaO}/\text{No Al}$ sorbent was almost identical to that of the CaO derived from $\text{Ca}(\text{OH})_2$ both with regards to the shape of the curve as well the conversion at the first and 20th cycles. The conversions in the first cycle were 66.6 and 66.5% and the conversions in the 20th cycle were 33.3 and 35.7% for the $\text{CaO}/\text{No Al}$ and the CaO derived from $\text{Ca}(\text{OH})_2$ respectively. Note that the CaO derived from $\text{Ca}(\text{OH})_2$ presented in Section 6.5.1.1 reached a conversion of 77.2%. This displayed the effect of the high temperature calcination stage on the capture capacity of this sorbent. The sorbent tested in Section 6.5.1.1 had been decomposed at 700 °C prior to the carbonation experiment while it had been calcined at 900 °C at the beginning of the looping experiment.

Note that no N_2 adsorption was carried out on cycled sorbents and this limits the discussion on the effects of surface area and pore size distribution in relation to cycling. The reason for this was the sample amount used for TGA and N_2 adsorption respectively. 10mg of sample was used for TGA cycling and 2-3g of sorbent was needed to carry out N_2 adsorption.

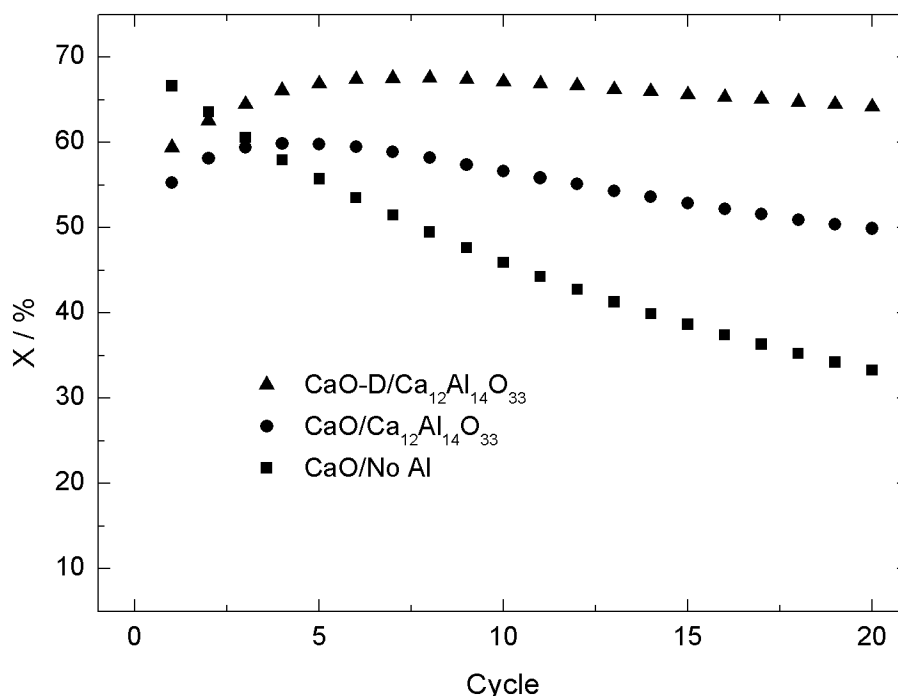


Figure 6. 33. Conversion as function of cycle number for the $\text{Ca}_{12}\text{Al}_{14}\text{O}_{33}$ sorbents.

6.6 REACTOR CARBONATION USING PELLETS

The TGA experiments presented above were carried out using samples with a small particle size. The selected sorbents for pelletisation were CaO powder, CaO derived from Ca(OH)₂, CaO/Ca₁₂Al₁₄O₃₃ and CaO-D/Ca₁₂Al₁₄O₃₃. Sorbent pellets were prepared according to Chapter 2, Section 2.5. Earlier work on experimental rigs with reactors of similar size has been carried out with sorbent particles in the size range of 0.66-2.0 mm.^{23,55} Pellets manufactured by preparation of a paste followed by sieving and drying were 0.8-4 mm.^{151,152,277} The sorbent particle size range chosen for this work was 1.0-1.4 mm.

The sample was first calcined at 900 °C under a N₂ flow of 350 ml min⁻¹ to remove impurities such as Ca(OH)₂ as well as to decompose any CaCO₃ present in the sample (Figure 6.34). 900 °C was used here as opposed to the 650 °C which was used for TGA because a temperature of 900 °C is more likely to be applied for large scale applications.²⁹⁹ After calcining for 10 min the temperature of the rig was reduced to 200 °C at a ramp rate of 5 °C min⁻¹. This was the fastest ramp rate allowed by the rig setup under the given N₂ flow. A faster ramp was made difficult due to the robust heat insulation of the electrical furnace. A flow of 50 ml min⁻¹ of CO₂ was then switched on and was allowed to fill uniformly the tubing, glassware etc for 3 min (resulting in a CO₂ concentration of 12.5 vol%). Note that this CO₂ concentration is close to the conditions which could be expected for large scale CO₂ capture (≈10 vol%²⁸⁴) as opposed to the TGA carbonation work carried out in Section 6.5.1. The temperature was then ramped to 650 °C at 3 °C min⁻¹ and kept for 30 min. The CO₂ gas flow was chosen on the basis of the flow range of the Uras 26 gas analyser unit used to quantify CO₂ in the reactor off-gas. The flow range of the Uras 26 unit was 333 ⅓ - 1666 ⅔ ml min⁻¹. The CO₂ concentration was chosen both based on the Uras 26 detection limits (0-30%) and the expected CO₂ concentration in flue gasses during large scale CO₂ capture (≈10 vol%²⁸⁴). CO₂ concentrations of 14-15 vol% have been used previously for rigs of similar size.^{42,157}

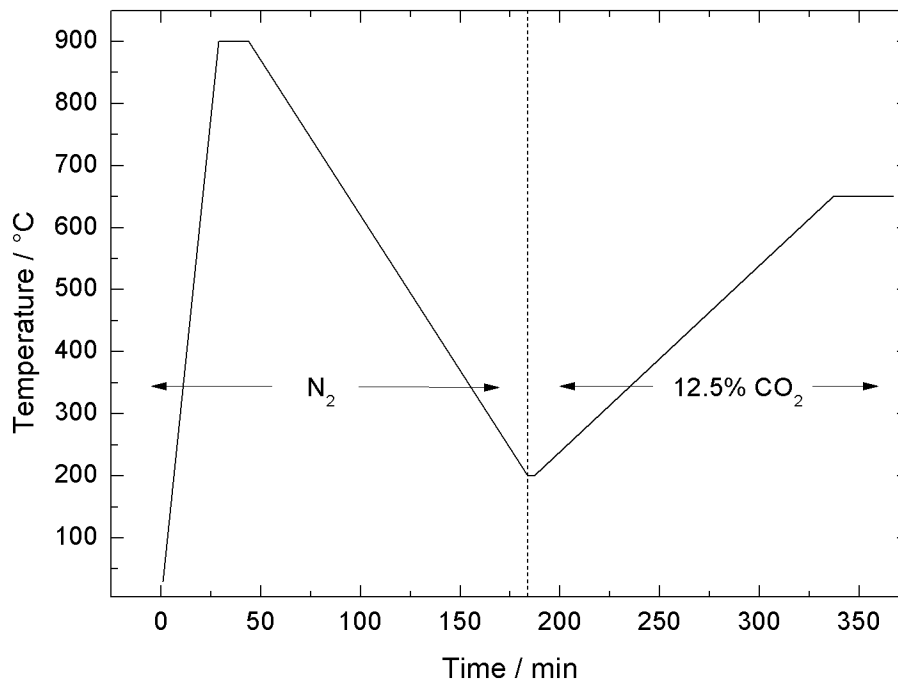


Figure 6. 34. Carbonation bench scale reactor temperature program.

6.6.1 CAO SORBENTS

Given that pellets were prepared for the CO₂ capture reactor experiment, the CaO powder sorbent will be referred to as CaO in this section. During the reactor run with CaO the conversion curve (conversion as a function of time) displayed a similar s-shape as during the TGA (Figure 6. 35). However the curve was smoother which was attributed to the slower temperature ramp used. The CaO reached a conversion of only 6.2% at the end of the 650 °C temperature hold which was much lower than what could be expected from the TGA data (21.4%). The CO₂ partial pressure was lower in the reactor but the carbonation time was much longer. The low conversion was attributed to mass transfer limitations in the pellets. The CaO displayed little or no porosity and so surface area is highly dependent on particle size. It would be expected therefore that after the formation of a uniform CaCO₃ layer there will be more unreacted CaO in a larger pellet particle compared a smaller one with everything else being equal.

An attempt was made to investigate the CaCO₃ layer around the CaO pellets. Carbonated CaO pellets were fixed in resin (according to the method described in Section). The resin and pellet were then ground and polished so that SEM imaging and EDX mapping of a cross section of the pellet was made possible. However, the non uniform shape of the pellets made it extremely difficult to grind and polish the pellet so that reliable cross section information could be derived. The pellet was also heavily damaged due to its low mechanical strength. Consequently, reliable SEM imaging and EDX mapping of cross sections was not possible.

A direct comparison of TGA and reactor results by means of plotting the data in the same Figure is problematic since the TGA carbonation experiment was about half as long as the reactor experiment (Figure 6. 24, Figure 6. 35) i.e. 5000s compared to 10000s.

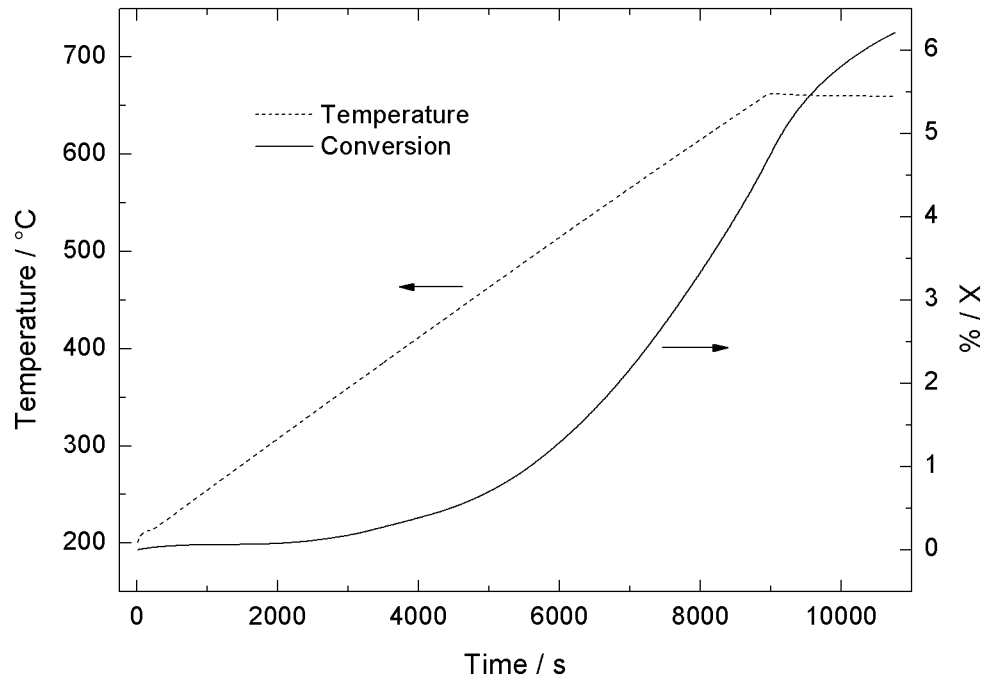


Figure 6. 35. Carbonation of CaO in the bench scale reactor.

The CaO pellets derived from Ca(OH)₂ reached a conversion of 84.2% which was higher than the conversion reached during the TGA experiment (77.2%) (Figure 6. 36). The preparation of pellets did not affect the CO₂ capture capacity of this sorbent. The Ca(OH)₂ which the pellets were made out of displayed porosity (Section 6.4.1) and the pellets consisting of Ca(OH)₂ were decomposed to CaO in the reactor during the calcination phase. This ensured increased porosity as well as insuring that the sorbent retained a low density. The low density was evidenced by the bed height of the Ca(OH)₂ pellets (53 mm) in relation to the CaO pellets (39 mm). The longer carbonation time in the CO₂ capture reactor experiment enabled higher conversion compared to the TGA experiment.

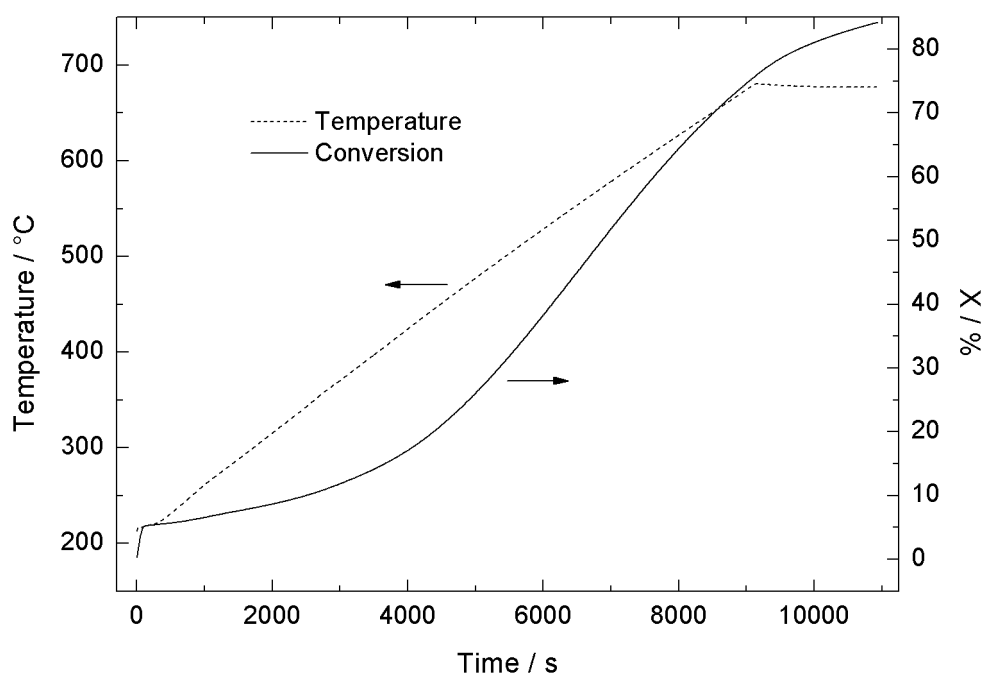


Figure 6. 36. Carbonation of CaO derived from $\text{Ca}(\text{OH})_2$ in the bench scale reactor.

6.6.2 $\text{Ca}_{12}\text{Al}_{14}\text{O}_{33}$ SORBENTS

The $\text{CaO}/\text{Ca}_{12}\text{Al}_{14}\text{O}_{33}$ and the $\text{Ca-D}/\text{Ca}_{12}\text{Al}_{14}\text{O}_{33}$ pellet sorbent displayed final conversions of 25.0 and 17.7% respectively which was much lower than the conversion that were reached during carbonation in TGA (Figure 6. 37). Also, The $\text{CaO}/\text{Ca}_{12}\text{Al}_{14}\text{O}_{33}$ pellets displayed a lower conversion than the $\text{CaO-D}/\text{Ca}_{12}\text{Al}_{14}\text{O}_{33}$ pellets while the situation was the reverse during the TGA experiments. The lower conversions were attributed to the pelletisation as in the case of the CaO (Section 6.6.1). The pelletisation affected the $\text{CaO-D}/\text{Ca}_{12}\text{Al}_{14}\text{O}_{33}$ sorbent more than the $\text{CaO}/\text{Ca}_{12}\text{Al}_{14}\text{O}_{33}$ sorbent. The two sorbents displayed very similar phase composition, surface area and porosity and so the more severe effect of pelletisation on the $\text{CaO-D}/\text{Ca}_{12}\text{Al}_{14}\text{O}_{33}$ sorbent was attributed to the differences in morphology between the two sorbents. The surfaces of the $\text{CaO-D}/\text{Ca}_{12}\text{Al}_{14}\text{O}_{33}$ sorbent particles were smoother than the $\text{CaO}/\text{Ca}_{12}\text{Al}_{14}\text{O}_{33}$ particles (Figure 6. 15, Figure 6. 17) which could have affected the stacking of the particles during compression and hence have had an effect on the CO_2 capture capacity. Other components could also affect the response to pelletisation but the characterization carried out here was limited to phase composition, surface area, porosity and morphology.

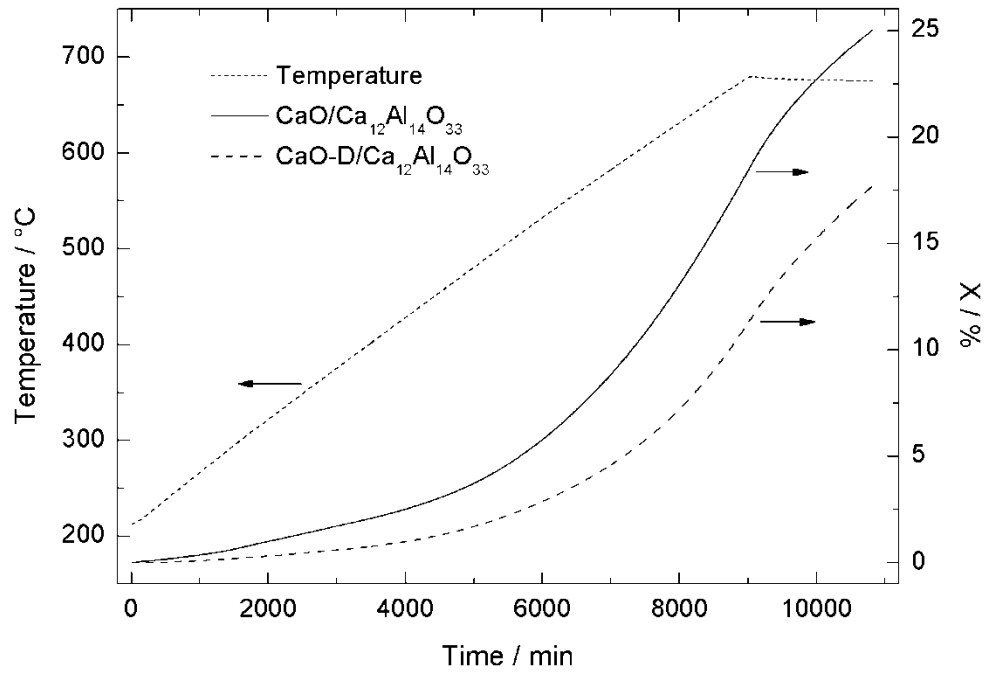


Figure 6. 37. Carbonation of CaO/Ca₁₂Al₁₄O₃₃ and CaO-D/Ca₁₂Al₁₄O₃₃ in the bench scale reactor.

CHAPTER 7: INVESTIGATION OF CO₂ SORBENTS USING IN SITU XRD

“Science is simply common sense at its best that is, rigidly accurate in observation, and merciless to fallacy in logic”

Thomas Huxley

7.1 MOTIVATION FOR WORK

In the previous chapter thermogravimetric analysis (TGA) and a bench scale bed reactor were used. These are the most commonly used techniques for the study of CO₂ capture by Ca-based sorbents but they have a number of disadvantages with regards to hydrated sorbents containing Ca(OH)₂. TGA for example cannot readily distinguish between a change in mass derived from the formation and/or decomposition of CaCO₃ and Ca(OH)₂. It is possible to quantify outlet concentrations of gaseous products including CO₂ and H₂O by coupling TGA with mass spectrometry (MS). By doing so, Blamey et al.⁴⁹ were able to simultaneously monitor mass change and steam evolution when studying a range of different Ca(OH)₂ based sorbents. However, accurate quantification of outlet gases is made difficult by the small amounts of sample which the TGA apparatus will allow while using larger sample masses result in mass transfer limitations. Bench scale bed reactors can be scaled up to allow for larger sample mass so that reactor outlet gas concentrations and steam partial pressures can be accurately quantified.^{42,48,287,300} With this technique, outlet gas concentrations and steam partial pressure measurements are related to known inlet concentrations and partial pressures, allowing for rates of production or consumption to be calculated. To obtain extents of CO₂/H₂O intakes or releases, the rates require integrating over the reaction time, a calculation prone to error propagation and over-reliant on accurate knowledge of the duration of the reactions. This limits the ability to relate the measurements to accurate extent of formation and/or decomposition of CaCO₃ and Ca(OH)₂. Moreover, the larger sample mass used in bed reactors introduces mass transfer limitations.

X-ray diffraction (XRD) has been widely used for the purpose of phase identification in Ca-based CO₂ sorbents. Li et al.^{53,54} for example, used XRD to determine the presence of mayenite (Ca₁₂Al₁₄O₃₃) in synthetic Ca-based sorbents. Phase changes from CaO to CaCO₃ have also been identified by collecting dolomite aliquots at different times during steam reforming coupled with in situ CO₂ capture.³⁰¹

When XRD is combined with Rietveld refinement it is possible to retrieve further information. Montes-Hernandez et al.³⁰² carried out XRD on Ca(OH)₂ crystallites that had been carbonated at different pressures. They were able to show a correlation between carbonation pressure and crystallite size by calculating crystallite size from the XRD results using Rietveld refinement. Koirala et al.³⁰³ compared CaO doped with different levels of Zr. A CaZrO₃ phase was identified which exhibited a larger crystal diameter with a higher level of Zr doping. Xu et al.³⁰⁴ carried out XRD analysis of CaAl-layered double hydroxides synthesised using an ethanol/water mixture of varying ratios. The full width at half maximum (FWHM) of the (002) and (004) diffraction peaks were then used to calculate the crystallite size in the c-direction using the Scherrer equation.³⁰⁵ This way they were able to show a correlation between ethanol

to water volume ratio and crystallite size. Detailed information on differences in crystallite size in the different phases of dolomite samples heated to temperatures of 550 to 850 °C has been retrieved from the study of peak broadening.³⁰⁶ This information could then be used to explain observations made during dolomite decomposition using TGA.

In situ XRD analysis is a technique which has been used to study phase changes³⁰⁷⁻³⁰⁹ decomposition³¹⁰⁻³¹² as well as crystal size and strain effects^{313,314} in both Ca-based sorbents and other sorbents such as perovskites and ternary oxides in situ. Lucas et al.³⁰⁸ used in situ XRD to study the effects of heating on CaCO₃. They were able to show a phase change from the aragonite form to the calcite form at a temperature of 450 °C. Efimov et al.³⁰⁷ used in situ XRD to show that BaCO₃ was formed in a two phase perovskite when it was heated to 900 °C in an atmosphere containing 50% CO₂ and 50% N₂. By carrying out multiple XRD scans and analysing the resulting spectra using Rietveld analysis, they were able to plot the BaCO₃ fraction as a function of time. Liu et al.³⁰⁹ studied phase changes in a synthetic two phase sorbent containing CaO and Ca₁₂Al₁₄O₃₃. The amount of CO₂ around the sample was increased from 0 to 50 vol% at a constant temperature of 750 °C and the formation of a CaCO₃ phase was observed. By quantifying the three phases using Rietveld refinement Liu et al. were able to show that the CaO converted to CaCO₃ while the Ca₁₂Al₁₄O₃₃ phase remained inert.

Garcia-Martinez et al.³¹² studied the decomposition of sulphated Ca(OH)₂ using XRD, and observed formation of CaO derived from Ca(OH)₂ beginning at 400 °C with no Ca(OH)₂ left at 600 °C, in addition to the formation of CaSO₄ and CaS from CaSO₃ which had formed during sulphation. Engler et al.³¹⁰ examined the decomposition of dolomite in CO₂ and in air, and provided detailed descriptions of both decomposition mechanisms. They observed that in a CO₂ atmosphere dolomite first decomposes to CaCO₃ and MgO at 500-765 °C with a subsequent decomposition of CaCO₃ to CaO at temperatures above 900 °C. In an air atmosphere the dolomite first decomposed to CaCO₃, MgO and CaO at 700-750 °C followed by decomposition of the CaCO₃ to CaO at around 780 °C. Vielle et al.³¹¹ used in situ XRD to study the decomposition of [Ca₂Al(OH)₆]Cl·2H₂O and compared it to TGA mass loss curves. The TGA results showed mass loss at temperature intervals of 25-280, 280-400 and above 400 °C, which was in agreement with the phase changes and changes in peak intensity observed by XRD in the same temperature intervals.

Rodriguez et al.³¹⁴ and Fernandez-Garcia et al.³¹³ combined XRD with Rietveld refinement to measure crystallite size and strain in mixed metal oxides and ceria based ternary oxides respectively. Spectra were collected at different temperatures, and the crystallite size and strain was calculated from the width of the diffraction peaks. In addition to size and strain effects, Rietveld refinement can also be used for quantitative phase analysis. Hill and Howard⁵⁶ introduced a method for using the scale factors derived from Rietveld refinement to quantify the weight percentage of each phase in a spectrum. They tested the method using TiO₂ and Al₂O₃

mixtures of known compositions and reported a relative error of 1-2%. Mixtures containing poorly crystalline phases however caused an error of 6.8%. Bish and Post³¹⁵ and Kontoyannis and Vagenas³¹⁶ used quantitative phase analysis to measure the wt% of mineral mixtures with known compositions and reported that the analysis had a relative error of 0.2-5.4%. Such an analysis provides the basis for studying the formation and/or decomposition of CaCO_3 and Ca(OH)_2 in Ca-based sorbents during CO_2 capture in the presence of steam, or during surface area regeneration by hydration.

In this chapter in situ XRD analysis will be combined with Rietveld refinement to study CO_2 capture and dehydration of a number of different Ca-based sorbents at temperatures between 25 and 800 °C in atmospheres of CO_2 and N_2 . In order to test the reliability of the in situ XRD method, the results were benchmarked against those of TGA, a well established technique for the study of CO_2 sorbents.

In situ XRD offers the ability to obtain information which cannot be retrieved using conventional techniques. This ability was tested in the present work by using in situ XRD to investigate partially hydrated CaO as well as another CO_2 sorbent, namely the $\text{CaO/Ca}_{12}\text{Al}_{14}\text{O}_{33}$ sorbent which was investigated in Chapter 6.

An accurate investigation of partially hydrated CaO is difficult using conventional techniques. Hydration alters the properties of CaO based sorbents with regards to their CO_2 capture capacity as well as their stability and mechanical strength and is therefore important to understand.^{36,44,218} An in depth investigation of partially hydrated CaO is therefore performed here with in situ XRD. $\text{CaO/Ca}_{12}\text{Al}_{14}\text{O}_{33}$ sorbents have displayed improved stability over multiple CO_2 capture and release cycles as seen in Chapter 6 and is therefore of interest as the stability of Ca-based sorbents is the major economic challenge of their use for large scale CO_2 capture.^{53,54,269} The interaction between the CaO and the $\text{Ca}_{12}\text{Al}_{14}\text{O}_{33}$ in $\text{CaO/Ca}_{12}\text{Al}_{14}\text{O}_{33}$ sorbents is not fully understood and in situ XRD will therefore be used to study phase changes in the sorbent as a function of temperature in both N_2 and CO_2 .

7.2 AIMS AND OBJECTIVES

The aims of this chapter are:

- To use in situ XRD in combination with Rietveld refinement to quantify phase changes in Ca-based CO_2 sorbent sorbents.
- To study carbonation of CaO and Ca(OH)_2 using in situ XRD combined with Rietveld refinement and benchmark the results against those derived by TGA.
- To carry out an in depth investigation of the CO_2 capture mechanism in partially hydrated CaO.

- To apply in situ XRD analysis to study the characteristics of CaO/Ca₁₂Al₁₄O₃₃.

The objectives of this chapter are:

- To ensure accurate control of the atmosphere and the temperature in the in situ XRD setup.
- To ensure accurate quantification of phase composition that will reflect phase conversion as a function of temperature.
- To carry out carbonation experiments with CaO and Ca(OH)₂ in TGA and XRD with the same temperature programs and atmospheres, derive carbonation capacities and compare the results.
- To carry out carbonation experiments with in situ XRD on partially hydrated CaO and CaO/Ca₁₂Al₁₄O₃₃ and derive carbonation capacities.

7.3 ACCURACY OF THE IN SITU XRD METHOD

7.3.1 ATMOSPHERE AND TEMPERATURE

The experimental setup is outlined in Chapter 2, Section 2.9. The HTK-1200 high temperature chamber was used to control the temperature and the mass flow controllers were used to control the gas flows into the chamber. All experiments were carried out at ambient pressure in either 100% CO₂ or 100% N₂. According to the manufacturer, the HTK-1200 had a volume of 350 ml and quarter inch diameter tubing 4 m long was used giving a total volume of 856 ml for the whole setup. To ensure that the atmosphere was either 100% CO₂ or 100% N₂ a gas flow rate of 50 ml min⁻¹ was kept for 1h at room temperature prior to the experiment to ensure that all other gases had been purged. The flow through the setup was continuously monitored by observing flow of bubbles through the water in the Dreschel bottle.

Due to thermal inertia, the measured temperature on the sample holder usually differs from the set temperature as it follows the heating ramp program. In order to determine the actual sample temperature, a calibration method was employed.

The actual temperature of a sample inside the HTK-1200 high temperature chamber for any given temperature setting was determined using materials that undergo phase transitions at known temperatures (Table 7. 1).

Table 7. 1. Materials used to determine the actual temperature of a sample for any given temperature setting.

Material	Phase transition temperature (°C)
KNO ₃	130
KSO ₄	583
BaCO ₃	810

For each material, a number of scans were carried out at different temperature settings and the resulting spectra were analysed with the aim of finding a known phase transition (Figure 7. 1). The temperature settings at which the phase transitions occurred were plotted against the temperatures at which the transitions are known to occur (Figure 7. 2). By drawing a trend line through the points in the graph, the actual temperature could be derived for any given temperature setting using the trend line equation (Figure 7. 2).

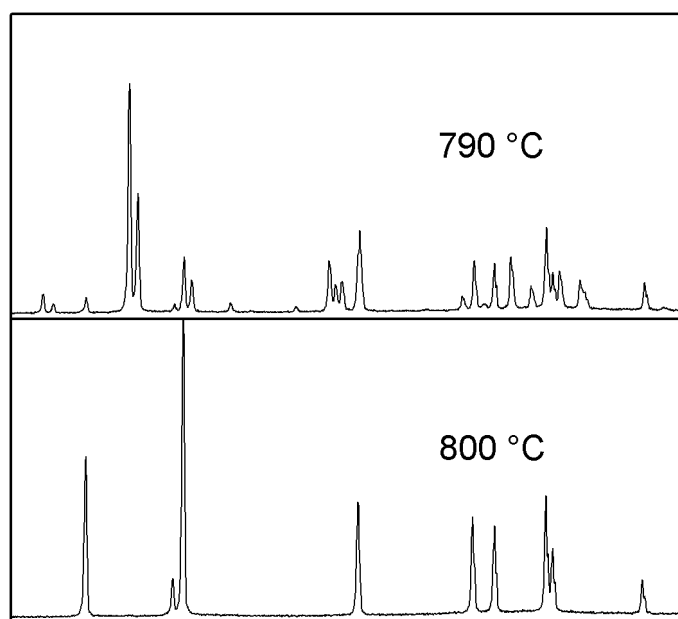


Figure 7. 1. Example of a phase change due to a change in temperature (derived from BaCO₃).

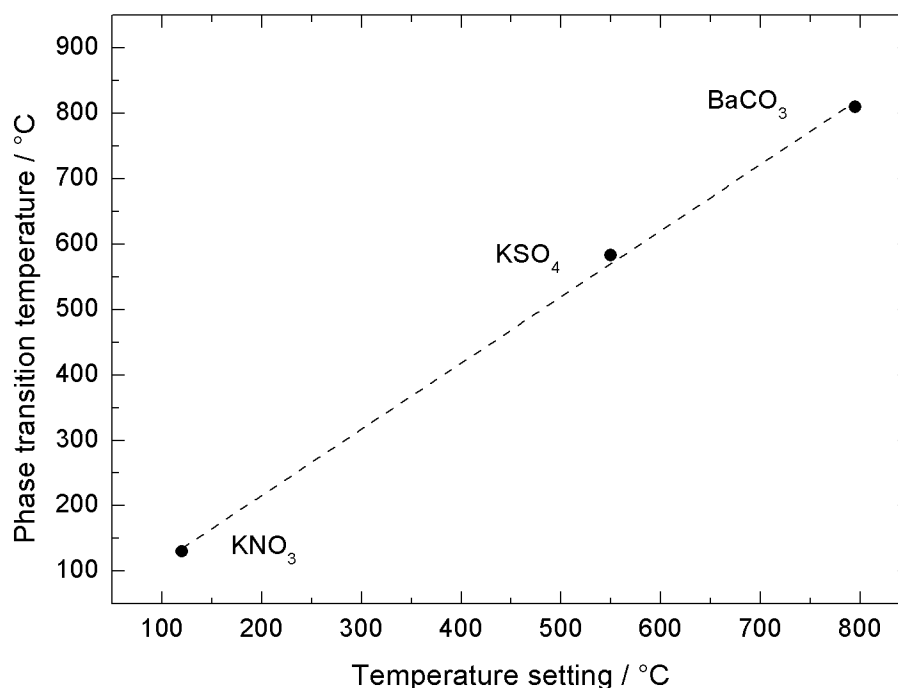


Figure 7. 2. Sample temperature calibration curve using known materials phase transition temperatures.

7.3.2 SAMPLE PREPARATION AND DATA COLLECTION

The collection of XRD data relies on measuring differences in diffraction of crystallite samples at angles of 2θ . To ensure reliable diffraction data it must therefore be ensured that the diffraction angle relative to the sample is correct over the whole range of 2θ .

To achieve reliable data the sample was ground to a fine powder using a pestle and mortar. It was then packed tightly into the sample holder and the surface of the sample was flattened using a microscope slide. About 220 mg of sample was needed to fill the sample holder. After the sample holder had been placed inside the HTK-1200 and prior to data collection, the height of the sample holder was adjusted. An incorrect distance between the X-ray gun and the sample will result in a shift of the peaks in the resulting spectrum. A scan was carried out over the 2θ range containing the peak with the highest intensity and the position of the peak was compared with expected position from the relevant ICDD reference.

7.3.3 PHASE QUANTIFICATION

The accuracy of the Rietveld refinement was tested by analysing samples of known composition. Known amounts of Ca(OH)₂ and CaCO₃ were mixed together, and the resultant mixtures were analysed using XRD and Rietveld refinement. Ca(OH)₂ was chosen over CaO because CaO is highly hygroscopic and is difficult to maintain as single phase. CaCO₃ was prepared by heating Ca(OH)₂ (prepared according Chapter 2, Section 2.3) to 700 °C in a pure CO₂ atmosphere in a quartz reactor inserted into a tube furnace (Figure 7. 3). A gas flow of 50

ml min^{-1} was maintained through the quartz reactor using a mass flow controller (MKS, UK). XRD analysis and Rietveld refinement was first carried out on the single phase Ca(OH)_2 and on the CaCO_3 produced in the reactor (Figure 7. 4 and Figure 7. 5).

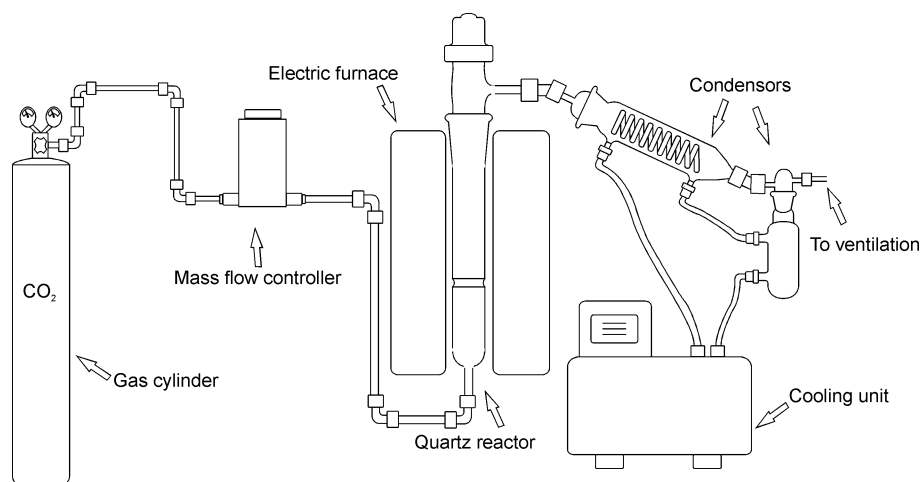


Figure 7. 3. CaCO_3 preparation.

The Ca(OH)_2 XRD data could be indexed to Ca(OH)_2 and CaCO_3 in the calcite form (ICDD references 04-006-9147 and 04-007-0049) hence the Ca(OH)_2 was not single phase (Figure 7. 4). In this and all subsequent XRD data figures, the XRD raw data is shown as crosses, while the model generated by the Rietveld refinement is shown as a solid line and the residual (the difference between the raw data and the model) is shown as a solid line below the refinement data. The upper vertical lines are derived from the ICDD references and mark the expected positions of the peaks for each phase, in this case CaCO_3 and Ca(OH)_2 .

The refinement returned values of 97 wt% for the Ca(OH)_2 phase and 3 wt% for the CaCO_3 phase. Refinement quality can be evaluated by considering the residual. Ideally, this would be zero at all points, indicating that the refinement exactly fitted the raw data, but this is difficult to achieve in practice. Small deviations appeared around some of the peaks, which could in part be attributed to experimental scatter. It would be possible to improve the residual by extending the scan time; hence there is a trade-off between data quality and scanning time.

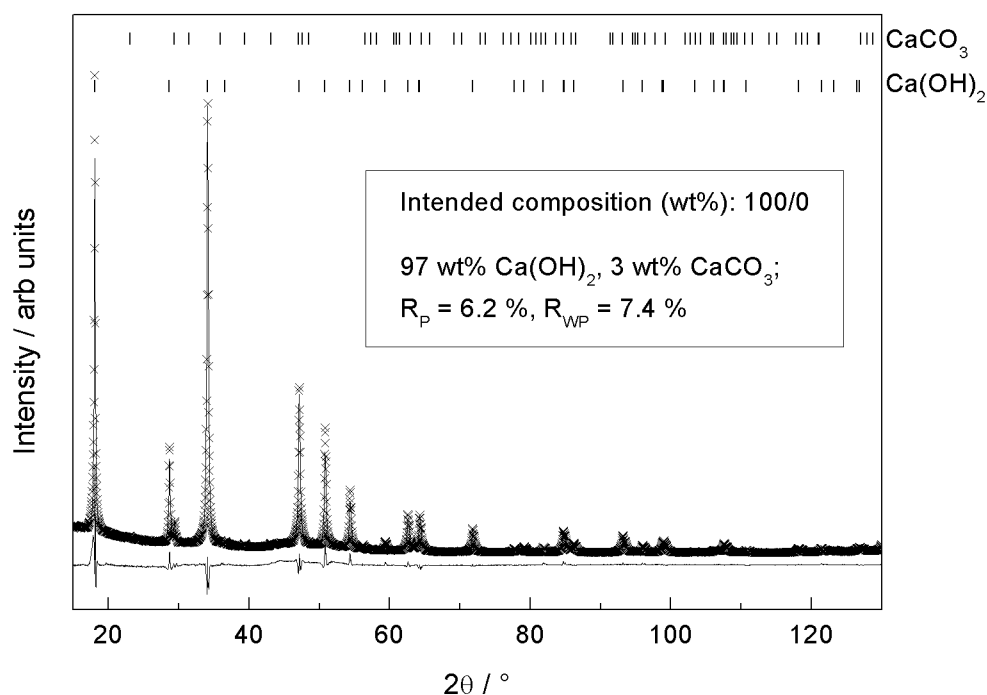


Figure 7. 4. XRD spectrum of Ca(OH)_2 . Crosses = raw data, upper solid line = refinement model, lower solid line = residual. Insert showing phase composition (in wt%), residual (R_p) and weighted residual (R_{wp}). Vertical lines show the expected positions of diffraction peaks for Ca(OH)_2 and CaCO_3 .

The quality of the fit is quantified arithmetically by the residual (R_p) and the weighted residual (R_{wp}).^{317,318} Lower values indicate a better fit and values of 10% and below are considered typical for XRD data.³¹⁹ Hence the values achieved here (6.2 and 7.4% for R_p and R_{wp} respectively) were considered satisfactory. There was no evidence of an amorphous phase which would manifest itself through broad diffuse scattering.^{311,320,321} This was advantageous since amorphous material reduces the quality of the refinement.⁵⁶

The CaCO_3 produced in the reactor was found to be single phase calcite (ICDD reference 04-007-0049) (Figure 7. 5). In other words, all peaks could be attributed to calcite. The R_p and R_{wp} values were 5.6 and 7.6% respectively hence the refinement quality was again acceptable. There was no evidence of amorphous phase in the CaCO_3 just like in the Ca(OH)_2 .

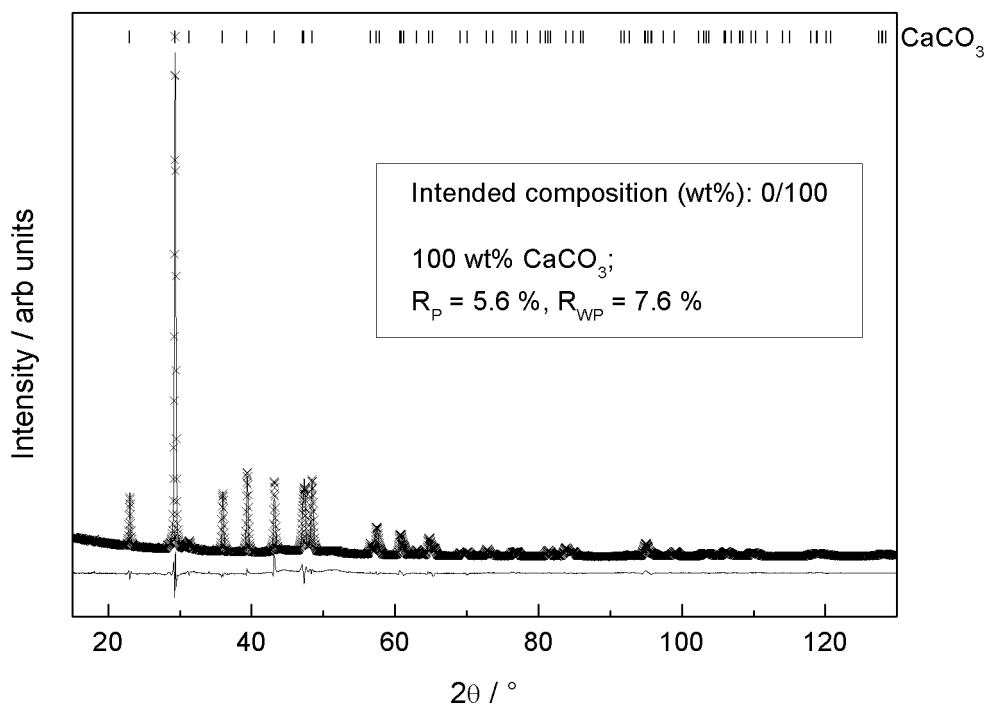


Figure 7. 5. XRD spectrum of CaCO₃ prepared according to section 7.3.3. As Fig. 7.4. Vertical lines show the expected positions of diffraction peaks for CaCO₃.

Mixtures containing 25, 50 and 75 wt% CaCO₃ (Figure 7. 6, Figure 7. 7 and Figure 7. 8) were prepared. For each mixture, a total of 2 g was weighed (e.g. in the case of the 50/50 mixture 1 g of Ca(OH)₂ and 1 g of CaCO₃ was used). The Ca(OH)₂ and CaCO₃ were mixed using a pestle and mortar thus crushing the mixture to a fine powder. XRD analysis and Rietveld refinement was carried out on the three mixtures and the results were in close agreement with their intended composition. R_P and R_{WP} values below 10% were achieved in all cases. Rietveld refinement has been shown elsewhere to provide a reliable means of determining the phase concentration in mixtures of crystalline compounds.^{56,315,316} Note that the maximum value of the Y axis was shifted to lower values as the relative amount of Ca(OH)₂ was reduced. This was done because the intensity of some of the Ca(OH)₂ peaks were much higher than that of the CaCO₃ peaks.

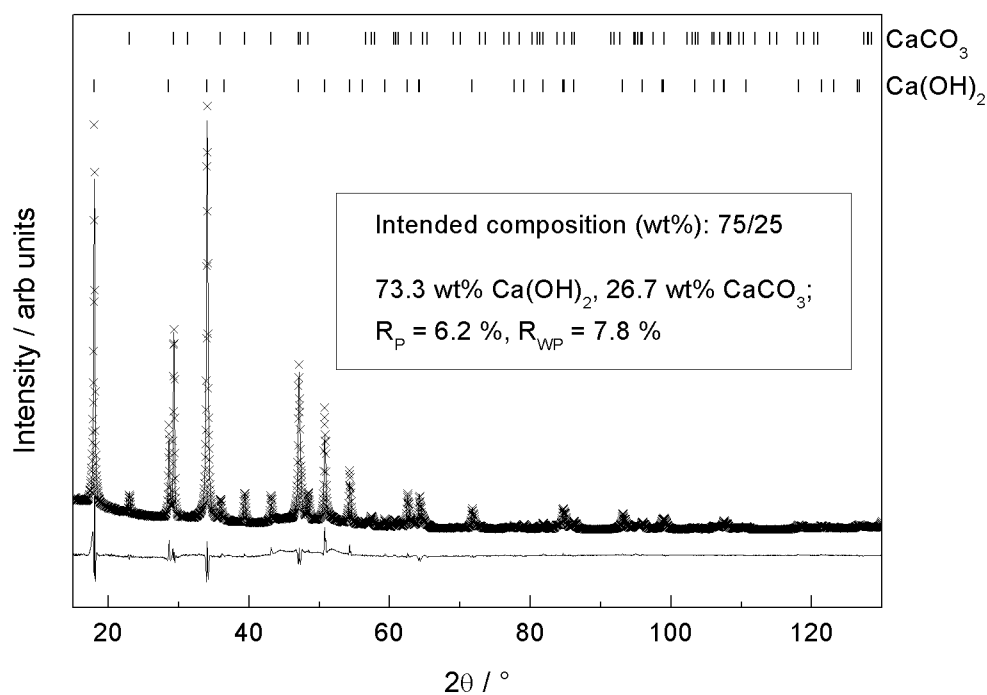


Figure 7. 6. XRD spectra of a mixture of Ca(OH)₂ and CaCO₃ with and intended composition of 75 wt% Ca(OH)₂ and 25 wt% CaCO₃. As Fig. 7.4. Vertical lines show the expected positions of diffraction peaks for Ca(OH)₂ and CaCO₃.

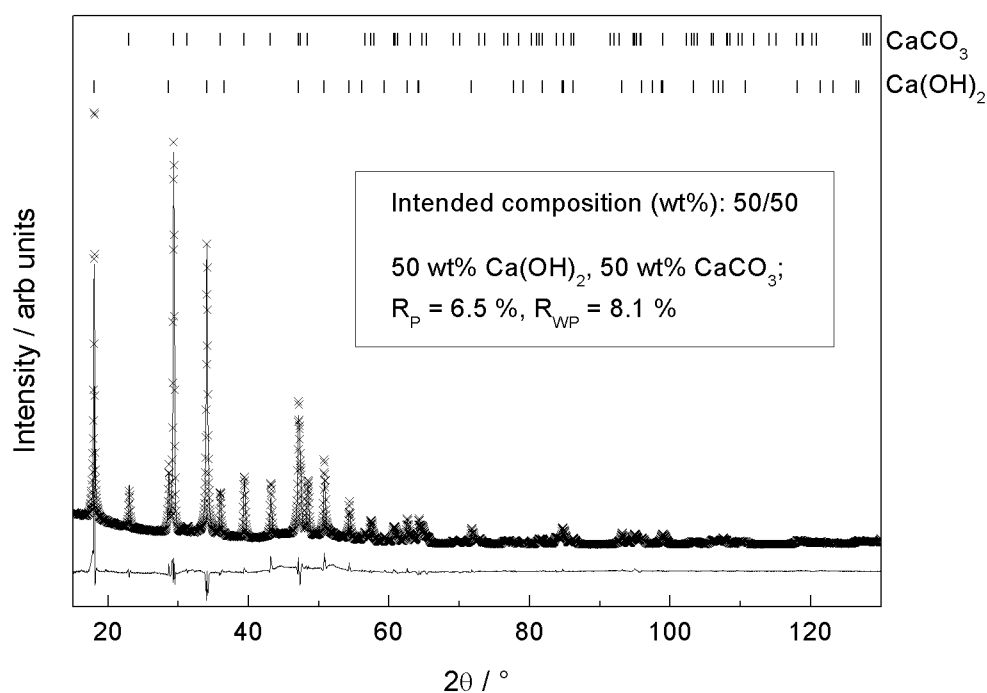


Figure 7. 7. XRD spectra of a mixture of Ca(OH)₂ and CaCO₃ with and intended composition of 50 wt% Ca(OH)₂ and 50 wt% CaCO₃. As Fig. 7.4. Vertical lines show the expected positions of diffraction peaks for Ca(OH)₂ and CaCO₃.

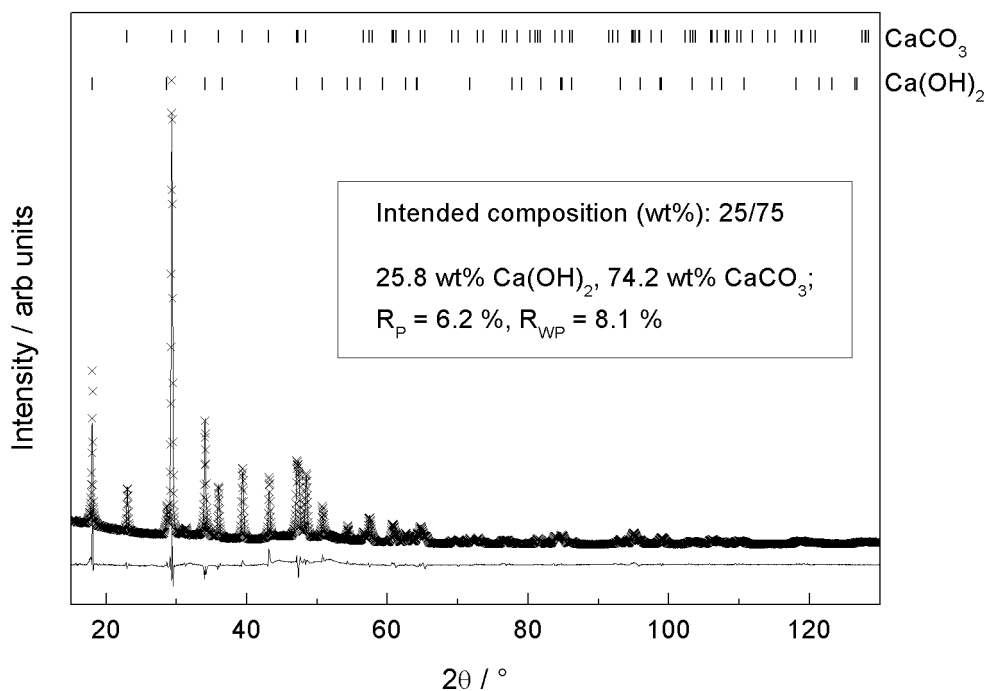


Figure 7. 8. XRD spectra of a mixture of Ca(OH)₂ and CaCO₃ with an intended composition of 25 wt% Ca(OH)₂ and 75 wt% CaCO₃. As Fig. 7.4. Vertical lines show the expected positions of diffraction peaks for Ca(OH)₂ and CaCO₃.

In summary, the accuracy of the refinement (as determined by the residual and quantified by the R_p and R_{WP} values) was acceptable and the results were in close agreement with the intended composition of the mixtures. It was therefore concluded that the method used here provided a reliable measurement of the composition of the Ca-based CO₂ sorbents.

As outlined in Chapter 2, XRD data was collected for the 2θ range 14.993-130.000 ° at a scan speed of 0.190986 ° s⁻¹ for a total of 10 min and 16s, and twelve such scans were carried out back to back for a total scan time of 2h, 3 min and 12s at each temperature. A longer scan time improves the residual and this is why a total scan time of more than 2h was used. However, at most temperatures a phase shift occurred as the scan was carried out which caused an error. Figure 7. 9 shows the results of scans nr 1, 6 and 12 collected for CaO at 500 °C. A close up of the scan range 2θ 46-50 ° revealed an increase in the intensity for two peaks corresponding to the calcite phase from scan 1 to 12.

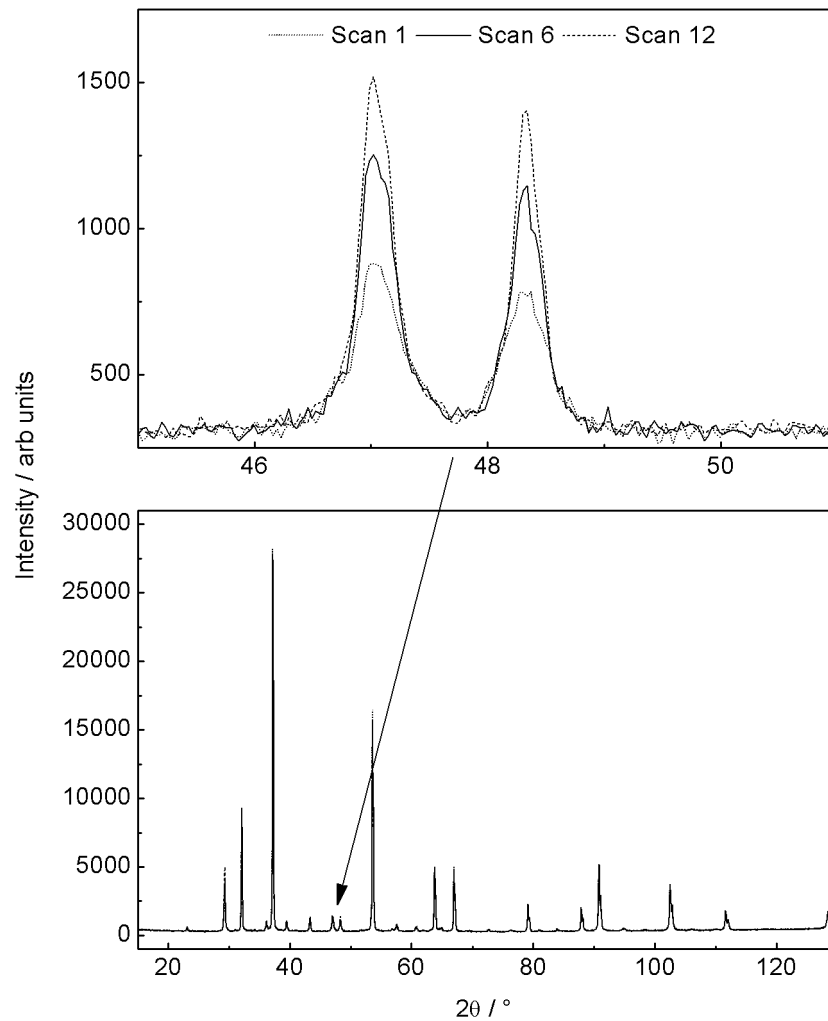


Figure 7. 9. XRD spectrum of scans nr 1, 6 and 12 collected for CaO at 500 °C in a CO₂ atmosphere and a close up of the scan range 2θ 46-50 °.

When peak intensity increases with time, the scan speed needs to be high in order to avoid discrepancy between high and low angle peaks. In order to reduce this discrepancy while simultaneously improve the residual, twelve 10 min scans were carried out instead of one 2h scan.

7.4 BENCHMARKING AGAINST TGA

7.4.1 INTRODUCTION

TGA is a common technique for investigating CO₂ capture by Ca-based sorbents. Therefore, as far as possible, the results from the in situ XRD experiments were benchmarked against results from TGA using the same samples and the same temperature programs under the same atmospheres. Due to the inherent problem with studying partially hydrated CaO in TGA, CaO and Ca(OH)₂ were selected for the benchmarking experiments. Ca(OH)₂ was prepared

according to Chapter 2, Section 2.3, while CaO was prepared by heating commercially available CaO powder (99.95% purity, metal basis, Alfa Aesar) to 700 °C in N₂ to decompose Ca(OH)₂ impurities identified by XRD in Chapter 6. This was conducted in both the TGA and XRD setups directly prior to carbonation which was carried out in CO₂ at temperatures between 25 and 800 °C. Due to the effect of sample mass in TGA on mass transfer and diffusion effects, all TGA experiments were carried out twice, once with 2 mg of sample and once with 10 mg. The results from TGA and in situ XRD are compared and discussed below but first the details of the methodology are given.

7.4.2 METHODOLOGY

7.4.2.1 CARBONATION EXPERIMENT

Carbonation was carried out in CO₂. The temperature was increased to 200, 300, 400, 500, 600, 700 and 800 °C with a heating rate of 40 °C min⁻¹ with a 2h hold at each temperature. For in situ XRD, scans were carried out at each temperature as outlined above and in the case of TGA, mass readings were logged every 30s.

7.4.2.2 CALCULATIONS OF CARBONATION FROM TGA DATA FOR COMPARISON WITH IN SITU XRD

Rietveld refinement returns phase composition in wt%, and so, to allow for a simple comparison with the in situ XRD results, the TGA carbonation data was presented in wt% of the assumed CaCO₃ phase. The wt% CaCO₃ in the sample at any given temperature was derived from the sample mass (m_t , see Equation 7. 1, Equation 7. 2 and Equation 7. 3) recorded at the end of each 2h hold. TGA data is often presented in percentage conversion to CaCO₃ on a molar basis.^{40,144,146} However in single phase samples such as CaO and Ca(OH)₂ this can be converted to wt% CaCO₃. The wt% CaCO₃ (X_{CaCO_3}) at any given time in CaO was defined according to Equation 7. 1 where X = weight %, W = molar mass, m_t = mass reading at time t and m_i is the initial mass:

$$X_{CaCO_3}(m_t) = \left(\frac{\left(\frac{m_t - m_i}{W_{CO_2}} \right) \times W_{CaCO_3}}{m_t} \right) \times 100$$

Equation 7. 1. Definition of wt% CaCO₃ (X_{CaCO_3}) at time t in CaO where X = weight %, W = molar mass, m_t = mass reading at time t and m_i is the initial mass

For calculation of the wt% CaCO₃ (X_{CaCO_3}) in the case of CaO it was assumed that any difference in mass at a given time from the starting mass was due solely to the formation of CaCO₃ via CaO carbonation (Reaction 3. 1).

In the case of Ca(OH)₂, three reactions were possible as the temperature was increased during the carbonation experiment, namely direct Ca(OH)₂ carbonation (Reaction 5. 7), Ca(OH)₂ decomposition to CaO (Reaction 6. 1) as well as conversion CaO carbonation (Reaction 3. 1). Evidence for CO₂ capture by Ca(OH)₂ through Reaction 5. 7 was reported by Blamey et al.⁴⁹ who observed simultaneous evolution of H₂O and increase in mass when studying Ca(OH)₂ samples using TGA-MS. Using TGA it has been shown that Ca(OH)₂ readily decompose at temperatures above 400 °C in N₂ at such a rate that all Ca(OH)₂ could be assumed to have decomposed by the end of the 2h hold during the carbonation experiment carried out here.²⁸⁶

All three reactions could occur simultaneously, however they all result in changes in sample weight and cannot be differentiated from each other with TGA. Therefore, to calculate the conversion to CaCO₃ it has to be assumed that carbonation occurs either through Ca(OH)₂ carbonation (Reaction 5. 7) or through a combination of Ca(OH)₂ decomposition to CaO and CaO carbonation (Reaction 6. 1 and Reaction 3. 1). To investigate the Ca(OH)₂ decomposition reaction separately, decomposition of Ca(OH)₂ was carried out in N₂ by heating to 100, 200, 300, 400, 500, 600 and 700 °C with a 10 min temperature hold at each temperature and a ramp of 40 °C min⁻¹. The 10 min holds were carried out to enable comparison with XRD, however the XRD results are not shown here. The starting mass was 10 mg. Note that Rietveld refinement had revealed that the Ca(OH)₂ contained 3 wt% CaCO₃ (Figure 7. 4). Assuming this sample composition, the sample mass was converted to conversion to CaO (Figure 7. 10). Conversion began at 400 °C and reached 40% after 10 min. With a temperature increase to 500 °C the conversion reached 80%. Complete conversion was reached at 700 °C. Note that the hold time here was 10 min and during the carbonation experiments the hold time was 2h. Therefore the decomposition of the Ca(OH)₂ can be expected to be much higher at the end of each hold during the carbonation experiments. However the extent of the decomposition at any given time could not be accurately determined using the TGA setup and subsequently an assumption had to be made. Based on the data presented here, the more accurate assumption is that of complete decomposition.

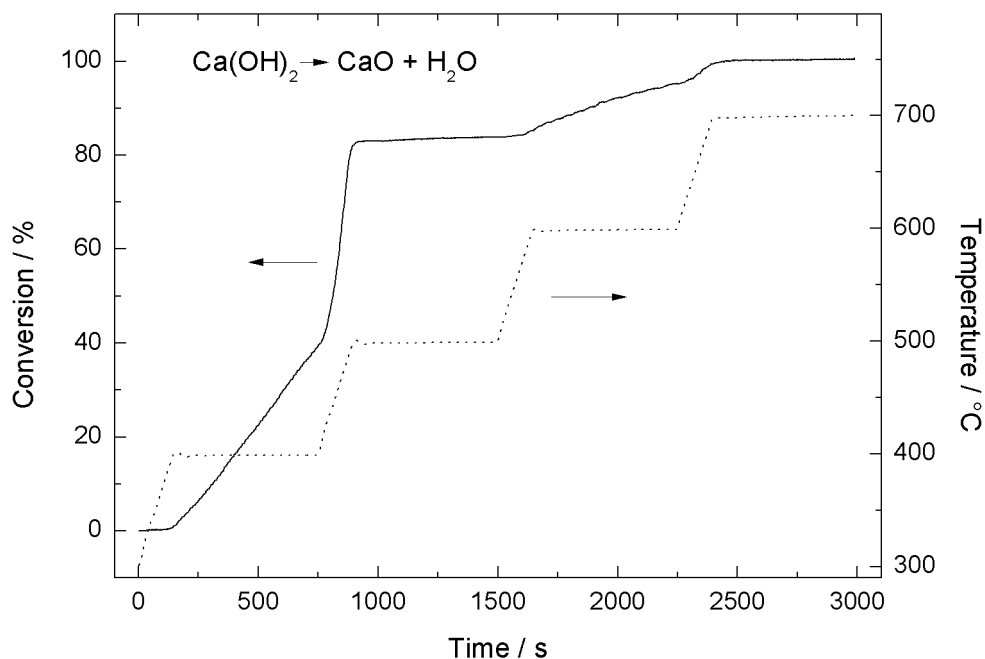


Figure 7. 10. Conversion of $\text{Ca}(\text{OH})_2$ to CaO in TGA in an N_2 atmosphere.

From these results it was concluded that decomposition of $\text{Ca}(\text{OH})_2$ to CaO (Reaction 6. 1) does occur at temperatures of $350\text{ }^\circ\text{C}$ and above. Hence for temperatures up to $400\text{ }^\circ\text{C}$ it can be assumed that conversion proceeds through $\text{Ca}(\text{OH})_2$ carbonation (Reaction 5. 7) while at temperatures of $350\text{ }^\circ\text{C}$ it can be assumed that carbonation occurs through a combination of $\text{Ca}(\text{OH})_2$ decomposition to CaO and CaO carbonation (Reaction 6. 1 and Reaction 3. 1). Consequently, the wt% CaCO_3 (X_{CaCO_3}) at any given time in $\text{Ca}(\text{OH})_2$ was defined according to Equation 7. 2 at temperatures of 200 and $300\text{ }^\circ\text{C}$ and according to Equation 7. 3 at temperatures at $400\text{ }^\circ\text{C}$ and above. In short, Equation 7. 2 assumes that all weight change is due addition of CO_2 and simultaneous removal of H_2O via $\text{Ca}(\text{OH})$ carbonation (Reaction 5. 7). Equation 7. 3 assumes that all initial $\text{Ca}(\text{OH})_2$ has decomposed to CaO (via Reaction 6. 1) and that all weight change is due to subsequent addition of CO_2 via CaO carbonation (Reaction 3. 1). As the $\text{Ca}(\text{OH})_2$ contained 3 wt% CaCO_3 m_i in Equation 7. 2 and Equation 7. 3 was defined as 97% of the sample mass reading at the start of the experiment.

Note that Materic et al.²⁸⁷ has shown that $\text{Ca}(\text{OH})_2$ can decompose at higher temperatures in CO_2 compared to N_2 , an effect named “superheated dehydration” which would affect the validity of the assumptions made with regards to $\text{Ca}(\text{OH})_2$ decomposition. However Blamey et al.⁴⁹ has shown that the effect is due to the formation of a protective carbonate layer and that the superheated dehydration will not occur in samples with a small particle size. The protective carbonate layer hinders water from escaping from inside the particle. In small particles, the carbonate layer does not reach a sufficient thickness to do this. Particle size has also been observed to affect the appearance of the carbonation curve³²² which is turn indicated an effect

on the reaction mechanism. Particles size could also have an effect on heat and mass transfer during calcination as discussed in Chapter 6, Section 6.5.2. All samples used here were in the form of fine powders, hence superheated dehydration was assumed not to occur. The use of powders were necessary for direct comparison with the in situ XRD data as the samples needed to be in powder form to enable reliable XRD results. As a result, the effect of particle size could not be readily investigated.

$$X_{CaCO_3}(m_t) = \left(\frac{\left(\frac{m_t - m_i}{W_{CO_2} - W_{H_2O}} \right) \times W_{CaCO_3}}{m_t} \right) \times 100$$

Equation 7. 2. Definition of wt% CaCO₃ (X_{CaCO₃}) at time *t* in Ca(OH)₂ at temperatures of 200 and 300 °C where X = weight %, W = molar mass, m_{*t*} = mass reading at time *t* and m_{*i*} is the initial mass

$$X_{CaCO_3}(m_t) = \left(\left(\frac{m_t - \left(\frac{m_i}{W_{Ca(OH)_2}} \right) \times W_{CaO}}{W_{CO_2}} \right) \times \frac{W_{CaCO_3}}{m_t} \right) \times 100$$

Equation 7. 3. Definition of wt% CaCO₃ (X_{CaCO₃}) at time *t* in Ca(OH)₂ at temperatures of 400 °C and above where X = weight %, W = molar mass, m_{*t*} = mass reading at time *t* and m_{*i*} is the initial mass

7.4.2.3 SAMPLE PREPARATION

To prepare CaO, commercially available CaO powder was heated to 100 °C then to 200, 300, 400, 500, 600 and 700 °C with a heating rate of 40 °C min⁻¹ under a flow of N₂ (99.998 % + minimum, oxygen free from BOC, UK) at a flow rate of 50 ml min⁻¹ controlled by a mass flow controller (MKS, UK) with a 10 min hold at each temperature. The 10 min hold allowed for an XRD scan to be carried out at each temperature so that the removal of the Ca(OH)₂ could be monitored in the XRD setup. The same temperature program was subsequently used in the TGA system to allow for direct comparison. The CaO was then cooled to room temperature in N₂ and the atmosphere was then switched to CO₂ (99.995 %, CP grade from BOC, UK) prior to the carbonation experiment. Ca(OH)₂ was manufactured according to Chapter 2, Section 2.3 and used directly without pretreatment.

7.4.3 RESULTS AND DISCUSSION

7.4.3.1 PREPARATION OF CAO

XRD data showed that there existed a Ca(OH)_2 phase in the commercially available CaO powder at room temperature (Figure 7. 11). At 700 °C this phase was no longer existent, leaving single phase CaO which is examined in detail in Section 7.4.3.2. The results were in a agreement with the TGA data which revealed complete conversion to single phase CaO (Figure 7. 10). In summary, both XRD and TGA data showed that the commercial CaO powder contained Ca(OH)_2 impurities which were successfully removed by heating to 700 °C in N_2 thus leaving a single phase CaO.

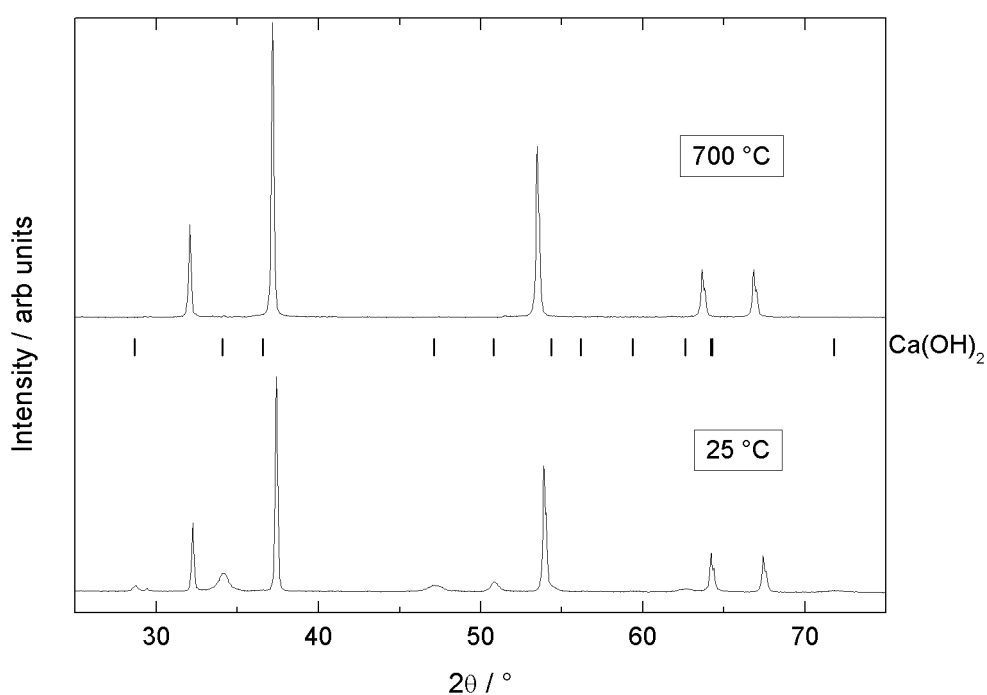


Figure 7. 11. Phase change before and after preparation of CaO from commercially available CaO powder with in situ XRD.

7.4.3.2 CARBONATION OF CAO

During carbonation the data from in situ XRD displayed a clearly visible phase change as a function of temperature just like during the preparation of CaO. At 25 °C the data could be indexed to single phase CaO (ICDD reference 00-037-1497)(Figure 7. 12). The data from 20° to 60° are shown here for clarity. The results showed that the Ca(OH)_2 phase had not reformed as the sample was cooled down to room temperature. At 800 °C, the intensity the CaO peaks were reduced while a series of peaks corresponding to a CaCO_3 calcite phase were observed.

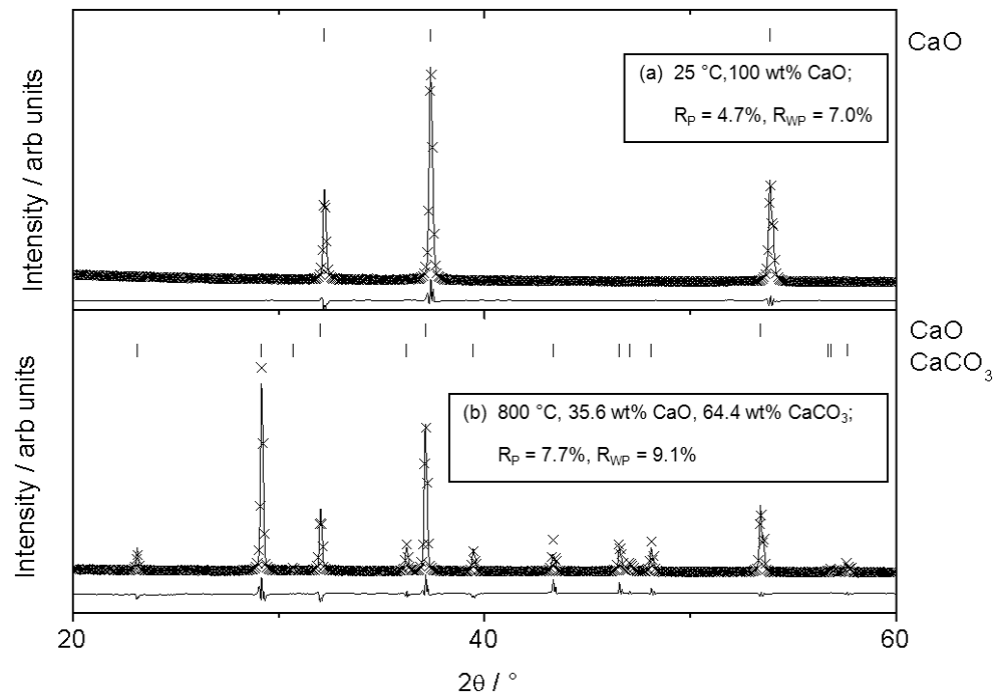


Figure 7. 12. XRD spectra of CaO at 25 and 800 °C in a CO₂ atmosphere. As Fig. 7.4. Vertical lines show the expected positions of diffraction peaks for CaO and CaCO₃.

The wt% CaCO₃ derived from in situ XRD and from TGA on 2 and 10 mg of sample using the temperature program described in Section 7.4.2.1 was plotted over temperature for comparison (Figure 7. 13). Both the XRD and TGA data follow the same shape of curve with XRD indicating a conversion between those of TGA with 2 and 10 mg of sample. At 800 °C, TGA data showed a value of 53.3 and 71.8 wt% for 10 and 2 mg respectively while XRD provided a value of 64.4 wt%. The extent of CaO carbonation is dependent on carbonation time and CO₂ partial pressure such that the conversion increases with longer carbonation time and higher CO₂ partial pressure.^{159,280,323} The carbonation time used here was 14h in total which is much longer than what is commonly found in the literature. However taking the conversions at 700-800 °C for example, the observed carbonation values fell within the spread of anticipated values from the literature.^{40,47}

Sample mass had a significant impact on the conversion derived from TGA data (the dependence on sample mass of TGA results is well known³²⁴). This was attributed to diffusion limitations which increase with increasing sample mass in the TGA setup. Hence the discrepancies between the TGA and XRD results were attributed to differences in diffusion conditions between the two setups. There was for example a significant difference in the contact area between sample and CO₂ between the TGA and the XRD setup. The sample holders used were both cylindrical but with very different dimensions. The XRD sample holder had an area of 250 mm² and a depth of 0.75 mm, whereas the TGA sample holder had an area of 70 mm²

and a depth of 2 mm. The larger size of the XRD sample holder meant that a larger amount of sample was used. While 2 and 10 mg of sample was used in the TGA setup, about 220 mg of sample was used for XRD.

The flow of CO_2 past the samples was also different. In the TGA setup the gas flowed from above the sample and was forced to flow upwards again after having made contact with the sample before continuing through the setup. In the XRD setup the gas entered underneath the sample and flowed around it.

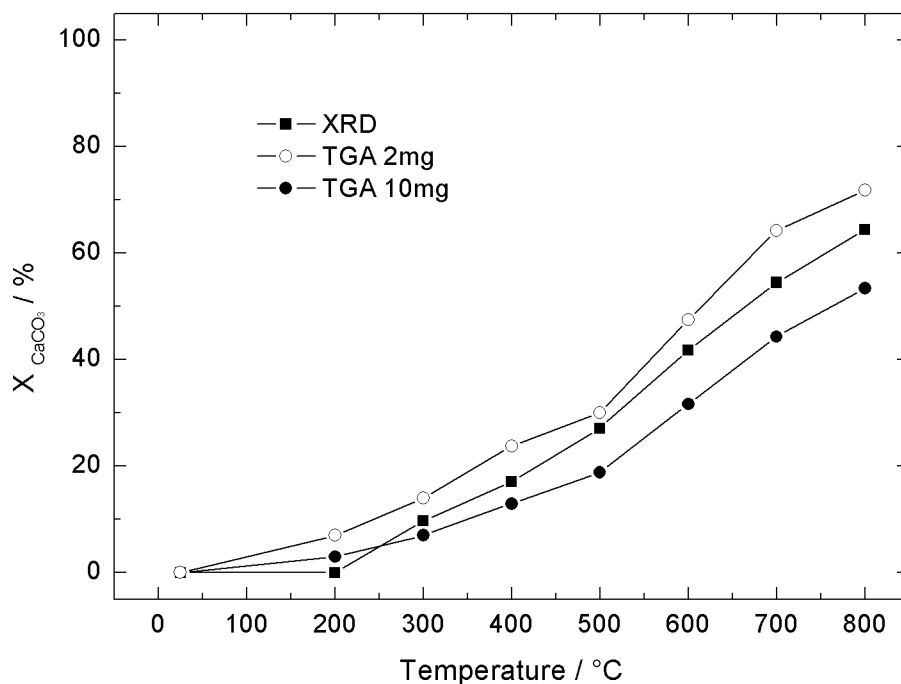


Figure 7. 13. Conversion to CaCO_3 from CaO in a CO_2 atmosphere as a function of temperature, using XRD and TGA. Both are calculated as wt% CaCO_3 . Heating rate $40\text{ }^\circ\text{C min}^{-1}$, 2h hold at each temperature.

7.4.3.3 CARBONATION OF $\text{Ca}(\text{OH})_2$

At $25\text{ }^\circ\text{C}$ there was considerable broadening of the diffraction peaks in the $\text{Ca}(\text{OH})_2$ XRD data which was visible when the 2θ range from 20 to 60 ° was examined (Figure 7. 14). An analysis of this broadening using the size/strain algorithm in the X'Pert Highscore Plus software package used indicated that it was a combination of both size and strain broadening (size = 96 nm, strain = 0.082 %). This could be attributed to the hydration process described in Chapter 2, Section 2.3. Considerable strain and size effects have been observed elsewhere from neutron diffraction studies of $\text{Ca}(\text{OD})_2$, where D is deuterium.³²⁵ The $\text{Ca}(\text{OH})_2$ contained a small amount of CaCO_3 (3 wt%) at $25\text{ }^\circ\text{C}$ as discussed above. At $800\text{ }^\circ\text{C}$ a transformation to 100 wt% CaCO_3

had occurred (Figure 7. 14). The broadening of these peaks was entirely instrumental, in other words size and strain broadening was absent in the CaCO₃ phase.

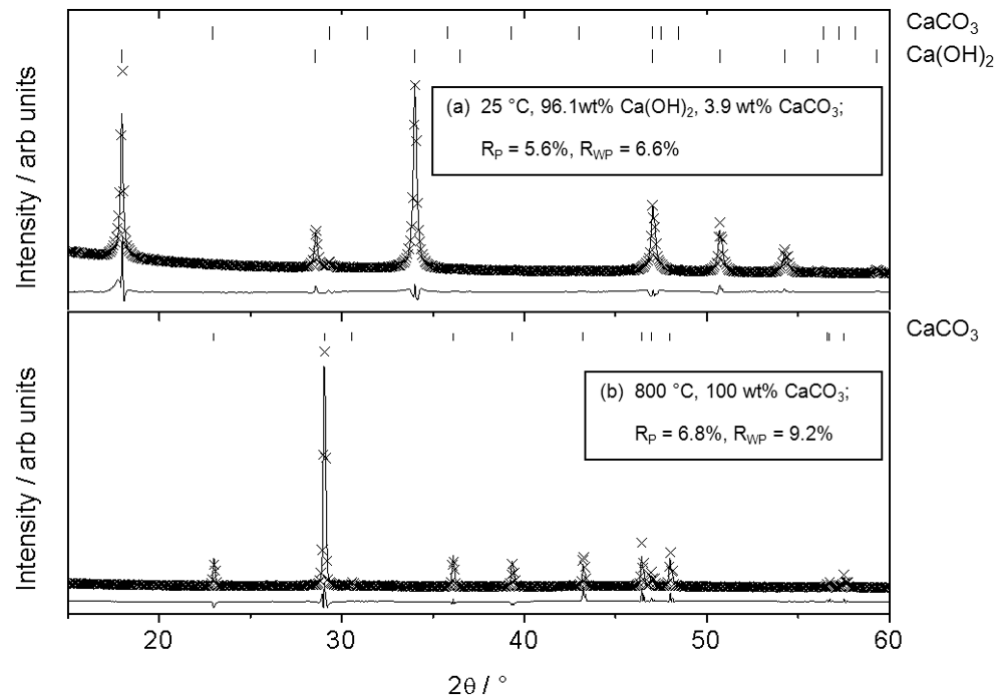


Figure 7. 14. XRD spectra of Ca(OH)₂ at 25 and 800 °C in a CO₂ atmosphere. As Fig. 7.4. Vertical lines show the expected positions of diffraction peaks for Ca(OH)₂ and CaCO₃.

Figure 7. 15 shows collected XRD data as a function of temperature for Ca(OH)₂ in the 2θ range 15-40 °. No peaks that could be indexed to a CaO phase were observed. The approximate location of diffraction peaks derived from a CaO phase (the positions would change with temperature) are shown on the x-axis in at 2θ ~ 32.2 and 37.6 °. This observation indicated that Ca(OH)₂ converted directly to CaCO₃ through Reaction 5. 7. Short lifetime CaO intermediates are possible, but no evidence for them could be identified using the methodology applied here.

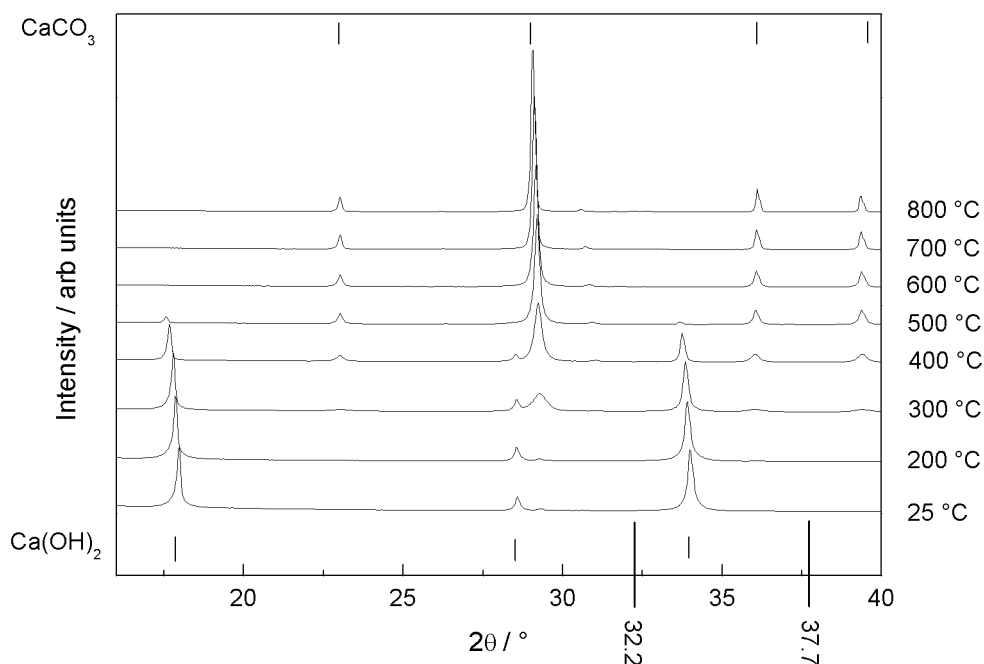


Figure 7. 15. XRD spectra of Ca(OH)_2 transforming to CaCO_3 as a function of temperature. The location of CaCO_3 and Ca(OH)_2 diffraction peaks are shown via tick marks at the top and bottom respectively. CaO phase was not detected as an intermediate phase (absent peaks at $2\theta \sim 32.2$ and 37.7°).

The conversion to CaCO_3 as a function of temperature as determined by XRD and TGA is shown in Figure 7. 16. As with CaO the shape of the curves was similar. XRD data showed 100 wt% CaCO_3 at 600 °C and above while TGA indicated a conversion to 90.1-92.2 wt%. Note that above 400 °C the TGA calculations assumed complete decomposition of the unreacted Ca(OH)_2 phase to CaO (Section 7.4.2.2) because Ca(OH)_2 readily decomposes to CaO at these temperatures (Section 7.4.2.2). However, decomposition was not complete at 400 °C, as observed with TGA (Figure 7. 10). Hence the assumption made here could result in an overestimation of the wt% CaCO_3 at 400 °C which was observed here. The differences in conversion between Ca(OH)_2 and CaO were in agreement with earlier work by Wu et al.²⁸⁰ and has been attributed to the increased surface area which is derived from CaO hydration.^{42,46,47,280} Indeed, the B.E.T. surface area of the CaO and Ca(OH)_2 were 3.5 and 24.9 $\text{m}^2 \text{g}^{-1}$ respectively (see Chapter 6, Section 6.4.1). However the difference in conversion may not be attributed to a difference in surface area alone since Ca(OH)_2 has been shown to be more reactive towards CO_2 than CaO .^{49,287} Sample mass had no impact on the conversion of Ca(OH)_2 in the TGA system where diffusion limitations were lower due to its higher surface area.

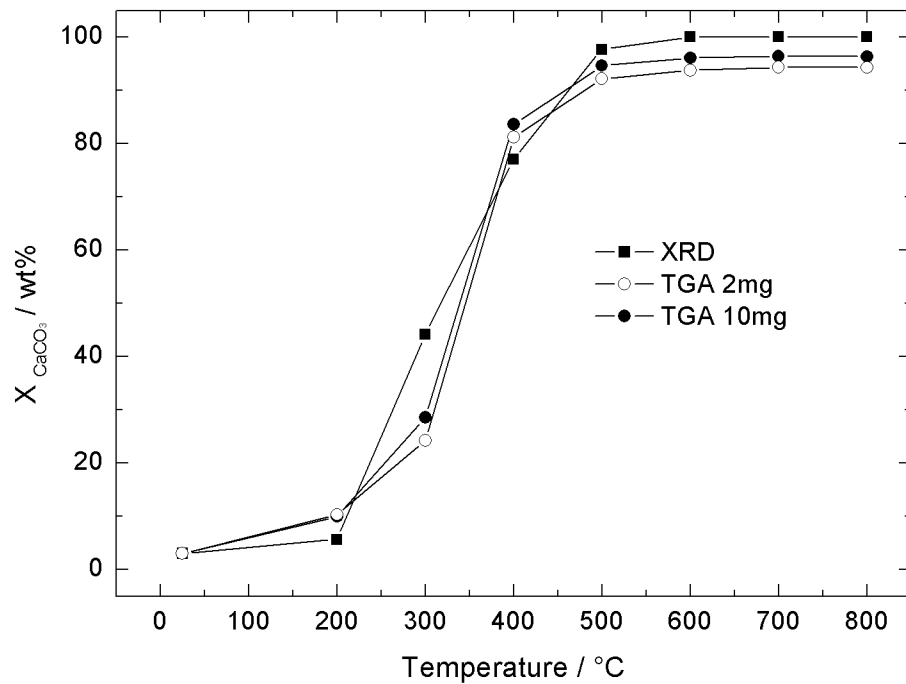


Figure 7. 16. Conversion to CaCO₃ from Ca(OH)₂ in a CO₂ atmosphere as a function of temperature, using XRD and TGA. Both are calculated as wt% CaCO₃. Heating rate 40 °C min⁻¹, 2h hold at each temperature.

At temperature of 500 °C and above, XRD data consistently showed a higher conversion than TGA. When the sample was removed from the XRD and TGA setup it had formed a pellet. This could be explained by sintering which is known to occur during carbonation of Ca-based sorbents and causes densification and loss of porosity.^{117,326} Carbonation is initiated at the gas/solid interface between a sorbent particle and the surrounding CO₂ containing atmosphere. Therefore, the Ca(OH)₂ particles at the top of the sample would be expected to be converted to CaCO₃ first. As a result the particles at the top could be expected to convert to a higher extent than the ones at the bottom. This would not affect the TGA results. However, if the penetration depth of the X-ray beam was less than the thickness of the CaCO₃ layer this would result in an overestimation of the wt% CaCO₃ of the sample during in situ XRD carbonation (Figure 7. 17).

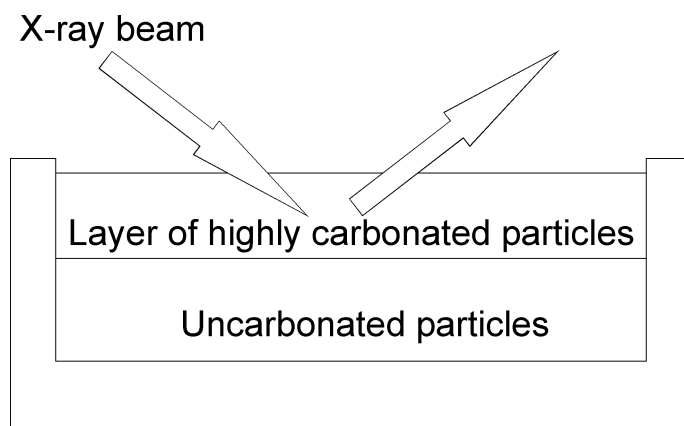


Figure 7. 17. Illustration of an X-ray beam reflecting off highly carbonated particle in a sample containing a mixture of highly carbonated particles and uncarbonated particles.

To investigate this, a Ca(OH)_2 sample was heated at $800\text{ }^\circ\text{C}$ in CO_2 in the in situ XRD setup until the data displayed a single phase CaCO_3 diffraction pattern (Figure 7. 18). Note that the fit is worse than before because the scan presented here was carried out for 10 min while the other results were carried out for a total of 2h. However, no peaks corresponding to either Ca(OH)_2 or CaO were identified. As shown above, Ca(OH)_2 decomposes to CaO at temperature above $400\text{ }^\circ\text{C}$ and so if any other phase was to be found it would be expected to be CaO .

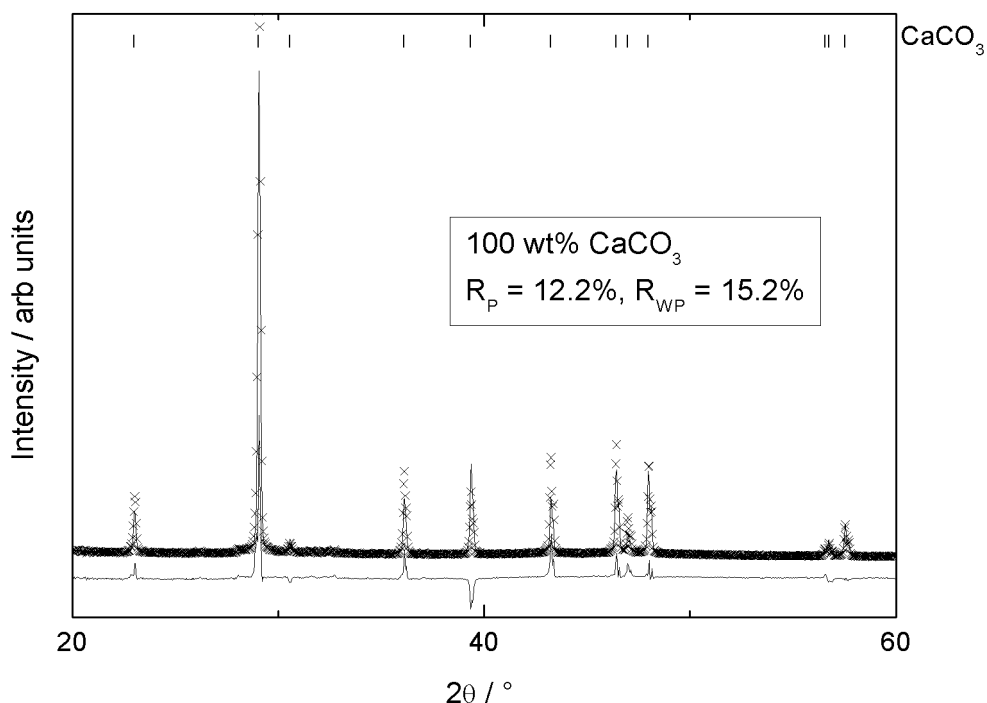


Figure 7. 18. XRD spectrum of Ca(OH)_2 heated to $800\text{ }^\circ\text{C}$ in CO_2 . As Fig. 7.4. Vertical lines show the expected positions of diffraction peaks for CaCO_3 .

The sample was cooled down to room temperature. The sample had formed a pellet like it had done in previous experiments. This pellet was turned upside down and the back of it was scanned. The pellet was then crushed to a powder which was scanned again. Both these scans resulted in spectra containing peaks corresponding to single phase CaCO₃ (Figure 7. 19). Given the hygroscopic nature of CaO, formation of Ca(OH)₂ could be expected from any CaO in the sample, especially when the pellet was crushed. However, no CaO or Ca(OH)₂ phase was identified. The highest intensity peaks for CaO and Ca(OH)₂ are found at 2θ 37.4 ° and 34.1 ° respectively (ICDD reference 00-037-1497 and 04-006-9147). Those positions are marked with dotted circles in Figure 7. 19 but no peaks were found there. It was concluded that the overestimation of the wt% CaCO₃ in the sample was not the result of insufficient X-ray penetration depth.

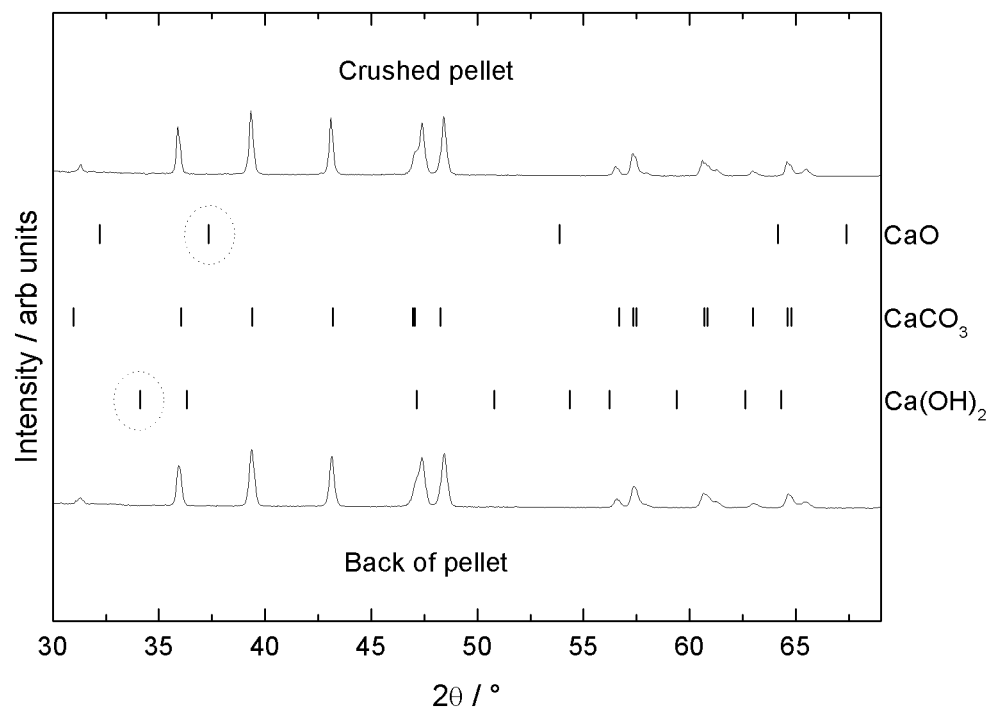


Figure 7. 19. XRD spectra of the back of the pellet formed during carbonation and of the powder resulting from crushing that pellet. As Figure 7. 4. Vertical lines show the expected positions of diffraction peaks for CaO, Ca(OH)₂ and CaCO₃.

7.5 PARTIALLY HYDRATED CAO

7.5.1 INTRODUCTION

As outlined in Section 7.1 the study of hydrated CaO based sorbents using conventional techniques such as TGA is problematic. As described in Section 7.4.2.2 a number of assumptions have to be made about the reaction mechanism(s) in order to derive information on

carbonation of hydrated CaO from TGA data. To investigate a partially hydrated sorbent presents further challenges. Prior to TGA, the relative amounts of CaO and Ca(OH)₂ in the sample has to be known. This could be achieved by hydrating a dry CaO sample by introducing a known amount of steam into the TGA and quantifying the steam in the outlet, which would be very difficult to achieve in practice with a high enough accuracy. Another method would be to decompose an aliquot of a partially hydrated sample in an inert atmosphere and quantify the change in weight. However, homogenous hydration of the sample would have to be assumed. Also, in a partially hydrated sample, CaO and Ca(OH)₂ carbonation as well as Ca(OH)₂ decomposition to CaO is possible at temperatures below 400 °C as opposed to only CaO carbonation in the case of pure CaO and only Ca(OH)₂ carbonation in the case of pure Ca(OH)₂. In situ XRD was carried out on partially hydrated CaO in order to investigate the reaction mechanism.

7.5.2 METHODOLOGY

The same carbonation experiment as described above was carried out on a partially hydrated sample. Rietveld analysis was carried out as before to investigate phase changes as a function of temperature.

7.5.3 RESULTS AND DISCUSSION

7.5.3.1 SAMPLE PREPARATION

The commercial CaO powder used in Section 7.4.3 was used to study partially hydrated CaO. After having been exposed to air for 5 min at room temperature, the CaO powder contained 64.7 wt% CaO, 33.6 wt% Ca(OH)₂ and a small amount of CaCO₃ (1.7 wt%) (Figure 7.20).

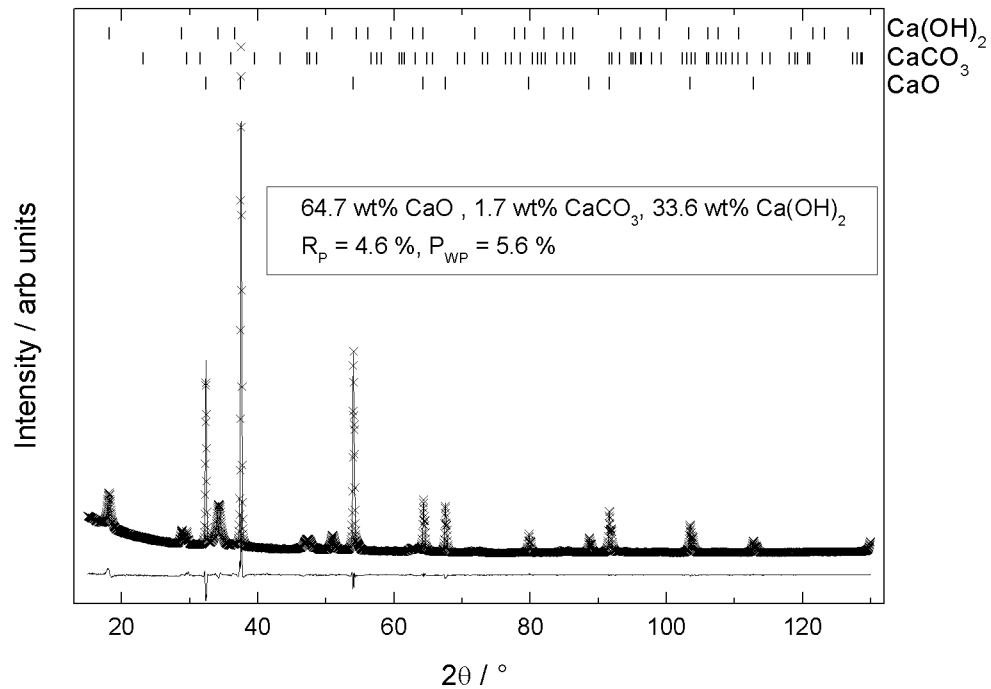


Figure 7. 20. XRD spectrum of partially hydrated CaO. As Fig. 7.4. Vertical lines show the expected positions of diffraction peaks for CaO, Ca(OH)₂ and CaCO₃.

7.5.3.2 CARBONATION

When phase composition was plotted versus temperature it was observed that at temperatures above 300 °C, the concentration of Ca(OH)₂ rapidly diminished, and formed CaCO₃ in preference to CaO (Figure 7. 21). At 600 °C the Ca(OH)₂ phase was gone. Note that although this sample contained significant amounts of Ca(OH)₂, complete conversion to CaCO₃ did not occur. The pure Ca(OH)₂, reached 100 % conversion while the partially hydrated sample only reached 65.3 %.

Note that the different phases of the same sample (partially hydrated CaO) is shown in Figure 7. 21 while the wt% CaCO₃ in each sample is shown in Figure 7. 13 and Figure 7. 16.

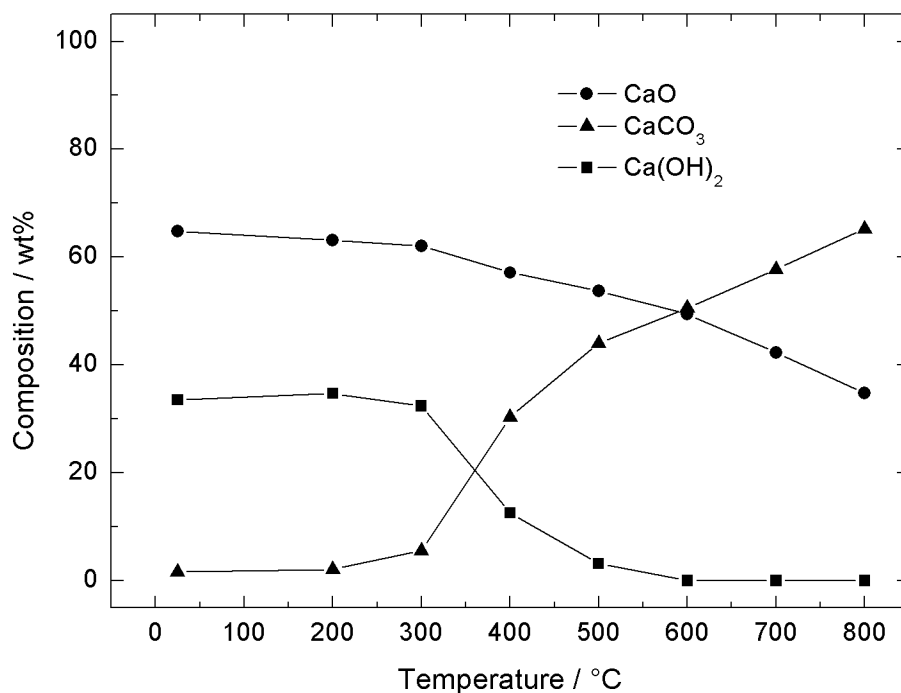


Figure 7. 21. Composition of partially hydrated CaO as a function of temperature in a CO₂ atmosphere derived from in situ XRD analysis. Heating rate 40 °C min⁻¹, 2h hold at each temperature.

The wt% CaCO₃ as a function of temperature for the partially hydrated CaO was viewed alongside that of the pure Ca(OH)₂ and the pure CaO (Figure 7. 22). The conversion to CaCO₃ was faster in the partially hydrated CaO compared to the pure CaO between 300 and 600 °C and reached a very similar extent of conversion at 800 °C. The conversion was much faster in the case of pure Ca(OH)₂ and reached a much higher extent of conversion. Note that the conversion in the partially hydrated was faster than CaO in the temperature range where there was still a Ca(OH)₂ phase in the sample (Figure 7. 21). The results indicated that the Ca(OH)₂ phase readily converted to CaCO₃ through Ca(OH)₂ carbonation until the Ca(OH)₂ phase was removed from the sample. After that, conversion proceeded through CaO carbonation. Complete hydration to pure Ca(OH)₂ increased both the speed of conversion as well as the total conversion. However the results showed that a partial hydration to 33.6 wt% Ca(OH)₂ could increase the speed of conversion to only a limited extent and did not have any effect on the total conversion. Potentially, a hydration level would exist above which complete conversion to CaCO₃ would be possible.

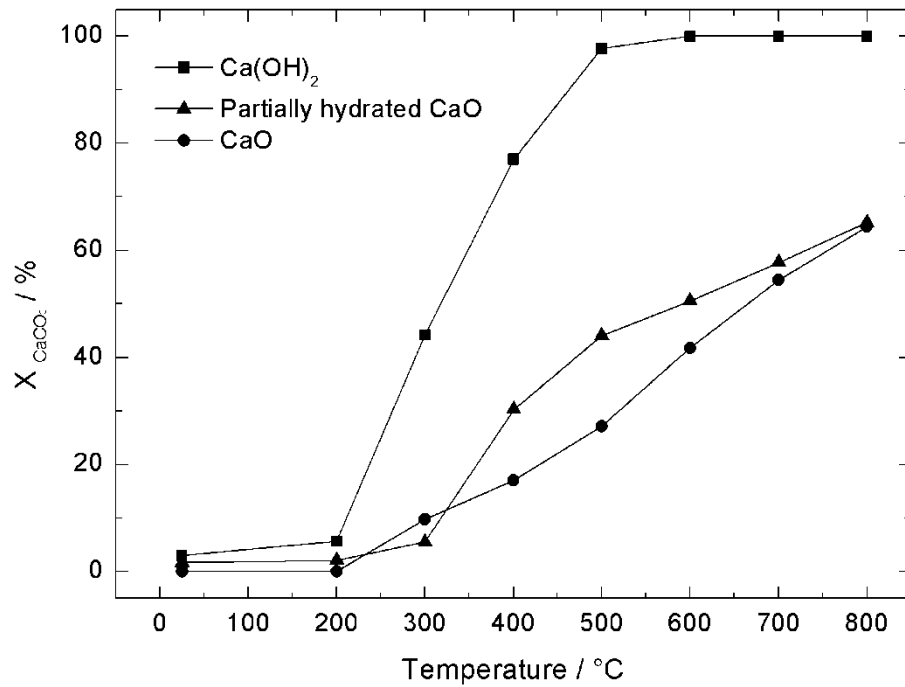


Figure 7. 22. Wt% CaCO₃ as a function of temperature for CaO, partially hydrated CaO and Ca(OH)₂ derived from in situ XRD analysis. Heating rate 40 °C min⁻¹, 2h hold at each temperature.

The Ca(OH)₂ peaks displayed anisotropic peak broadening (i.e. some peaks were broader than others). The highest intensity Ca(OH)₂ peak (at 2θ 34.1 °) is shown in Figure 7. 23, while the others are left out for clarity. Note that the y-axis scale is the same in all four graphs in Figure 7. 23. The CaO peak at 2θ 32.2 ° is shown as a reference. Note that the peak broadening for the CaO phase was much smaller than for the Ca(OH)₂ phase. As the temperature increased, this broadening reduced and the peaks became sharper. Simultaneously, there was no change in peak broadening for the CaO phase. Above 300 °C the intensity of the Ca(OH)₂ peaks reduced while the intensity of the CaO peaks remained stable. Simultaneously the CaCO₃ peaks increased in intensity thus providing a higher wt% value from the Rietveld refinement. This showed that the Ca(OH)₂ phase converted to CaCO₃ through Reaction 5. 7 while the CaO phase remained unaffected up to 500 °C.

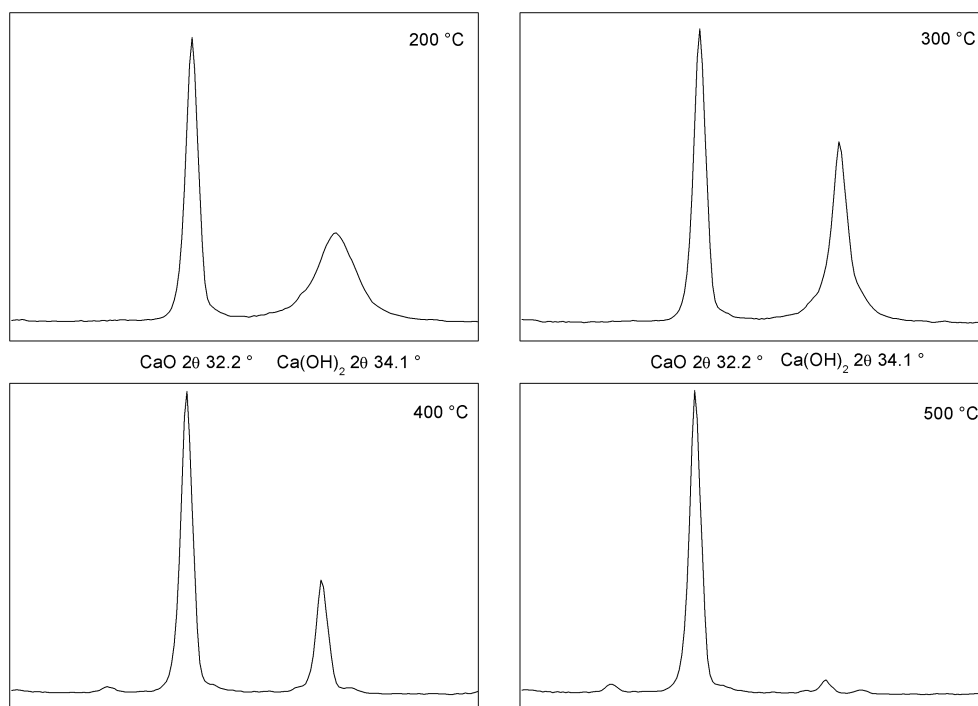


Figure 7. 23. XRD spectra at 2θ 30-36 ° at temperatures of 200-500 °C displaying the broadening of the Ca(OH)_2 peak at 2θ 34.1 °.

The source of the anisotropic peak broadening could be instrumental, strain or size effects in the Ca(OH)_2 phase. A thorough analysis of this anisotropic broadening was difficult with the XRD setup used here due to significant instrumental broadening and the development of asymmetric peaks at low angles as a result of axial divergence. This is particularly problematic for $2\theta < 50^\circ$ ³²⁷ and is therefore a significant factor in the case of Ca(OH)_2 as the highest intensity Ca(OH)_2 diffraction peak is found at 2θ 34.1 ° (Figure 7. 19). Therefore, high resolution synchrotron diffraction was used to study the anisotropic broadening of the Ca(OH)_2 phase in partially hydrated CaO.

7.5.4 HIGH RESOLUTION SYNCHROTRON DIFFRACTION

Commercial CaO was sealed in a capillary tube, loaded in air and investigated at room temperature using beamline I11 at the Diamond Light Source (Didcot, UK).³²⁸ A spectrum was collected from 2θ 3-150 ° using radiation with an energy of 15 KeV ($\lambda \approx 0.826 \text{ \AA}$) and Rietveld analysis was carried out using GSAS.³²⁹ Profile function 3 was used with the profile options Y, P and γ_{11} , γ_{22} , γ_{33} , γ_{12} , γ_{13} , γ_{23} were refined in order to simulate anisotropic broadening.

Figure 7. 24 shows significant broadening of the (001), (100) and (002) Ca(OH)_2 peaks. A CaO peak at 2θ 17.1 ° is shown which is extremely sharp. The (001 and (002) peaks were clearly broader than the (002) peak as shown by their FWHM values.

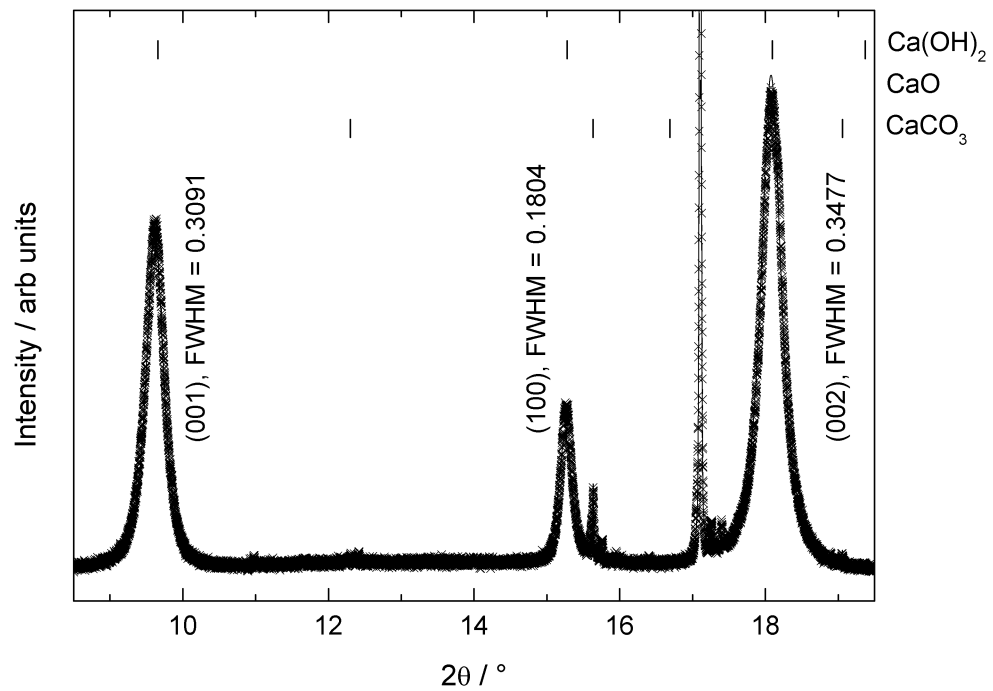


Figure 7. 24. High resolution synchrotron spectrum of partially hydration CaO for 2θ 9-19 °. As Fig. 7.4. Vertical lines show the expected positions of diffraction peaks for CaO, Ca(OH)₂ and CaCO₃. Peak labels showing the full width half maximum (FWM).

The anisotropic broadening was quantified using Williamson-Hall plots (Figure 7. 25).³³⁰ $\beta \cos \theta$ was plotted against $\sin \theta$ for the (001) and (100) families and the average microstrain and coherence length (size effects) were determined through a determination of the gradient and the intercept, and the instrumental broadening. The stress was calculated from the microstrain and Young's modulus for Ca(OH)₂ (35.24 GPa³³¹).

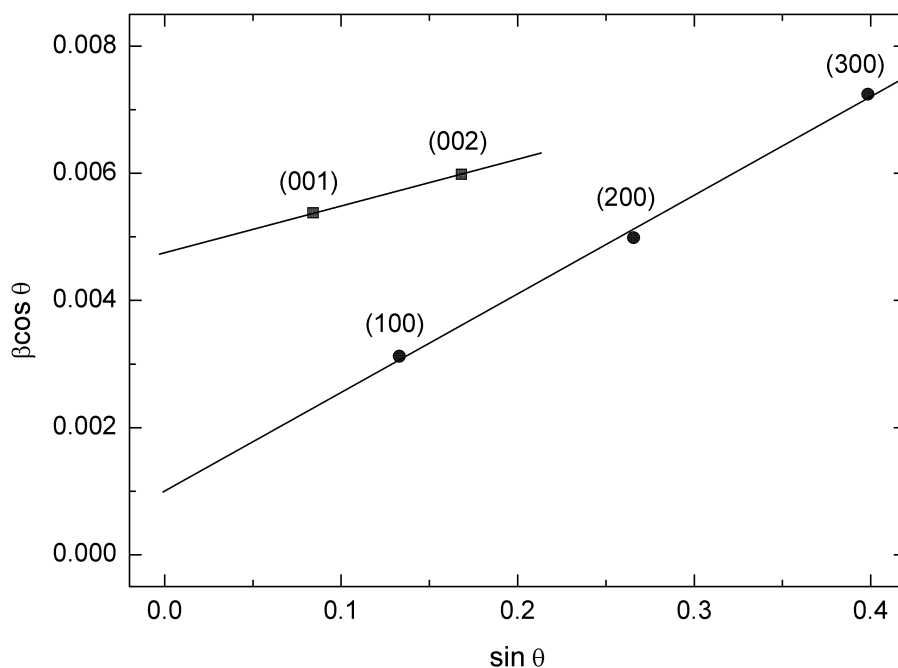


Figure 7. 25. Williamson-Hall plots for the Ca(OH)_2 phase of the partially hydrated CaO from data collected using high resolution synchrotron diffraction.

The results from the Williamson-Hall plots are listed in Table 7. 2. The microstrain in the (100) direction (a-axis) is almost twice as high as in the (001) (c-axis) direction. This can be attributed to the presence of a Ca(OH)_2 shell around a CaO core with the (001) direction normal to the CaO surface and the (100) parallel to the surface (Figure 7. 26).

Table 7. 2. Derived data from a Williamson Hall plot of high resolution synchrotron data of Ca(OH)_2 in partially hydrated CaO. For comparison, the derived strain, size and stress are also shown for pure Ca(OH)_2 , as determined using XRD at Leeds with subsequent Rietveld analysis.

	Slope	Intercept	Average strain / %	Size / nm	Stress / MPa
(001) direction	0.00722	0.00477	0.36	16	130
(100) direction	0.01551	0.00099	0.78	75	270

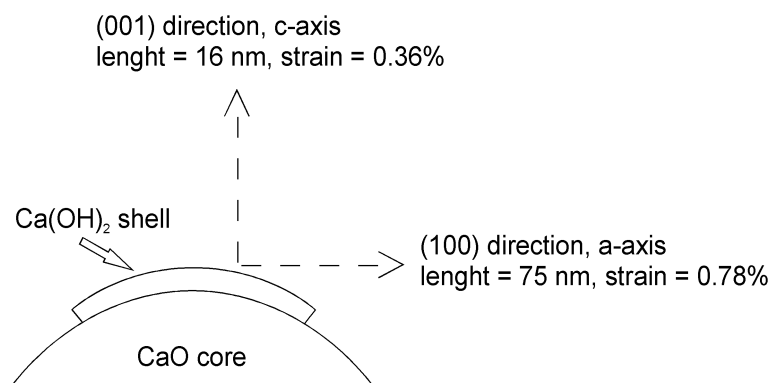


Figure 7. 26. Illustration of a Ca(OH)_2 shell around a CaO core.

A flexural strength of 14-15 MPa for Ca(OH)₂ was extrapolated from literature for porous portlandite.³³¹ The stresses calculated here were much higher (130 and 270 MPa in the (100) and (001) directions respectively, Table 7. 2). The provides evidence of high internal stress in the material during hydration which can explain the loss of mechanical strength during hydration of Ca-based materials.

7.6 INVESTIGATION OF CaO/Ca₁₂Al₁₄O₃₃ CARBONATION

7.6.1 INTRODUCTION

An investigation of the carbonation of CaO/Ca₁₂Al₁₄O₃₃ sorbent investigated in Chapter 6 was carried out using the same in situ XRD setup and methodology as for carbonation of CaO and Ca(OH)₂. XRD was used in Chapter 6 to confirm the formation of a Ca₁₂Al₁₄O₃₃ phase during sorbent preparation. In situ XRD was carried out on the sorbent in order to investigate phase changes during decomposition and carbonation.

7.6.2 RESULTS AND DISCUSSION

7.6.2.1 PREPARATION

The sample was prepared as the CaO sample was by heating to 700 °C in N₂ to remove Ca(OH)₂ impurities (as described in Section 7.4.3.1). Prior to preparation, the sorbent contained 17.2 wt% Ca(OH)₂, 56.6 wt% CaO and 26.2 wt% Ca₁₂Al₁₄O₃₃. (Figure 7. 27).

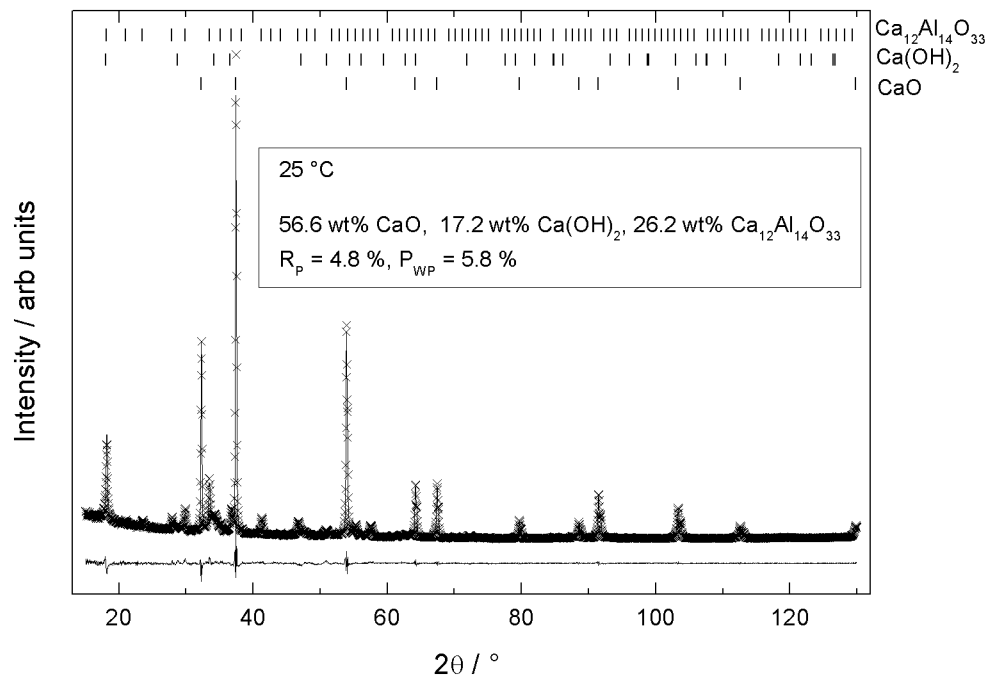


Figure 7. 27. XRD spectrum of CaO/Ca₁₂Al₁₄O₃₃. As Fig. 7.4. Vertical lines show the expected positions of diffraction peaks for CaO, Ca(OH)₂ and Ca₁₂Al₁₄O₃₃.

After preparation, prior to carbonation (i.e. back at 25 °C after heating to 700 °C) the Ca(OH)_2 phase had been removed and the sorbent contained 70.8 wt% CaO and 29.2 wt% $\text{Ca}_{12}\text{Al}_{14}\text{O}_{33}$ (Figure 7. 28). It was hypothesized that the Ca(OH)_2 had decomposed to CaO while the $\text{Ca}_{12}\text{Al}_{14}\text{O}_{33}$ phase had remained inert. To test this, the expected wt% CaO from such a decomposition route was calculated and compared with the results of the refinement carried out after preparation.

100 g of sample was assumed, and so the mass of CaO after preparation would be 69.6 g according to :

$$\text{Mass CaO after preparation} = \left(\frac{56.6}{W_{\text{CaO}}} + \frac{17.2}{W_{\text{Ca(OH)}_2}} \right) \times W_{\text{CaO}}$$

Where W = molar mass.

Assuming that the $\text{Ca}_{12}\text{Al}_{14}\text{O}_{33}$ phase had remained inert, the total sample mass after preparation would then be $69.6 + 26.2 = 95.8$ g. Note that 26.2 g was the mass of the $\text{Ca}_{12}\text{Al}_{14}\text{O}_{33}$ phase before preparation assuming 100 g of sample (Figure 7. 27). This provided an expected composition of 72.6 wt% CaO and 27.3 wt% $\text{Ca}_{12}\text{Al}_{14}\text{O}_{33}$. The Rietveld refinement returned values for CaO and $\text{Ca}_{12}\text{Al}_{14}\text{O}_{33}$ of 70.8 and 29.2 wt% respectively. It was concluded that the Ca(OH)_2 phase had been removed and the $\text{Ca}_{12}\text{Al}_{14}\text{O}_{33}$ phase had remained inert as the values were considered close enough to the expected values given the error of the Rietveld refinement.

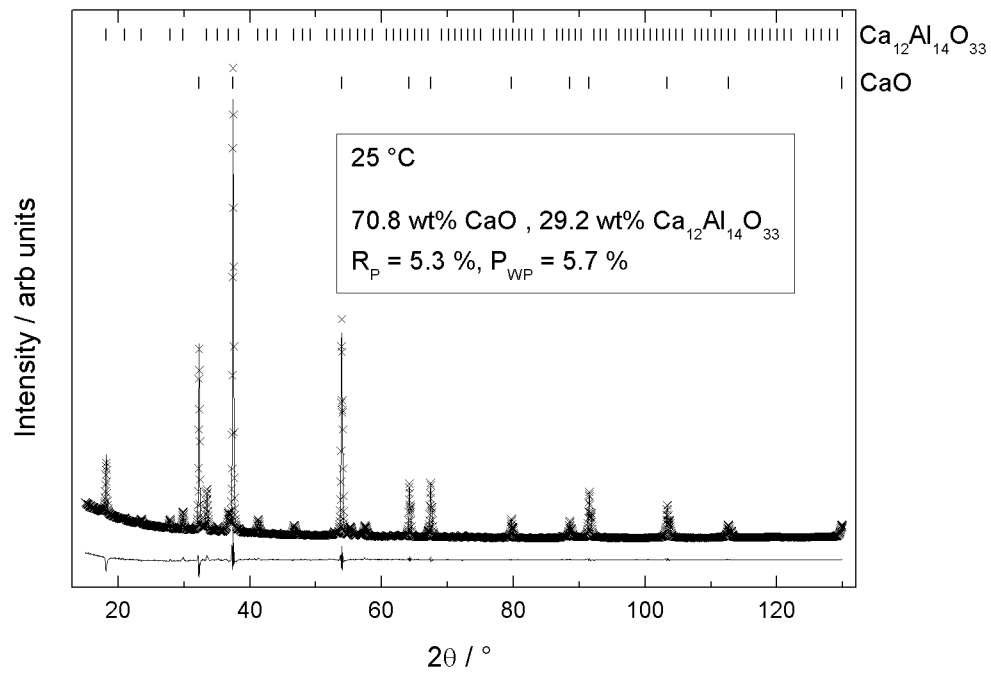


Figure 7. 28. Spectrum of CaO/Ca₁₂Al₁₄O₃₃ after removal of the Ca(OH)₂ phase by heating to 700 °C in N₂. As Fig. 7.4. Vertical lines show the expected positions of diffraction peaks for CaO, and Ca₁₂Al₁₄O₃₃.

7.6.2.2 CARBONATION

Carbonation was carried out as described above (Section 7.4.2.1) after sample preparation. The CaO phase converted to CaCO₃ with increased temperature beginning at a temperature above 200 °C (Figure 7. 29) which is what was observed for both CaO and Ca(OH)₂ in the previous in situ XRD experiments (Figure 7. 13 and Figure 7. 16).

Note that the different phases of the same sample (CaO/Ca₁₂Al₁₄O₃₃) is shown in Figure 7. 29 and so the curve representing CaCO₃ can be compared with the wt% CaCO₃ data from Figure 7. 13 and Figure 7. 16. The B.E.T. surface area of the CaO/Ca₁₂Al₁₄O₃₃ sorbent was 9.1 m² g⁻¹ which was higher than that of the CaO precursor (3.5 m² g⁻¹) but lower than that of the Ca(OH)₂ (24.9 m² g⁻¹). This explained the observation given that surface area has a major impact on the reactivity of Ca-based sorbents towards CO₂. The work of Martavaltzi and Lemonidou²⁷⁵ is of particular relevance to the work presented here. They prepared Ca-based sorbents with Ca₁₂Al₁₄O₃₃ as a binder using in a number of different ways resulting in 7 batches of the same sorbent with differing composition, surface area etc. All batches were tested for CO₂ capture using TGA and CO₂ capture capacity was plotted against surface area. It was found that there was a correlation between CO₂ capture capacity and surface area with an R² value of 0.94.

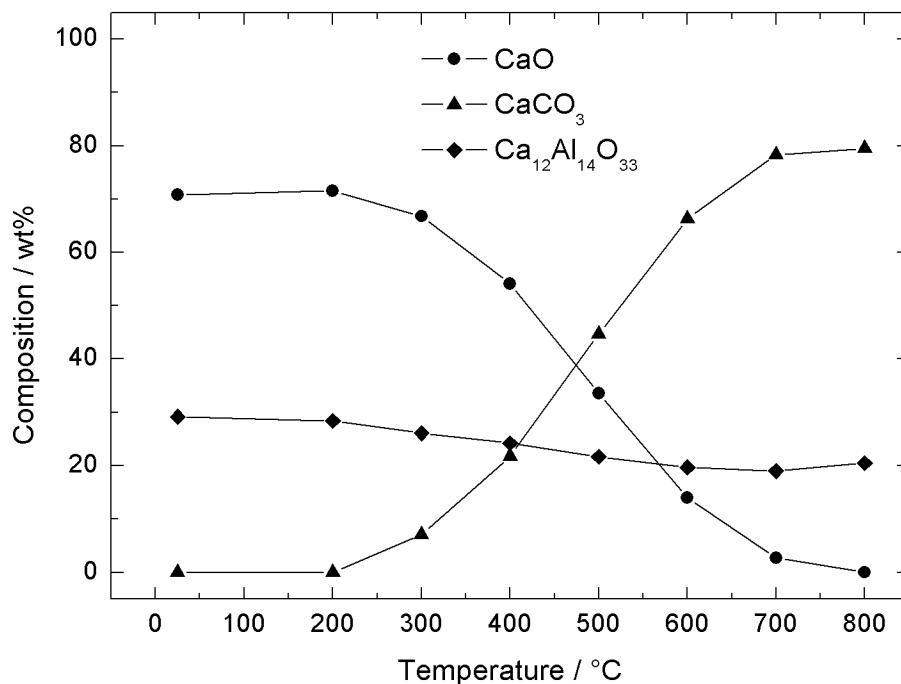


Figure 7. 29. Composition of CaO/Ca₁₂Al₁₄O₃₃ as a function of temperature in a CO₂ atmosphere derived from in situ XRD analysis.

At 800 °C the CaO phase had converted completely to CaCO₃ which was in agreement with the literature on CaO/Ca₁₂Al₁₄O₃₃ sorbents. Complete conversion was reached after carbonation for 12h in 20% CO₂.²⁷⁷ The conversion after 30 min of carbonation increased from 61 to 75% when the CO₂ partial pressure was increased from 7.5 to 15% at 650 °C.³³² Conversion also increased with increased temperature in the range from 500 to 690 °C. Given that a conversion time of 14h CO₂ concentration 100% was used here, complete conversion would be expected based on the literature.

As the relative amount of Ca₁₂Al₁₄O₃₃ increased, the CO₂ capture capacity reduced, indicating that the Ca₁₂Al₁₄O₃₃ phase was not involved in CO₂ capture.²⁷⁵ Previous work combining in situ XRD and Rietveld refinement has demonstrated that the Ca₁₂Al₁₄O₃₃ phase remained inert during carbonation at 750 °C for 1073 min as the CO₂ concentration varied between 0 to 50%.³⁰⁹ As seen in Figure 7. 29, the wt% of Ca₁₂Al₁₄O₃₃ reduced with temperature which would be expected if the Ca₁₂Al₁₄O₃₃ phase was inert because CaCO₃ is heavier than CaO. However, further investigation of the results was needed to investigate whether or not the Ca₁₂Al₁₄O₃₃ phase was inert. The mass of Ca₁₂Al₁₄O₃₃ at each temperature was calculated.

The initial sample mass was assumed to be 100 g. The mass of Ca atoms was calculated as below: Where W = molar mass and mFr = mass fraction (which is multiplied by 100 since 100 g was assumed). The mass fraction data derived from the initial scan carried out at room temperature

$$\begin{aligned} Mass_{Ca\ Ambient} = & \left(\left(\frac{W_{Ca}}{W_{CaO}} \right) \times (mFr_{CaO} \times 100) \right) + \left(\left(\frac{W_{Ca}}{W_{CaCO_3}} \right) \times (mFr_{CaCO_3} \times 100) \right) \\ & + \left(\left(\frac{12 \times W_{Ca}}{W_{Ca_{12}Al_{14}O_{33}}} \right) \times (mFr_{Ca_{12}Al_{14}O_{33}} \times 100) \right) \end{aligned}$$

The mass of Ca atoms in the sample remains constant since the molar ratio of Ca in CaO, CaCO₃ and Ca₁₂Al₁₄O₃₃ is 1:1:12.

The mass of the sample at a given temperature (m_T) was set to the unknown 'Y' and the mass of Ca atoms at a given temperature $m_{T,Ca}$ was defined as: below where the mass fraction data was derived from a scan carried out at any given temperature. The mass of the sample at a given temperature was then obtained by solving for Y.

$$\begin{aligned} m_{T,Ca} = & \left(\left(\frac{W_{Ca}}{W} \right) \times mFr_{CaO} Y \right) + \left(\left(\frac{W_{Ca}}{W_{CaCO_3}} \right) \times mFr_{CaCO_3} Y \right) \\ & + \left(\left(\frac{W_{Ca}}{W_{Ca_{12}Al_{14}O_{33}}} \right) \times mFr_{Ca_{12}Al_{14}O_{33}} Y \right) \end{aligned}$$

The mass of Ca₁₂Al₁₄O₃₃ in the sample at any given temperature was calculated accordingly:

$$m_{Ca_{12}Al_{14}O_{33}} = mFr_{Ca_{12}Al_{14}O_{33}} \times m_T$$

The mass of Ca₁₂Al₁₄O₃₃ at each temperature, as derived from Rietveld refinement and the above calculations varied between 26.3 and 32.0 g (assuming 100 g starting sample mass) therefore there was a 21 % difference between the highest and lowest value (Table 7. 3). The median value was 27.9 and the first and third quartile was 26.6 and 29.1.

Table 7. 3. $\text{Ca}_{12}\text{Al}_{14}\text{O}_{33}$ mass at temperatures between 25 and 800 °C assuming 100 g starting sample mass.

Temperature (°C)	Mass of $\text{Ca}_{12}\text{Al}_{14}\text{O}_{33}$ (g)
25	29.2
200	28.3
300	26.6
400	26.3
500	26.7
600	27.6
700	28.9
800	32.0

However, the residual varied significantly as shown by the spread of the R_P and R_{WP} values. At temperatures above 500 °C the R_P and R_{WP} values increased significantly as a function of temperature (Figure 7. 30). In fact, between 400 and 800 °C, both the R_P and R_{WP} had doubled from 4.6 and 5.2 to 10.0 and 12.7 respectively. If the data gathered above 500 °C were disregarded the difference between the highest and lowest value was reduced to 11%. If only the data with R_P values below 5 were considered, the difference was only 1%.

It was concluded that the $\text{Ca}_{12}\text{Al}_{14}\text{O}_{33}$ phase remained inert during carbonation because the deviations in the results could be attributed to variations in the quality of the refinement. The results were in agreement with Liu et al.³⁰⁹ who reported that the $\text{Ca}_{12}\text{Al}_{14}\text{O}_{33}$ phase remained inert during carbonation.

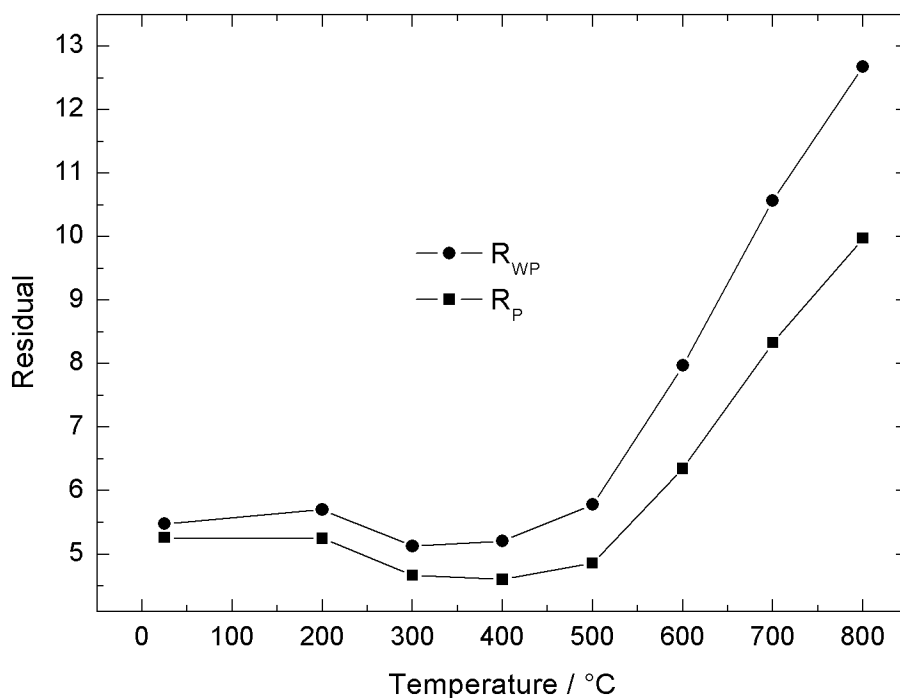


Figure 7. 30. R_P and R_{WP} values from the in XRD spectra collected during in situ XRD analysis of $\text{CaO}/\text{Ca}_{12}\text{Al}_{14}\text{O}_{33}$.

The Ca₁₂Al₁₄O₃₃ phase was indexed to ICDD reference 04-009-6698 which comprised 144 peaks in the range 2θ 15-130 ° compared to 12 for CaO for a total of 156 peaks (Figure 7. 28). Note that the refinement was excellent with an R_P of 5.3 % and an R_{WP} of 5.7 %.

In the presence of a CaCO₃ phase (e.g. at 700 °C, Figure 7. 31) which comprises 75 peaks, a total of 229 peaks were identified by the software instead of the expected 231 (144 + 12 + 75), i.e. 12 for CaO, 144 for Ca₁₂Al₁₄O₃₃ and 73 for CaCO₃. This meant that 2 of the CaCO₃ peaks overlapped with Ca₁₂Al₁₄O₃₃ peaks. Such peak overlap will cause an error in the refinement as evidenced by the R_P and R_{WP} values (8.3 and 10.6 respectively at 700 °C). Note that the error resulting from the peak overlap was insignificant at low conversions (Figure 7. 30), but increased as the intensity of the CaCO₃ peaks increased. Note that for clarity the scale Y-axis in Figure 7. 28 and Figure 7. 31 are different.

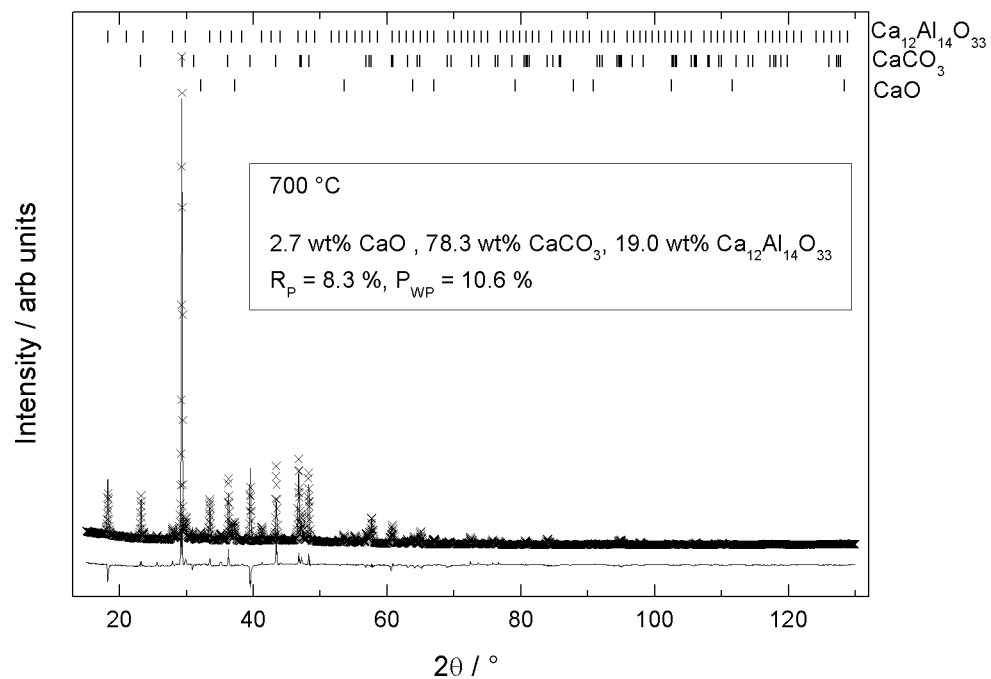


Figure 7. 31. XRD spectra of CaO/Ca₁₂Al₁₄O₃₃ at 700 °C in a CO₂ atmosphere. As Fig. 7.4. Vertical lines show the expected positions of diffraction peaks for CaO, CaCO₃ and Ca₁₂Al₁₄O₃₃.

CHAPTER 8: NICHROME WIRE REACTOR FOR STEAM REFORMING OF LIQUID FEEDSTOCK

“The world little knows how many of the thoughts and theories which have passed through the mind of a scientific investigator, have been crushed in silence and secrecy by his own severe criticism and adverse examination”

Michael Faraday

8.1 MOTIVATION FOR WORK

As concluded in Chapter 5, sorption enhanced steam reforming (SESR) of ethanol or glycerol is a viable route to the production of high purity H_2 gas. Steam reforming (SR) is the most heavily researched thermochemical route to hydrogen production from glycerol and SESR has produced the most promising results with regard to the purity of the resulting H_2 gas, as reported in Chapter 4.

In industry, SR has traditionally been used to produce hydrogen from natural gas and the equipment has comprised of tubular steam reformers heated by side fired burners.¹⁸ Catalyst pellets are placed inside the reformers and natural gas and steam are passed through them while the burners are used to control the heat flow to them. Reactors described in the literature which has been used for SR of ethanol and glycerol has been operated in similar ways. Often, a tubular reactor has been filled with catalyst and inserted into an electrical oven before a mixture of feedstock and steam is passed through it using a carrier gas (Figure 8. 1).⁵⁰⁻⁵²

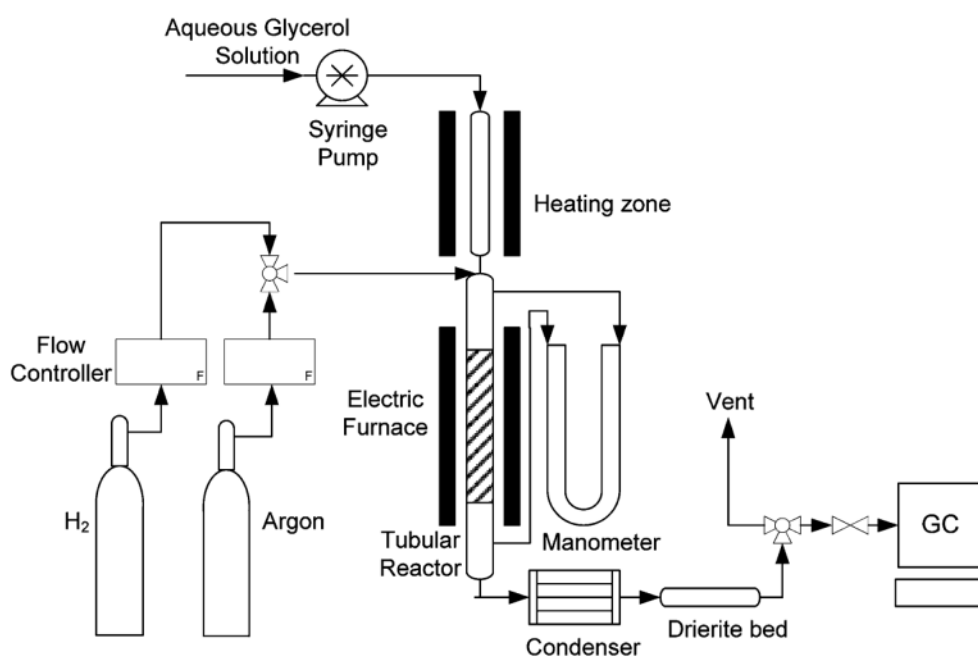


Figure 8. 1. Common experimental setup for SR of glycerol. Reprinted with permission from Cheng et al.⁵² Copyright 2010 American Chemical Society.

This setup incurs an energy penalty since the heat transfer encounters several thermal resistances from its place of origin to its point of use. Thermal barriers can be minimised by generating the heat directly where it is needed. In this chapter, a wire reactor for catalytic steam reforming of the liquid feedstocks ethanol and glycerol is tested. The reactor design is outlined in detail in Chapter 2 but its key feature is a nichrome resistance wire which functions both as a heating element and a catalyst. This allows for the heat needed for the steam reforming reaction

to be supplied from the catalytic surface on which it occurs. By adding a Ca-based CO₂ sorbent into the reactor, it is possible to supply more heat through the exothermic carbonation reaction, as well as benefitting from the higher H₂ yield and purity caused by sorption enhancement. The wire reactor tested in this chapter aims at generating the heat directly where it is needed by using a nichrome wire as both the heating element and catalyst.

Note that the use of electricity for heating at large scale is inefficient due to the losses involved in electricity production (especially when heat is used to produce electricity, e.g. at a coal fired power plant). Therefore, the reactor described here is suggested for use at small scale, preferably with locally produced renewable electricity. It could for example be used on site at a biodiesel production plant where crude glycerol is produced as a waste stream.

SESR involves the addition of a CO₂ sorbent to the steam reforming reactor which causes a shift in the reforming reaction according to Le Chatelier's principle. Due to the good match between temperatures of highest H₂ yields of most organic compounds with those of the CaO carbonation reaction, Ca-based sorbents are often used in the SESR of liquid feedstock. The result is a higher purity H₂ gas and higher H₂ yield, which requires a reduced need for downstream purification processes.²⁰ Another improvement of SESR in relation to SR is that it can be operated at a lower temperature due to the exothermicity of the carbonation reaction, which means that less energy is needed to heat the steam reforming reactor.^{218,220} However, the CO₂ sorbent eventually becomes saturated and heat is needed to regenerate it, which incurs an energy penalty on the SESR process. The wire reactor investigated in this chapter will be used for SESR aiming to improve on the results obtained during SR.

This chapter first presents the work carried out to determine what temperature and molar steam to carbon ratio (S:C) to use and to set up a standard operating procedure for running the reactor. Input mixture flow and carrier gas flow are adjusted to ensure accurate quantification of species in the reactor off-gas. Next, the results from steam reforming experiments using glycerol and ethanol as the feedstock are presented. The catalytic properties of the nichrome wire are then investigated by examining the effect of wire morphology and redox treatment on steam reforming. A number of methods for inserting a sorbent into the reactor are evaluated.

8.2 METHODOLOGY AND DEFINITIONS

The raw data analysis including elemental balances is outlined in detail in Chapter 2, Section 2.12.2. Feedstock conversion (Equation 8. 1) was calculated from the known feedstock input molar flow rate ($n_{C_nH_mO_k, in}$) and the feedstock output molar flow rate ($n_{C_nH_mO_k, out}$) calculated from the elemental balances.

$$\text{Feedstock conversion (\%)} = 100 \times \left(\frac{(n_{C_nH_mO_k,in} - n_{C_nH_mO_k,out})}{n_{C_nH_mO_k,in}} \right)$$

Equation 8. 1. Definition of feedstock conversion. $n_{C_nH_mO_k,out}$ = feedstock output molar flow rate, $n_{C_nH_mO_k,in}$ = feedstock input molar flow rate.

Water conversion (Equation 8. 2) was calculated from the known water input molar flow rate ($n_{H_2O,in}$) and the water output molar flow rate ($n_{H_2O,out}$) calculated from the elemental balances.

$$\text{Water conversion (\%)} = 100 \times \left(\frac{(n_{H_2O,in} - n_{H_2O,out})}{n_{H_2O,in}} \right)$$

Equation 8. 2. Definition of water conversion. $n_{H_2O,out}$ = water output molar flow rate, $n_{H_2O,in}$ = water input molar flow rate.

The molar production rates of H_2 , CO , CO_2 and CH_4 were calculated from the dry total output molar flow rate ($n_{out,dry}$, calculated using the mass balances) and the dry output molar fractions (y_α) calculated from the gas analyser readings (Equation 8. 3):

$$\text{Molar production rate } (\mu\text{mol s}^{-1}) = (n_{out,dry} \times y_\alpha) \times 1 \times 10^6$$

Equation 8. 3. Calculation of molar production rate. $n_{out,dry}$ = dry total output molar flow rate, y_α = dry output molar fraction, $\alpha = H_2, CO, CO_2$ or CH_4 .

H_2 yield (Equation 8. 4) was calculated from the molar production rate of H_2 and the feedstock input molar flow rate ($n_{C_nH_mO_k,in}$) accordingly:

$$H_2 \text{ yield (mol } H_2 \text{ per mol of feedstock)} = \frac{n_{out,dry} \times y_{H_2}}{n_{C_nH_mO_k,in}}$$

Equation 8. 4. Definition of H_2 yield. $n_{out,dry}$ = dry total output molar flow rate, y_{H_2} = dry output H_2 molar fraction, $n_{C_nH_mO_k,in}$ = feedstock input molar flow rate.

H₂:CO ratio (Equation 8. 5) was calculated from the molar production rates of H₂ and CO:

$$H_2:CO = \frac{y_{H_2}}{y_{CO}}$$

Equation 8. 5. Calculation of H₂:CO ratio. y_{CO} and y_{H_2} = dry output H₂ and CO molar fractions respectively.

Selectivity to hydrogen containing products (H₂ and CH₄) was calculated from the dry output molar fractions of H₂ and CH₄ (Equation 8. 6) while selectivity to carbon containing products was calculated from dry output molar fractions of CO, CO₂ and CH₄ (Equation 8. 7).

$$\text{Selectivity to hydrogen containing products (\%)} = 100 \times \left(\frac{y_\alpha}{\sum y_{H_2}, y_{CH_4}} \right)$$

Equation 8. 6. Definition of selectivity to hydrogen containing products (H₂ and CH₄). α = H₂ or CH₄, y = dry output molar fraction.

$$\text{Selectivity to carbon containing products (\%)} = 100 \times \left(\frac{y_\alpha}{\sum y_{CO}, y_{CO_2}, y_{CH_4}} \right)$$

Equation 8. 7. Definition of selectivity to carbon containing products (CO, CO₂ and CH₄). α = CO, CO₂ or CH₄, y_{CO} , y_{CO_2} and y_{CH_4} = dry output molar fractions of CO, CO₂ and CH₄ respectively.

8.3 AIMS AND OBJECTIVES

The aims of this chapter are:

- To implement optimization steps in order to ensure rigorous investigation of the reactor capabilities.
- To understand the effect of nichrome wire morphology and redox pretreatment on the catalytic activity of the wire.
- To investigate the feasibility of sorption enhanced steam reforming using the wire reactor by adding a Ca-based CO₂ sorbent.
- To suggest improvements that can be made to the wire reactor and suggest future work.

In order to meet these aims the following objectives were set up:

- Use a combination of thermodynamic equilibrium analysis and experimental work to find optimum temperature and molar steam to carbon ratio (S:C) for the wire reactor.
- Adjust the input mixture (feedstock and water) flow and the carrier gas flow to enable accurate reactor off gas quantification.
- Establish a standard operating procedure (SOP).
- Combine image analysis, EDX and experimental work to investigate the effects of nichrome wire morphology and redox pretreatment on the catalytic activity of the nichrome wire.
- Compare the ability of the wire reactor to steam reform two different liquid feedstocks, namely glycerol and ethanol.
- Test different means of incorporating Ca(OH)_2 into the wire reactor and evaluate the effects on the steam reforming process.

8.4 SELECTING OPTIMUM TEMPERATURE AND MOLAR STEAM TO CARBON RATIO

The temperature and S:C ratio used in the experiments were chosen based on thermodynamic equilibrium analysis of the steam reforming of glycerol and ethanol which are reviewed in detail in Chapter 5. In summary the analysis showed that a temperature of between 500 and 600 °C will produce the highest H_2 yields at equilibrium depending on what S:C ratio is used. An optimum S:C ratio does not exist but rather the results will improve with increased S:C. However, in practice a high S:C incurs an energy penalty due to the heat needed to raise steam which means that a trade-off has to be made between H_2 yield and energy efficiency. The S:C ratio of 3 was chosen because above this value, the incremental improvement in hydrogen yield becomes small. A S:C of 3 is also commonly used in the literature. Based on this a temperature of 600 °C was chosen. A temperature of 600 °C and a S:C of 3 has commonly been used previously for steam reforming of both glycerol^{176,180,216,220} and ethanol.^{16,259,265,333}

8.5 FLOW ADJUSTMENTS FOR ACCURATE QUANTIFICATION

Evaluation of the wire reactor's performance with regards to catalytic activity, H_2 yield, H_2 to CO ratio (H_2 :CO), molar production rates and selectivity was based on data logged during continuous analysis of the gaseous products using the online analysers (TCD for hydrogen, NDIR for CO, CO_2 and CH_4). Therefore, accurate quantification of the reactor off-gas was crucial. To achieve this, the carrier gas flow was adjusted to comply with the tolerated flow

range and the input mixture (feedstock and water) flow was adjusted so that the gaseous concentrations were in the analysers detection range.

8.5.1 CARRIER GAS FLOW

The adjustable settings were carrier gas flow, reactor temperature, input mixture (feedstock and water) flow and the S:C ratio. If the steam reforming reaction was to occur then the temperature and the S:C ratio needed to be near the optimum values identified by thermodynamic equilibrium analysis, and the residence time needed to be long enough. However, the gas analysers had a limited tolerated flow range of $333 \frac{1}{3}$ -1500 ml min⁻¹ (See Chapter 2 for details). To get accurate readings the carrier gas flow had to be in the tolerated flow range.

The input mixture flow was investigated by disconnecting the reactor top and starting a carrier gas flow and an input mixture flow to observe how the input mixture entered the reactor (Figure 8. 2). When a carrier gas flow of 350 ml min⁻¹ was used, the input mixture formed droplets which fell from the spray injection system inlet with a frequency of ≈ 1 drop s⁻¹. A minimum carrier gas flow of 2000 ml min⁻¹ was needed to create an input mixture spray. This meant that there was a trade-off between accurate analyser readings and quality of input mixture spray injection.

Given the importance of the accuracy, a carrier gas flow of 350 ml min⁻¹ was chosen in order to keep the reactor off-gas flow within the tolerated flow range. Using different means of off-gas analysis could solve the issue of trade-off between accurate product species quantification and spray injection quality. One example would be gas chromatography which has been used successfully by others.^{51,181,209} With this technique, regular injections from the reactor off-gas feed could be carried out by the gas chromatograph and carrier gas flow would not impact on the accuracy of the quantification.

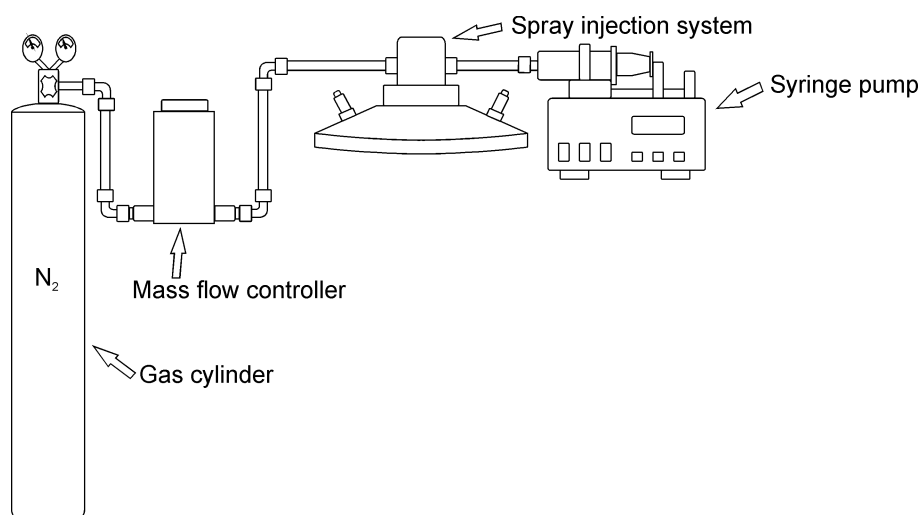


Figure 8. 2. Schematic of the setup used to investigate input mixture flow.

8.5.2 INPUT MIXTURE FLOW

Multiple thermodynamic equilibrium analysis were carried out with input mole fractions corresponding to a S:C of 3, a carrier gas flow of 350 ml min⁻¹ and input mixture flows (mixture of feedstock and water) of 6, 12, 24 and 48 ml h⁻¹. The results were used to find a starting point for a set of test runs with different input mixture flows. An input mixture flow was then chosen based on readily quantifiable concentrations using the gas analysers. The detection range of the gas analysers were 0-60% for H₂ and 0-30% for CO, CO₂ and CH₄. As the input compound compositions were changed to simulate increased input mixture flow, the concentrations of all gaseous products augmented as shown in Table 8. 1 with glycerol as the feedstock.

Table 8. 1. Gas concentrations derived from thermodynamic equilibrium analysis of glycerol for input compound compositions corresponding to a S:C of 3 and input mixture flows (ml h⁻¹) between 6 and 48 ml h⁻¹ at 597 °C*

Feedstock flow	Input fractions			Gas concentrations			
	Glycerol	H ₂ O	N ₂	H ₂	CO	CO ₂	CH ₄
6	0.02	0.21	0.77	14.4	1.7	5.2	0.1
12	0.04	0.33	0.63	23.4	2.8	8.6	0.2
24	0.05	0.49	0.46	34.3	4.1	12.7	0.5
48	0.07	0.63	0.30	44.9	5.3	16.8	0.8

*Note that the EQUIL code uses the Kelvin temperature scale.

Input compound compositions corresponding to input mixture flows above 24 ml h⁻¹ were needed for the thermodynamic equilibrium analysis to return mole fractions of H₂ and CO₂ which corresponded to concentrations that were close to the centre of the gas analyser detection range. Hence input mixture flows above 24 ml h⁻¹ were needed to provide H₂ and CO₂ concentrations that were close to the centre of the gas analyser detection range at equilibrium. However, the thermodynamics of the steam reforming reaction did not allow for CO and CH₄ concentrations of the same order. A set of test runs with input mixture flows between 6 and 24 ml h⁻¹ showed that thermodynamic equilibrium was not achieved and the concentration of H₂ was lower while the concentrations of CO, CO₂ and CH₄ were higher than predicted by thermodynamic analysis. Finally, a flow of 12 ml h⁻¹ was chosen. Given these conditions, an H₂ yield of 5.02 and a water conversion of 28.5% was expected at 597 °C at equilibrium for ethanol steam reforming. For glycerol steam reforming an H₂ yield of 6.08, an H₂:CO of 8.3:1 and a water conversion of 24% was expected.

8.6 ESTABLISHING A STANDARD OPERATING PROCEDURE

After thermodynamic analysis and a set of test runs, a standard operating procedure (SOP) was established and this was subsequently used for the rest of the work. The first steps of the SOP involved startup of the wire reactor and consisted of the following steps.

- Start the reactor off-gas cooling system.
- Pass carrier gas through the reactor setup to fill it with an N₂ atmosphere.
- Stop carrier gas flow and heat up the wire reactor to 600 °C.
- Keep the wire reactor at 600 °C for 30 min to allow for the reactor walls to heat up.
- Turn carrier gas on until the temperature is at steady state.

After startup an air purge step and a reduction step of the catalytic wire under H₂ flow were also added, described in detail below.

8.6.1 AIR PURGE STEP

A common cause of catalyst deactivation is the buildup of coke on the catalyst surface.^{176,179,180} An air purge step was introduced with the aim of removing coke from the nichrome wire. In practice this meant passing air over the wire reactor at 600 °C with a flow rate of 350 ml min⁻¹ using a mass flow controller. The CO₂ concentration in the reactor off-gas was used as an indicator of the burning of coke and was subsequently monitored during the air purge step (see Figure 8. 3 for an example). When the CO₂ concentration was close to zero the air purge step was ended.

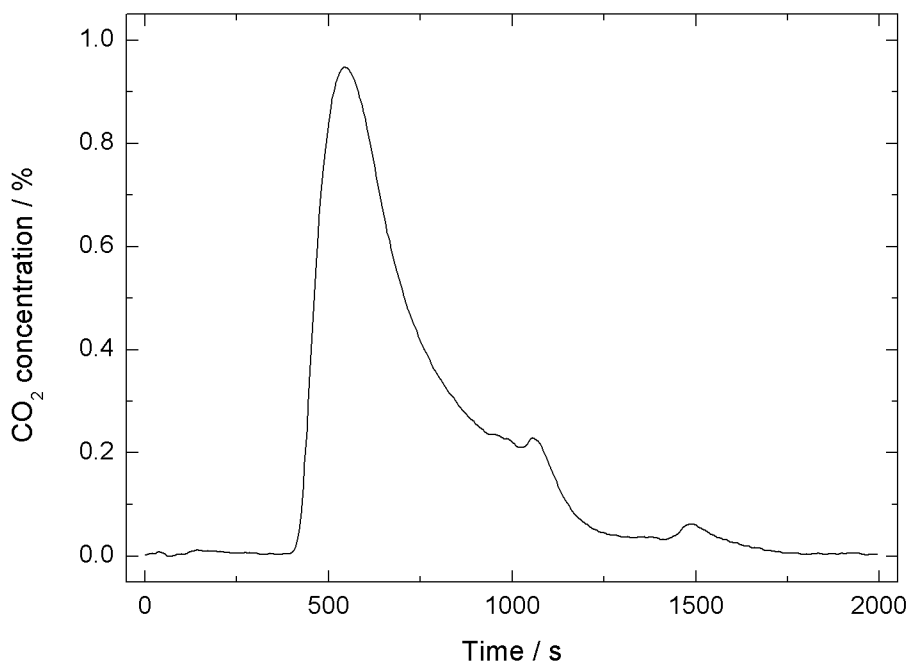


Figure 8. 3. CO₂ concentration in the reactor off gas with time on stream for a typical air purge step.

8.6.2 H₂ REDUCTION STEP

When using conventional catalysts, a reduction step is used to chemically reduce the metal oxides back to metals in the catalyst.^{51,209,217} Therefore, a H₂ reduction step was incorporated to the standard operating procedure and was carried out after the air purge step prior to starting the input mixture flow. In practice this meant passing an H₂/N₂ gas mixture (5% H₂ in N₂) through the reactor (heated to 600 °C) at 350 ml min⁻¹ using a mass flow controller. The gas mixture was passed through the reactor until the reactor off-gas contained 5% H₂ and was then switched off.

8.7 TEST OF FEEDSTOCK

The runs described below were carried out using the SOP outlined above at 600 °C, with S:C of 3:1, carrier gas flow of 350 ml min⁻¹ and input mixture flow of 12 ml h⁻¹ using glycerol and ethanol as feedstock. These two runs will be referred to as Run 1 (using glycerol as the feedstock) and Run 2 (using ethanol as the feedstock).

8.7.1 GLYCEROL (RUN 1)

When the entire data set was considered, it was observed that the CO₂ and CH₄ readings increased and a white gas was visible in the Si gel trap (Figure 8. 4). This was attributed to the formation of glycerol pyrolysis products with IR absorption characteristics similar to those of CO₂ and CH₄ which built up inside the analyser detector with time on stream causing gas

analyser contamination. This meant that the CO_2 and CH_4 readings were not considered representative of the CO_2 and CH_4 concentrations in the reactor off-gas and consequently reliable calculations of the feedstock and water conversion could not be obtained.

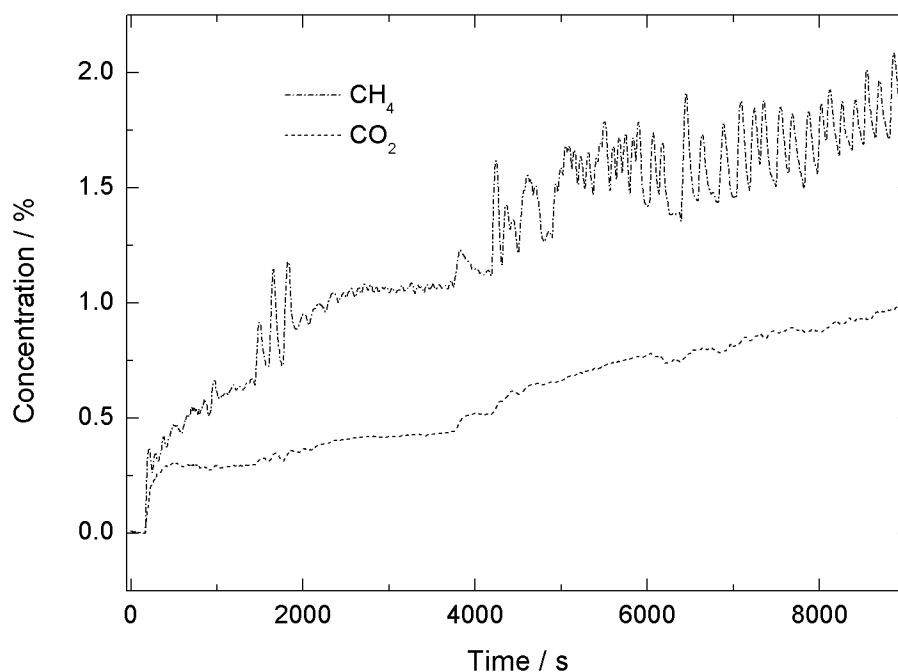


Figure 8. 4. CO_2 and CH_4 gas analyser readings during SR of glycerol (Run 1) at $600\text{ }^\circ\text{C}$ with a S:C ratio of 3:1.

At steady state the molar production rates of H_2 and CO were 20.3 and $18.7\text{ }\mu\text{mole s}^{-1}$ respectively which resulted in a H_2 : CO of 1.1:1 ($AD_{(401)} = 2.32$, $p < 0.05$) while the production rates of CH_4 and CO_2 were much lower (Figure 8. 5). Given the issue with the CH_4 and CO_2 readings described above the actual production rates were likely to be even lower. The glycerol decomposition reaction produces H_2 and CO in a molar ratio of $1\frac{1}{3}$:3 (Reaction 4. 1) which is only slightly higher than the H_2 : CO observed here. Even though the CH_4 and CO_2 readings were not considered reliable for accurate quantification, the data could however be used to conclude that production of CH_4 and CO_2 did indeed take place. The CO methanation reaction uses 3 mole of H_2 and one mole of CO to produce CH_4 and H_2O , hence the production of CH_4 through the CO methanation reaction reduces the H_2 : CO (Reaction 4. 2). The production of CO_2 from the WGS reaction (Reaction 1. 2) increases the H_2 : CO but the production of CO_2 is significantly lower than that of CH_4 (Figure 8. 4). Therefore, the observations were attributed to a combination of glycerol decomposition in combination with methanation and a small amount of WGS.

The H_2 yield at steady state was 1.4 ($AD_{(401)} = 6.4$, $p < 0.05$). The results showed that the system was far from thermodynamic equilibrium since the expected H_2 : CO and H_2 yield were

8.3:1 and 6.1 respectively (Section 8.5.2). The gas concentration readings oscillated heavily during the run, causing the molar production rate data to produce a saw tooth shape (Figure 8. 5). This was attributed to the formation of input mixture droplets which were observed in Section 8.5.1.

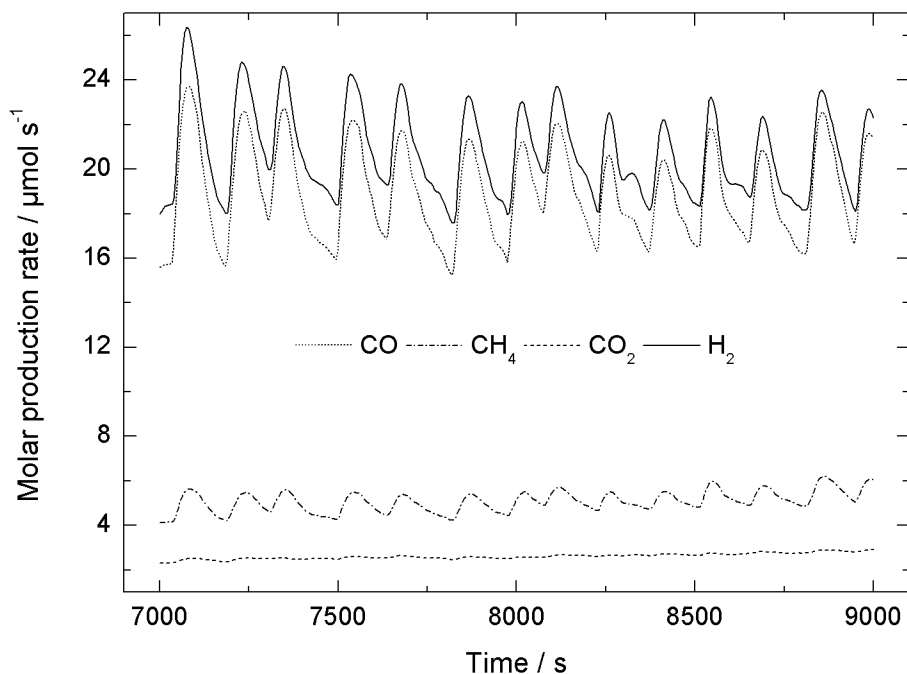


Figure 8. 5. Molar production rates of CO, CH₂, CO₂ and H₂ during SR of glycerol (Run 1) at 600 °C with a S:C ratio of 3:1.

8.7.2 ETHANOL (RUN 2)

This section presents the results from a run carried out with ethanol as the feedstock and it will be referred to as Run 2. During Run 2 there was no indication of gas analyser contamination (Figure 8. 6). Hence it was possible to test the hypothesis regarding the nature of the thermodynamic conversion as well as to determine feedstock and water conversion. Also, the concentration of gaseous products reached steady state and this is why the entire data set is not shown in Figure 8. 6. Instead, only the readings recorded between 4000 and 6000s are presented and investigated below.

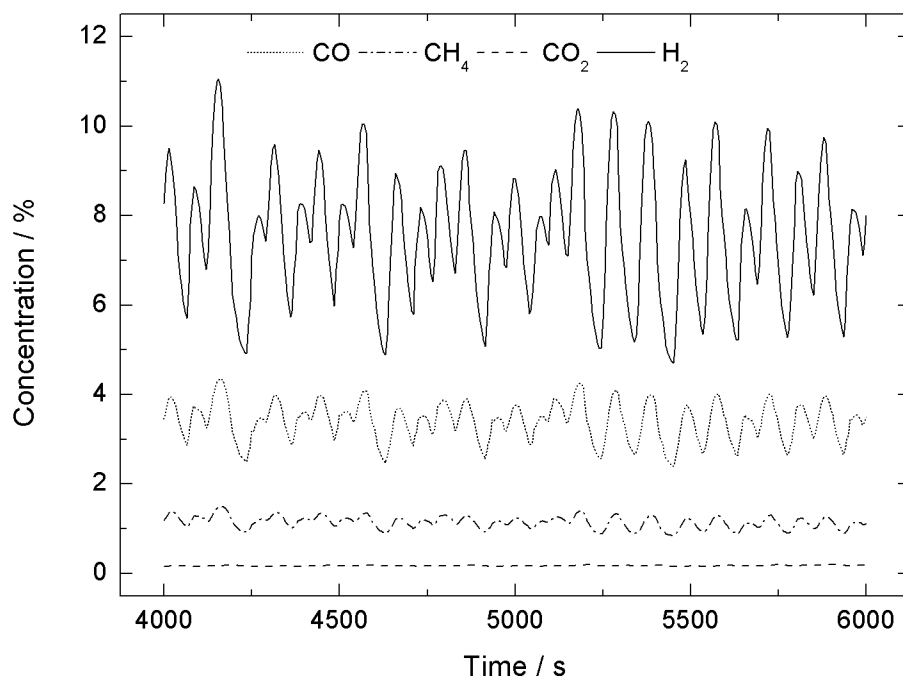


Figure 8. 6. CO, CH₄, CO₂ and H₂ gas analyser readings during SR of ethanol (Run 2) at 600 °C with a S:C ratio of 3:1.

The H₂:CO of the data set (between 4000-6000s) was 2.2:1 ($AD_{(401)} = 4.84$, $p < 0.05$) while the expected H₂:CO at thermodynamic equilibrium at 597 °C was 8:1, hence the system was far from equilibrium. However, the H₂:CO was close to the 2:1 which would be expected from ethanol steam reforming without any WGS or methanation involved (Reaction 5. 2).

Over the same time on stream the feedstock conversion was 32.7% ($AD_{(401)} = 1.50$, $p < 0.05$) and the water conversion was 6.3% ($AD_{(401)} = 2.51$, $p < 0.05$). The expected water conversion at equilibrium was at 597 °C was 28.5%. With the method used here for thermodynamic analysis, the feedstock conversion is complete at all temperatures and therefore the feedstock conversion observed during experimental work was not related to the results of the thermodynamic analysis. Given that the CO₂ molar production was very low ($0.5 \mu\text{mole s}^{-1}$, $AD_{(401)} = 1.99$, $p < 0.05$) it was reasonable to assume that the WGS reaction made an insignificant contribution to the water conversion. Hence, the water conversion was attributed to the ethanol steam reforming reaction. Assuming that all feedstock conversion occurred via the ethanol steam reforming reaction, the ratio of feedstock conversion to water conversion would be 5.9:1 at S:C of 3:1. The ratio of measured feedstock conversion to water conversion was close to this (5.2:1) supporting the assumption. But a significant amount of CH₄ was also produced ($3.2 \mu\text{mole s}^{-1}$, $AD_{(401)} = 1.24$, $p < 0.05$) and the CO methanation reaction reduces water conversion. Note that the WGS reaction increases water conversion and can therefore compensate for this reduction. However, the observed CO₂ molar production ($0.5 \mu\text{mole s}^{-1}$) was much lower than the CH₄ molar production ($3.2 \mu\text{mole s}^{-1}$) (Figure 8. 7). Consequently the

evidence did not support such compensation in water conversion via the WGS reaction. The selectivity to CO was 72.2 ($AD_{(393)} = 1.98$, $p < 0.05$) while the selectivity to CH₄ and CO₂ were 24.2 ($AD_{(401)} = 1.98$, $p < 0.05$) and 3.5 ($AD_{(401)} = 9.16$, $p < 0.05$) respectively. The results were consistent with ethanol steam reforming with formation of CH₄ through the CO methanation reaction with an insignificant contribution from the WGS reaction.

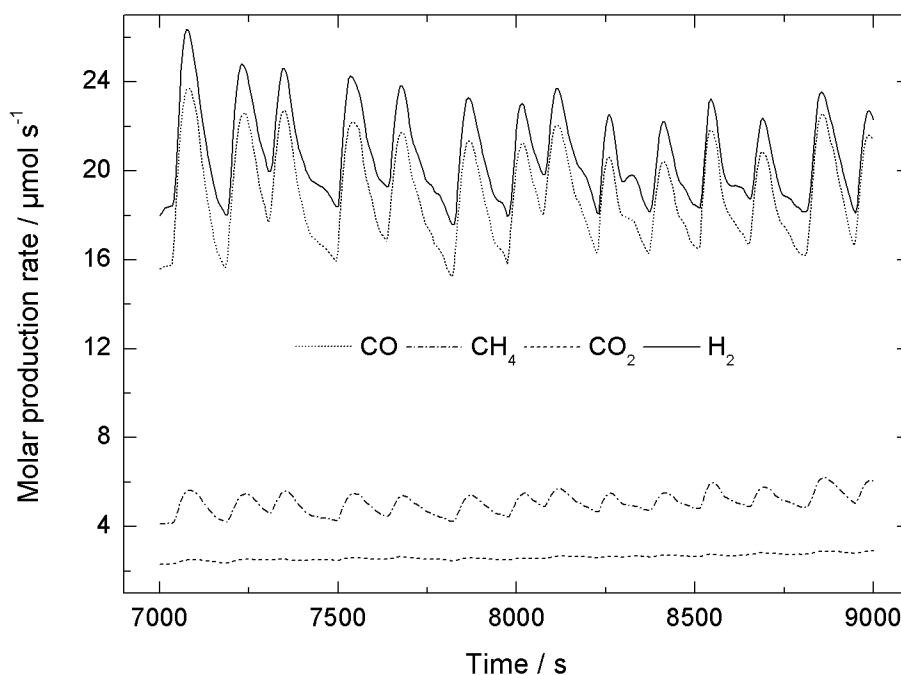


Figure 8. 7. Molar production rates of CO, CH₄, CO₂ and H₂ during SR of ethanol (Run 2) at 600 °C with a S:C ratio of 3:1.

In summary, SR of ethanol was easier to study using the wire reactor than SR of glycerol due to the issue with analyser contamination caused by decomposition products of glycerol. Steam reforming was achieved with ethanol; however the feedstock conversion was low and WGS was insignificant, providing opportunities for optimising the conditions for higher H₂ yield.

8.8 INTRODUCTION OF AN ALUMINA STACK

The gas concentration readings oscillated significantly with time on stream at steady state (Figure 8. 4, Figure 8. 6). This was attributed to the formation of droplets of input mixture which were observed in Section 8.5.1. To even out delivery of the input mixture flow a stack of alumina pellets ('Al stack') was placed on top of the monolith. The Al stack consisted on three alpha alumina catalyst support pieces supplied by Johnson Matthey (UK) (Figure 8. 8) which were piled on top of each other and joined with Pyro Putty[®] (Aremco, USA). The alumina support pieces had four channels, and the piling achieved by turning each piece 90 ° relative to

the one below it, so that the stack contained a 3D network of channels. When the Al stack was in place on top of the monolith housing the nichrome wire, the input mixture would make contact with it immediately after entering the reactor. The input mixture would then travel through the 3D channel network assisted by gravity. This aimed to increase the residence time of the input mixture in the reaction zone as well as prevent the formation of large input mixture droplets. The Al stack was used for the remainder of the work.

Figure 8. 7 and Figure 8. 13 represent the molar production rates as determined before and after the addition of the Al stack.

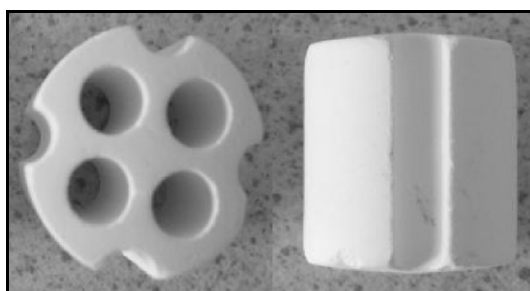


Figure 8. 8. Top and side images of Al support pieces used to make the Al stack. The pieces are 20 mm long and 15 mm wide.

8.9 CATALYTIC ACTIVITY OF THE NICHROME WIRE

Catalytic activity is affected by the morphology and the pretreatment of the catalyst. This section investigates the morphology and the catalytic activity of two different nichrome resistance wires referred to as wire 1 and wire 2. Wire 1 was supplied by (but not manufactured by) Johnson Matthey (UK) together with the reactor. Wire 2 was purchased from Omega Ltd. (UK). Both wires contained 80% Ni and 20% Cr and had a diameter of 0.8 mm. The effect of the pretreatment method of the nichrome wire that exhibited superior catalytic activity was then investigated with the aim on increasing the activity further.

8.9.1 INVESTIGATION OF NICHROME WIRE CHARACTERISTICS

The morphology of the nichrome wire surfaces was investigated using photography (Figure 8. 9, Figure 8. 10). This was carried out at 10X magnification on 50 mm lengths of wire using a BX51 microscope (Olympus, Japan) and a Zeiss AxioCcam Mrc5 camera (Carl Zeiss ltd, UK). Wire 1 displayed a series of lines along the length of the wire, indicating that it had manufactured using the draw method. The morphology of Wire 2 suggested that it had been annealed.

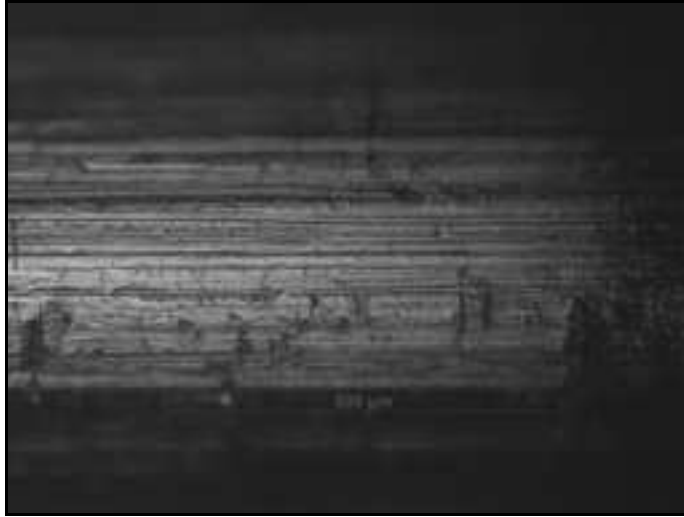


Figure 8. 9. Photograph (10X magnification) of the nichrome wire supplied by Johnson Matthey (wire 1).

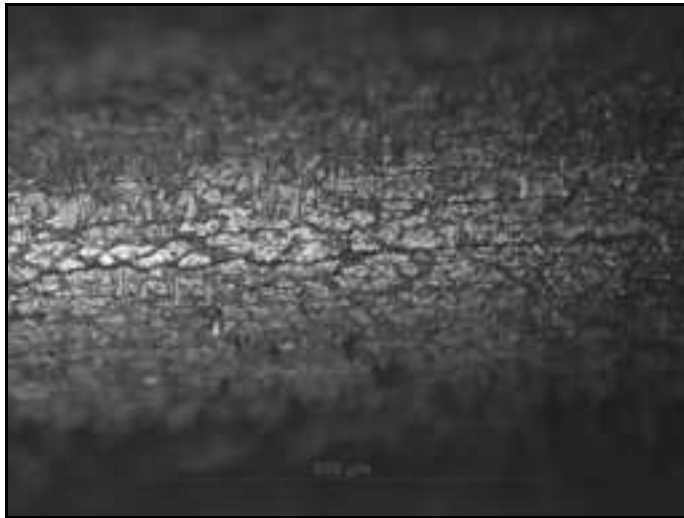


Figure 8. 10. Photograph (10X magnification) of the nichrome wire purchased from Omega (wire 2).

The cross section of wire 2 was investigated using SEM-EDX. A 10 mm long piece of wire was embedded in epoxy resin (using EpoThin[®] resin and hardener from Buehler, UK) which was then ground and polished. EDX mapping of the cross section revealed the presence of nickel, chromium, and oxygen (Figure 8. 11). Silica was also found in the resin. Note that there was oxygen in the resin as well and consequently the contours of the wire was not visible when oxygen was mapped (Figure 8. 12). An analysis of the oxygen also made difficult by the fact there exist peak overlap between chromium and oxygen (Figure 8. 12).

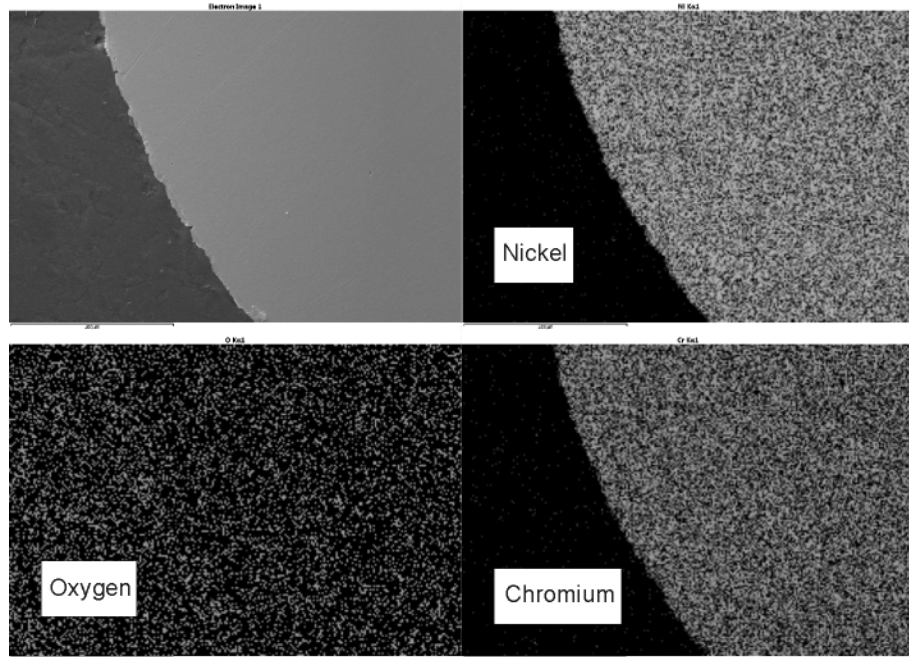


Figure 8. 11. SEM image (top left) and EDX maps of nickel, oxygen and chromium collected from a cross section of the wire purchased from Omega (wire 2).

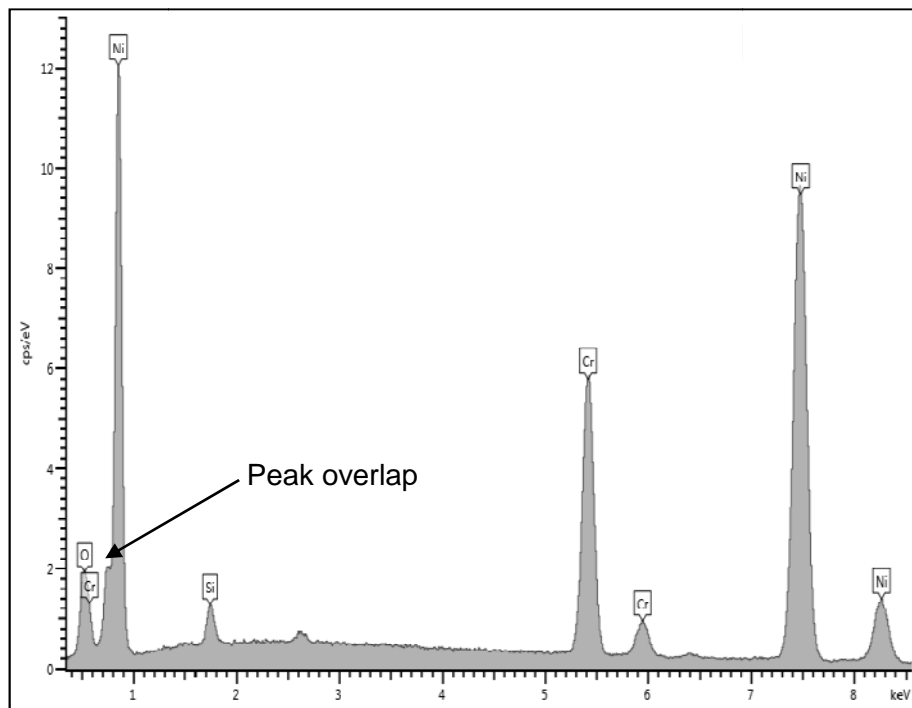


Figure 8. 12. EDX peaks derived from a cross section of the wire purchased from Omega (wire 2) showing overlap between a peak derived from oxygen and a peak derived from chromium.

8.9.2 EFFECT OF NICHROME WIRE MORPHOLOGY ON STEAM REFORMING (RUN 3)

A run was carried out with wire 2 and the Al stack with ethanol as the feedstock. This run will be referred to as Run 3. The results were compared to those obtained during Run 2 where wire 1 was used (Figure 8. 7). The feedstock conversion was 46.7% ($AD_{(782)} = 2.18$, $p < 0.05$) and the water conversion was 6.4% ($AD_{(783)} = 1.39$, $p < 0.05$). This was a significant increase in feedstock conversion compared to Run 2 (32.7%, $MW_{(1183)} = 80.60e^3$, $p < 0.05$) but not in water conversion (6.3%, $MW_{(1184)} = 23.24e^4$, $p > 0.05$). Consequently, the ratio of feedstock conversion to water conversion was higher in Run 3 (7.3 :1 compared to 5.2:1 for Run 2 where wire 1 was used).

The H_2 yield was 1.4 ($AD_{(779)} = 1.43$, $p < 0.05$), i.e. 35% higher than in Run 2 (where wire 1 was used). Given the fact that the feedstock conversion was 43% higher than in run 2 the H_2 yield would be expected to have been more than 35% higher.

The production rate of all gases had increased compared to Run 2 (with wire 1) while the order of the molar production rates remained the same, i.e. $H_2 > CO > CH_4 > CO_2$ (Table 8. 7) (Figure 8. 13). Hence more of the feedstock was gasified when wire 2 was used.

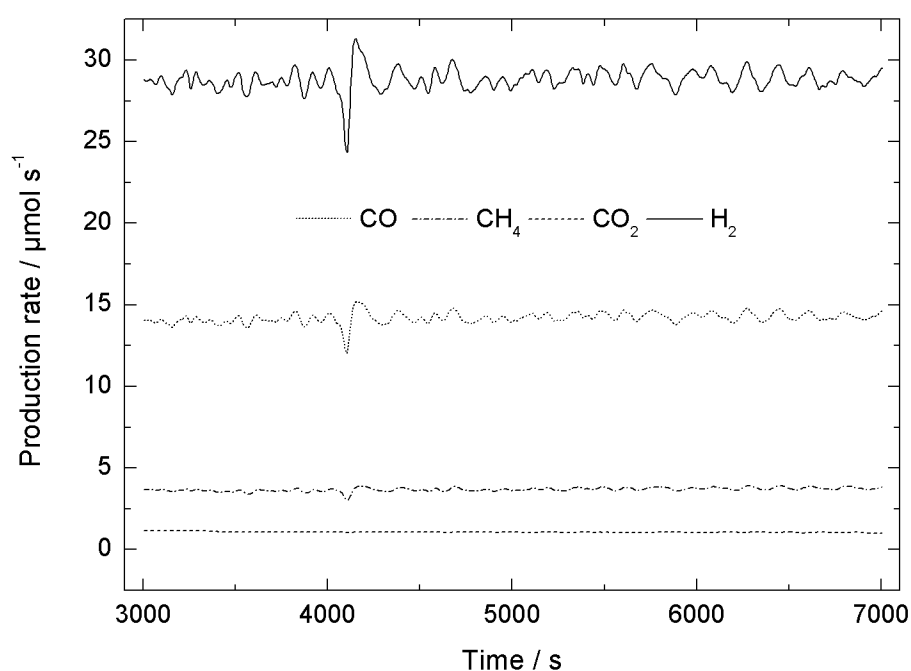


Figure 8. 13. Molar production rates of CO, CH₄, CO₂ and H₂ during SR of ethanol using wire 2 (Run 3) at 600 °C with a S:C ratio of 3:1.

It was first hypothesized that the difference in ratio of feedstock to water conversion was due to an increase in CO methanation (Reaction 4. 2) or by a reduction in WGS (Reaction 1. 2). The selectivity to hydrogen and carbon containing products of the two runs (Runs 2 and 3 using wire 1 and 2 respectively) was compared to investigate if the results could be explained by a

shift in the CO methanation reaction or in the WGS reaction. The selectivity to CH₄ was higher in Run 2 (wire 1) than in Run 3 (wire 2) (Table 8. 2) while the selectivity to CO₂ was lower in Run 2 (wire 1) than in Run 3 (wire 2). This meant that the lower ratio of water conversion to feedstock conversion in Run 3 (wire 2) could not be explained by a shift in the CO methanation reaction or in the WGS reaction as hypothesized above as this would have produced opposite results.

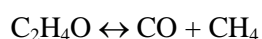
Table 8. 2. Selectivity to carbon and hydrogen containing species during SR of ethanol with wire 1 and 2.

Run	Selectivity (C)			Selectivity (H)	
	CO	CO ₂	CH ₄	H ₂	CH ₄
2 (wire 1)	72.2	3.5	24.2	86.8	13.2
3 (wire 2)	75.0	5.6	19.4	88.7	11.3

The lower relative water conversion in Run 3 could also be attributed to a shift from ethanol steam reforming towards decomposition of ethanol in the absence of water. This can occur through the formation of acetaldehyde by dehydrogenation of ethanol (Reaction 8. 1) and subsequent decarbonylation of the acetaldehyde (Reaction 8. 2).^{255,259,334,335} Through this route H₂, CO and CH₄ can form without any water being converted.



Reaction 8. 1. Dehydrogenation of ethanol.



Reaction 8. 2. Decarbonylation of acetaldehyde.

The shift from ethanol steam reforming towards decomposition of ethanol in the absence of water was further supported by the H₂:CO which was lower in Run 3 where wire 2 was used (2.0:1 (AD₍₇₉₃₎ = 4.05, p < 0.05) than run 2 where wire 1 was used (2.2:1). This would be expected since the H₂:CO of the decomposition reaction and the ethanol steam reforming reaction is 1:1 and 2:1 respectively.

The delivery of the input mixture (feedstock and water) into the reactor was more regular in Run 3 than in Run 2 (using wire 1 and without the Al stack) indicating that the Al stack worked. It is also believed that part of the improvement in feedstock conversion observed during Run 3 was in part due to an increased residence time made possible by the Al stack. However, it was not possible to differentiate between the effect of wire 2 compared to wire 1 and the effect of the Al stack with regards to feedstock conversion.

8.9.3 NICHROME WIRE PRETREATMENT

To make their morphology and characteristics more favorable for catalytic activity the wires were pretreated using alternating oxidizing and reducing environments. The pretreatment was tested on 50 mm lengths of wire using the quartz reactor described in Chapter 2. The wires were placed inside the reactor which was sealed, filled with N_2 using a mass flow controller and heated to 700 °C (Figure 8. 14). The atmosphere inside the quartz reactor was then changed between oxidizing and reducing using air and an H_2/N_2 gas mixture (5% H_2 in N_2), respectively, according to Table 8. 3.

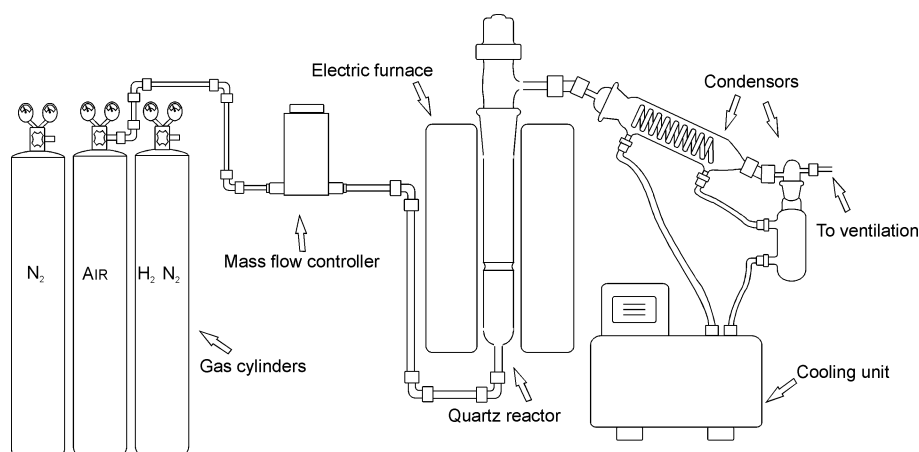


Figure 8. 14. Schematic of the setup used to carry out redox pretreatment on 50 mm lengths of nichrome resistance wires.

Table 8. 3. The gases used to create oxidizing and reducing atmospheres during the redox pretreatment and the duration for which they were used during a redox cycle.

Gas	Duration (min)
Air	15
N_2	5
H_2/N_2	15
N_2	5

Two lengths of wire 2 were placed inside the quartz reactor depicted above and the procedure outlined in Table 8. 3 was repeated 5 times. One of the lengths of wire was removed from the reactor while the other one was subjected to a further 5 cycles. The lengths of wire were then photographed to gauge the visible effects of the pretreatment (Figure 8. 15, Figure 8. 17).

After 5 cycles the wire had changed its colour from grey to a mixture of grey, yellow, green with small spots of red and pink (Figure 8. 15). The morphology had remained

unchanged. The change in colour was attributed to the formation of oxides out of which several different species are possible, including alloys.

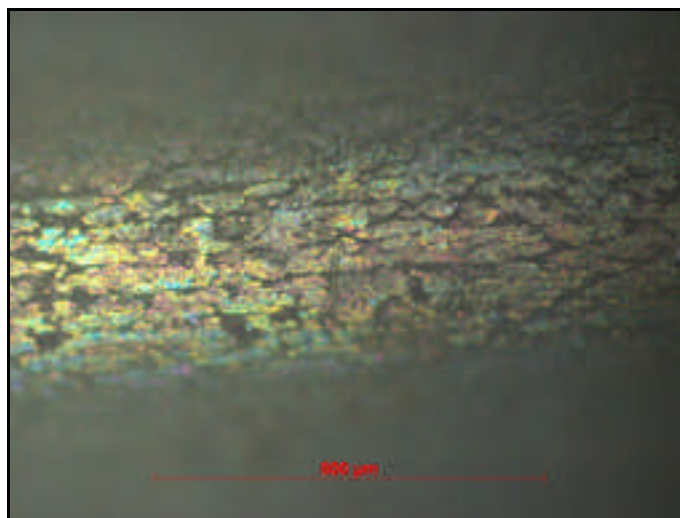


Figure 8. 15. Photograph (10X magnification) of the nichrome wire purchased from Omega Ltd (wire 2) after 5 redox cycles outlined in Table 8. 3 at a temperature of 700 °C.

The only well known Ni oxide compound is NiO which has been shown to form on Ni thin films at 200 °C in air³³⁶ hence it can be safely assumed that NiO formed on the nichrome wire surface during the oxidation stage of the pre treatment. NiO is green in colour and given that the wire had become green it could be deduced that NiO had formed during the pre treatment. However, temperature controlled reduction (TPR) experiments carried out on Ni containing catalysts have shown that NiO reduces at temperatures between 304-450 °C in atmospheres containing 5-10% H₂.^{205,213,217} This would suggest that it was unlikely that the green colour observed was due to the presence of NiO. However, interactions with other oxide species can increase the reduction temperature of NiO up to as much as 700-850 °C^{209,217,337} hence NiO could be present if it had interacted with Cr oxide species. Cr is more readily oxidized than Ni and has 10 possible oxidation states ranging from -IV to VI compared to 5 for Ni (ranging from 0 to IV).^{338,339} The most common Cr oxides are Cr₂O₃, CrO₂ and CrO₃. Both CrO₂ and CrO₃ are known to decompose to Cr₂O₃ at temperatures above 250 °C³³⁸ hence the formation of Cr₂O₃ was considered to be favoured under the conditions used for the pre treatment. CrO₂ is black in colour while CrO₃ is red and Cr₂O₃ is green.^{338,339} Consequently, based solely on the observations of colour, the formation of CrO₂ could not be confirmed, the red and pink spots could be attributed to the formation of small amounts of CrO₃ while Cr₂O₃ could not be distinguished from NiO. However, NiO is readily reduced while Cr₂O₃ is not. This can be illustrated by plotting equilibrium gas partial pressures ratio of p_{H₂O}/p_{H₂} over temperature (Figure 8. 16).³⁴⁰ At 700 °C, NiO will be reduced at a p_{H₂O}/p_{H₂} of 10²:1 which is

equal to 1% H_2 in H_2O while Cr_2O_3 will be reduced at a $p\text{H}_2\text{O}/p\text{H}_2$ of $10^{-5}:1$ which is equal to >99% H_2 in H_2O . During pre treatment, the reducing agent was a gas containing 5% H_2 in N_2 . Hence NiO would be expected to be readily reduced during the reducing stage of the pretreatment while Cr_2O_3 would not be expected to be reduced at all. Cr_2O_3 requires a stronger reducing agent like elemental Al which can be used to reduce Cr_2O_3 at temperatures above 1000 °C by aluminothermic reduction.³⁴¹ Note that alloys containing both Cr and Ni are also possible.

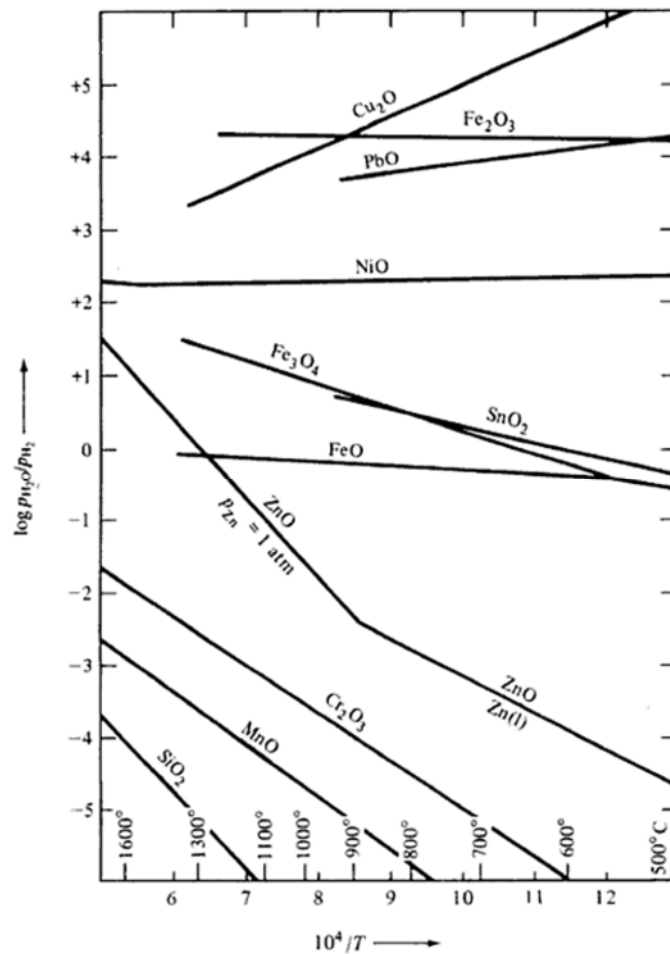


Figure 8. 16. Equilibrium gas ratio $p\text{H}_2\text{O}/p\text{H}_2$ as a function of inverse temperature for the reduction of various oxides.³⁴⁰ Reprinted with permission from Tapir Academic Press, Norway.

After 10 cycles, the colour of the wire was mostly green with a few pink and blue spots. The morphology had been evened out somewhat (Figure 8. 17). Given that the formation of Cr_2O_3 was highly likely during the oxidation stage and that the reduction stage could not reduce the Cr_2O_3 it could be deduced that more Cr_2O_3 was formed with each cycle. The increase in green colour with a higher number of cycles supported this conclusion because Cr_2O_3 is green.³³⁹ However, the colour could also be due to NiO which could possibly have remained in

its oxidized state if it had interacted with the Cr_2O_3 . It was however considered more likely that the NiO was reduced to Ni during the reduction stage.

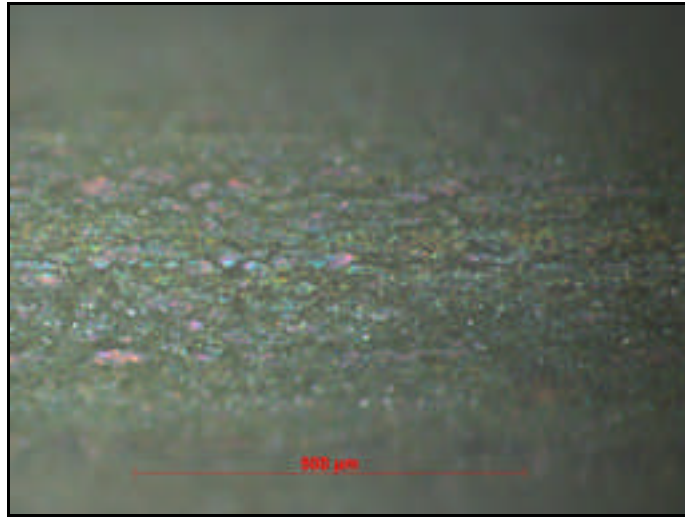


Figure 8. 17. Photograph (10X magnification) of the nichrome wire purchased from Omega Ltd (wire 2) after 10 repeats of the procedure outlined in Table 8. 3 at a temperature of 700 °C.

The cross section of wire 2 was investigated using SEM-EDX as described in Section 8.9.1. After 5 cycles it appeared as if the surface had become roughened and so a higher magnification was used (Figure 8. 18). There appeared to be a larger amount of oxygen around cavities at the surface.

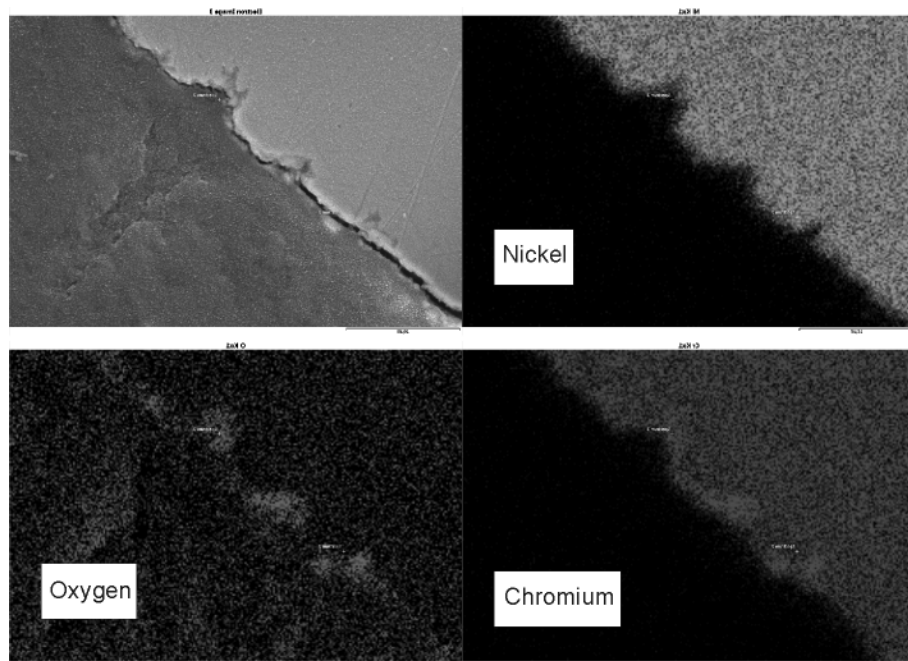


Figure 8. 18. SEM image (top left) and EDX maps of nickel, oxygen and chromium collected from a cross section of the wire purchased from Omega (wire 2) after 5 redox cycles.

There was no obvious increase in roughening after 10 cycles compared to after 5 cycles (Figure 8. 19) Formation of oxide species on the wire surface could not be confirmed with EDX partially because oxygen was detected across the wire as well as in the resin and partially because there exists a peak overlap of chromium and oxygen (Figure 8. 12). The boundary between wire and resin appeared less sharp after 5 and 10 cycles as it was before pretreatment. However, this was attributed to the higher resolution used for the images taken after 5 and 10 cycles.

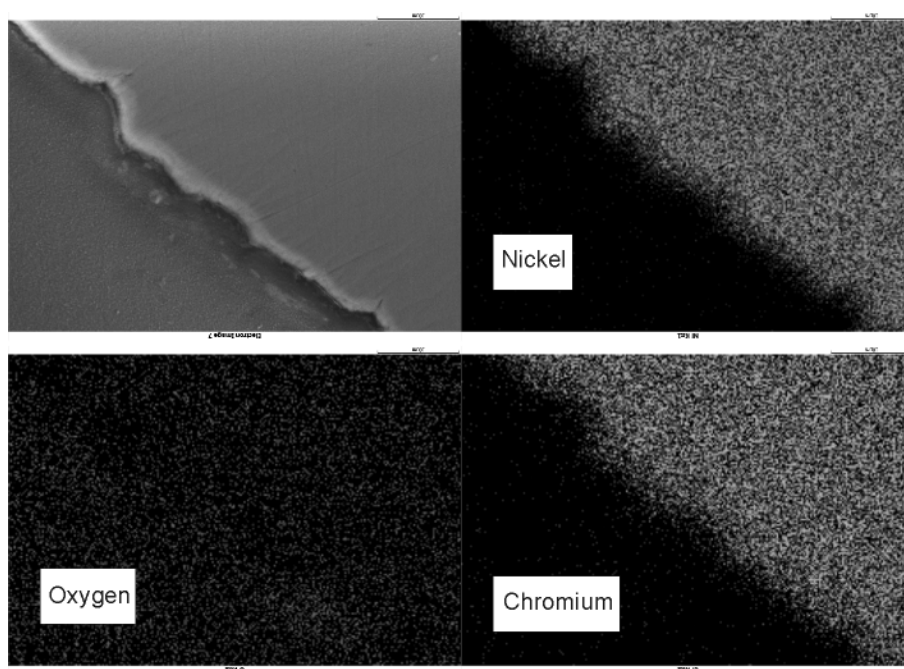


Figure 8. 19. SEM image (top left) and EDX maps of nickel, oxygen and chromium collected from a cross section of the wire purchased from Omega (wire 2) after 10 redox cycles.

8.9.4 EFFECT OF WIRE PRETREATMENT ON STEAM REFORMING (RUN 4)

The redox pretreatment procedure was carried out on the wire threaded through the monolith inside the wire reactor set up (wire 2). This was done by heating the reactor to 700 °C before passing air, N₂ and H₂/N₂ gas through it according to the procedure outlined in Table 8. 3 and repeating this 10 times. Another run was then carried out under the same conditions as Run 3 (i.e. before pretreatment). This will be referred to as Run 4 and hence represents the conditions after pretreatment. The H₂ yield after pretreatment was 1.9 ($AD_{(572)} = 2.26$, $p < 0.05$) which was an improvement of 32% over Run 3 (carried out before pretreatment). The H₂:CO also increased significantly from 2.0:1 before pretreatment to 4.3:1 ($AD_{(601)} = 11.22$, $p < 0.05$).

The feedstock conversion was 44.4% ($AD_{(554)} = 1.55$, $p < 0.05$) and the water conversion was 12.6% ($AD_{(583)} = 2.53$, $p < 0.05$) which showed that the wire pretreatment had no impact on feedstock conversion (which was 46.7% before wire pretreatment). However, the water conversion had almost doubled from 6.4% before pretreatment. The ratio of feedstock conversion to water conversion was 3.5:1. This was lower than before pretreatment, i.e. Run 3 (7.3:1) and for run 2 when wire 1 was used (5.2:1) and meant that water conversion was too high for the observations to be attributed solely to the ethanol steam reforming reaction.

Compared to Run 3 (before pretreatment), the H_2 and CO_2 molar production rates were higher while the CO and CH_4 concentrations were lower. The largest difference was in the CO_2 production rate which had increased from $1.1 \mu\text{mole s}^{-1}$ before pretreatment to $7.3 \mu\text{mole s}^{-1}$ ($AD_{(601)} = 3.33$, $p < 0.05$). The order of the molar production rates of the gaseous products had changed from $H_2 > CO > CH_4 > CO_2$ (Figure 8. 13) to $H_2 > CO > CO_2 > CH_4$ (Figure 8. 20), hence CH_4 and CO_2 had switched places such that the CO_2 production rate was now higher than the CH_4 production rate. The selectivity to H_2 had increased from 88.7 to 94.7 ($AD_{(601)} = 20.18$, $p < 0.05$) as a result of the pretreatment which was related to the changes in production rate and was evidence of a shift in the methanation reaction towards the left (methane steam reforming).

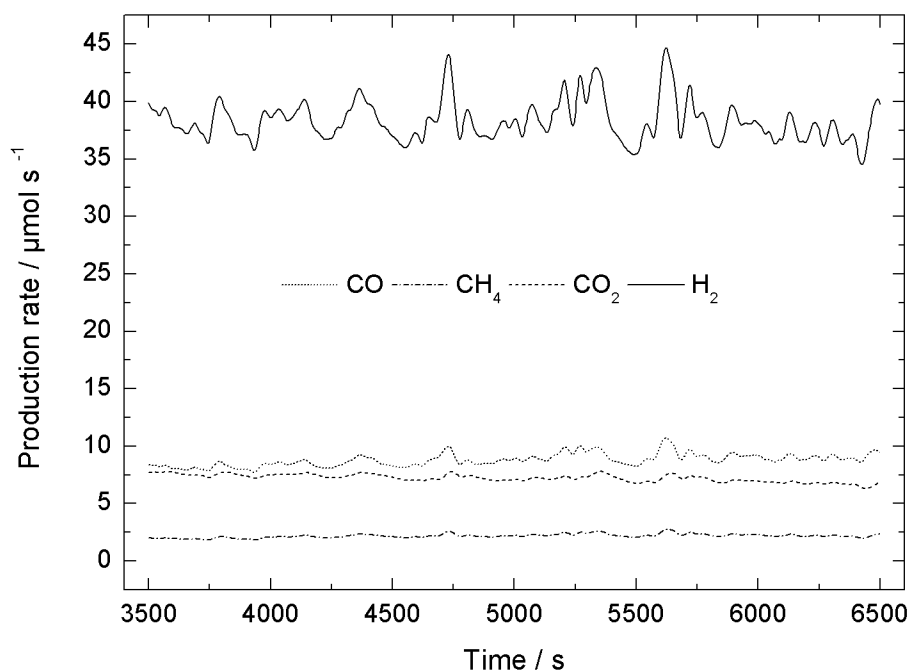


Figure 8. 20. Molar production rates of CO , CH_4 , CO_2 and H_2 during SR of ethanol after nichrome wire pretreatment (Run 4) at 600°C with a S:C ratio of 3:1.

Given the observed differences in water conversion and molar production rates, it was hypothesized that the pretreatment had resulted in an increase in WGS (Reaction 1. 2). This was tested by investigating the selectivity to CO and CO_2 before and after pretreatment. If the

pretreatment increased the activity of WGS then the selectivity to CO would be lower and that to CO₂ would be higher in Run 4 (after pretreatment) compared to Run 3 (before pretreatment). The data from the two runs showed that the selectivity to CO was significantly lower and that to CO₂ was significantly higher after pretreatment (Table 8. 4). It was concluded that the pretreatment improved the ability of the nichrome wire to carry out WGS which in turn increased the water conversion, the H₂ yield and the H₂:CO.

Table 8. 4. Median CO and CO₂ selectivity before and after nichrome wire pretreatment (comparing Run 3, before pretreatment with Run 4, after pretreatment).

Selectivity to CO		Statistical analysis
Before (Run 3)	75.0	
After (Run 4)	48.3	MW ₍₁₃₉₅₎ = 79.28e ⁴ , p < 0.05
Selectivity to CO ₂		Statistical analysis
Before (Run 3)	5.6	
After (Run 4)	39.4	MW ₍₁₃₃₇₎ = 27.12e ⁴ , p < 0.05

8.10 REPEATABILITY OF THE EXPERIMENTAL PROCEDURE (RUN 5)

Run 4 was repeated using the standard operating procedure developed in Section 8.6. This run will be referred to as Run 5 and was hence a replicate of Run 4. The main aim of this run was to test the repeatability of the experiment and the secondary aim was to log the power used to heat the wire reactor during steam reforming in order to learn how much energy was needed for the process.

The H₂ yield was 2.2 (AD₍₂₀₁₎ = 1.56, p < 0.05) which was higher than the H₂ yield achieved during Run 4. To understand the difference in H₂ yield, differences in observations made for Run 4 and 5 were investigated. The molar production rates of all gases were higher during Run 5 compared to Run 4 (Table 8. 7). When molar production rates with time on stream was compared it was observed that the input mixture flow appeared to have been smoother in Run 5 than in Run 4 (Figure 8. 21). It should be noted that Al stack could move slightly during handling and as such it could therefore have been in a slightly different position in this run compared to Run 4. The order of the molar production rates were the same as for run 4 (i.e. H₂ > CO > CO₂ > CH₄) (Figure 8. 21). The feedstock conversion was 51.1 ± 7.2% (AD₍₁₉₆₎ = 0.81, p > 0.05) which represented a 15% increase from Run 4 (MW₍₇₅₀₎ = 12.79e⁴, p < 0.05). The water conversion was 14.0% (AD₍₂₀₁₎ = 1.24, p < 0.05). This was 11% higher than Run 4. The selectivity to CO₂ was 38.2 (AD₍₁₉₅₎ = 1.53, p < 0.05) compared to 39.4 (AD₍₆₀₁₎ = 6.80, p < 0.05) during Run 4. Hence the slightly lower increase in water conversion compared to feedstock conversion could be attributed to a less pronounced WGS. The observations were attributed to the position of the Al stack which was in a more advantageous position during Run

5 as shown by the smoother input mixture flow. A more advantageous position involved providing a longer residence time with a subsequent increase in feedstock and water conversion.

The selectivity to H₂ was 95.2 (AD₍₂₀₁₎ = 2.46, p < 0.05) which was very similar to Run 4 (94.5 (AD₍₆₀₁₎ = 20.18, p < 0.05)). The carbon products selectivity to CO and CH₄ was 51.3 (AD₍₁₉₃₎ = 1.23, p < 0.05) and 10.6 (AD₍₂₀₁₎ = 1.08, p < 0.05) respectively and this was also similar to run 4 where the C selectivity to CO and CH₄ was 48.3 (AD₍₆₀₁₎ = 5.27, p < 0.05) and 12.1 (AD₍₆₀₁₎ = 11.23, p < 0.05)*.

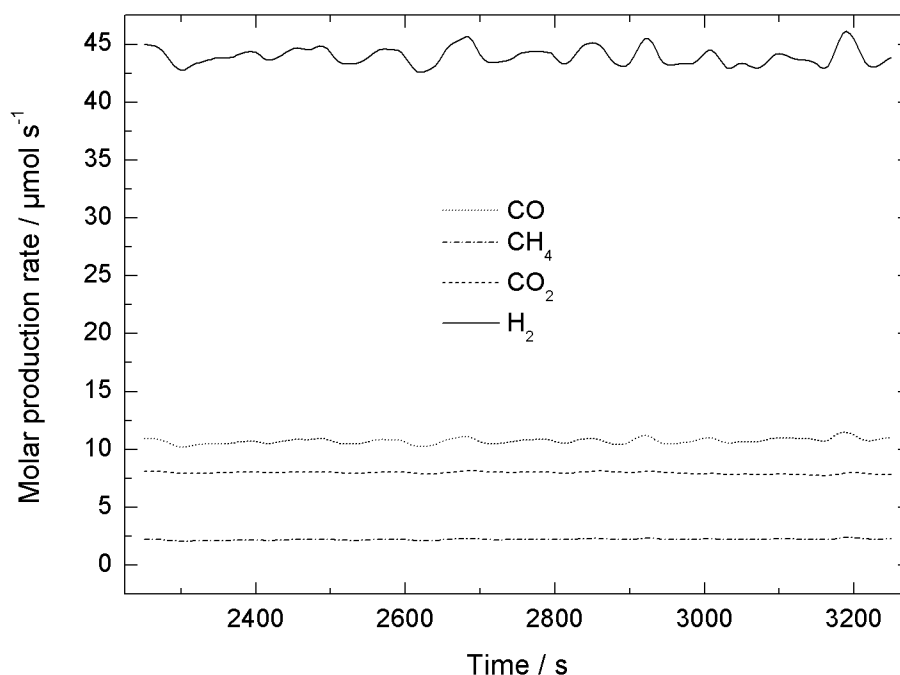


Figure 8. 21. Molar production rates of CO, CH₄, CO₂ and H₂ during a replicate of SR of ethanol (Run 5) at 600 °C with a S:C ratio of 3:1.

Decrease in catalyst activity with time on stream as a result of coke formation on catalyst surfaces has been reported in the literature.^{176,179,180} In Runs 4 and 5 gas production rates remained stable with time on stream with the exception of CO₂ which reduced from 7.7 μmole s⁻¹ (AD₍₄₁₎ = 2.33, p < 0.05) between 3500-3700s to 6.7 μmole s⁻¹ (AD₍₄₁₎ = 1.59, p < 0.05) between 6300-6500s in the case of run 4 (Figure 8. 20). During Run 5 the CO₂ production rate decreased from 8.0 ± 0.05 μmole s⁻¹ (AD₍₄₁₎ = 0.40, p > 0.05) between 2250-2450s to 7.8 ± 0.05 μmole s⁻¹ (AD₍₃₆₎ = 0.42, p < 0.05) between 3050-3250s (Figure 8. 21). Given these observations it was concluded that no significant catalyst deactivation occurred in this work. However the small reduction in CO₂ production rate indicated that significant deactivation could occur with longer time on stream given that stable feedstock conversion has been reported for 3-8h before the onset of catalyst deactivation.^{176,179}

An investigation of the glycerol decomposition pathway using density functional theory calculations and Brønsted–Evans–Polanyi (BEP) relationships showed how a number of dehydration steps on the catalyst surface were needed before adsorbed CO was made available on the surface for WGS.¹⁸⁶ The same can be assumed to apply to ethanol decomposition. Coke formation causes reduced contact between feedstock and catalyst surface and so it is reasonable to assume that fewer of the dehydration steps will occur with increased coke formation. From this assumption it can be concluded that less adsorbed CO would form as catalyst deactivation proceeds. Hence, an early sign of catalyst deactivation would be a reduction in CO₂ production caused by reduced WGS activity. The formation of CO₂ during the air purge step used as part of the standard operating procedure provided evidence for coke deposition on the nichrome wire and so the reduced CO₂ concentration can be attributed to coke formation during steam reforming.

The method used to heat the reactor and the method used to monitor the power supplied to it is described in detail in Chapter 2 but it is worth repeating that a constant electric potential difference of 46 V was maintained across the nichrome wire and an electric current of ≤ 9 A was supplied to produce heat. In practice, this meant that the electric current was being switched on and off in order to maintain a constant temperature. In the case of Run 5, the current was kept for about 2–3s and switched off for another 2–3s. Note that when the current was increased to ≈ 9 A the electric potential was reduced to ≈ 32 V as dictated by the resistance of the nichrome wire. To monitor the power supplied to the reactor, the electric potential difference and the electric current were logged every second for 30 min after the steam reforming process had reached steady state. The power was then derived by multiplying potential difference with current and plotted over time (Figure 8. 22). As a result of the method described above, many data points equaled zero since the data was logged while the current was switched off. For clarity, these data points are not shown, nor were they considered in the analysis of the data. Also, due to the distribution of values in the data the outliers were not removed. The median power supplied to the reactor was 288 W ($AD_{(62)} = 8.13$, $p < 0.05^*$).

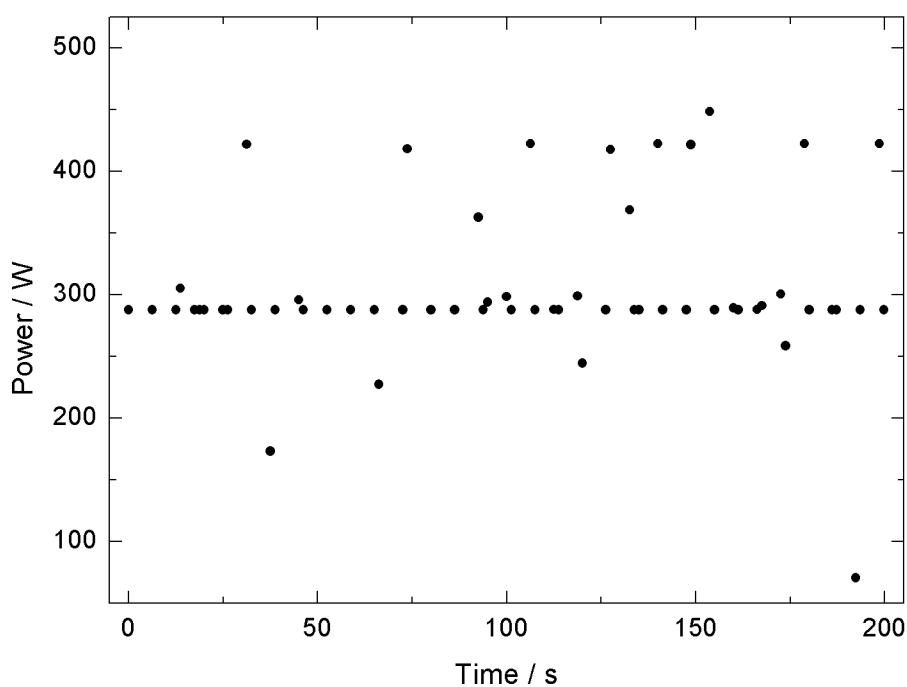


Figure 8. 22. The power supplied to the reactor as a function of time during SR of ethanol (Run 5) at 600 °C with a S:C ratio of 3:1.

The periodicity of the power supply and hence also of the surface temperature of the nichrome could possibly be part of the cause of the oscillations in the gas flows observed previously (Figure 8. 7, Figure 8. 13, Figure 8. 20).

The Eurotherm 2216e temperature controller used an on/off temperature control system. To reduce the periodicity of the power supply, alternative temperature control systems such as proportional integral (PI), proportional integral derivative (PID) or pulse width monitoring (PWM) could be used.

8.11 SORPTION ENHANCED STEAM REFORMING (SESR)

To further improve the performance of the wire reactor, a Ca-based sorbent was introduced with the aim of achieving sorption enhanced steam reforming (SESR). CaO derived from $\text{Ca}(\text{OH})_2$ was used as a sorbent because it had displayed the highest CO_2 capture capacity in Chapter 6. $\text{Ca}(\text{OH})_2$ was used which decomposed to CaO during the startup of the experimental runs described below and hence the carbonation of CaO could be added to the list of possible reactions in the system. With CaO in place the complete ethanol sorption enhanced steam reforming (SESR) reaction produces H_2 and CaCO_3 (Reaction 5. 9) as opposed to the H_2 and CO_2 products of the complete ethanol steam reforming (SR) reaction without sorption (Reaction 5. 4). Note that the complete ethanol SR reaction is endothermic ($+173\text{kJ mol}^{-1}$) while

the complete SESR reaction is exothermic (-183 kJ mol^{-1}) due to the heat released by CaO carbonation (Reaction 3. 1).

SESR using conventional steam reforming reactors is carried out by adding sorbent particles well mixed with catalyst particles into the reformer. Given the design of the wire reactor this method could not be applied. A number of different methods of introducing the sorbent to the wire reactor were tested. These included addition of sorbent pellets to the reactor and coating the monolith as well as the nichrome wire with sorbent. These methods are detailed below together with the results.

Thermodynamic equilibrium analysis of ethanol SESR is described in detail in Chapter 5. In summary the maximum H_2 yield is higher and is reached at a lower temperature during SESR compared to SR at thermodynamic equilibrium. Thermodynamic analysis was carried out with input compound compositions corresponding to the conditions in the wire reactor with a S:C of 3:1 and a CaO:C of 2:1. Under these conditions an H_2 yield of 5.95 and a water conversion of 38.8% was expected at $597 \text{ }^\circ\text{C}$ under thermodynamic equilibrium. Hence, both the H_2 yield and the water conversion are higher under sorption enhanced conditions than under conventional SR (5.02 and 28.5%, Section 8.5.2).

Experimental work reported in the literature has shown that it was possible to reach close to 100% H_2 product fraction for about 100 min (6000s) time on stream ($550 \text{ }^\circ\text{C}$, S:C 3:1) using dolomite as a CO_2 sorbent.²⁶⁵ A H_2 yield of 6 (which is the stoichiometric maximum according to the complete ethanol SESR reaction) was achieved for 30 min (1800s) using Li_4SiO_4 as a sorbent ($577 \text{ }^\circ\text{C}$, S:C 3:1).³³³

8.11.1 SORBENT PELLETS (RUN 6)

The first run with sorbent was carried out by adding sorbent pellets at the bottom of the reactor, just below the monolith (Figure 8. 23). This run will be referred to as Run 6. Before the run, the amount of $\text{Ca}(\text{OH})_2$ to add to the reactor was calculated. At steady state, during Run 5 the reactor off-gas contained $\approx 2.5\%$ CO_2 at a flow of 350 ml min^{-1} which corresponded to $0.36 \text{ mmole CO}_2 \text{ min}^{-1}$. It was decided to use 5g of $\text{Ca}(\text{OH})_2$ as the CO_2 capture capacity of this amount of sorbent equaled the amount of CO_2 expected to form during 1h 48 min of steam reforming at steady state. It was considered reasonable to expect about 1h of SESR with this amount of sorbent. 5g of $\text{Ca}(\text{OH})_2$ pellets with a diameter of 1.0-1.6 mm were prepared using the method described in Chapter 2, Section 2.5 and placed at the bottom of the reactor (Figure 8. 23). This corresponded to $67.5 \text{ mmole Ca}(\text{OH})_2$. The reactor was then heated to $600 \text{ }^\circ\text{C}$ and the air purge and H_2 reduction steps were carried out as before. Previous work (Chapter 6 and Chapter 7) had shown that $\text{Ca}(\text{OH})_2$ decomposes to CaO (Reaction 6. 1) at temperatures of $400 \text{ }^\circ\text{C}$ and above. Therefore it was assumed that the $\text{Ca}(\text{OH})_2$ had decomposed to CaO by the start of the run.

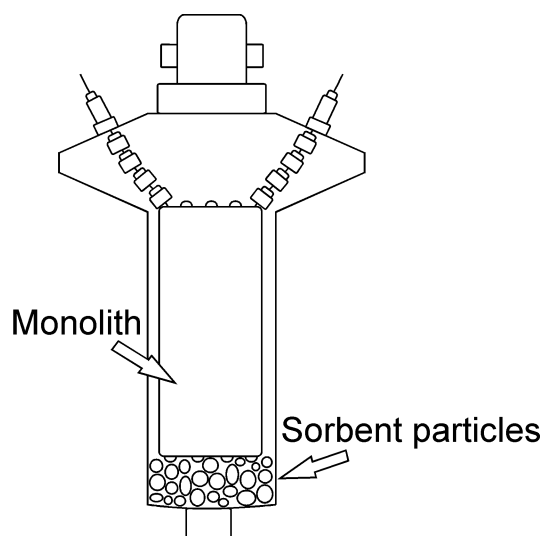


Figure 8. 23. Schematic of the nichrome wire reactor with sorbent particles below the monolith.

At steady state the H_2 yield in the presence of sorbent pellets was 1.7 ($AD_{(801)} = 24.59$, $p < 0.05$). At thermodynamic equilibrium, SESR has a higher H_2 yield than SR (5.95 for SESR compared to 5.02 for SR, Section 8.5.2, Section 8.11) and hence the H_2 yield was expected to be higher in the presence of sorbent pellets. However, the H_2 yield observed with sorbent particles was lower than without (1.9 and 2.2 for Runs 4 and 5 respectively, Table 8. 7). Note that Runs 4 and 5 were carried out under the same conditions of Run 6 with the exception that sorbent pellets were added to the reactor prior to Run 6. The results indicated that sorption enhancement was not achieved as a result of the addition of sorbent pellets. The $H_2:CO$ was 3.9 ± 0.04 ($AD_{(21)} = 0.33$, $p > 0.05$) between 2500 and 2600s, where the CO_2 concentration was negligible. Later (7500-7600s), the $H_2:CO$ had reduced to 2.7 ± 0.01 ($AD_{(18)} = 0.44$, $p > 0.05$) when the CO_2 concentration had increased to 0.8% ($AD_{(21)} = 1.18$, $p < 0.05$). This showed that the steam reforming process was far from thermodynamic equilibrium, for which the $H_2:CO$ would be 308:1 at 597 °C, and that it was shifted further away from equilibrium as the CO_2 sorbent was being saturated. The results also showed that the $H_2:CO$ achieved in the presence of the sorbent was lower than the $H_2:CO$ achieved without (4.1:1 to 4.3:1, Table 8. 7).

Ca-based CO_2 sorbent will become saturated, resulting in CO_2 breakthrough.^{222,265,332} To regain CO_2 capture capacity, the sorbent can be regenerated by stopping the input mixture flow through the reactor, replacing it with a flow of an inert gas and increasing the reactor temperature (thus reversing the CaO carbonation reaction).^{223,265} However, for every such cycle of sorption enhanced reforming and sorbent regeneration, the time on stream to CO_2 breakthrough is reduced due to the reduced CO_2 capture capacity of the Ca-based sorbent which occurs during regeneration due to sintering.^{223,265}

It has been demonstrated that the CO₂ capture capacity of sintered Ca-based sorbents can be regenerated by introducing steam for 5 min with a reactor temperature of 100 °C.⁴⁷ This method could be applied to SESR to increase the time to CO₂ breakthrough. Sorbent regeneration can also be achieved by mixing the sorbent with liquid water at 25 °C.²⁶² This method has the advantage of a low energy penalty compared to regeneration using steam but would involve either removing the sorbent from the reactor or flooding it.

It was observed that the current supplied to the reactor by the power supply unit was switched off for longer periods than it had been during earlier runs. Instead of being on for about 2-3s and switched off for another 2-3s the current was on for 2-3s and switched off for up to 15-20s (Figure 8. 24). This was further evidence of CO₂ capture via the CaO carbonation reaction as it is exothermic.

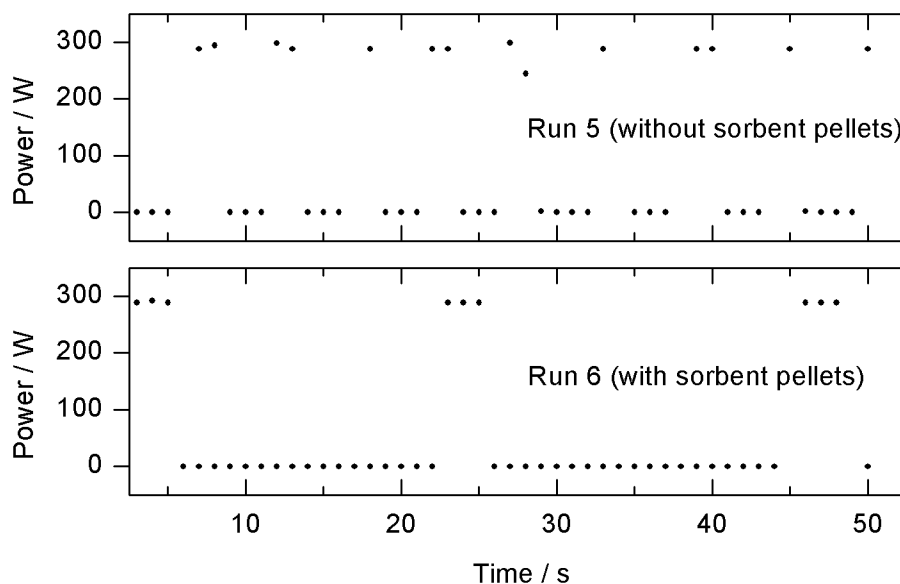


Figure 8. 24. Comparison of power supply over time for Run 5 (without sorbent pellets) and run 6 (with sorbent pellets).

However, this would at times cause a reduction in the conversion of feedstock to gaseous products as shown by the reoccurring drops in gas concentrations. The drops were followed by surges when the current was switched back on. It is important to note that the sorbent particles surrounded the thermocouple located below the monolith, which provided feedback to the power supply unit (Figure 2. 5). This meant that even though the temperature around the thermocouple below the monolith was maintained at 600 °C as the current was switched on and off, the temperature around the thermocouple above the monolith fluctuated. These fluctuations correlated with the fluctuation gaseous concentrations, most notably H₂ (Figure 8. 25).

The results were also further evidence that fluctuations in reactor off-gas concentrations could be due to the periodicity of the power supply (discussed in Section 8.10).

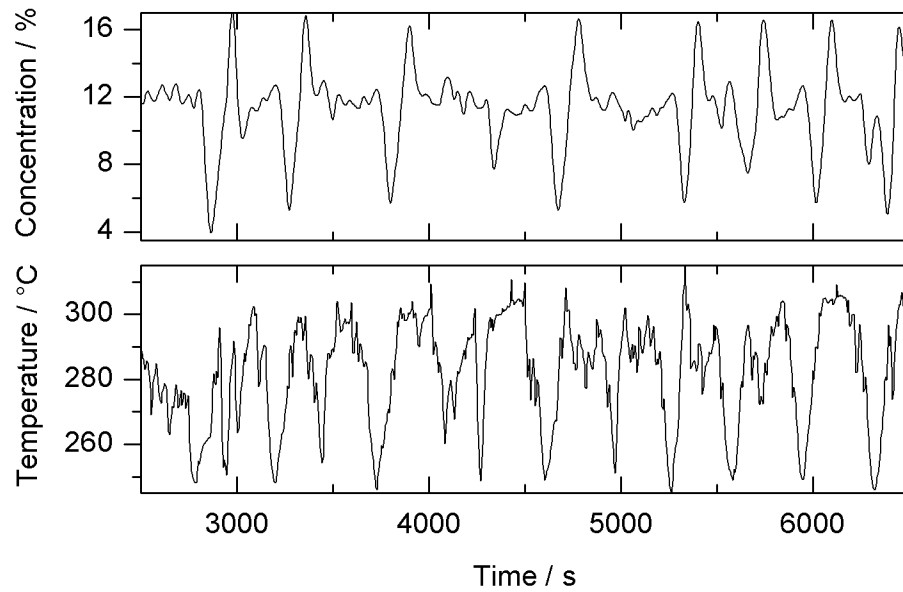


Figure 8. 25. H₂ concentration and temperature readings from above the monolith recorded during Run 6.

The addition of the sorbent pellets caused the order of the gaseous molar production rates to change from H₂ > CO > CO₂ > CH₄ (the order observed in Runs 4 and 5, without sorbent pellets) to H₂ > CO > CH₄ > CO₂ (Figure 8. 26). Hence, the molar production rates of CO₂ and CH₄ had switched so that the production of CH₄ was now higher than CO₂. This was attributed to the capture of CO₂ via CaO carbonation. Note that feedstock and water conversion could not be calculated from the concentrations of gaseous products because a portion of the CO₂ that was formed was removed from the gas phase by the sorbent and thus the total amount of CO₂ formed could not be quantified. Selectivity to carbon containing products could not be calculated either for the same reason. Note that calcining the sorbent pellets and quantifying the released CO₂ would only provide the total amount of CO₂ captured over the entire run while the concentration of the CO₂ intermediate at any given time was needed to determine feedstock and water conversion as well as selectivity to carbon containing products.

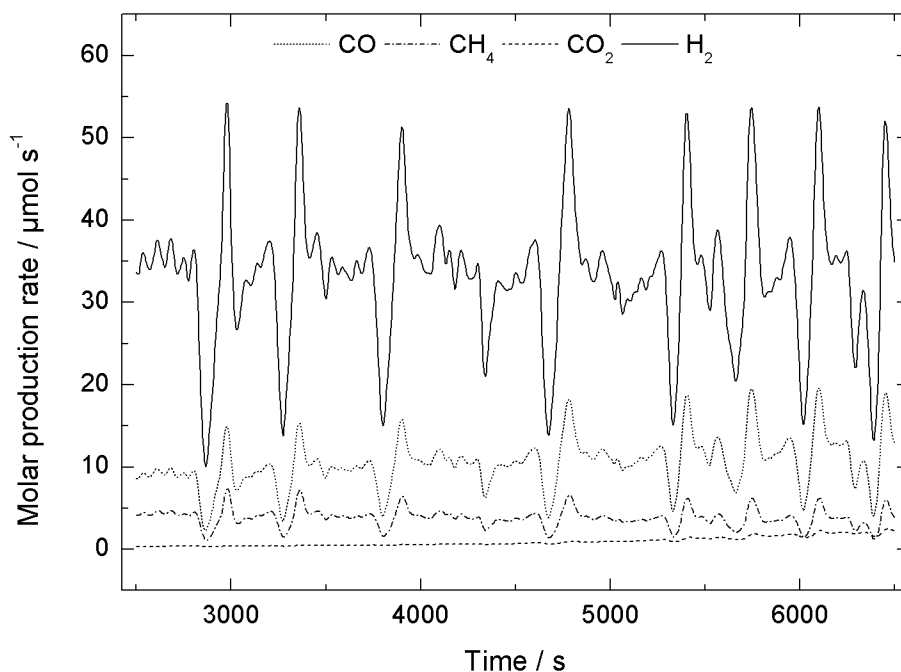


Figure 8. 26. Molar production rates of CO, CH₄, CO₂ and H₂ during Run 6 (with sorbent pellets below the monolith).

The CO₂ concentration in the reactor off-gas increased with time on stream which was in agreement with the work by Dou et al.^{23,218} who also reported the same observation which can be attributed to saturation of the CO₂ sorbent (CO₂ breakthrough). The H₂ yield was 1.7 ± 0.05 ($AD_{(21)} = 0.38$, $p > 0.05$) between 2500-2600 s and 1.7 ± 0.08 ($AD_{(21)} = 1.06$, $p > 0.05$) between 7500-7600s, showing that the saturation of the sorbent did not have a significant effect on the H₂ yield. Saturation of the sorbent was expected to impact negatively the H₂ yield given that the effects of sorption enhancement would be reduced with a reduced molar ratio of active sorbent.

Before sorbent saturation the CO₂ concentration in the reactor off-gas as measured by the gas analyser was 0.1% ($AD_{(21)} = 0.84$, $p < 0.05$)* between 2500-2600s and increased to 0.8% ($AD_{(21)} = 1.18$, $p < 0.05$) between 7500-7600s. This confirmed that the CO₂ concentration in the reactor off-gas increased with time on stream as the sorbent was being saturated. The CO₂ concentrations during runs 4 and 5 were 2.4% ($AD_{(601)} = 3.88$, $p < 0.05$) and 2.6% ($AD_{(201)} = 5.81$, $p < 0.05$)* respectively. The observations showed that, as expected, the amount of CO₂ in the reactor off-gas had been significantly reduced due to the presence of the sorbent pellets.

The production rate of CO increased with time on stream while there was no significant change in the production rates of H₂ and CH₄ over the same time period (Table 8. 5). Note that the CO₂ production rate was unknown given that the extent of carbonation was unknown.

Table 8. 5. Molar production rates of CO, CH₄ and H₂ at 2500-2600s time on stream and at 7500-7600 s time on steam.

	Molar production rate / $\mu\text{mole s}^{-1}$	
	2500-2600s	7500-7600s
CO	9.01 \pm 0.15 (AD ₍₂₁₎ = 0.21, p > 0.05)	12.28 (AD ₍₂₁₎ = 1.04, p < 0.05)
CH ₄	4.26 \pm 0.15 (AD ₍₂₁₎ = 0.85, p > 0.05)	3.48 (AD ₍₂₁₎ = 1.15, p < 0.05)
H ₂	34.82 \pm 0.99 (AD ₍₂₁₎ = 0.38, p > 0.05)	33.12 (AD ₍₂₁₎ = 1.06, p < 0.05)

In the absence of sorbent (Runs 4 and 5), the production rates of CO, CH₄ and H₂ production rates were 8.8-10.7, 2.2 and 37.9-43.9 $\mu\text{mole s}^{-1}$ respectively (Table 8. 7). This meant that the presence of sorbent had no significant impact on the CO production rate while the CH₄ production rate had increased slightly and the H₂ production rate was lower. The selectivity (H) to CH₄ in the presence of sorbent was 10.2 (AD₍₈₀₁₎ = 3.32, p < 0.05)* which was significantly higher than without sorbent was (4.8-5.4, see Table 8. 7). The increase in CO production rate with time on stream could not be explained by a shift in the CO methanation reaction because there was no corresponding reduction in CH₄. Nor could it be explained by a shift in the ethanol steam reforming reaction because there was no corresponding increase in H₂. It could be due to a shift in the WGS reaction towards the left which would be expected considering the increase in CO₂ off-gas concentration and Le Chateliers principle.

In summary, the addition of sorbent pellets failed to initiate sorption enhancement as shown by the H₂ yield. Instead, the results indicated that the sorbent pellets removed CO₂ from the syngas produced inside the reactor and did not have any effect on the equilibrium of the ethanol steam reforming reaction or the WGS reaction. In addition, the heat produced by the CaO carbonation reaction caused fluctuations in temperature and gas production, highlighting an issue with the reactor design. To address this issue, and to make the environment inside the reactor more suitable for sorption enhancement, a set of sorbent coating methods were tested.

8.11.2 SORBENT COATING

In order to address the challenges encountered when using sorbent pellets, coating methods were tested as an alternative way of introducing sorbent to the reactor. The aim of the work was to coat the surfaces of the monolith and/or the nichrome wire with sorbent instead of adding sorbent to the reactor in the form of pellets downstream of the wire. A coating of sorbent would move the sorbent closer to the catalytic surface so that ethanol steam reforming, WGS and CaO carbonation would occur in close proximity. The CaO carbonation reaction would then be able to shift the equilibrium of the ethanol steam reforming and the WGS reaction and cause sorption enhancement. Without a sorbent bed surrounding the thermocouple below the monolith, no fluctuations of temperature and thus in gas production would occur. Three coating methods were tested. The first two methods involved coating the monolith and the nichrome

wire respectively using a $\text{Ca}(\text{OH})_2$ solution. The final method involved replacing the monolith with a series of alumina support pieces which had been impregnated using a CaCl_2 solution.

8.11.2.1 MONOLITH COATING USING $\text{Ca}(\text{OH})_2$ SOLUTION (RUN7)

A $\text{Ca}(\text{OH})_2$ solution was prepared using the same method as when the $\text{Ca}(\text{OH})_2$ sorbent was prepared (Chapter 2, Section 2.3). 760 ml of deionised water was decanted into a glass beaker and heated on a hot plate whilst being agitated with a magnetic stirrer. Upon reaching $75\text{ }^\circ\text{C}$, 130 ml of 2-propanol was added together with 26.2g CaO . The solution was kept at $75\text{ }^\circ\text{C}$ and stirred for 1h. The monolith (with the nichrome wire threaded through it) was then submerged into the solution and the glass beaker was placed in an oven (heated to $120\text{ }^\circ\text{C}$) overnight (Figure 8. 27).

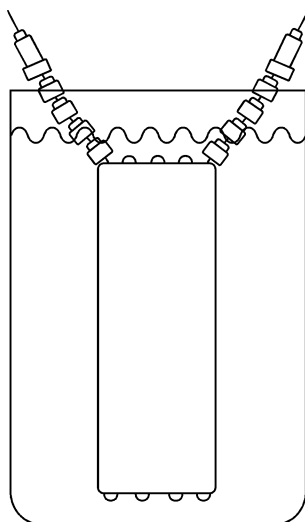


Figure 8. 27. Schematic of the monolith submerged in a $\text{Ca}(\text{OH})_2$ solution.

Images were taken of the monolith before and after the coating using a digital camera (Figure 8. 28). A thin layer of finely grained sorbent was observed on the surface of the monolith making the surface matt instead of shiny. There were also larger lumps of sorbent around the openings of some of the channels.

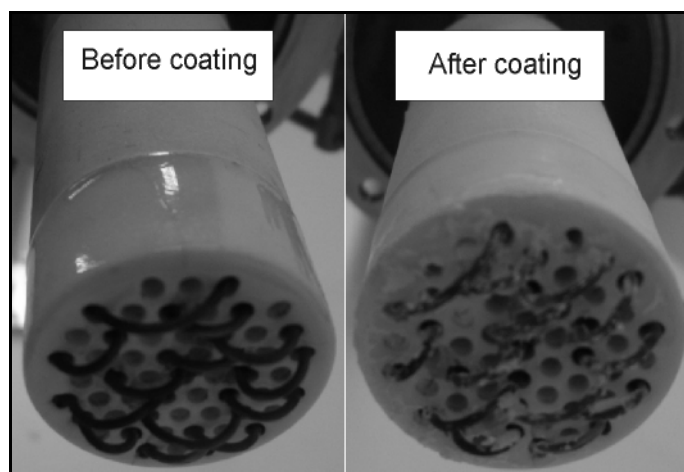


Figure 8. 28. Pictures taken of the monolith before and after monolith coating in a $\text{Ca}(\text{OH})_2$ solution.

A run was carried out with the coated monolith in place using the same conditions as Runs 4-6 (N_2 flow of 350 ml min^{-1} , a temperature of $600 \text{ }^\circ\text{C}$, an input mixture flow of 12 ml h^{-1} at S:C of 3:1 using ethanol as the feedstock). The run carried out with the coated monolith will be referred to as Run 7. The H_2 yield was 1.7 ($\text{AD}_{(601)} = 29.76$, $p < 0.05^*$) which was again lower than without sorbent (1.9 and 2.2 for Runs 4 and 5). Note that the outliers have been included in some of the data sets because their spread of values meant that a large percentage of the data points became outliers under the definition used here (see Chapter 2, Section 2.13 for more details). The H_2 :CO was 2.8:1 ($\text{AD}_{(601)} = 18.06$, $p < 0.05^*$), which was also lower than in the absence of sorbent (4.1:1 and 4.3:1). Hence, there was no evidence for sorption enhancement.

At steady state the order of the gaseous production rates were $\text{H}_2 > \text{CO} > \text{CO}_2 > \text{CH}_4$ as was observed during Runs 4 and 5 without sorbent (Figure 8. 29). Note that when sorbent pellets were used, CO_2 displayed the lowest production rate. The observation suggested little or no CO_2 capture. In the absence of sorbent (Runs 4 and 5), the production rates of CO, CH_4 and H_2 production rates were 8.8-10.7, 2.2 and $37.9\text{-}43.9 \text{ } \mu\text{mole s}^{-1}$ respectively (Table 8. 7). With monolith coating the CO, CH_4 and H_2 production rates were 12.4 ($\text{AD}_{(601)} = 29.28$, $p < 0.05^*$), 2.9 ($\text{AD}_{(601)} = 7.42$, $p < 0.05$) and $34.4 \text{ } \mu\text{mole s}^{-1}$ ($\text{AD}_{(601)} = 29.76$, $p < 0.05^*$). Hence, the CO and CH_4 production rate were slightly higher and the H_2 production rate was slightly lower after monolith coating compared to the runs carried out without sorbent. However, the differences were smaller than the differences between Runs 4 and 5 indicating that the differences could not confidently be attributed to the monolith coating.

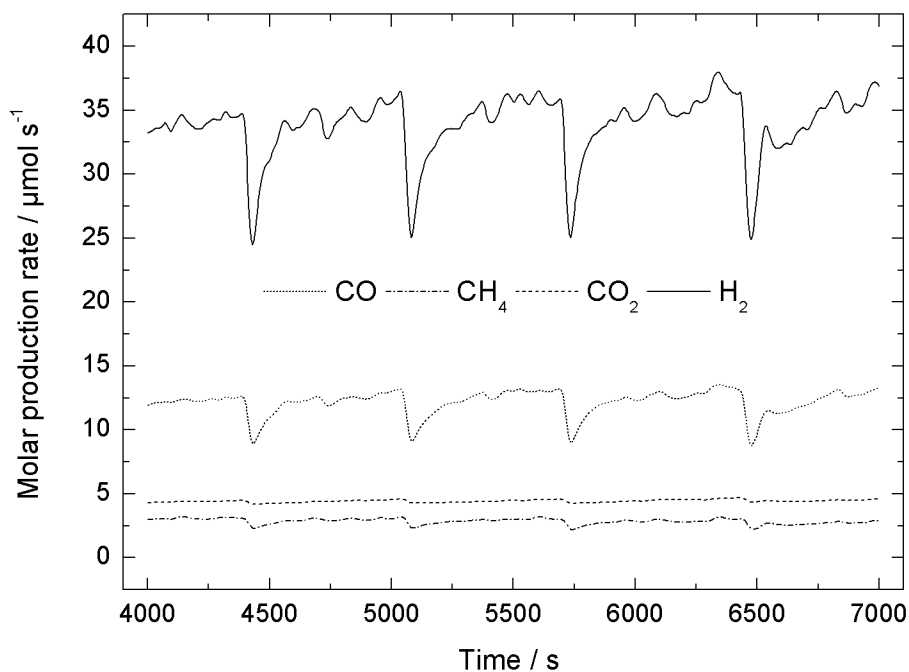


Figure 8. 29. Molar production rates of CO, CH₄, CO₂ and H₂ during Run 7 (monolith coated in a Ca(OH)₂ solution).

Due to the presence of sorbent, the CO₂ production rate could not be accurately determined; instead the CO₂ concentrations at different times on stream were investigated. Between 4000 and 4100 s the CO₂ concentration was 1.5 ± 0.005 ($AD_{(21)} = 0.22$, $p > 0.05$) and between 6900 and 7000 s it was 1.5 ± 0.007 ($AD_{(21)} = 0.34$, $p > 0.05$). Hence there was no significant change in the CO₂ concentration with time on stream which was the case when sorbent particles were used. This meant that there was no indication of sorbent saturation at steady state.

However, before the system reached steady state the CO₂ concentration steadily increased before reaching steady state while the other gases fluctuated irregularly (Figure 8. 30). The shape of the CO₂ concentration curve with time on stream indicated sorbent saturation as observed above during SESR using sorbent particles (Run 6) and by others.^{23,218}

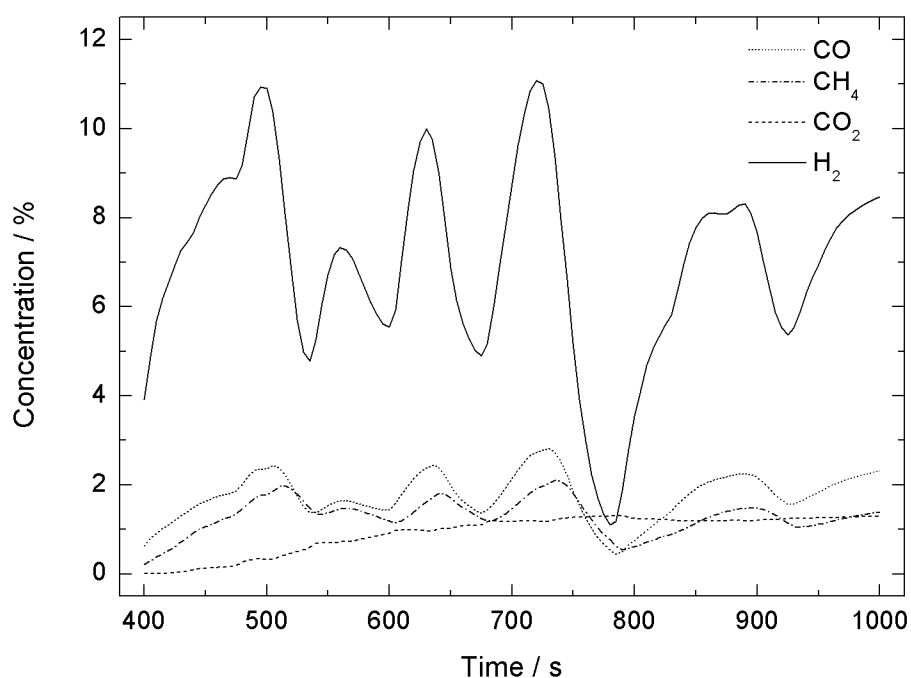


Figure 8. 30. Reactor off-gas concentrations of CO, CH₄, CO₂ and H₂ recorded between 400 and 1000s time on stream during Run 7 (monolith coated in a Ca(OH)₂ solution).

The quantity of Ca(OH)₂ on the monolith was determined by comparing the mass of Ca(OH)₂ which was left in the beaker after coating with the mass of the CaO that was dissolved in the beaker. Assuming that all CaO had converted to Ca(OH)₂ (which was reasonable to assume given the XRD results presented in Chapter 6), the monolith contained 0.4g Ca(OH)₂ which equaled 5.4 mmol. Given the CO₂ capture capacity of the Ca(OH)₂ and the previously observed CO₂ production during reforming without sorbent (0.4 mmole CO₂ min⁻¹, see Section 6.6.1), this amount of sorbent would be able to capture all CO₂ formed in the process for 480s (assuming complete conversion and full capture rate). This estimate was in agreement with the results which showed saturation occurring in about 600s (Figure 8. 30).

Reoccurring drops in gas production were observed but they were not followed by increases in production as observed in the presence of sorbent pellets during Run 6 (Figure 8. 29). The current supplied to the reactor by the power supply unit was switched on and off in the same time intervals as observed in the absence of sorbent (on for 2-3s and off for 2-3s). The reoccurring drops in gas production were therefore attributed to the position of the Al stack. It is reasonable to assume that the Al stack was positioned in a way which facilitated the formation of input mixture droplets at the bottom of the stack. This would cause a stop of input mixture flow for a limited time until the droplet sheared off, and would explain the drops in gas production.

Given that there was no evidence of CO₂ capture at steady state, the CO₂ production rate as well as the feedstock and water conversion were considered for Run 7. The CO₂ production

rate was $4.4 \mu\text{mole s}^{-1}$ ($AD_{(601)} = 1.12$, $p < 0.05$) which was lower than without sorbent (7.3 and $8.0 \mu\text{mole s}^{-1}$ for runs 4 and 5 respectively). Recall that the H_2 production rate was also lower than without sorbent while CO and CH_4 production rates were slightly higher. The selectivity (H) to CH_4 was 7.7 ($AD_{(594)} = 2.32$, $p < 0.05$) which was significantly higher than without sorbent (4.8 - 5.4 , Table 8. 7) which in part explained the differences in H_2 and CH_4 production rates. Selectivity (C) to CO_2 was significantly lower after monolith coating compared to the runs without sorbent (Table 8. 6).

Table 8. 6. Selectivity (C) to CO , CO_2 and CH_4 at steady state to before and after monolith coating.

	No sorbent (Runs 4 and 5)	Monolith coating (Run 7)
CO	48.3-51.3	62.9 ($AD_{(601)} = 35.48$, $p < 0.05$)*
CO_2	38.1-39.4	22.4 ($AD_{(601)} = 62.10$, $p < 0.05$)*
CH_4	10.6-12.0	14.6 ($AD_{(601)} = 3.66$, $p < 0.05$)

The feedstock and water conversion were 48.7% ($AD_{(601)} = 25.10$, $p < 0.05$ *) and 8.5% ($AD_{(601)} = 44.53$, $p < 0.05$ *) respectively. This showed that the feedstock conversion was similar to the conversions observed without sorbent (44.4 and $51.1 \pm 7.2\%$) (Table 8. 7) while the water conversion was lower than without sorbent (12.6 - 14.0%) (Table 8. 7). The lower water conversion was attributed to a reduced WGS due to the fact that the selectivity to CO_2 was lower after monolith coating compared to the runs without the presence of sorbent. The WGS reaction initiates with an interaction between adsorbed CO and H_2O ^{187,342,343} and monolith coating could have hindered CO adsorption. A visible change to the appearance of the monolith surface from shiny to matt was observed (Figure 8. 28) and so changes to the physical and chemical properties of the surface of the nichrome wire within the monolith channels (like for example CO adsorption ability) was likely.

In summary, monolith coating resulted in sorbent saturation prior to steady state meaning that no sorption enhancement was achieved. After sorbent saturation, the reactor performed worse than it did without sorbent which was attributed to a reduced ability to achieve WGS. Another method of adding sorbent to the reactor was needed.

8.11.2.2 NICHROME WIRE COATING USING $\text{Ca}(\text{OH})_2$ SOLUTION (RUN 8)

A $\text{Ca}(\text{OH})_2$ solution was prepared using 8.16g CaO and 50 ml 2-propanol. The monolith was suspended vertically and the solution was applied individually to each monolith channel using a glass pipette. The monolith was allowed to dry for 10 min . 3 coatings were added this way and the monolith was then left to dry overnight at room temperature. The aim of this method was to supply the sorbent directly to the wire and to the walls of the monolith channels in order to apply a larger amount of sorbent directly to its place of use. As the $\text{Ca}(\text{OH})_2$ solution

ran down the nichrome wire, a sorbent layer was deposited on it as demonstrated in Figure 8. 31 on a short length of nichrome wire. 2-propanol was chosen due to its high volatility in order to facilitate this process.

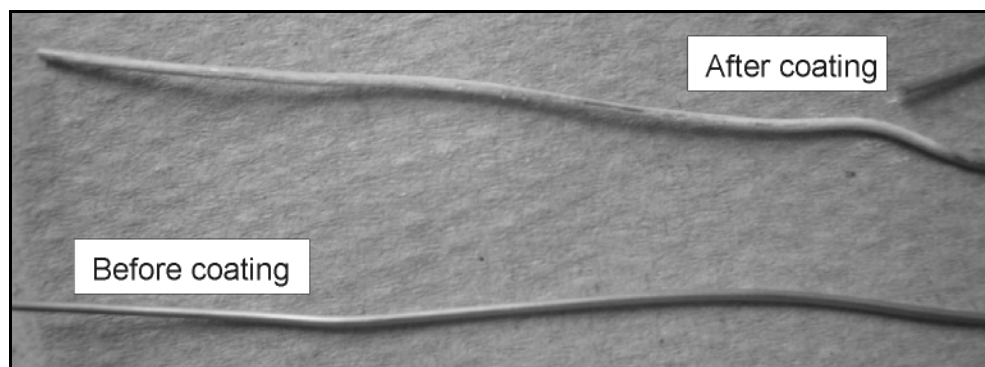


Figure 8. 31. A short length of nichrome resistance wire coated using a $\text{Ca}(\text{OH})_2$ solution shown next to an uncoated length of wire.

The quantity of $\text{Ca}(\text{OH})_2$ on the monolith was determined by weighing the monolith before and after wire coating. Assuming that the change in weight was solely due to the addition of $\text{Ca}(\text{OH})_2$ the mass of sorbent added was 1.9 mg which corresponded to 25.6 mmole of Ca. This was an improvement over the monolith coating method with which 5.4 mmole of Ca was added. An image was taken of the monolith after the wire coating and it was compared to the image taken before any coating had been carried out (Figure 8. 32). This method ensured that no sorbent was coated on the outside of the monolith as shown by the shiny surface of the monolith after coating. Instead, the nichrome wire was coated as shown by the colouration of the wire from black to white.

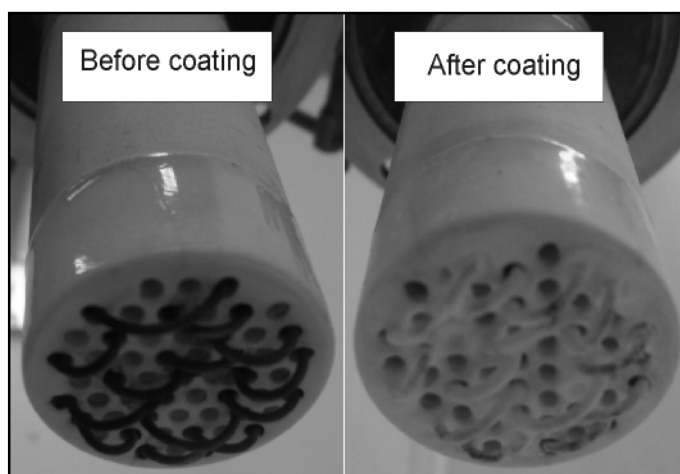


Figure 8. 32. Pictures taken of the monolith before and after wire coating using a $\text{Ca}(\text{OH})_2$ solution.

The run featuring wire coating is referred to as Run 8. After the system had reached steady state, the order of the gaseous molar production rates was $\text{H}_2 > \text{CO}_2 > \text{CH}_4 > \text{CO}$ at first and later changed to $\text{H}_2 > \text{CO}_2 > \text{CO} > \text{CH}_4$ within 2000s time on stream (Figure 8. 33). The H_2 yield increased from 0.8 ($\text{AD}_{(61)} = 1.43$, $p < 0.05$) between 2100-2400s to 1.1 ($\text{AD}_{(61)} = 0.98$, $p < 0.05$) between 5700-6000s. This was lower than without sorbent (1.9 and 2.2, Table 8. 7), hence sorption enhancement was not achieved. Therefore, CO_2 production rates as well as feedstock and water conversion was considered. The shift in the order of the CO and CH_4 production rates over time could be attributed to a shift towards the left of the CO methanation reaction (Reaction 4. 2).

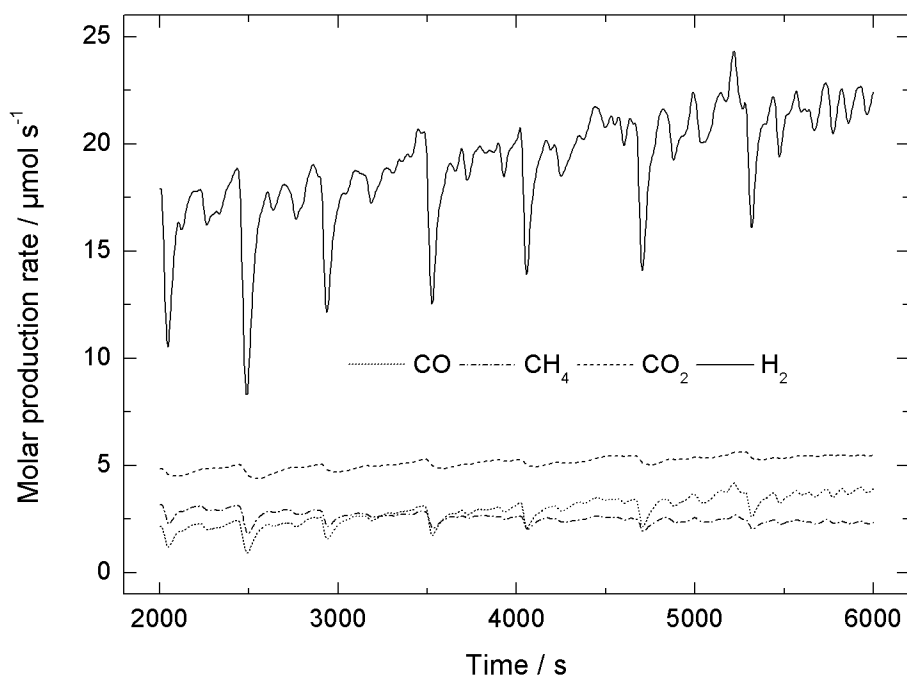


Figure 8. 33. Molar production rates of CO , CH_4 , CO_2 and H_2 during Run 8 (wire coating using a $\text{Ca}(\text{OH})_2$ solution).

Between 2100 and 2400s time on stream the CO production rate was $2.1 \mu\text{mole s}^{-1}$ ($\text{AD}_{(61)} = 0.80$, $p < 0.05$). It then increased to $3.8 \pm 0.12 \mu\text{mole s}^{-1}$ ($\text{AD}_{(61)} = 0.58$, $p > 0.05$) between 5700-6000 s (Figure 8. 34). Simultaneously, the CH_4 production rate showed a small decrease from $2.9 \mu\text{mole s}^{-1}$ ($\text{AD}_{(61)} = 2.01$, $p < 0.05$) to $2.3 \mu\text{mole s}^{-1}$ ($\text{AD}_{(61)} = 1.48$, $p < 0.05$). Given the molar balance of the reverse CO methanation reaction, Reaction 5. 1 (where 1 mole of CH_4 produces 1 mole of CO) the increased molar production of CO cannot be attributed solely to a shift in the CO methanation reaction because the corresponding reduction in CH_4 production is not large enough. However, over the same time period the H_2 production rate increased from $17.0 \mu\text{mole s}^{-1}$ ($\text{AD}_{(61)} = 1.43$, $p < 0.05$) to $22.0 \mu\text{mole s}^{-1}$ ($\text{AD}_{(61)} = 2.01$, $p < 0.05$) indicating

that an increased ethanol steam reforming could account for a part of the increase in CO production rate (Figure 8. 35).

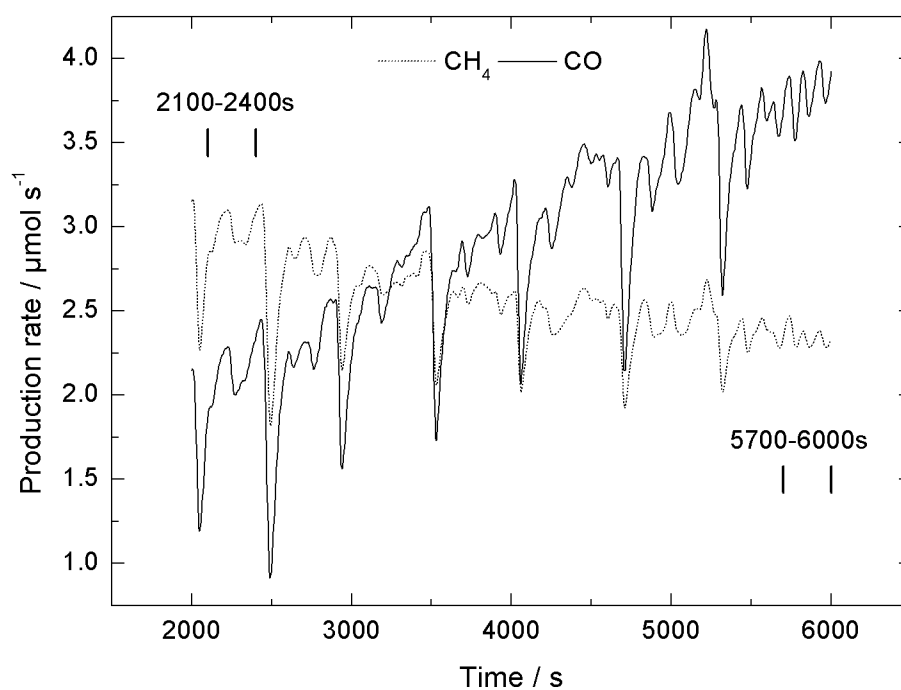


Figure 8. 34. Molar production rates of CH₄ and CO during Run 8 (wire coating using a Ca(OH)₂ solution).

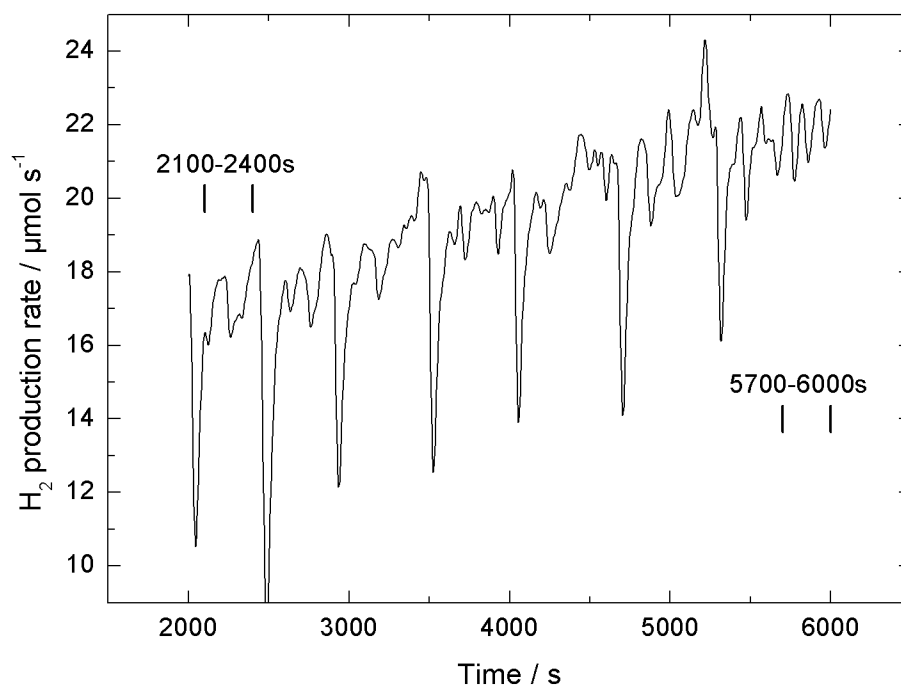


Figure 8. 35. Molar production rates of H₂ during Run 8 (wire coating using a Ca(OH)₂ solution).

The selectivity to hydrogen containing products with time on stream showed a continuous increase in the selectivity to H_2 with a simultaneous decrease in selectivity to CH_4 (Figure 8. 36). This meant that the hydrogen in the syngas was being shifted from CH_4 into H_2 .

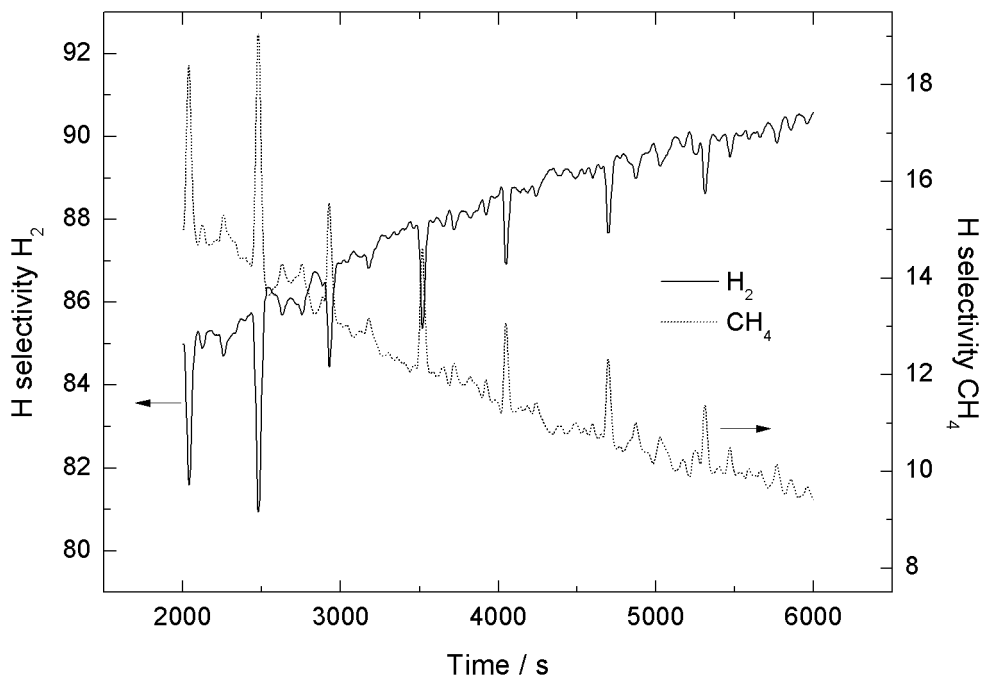


Figure 8. 36. Selectivity to hydrogen containing species (H_2 and CH_4) during Run 8 (wire coating using a $Ca(OH)_2$ solution).

The H_2 yield increased from 0.8 ($AD_{(61)} = 1.4$, $p < 0.05$) between 2100-2400s to 1.1 ($AD_{(61)} = 0.98$, $p < 0.05$) between 5700-6000s. The $H_2:CO$ was simultaneously reduced from 8.0:1 ($AD_{(60)} = 0.83$, $p < 0.05$) between 2100-2400s to 5.8:1 ($AD_{(61)} = 1.14$, $p < 0.05$) between 5700-6000 s. The CO_2 production rates increased slightly from $4.8 \mu\text{mole s}^{-1}$ ($AD_{(61)} = 3.80$, $p < 0.05$) (2100-2400s) to $5.5 \pm 0.02 \mu\text{mole s}^{-1}$ ($AD_{(61)} = 3.80$, $p > 0.05$) (5700-6000s). This did not support significant CO_2 capture and hence feedstock and water conversion was considered.

At steady state, the feedstock conversion increased with time on stream from 24.3% ($AD_{(61)} = 0.73$, $p < 0.05$) (2100-2400s) and reached $28.6\% \pm 0.4$ ($AD_{(61)} = 0.73$, $p > 0.05$) towards the end of the run (5700-6000s) (Figure 8. 37). This is significantly lower than what was observed without the presence of a sorbent (Runs 4 and 5, 44.4 and $51.1 \pm 7.2\%$) as well as after monolith coating (Run 7, 48.7%). The water conversion did not change significantly with time on stream. It was 6.4% ($AD_{(61)} = 2.28$, $p < 0.05$) between 2100-2400s and $7.6\% \pm 0.4$ ($AD_{(61)} = 0.70$, $p > 0.05$) between 5700 and 6000s. The feedstock and water conversion was significantly lower than without sorbent (Runs 4 and 5, 12.6 and 14.0%) but similar to what was achieved after monolith coating (Run 7, 8.5%).

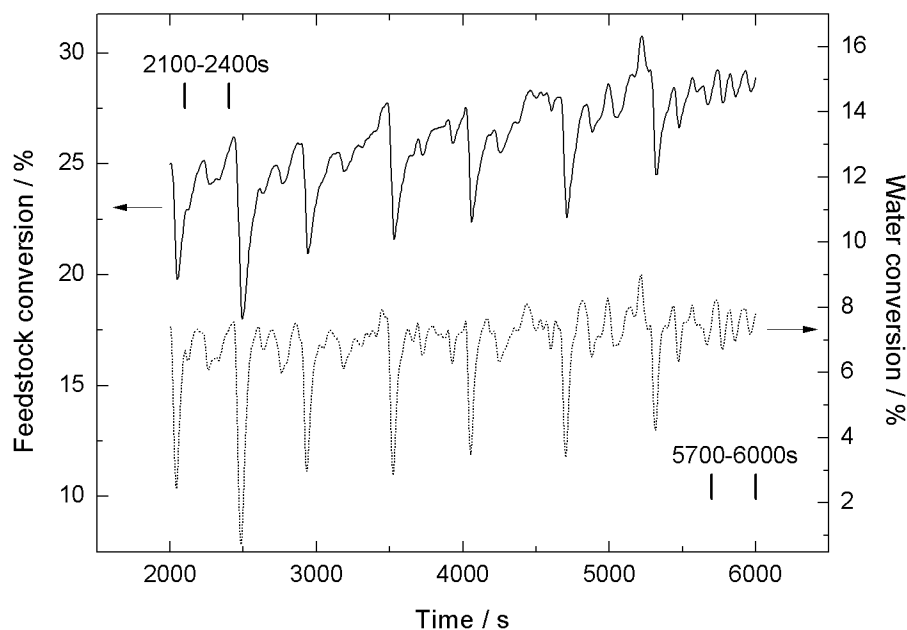


Figure 8. 37. Feedstock and water conversion during Run 8 (wire coating using a $\text{Ca}(\text{OH})_2$ solution).

Images taken of the monolith after the run showed that the sorbent coverage of on the nichrome wire had reduced (Figure 8. 38). The increase in feedstock conversion with time on stream was subsequently attributed to a loss of sorbent coating with subsequent increase in contact between feedstock and catalytic surface, with sorbent acting as material barrier.

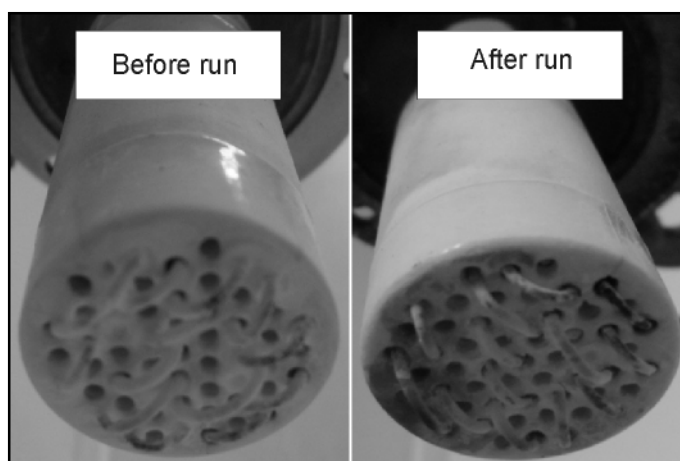


Figure 8. 38. Pictures taken of the monolith before and after Run 8 (wire coating using a $\text{Ca}(\text{OH})_2$ solution).

8.11.2.3 ALUMINA SUPPORT COATING USING CaCl_2 SOLUTION (RUN 9)

16 alumina support pieces were weighed and then dried overnight at 120°C in an oven. Note that half of the pieces were filed down beforehand (see below). The support pieces were

then left to cool to room temperature in a desiccator before being submerged in a saturated CaCl_2 solution for 2.5h. CaCl_2 was chosen due to its high solubility in water ($6.7 \text{ mmole ml}^{-1}$). Ca(OH)_2 has a solubility of $0.02 \text{ mmole ml}^{-1}$ hence a saturated solution of CaCl_2 will have a concentration of Ca atoms which is more than 100 times higher than a saturated Ca(OH)_2 solution. $\text{Ca(NO}_3)_2$ has a solubility of $7.4 \text{ mmole ml}^{-1}$ and could therefore have been used instead of CaCl_2 . However, $\text{Ca(NO}_3)_2$ is classified as harmful and oxidizing while CaCl_2 is classified as harmful. Therefore CaCl_2 was chosen because it was less hazardous which would be important for future applications in industry. Note that all solubility's cited above are for the anhydrous salts.

After impregnation the alumina pieces were dried in an oven at $120 \text{ }^\circ\text{C}$ for 2h. The pieces were then left to cool to room temperature before being weighed a second time. The weight increased by 10.6%. The above described process was repeated and this resulted in a further weight increase of 1.3% from the first coating which was considered negligible. The total weight increase was 11.2% or 8.9g. This equaled $117.8 \text{ mmole CaCl}_2$ and meant that more Ca was added compared to when sorbent pellets (67.5 mmol) and monolith coating (5.4 mmol) was used. 4 stacks of alumina support pieces with 4 pieces in each stack were arranged to form a quadrant, and a single length of nichrome wire (wire 2) was threaded through the pieces. The quadrant was then placed inside the reactor (Figure 8. 39). The pretreatment procedure was carried out as outlined above but a temperature of $650 \text{ }^\circ\text{C}$ was used as the reactor could not reach $700 \text{ }^\circ\text{C}$ with the new setup. This was attributed to the fact that a shorter length of wire was used here compared to when the monolith was used.

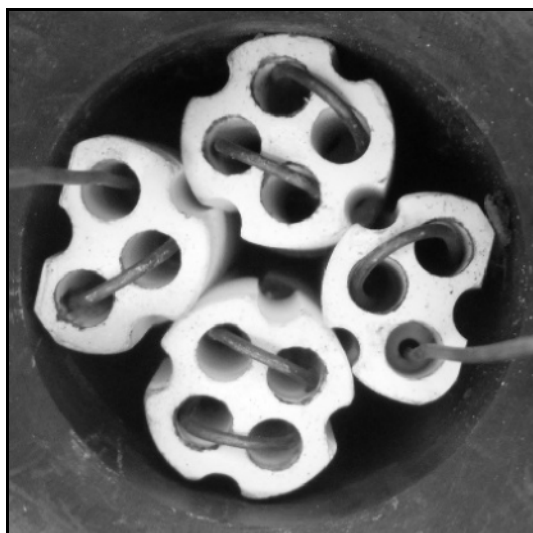


Figure 8. 39. Picture of the Al support pieces arranged in a quadrant inserted into the reactor with the nichrome wire (wire 2) threaded through them (as seen from above).

The run featuring the impregnated Al support pieces is referred to as Run 9. At steady state the order of the gaseous molar production rates was $\text{H}_2 > \text{CO}_2 > \text{CH}_4 > \text{CO}$ and this order was maintained for 7000s time on stream (Figure 8. 40), hence the system remained stable for a long time relative to what was observed after monolith coating and wire coating. The H_2 yield was 1.5 ($\text{AD}_{(1401)} = 68.77$, $p < 0.05^*$) which was low relative to that achieved with sorbent pellets (Run 6) and monolith coating (Run 7). It was also low relative to what was observed without sorbent (Table 8. 7). The $\text{H}_2:\text{CO}$ was 20.0:1 ($\text{AD}_{(1401)} = 37.31$, $p < 0.05^*$) which was the highest $\text{H}_2:\text{CO}$ observed both with and without sorbent.

The H_2 and CO production rates were $29.8 \mu\text{mole s}^{-1}$ ($\text{AD}_{(1401)} = 68.77$, $p < 0.05^*$) and $1.5 \mu\text{mole s}^{-1}$ ($\text{AD}_{(1401)} = 61.40$, $p < 0.05^*$) respectively and they were stable between 3000 and 10000s time on stream (Figure 8. 40). The CO production rate was the lowest observed out of all the experiments carried out, both with and without sorbent. This could explain the high $\text{H}_2:\text{CO}$ ratio.

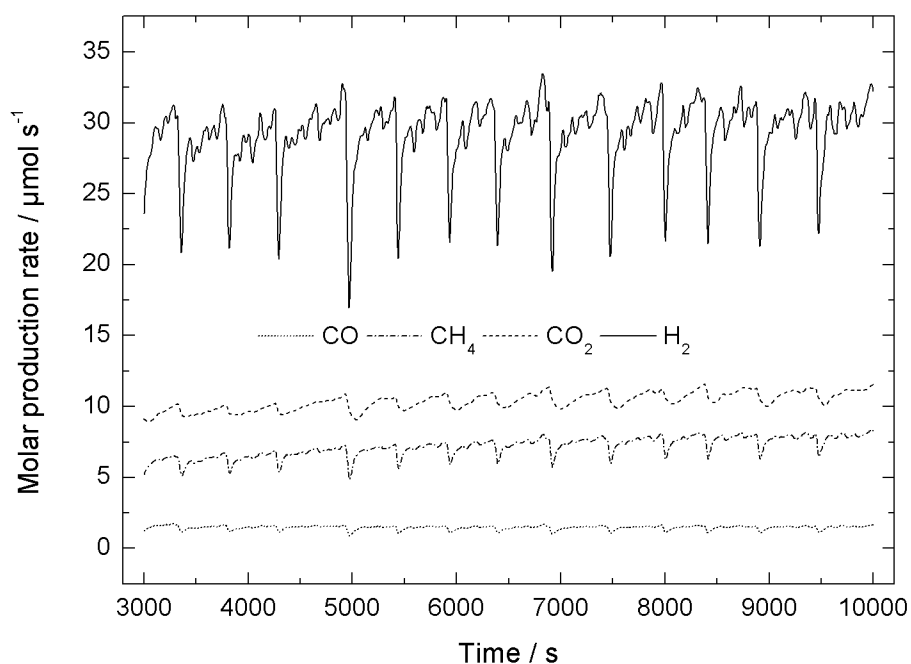


Figure 8. 40. Molar production rates of CO , CH_4 , CO_2 and H_2 during Run 9 (Al support impregnation).

The CO_2 and CH_4 both displayed a small increase in production rate (Figure 8. 41). When the rates between 3000 to 3500s and the rates between 9500 and 10000s time on stream were compared, the CO_2 rate increased from $9.4 \mu\text{mole s}^{-1}$ ($\text{AD}_{(101)} = 1.44$, $p < 0.05$) to $11.1 \mu\text{mole s}^{-1}$ ($\text{AD}_{(101)} = 5.64$, $p < 0.05^*$) while the CH_4 production rate increased from $6.2 \mu\text{mole s}^{-1}$ ($\text{AD}_{(92)} = 1.34$, $p < 0.05$) to $8.0 \mu\text{mole s}^{-1}$ ($\text{AD}_{(93)} = 0.81$, $p < 0.05$).

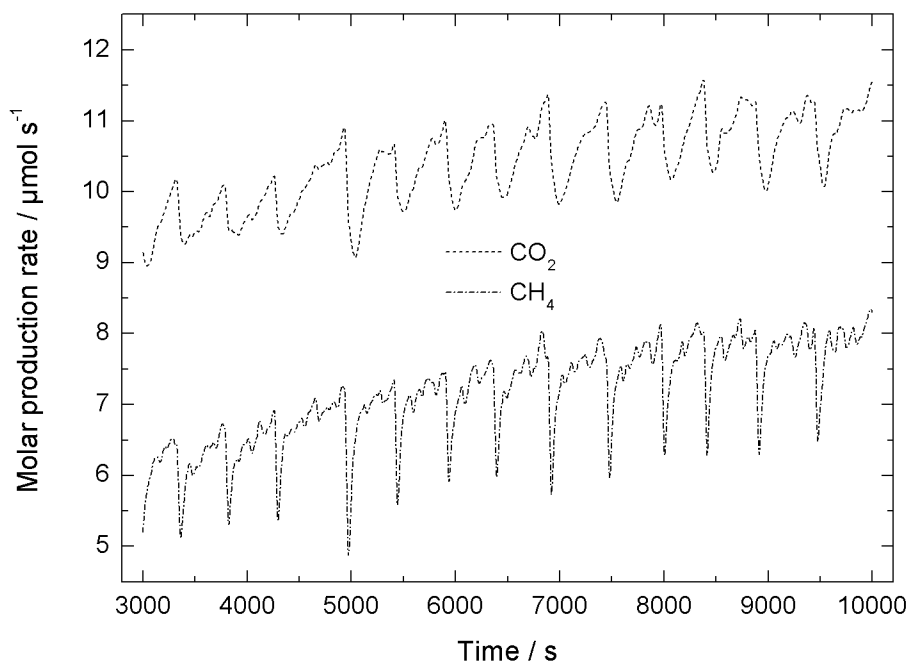


Figure 8. 41. Molar production rates of CO_2 and CH_4 during Run 9 (Al support impregnation).

The results with regards to CO_2 production rate can be attributed to CO_2 capture which is reduced with time on stream due to sorbent saturation causing the CO_2 production rate to increase. Given that the CaO carbonation reaction is exothermic, a saturation of the sorbent would be expected to create a more favourable environment for the CO methanation reaction. Hence, the increase in CH_4 production rate is consistent with sorbent saturation.

The selectivity (H) to H_2 reduced with time on stream while the selectivity to CH_4 was increased (Figure 8. 42). In other words, more hydrogen was being bound to carbon with time on stream. This explained why the feedstock conversion increased without an increase in H_2 production rate or H_2 yield.

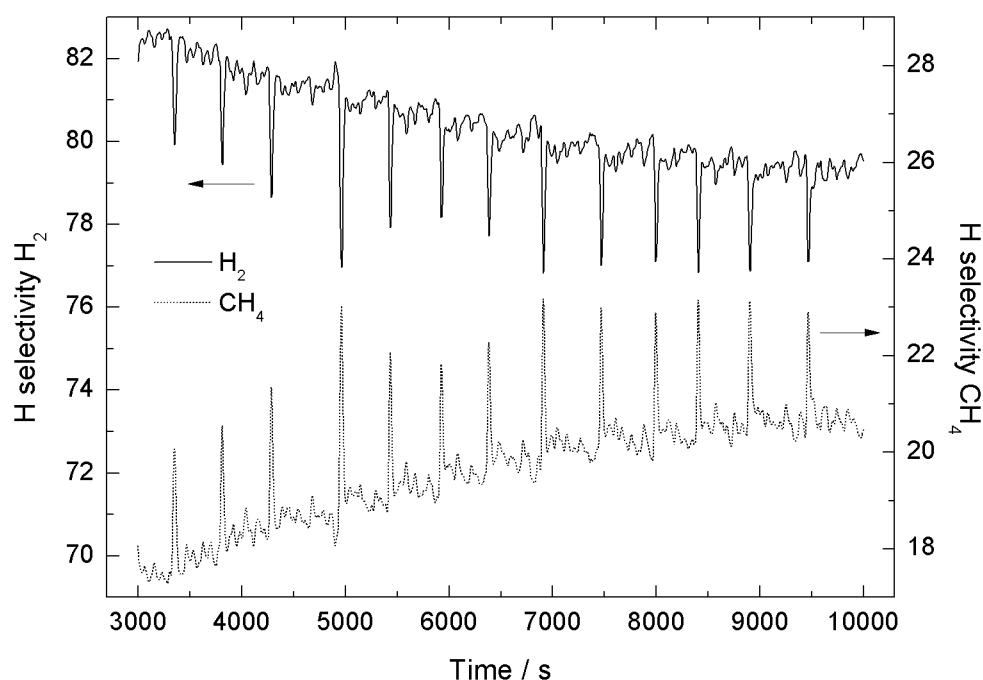


Figure 8. 42. Selectivity to hydrogen containing products (H_2 and CH_4) during Run 9 (Al support impregnation).

The feedstock conversion increased from 41.9% ($AD_{(101)} = 0.93$, $p < 0.05$) at 3000-3500s time on stream during steady state and reached 50.8% ($AD_{(91)} = 1.65$, $p < 0.05$) between 9500-10000s. The water conversion remained stable at 12.8% ($AD_{(1401)} = 134.74$, $p < 0.05^*$) (Figure 8. 43). The feedstock conversion was the highest achieved. However, note that the feedstock conversion increases sharply at the end of the steady state. The feedstock conversion for time on stream between 9500-10000s is cited here for consistency. The increase in feedstock conversion was attributed to the increased production rates of CH_4 and CO_2 and since the formation of CH_4 through CO methanation produces water (hence reverses water conversion) the water conversion remained unchanged. Note that the removal of CO_2 from the gas phase via the CaO carbonation reaction affected the elemental balances such that the conversions of feedstock and water were underestimated. As the sorbent was saturated and more CO_2 was left in the gas phase, the feedstock conversion subsequently increased. However the water conversion did not increase which was attributed to the increase in CO methanation as evidenced by the changes in CH_4 production rate but more significantly by the increase in selectivity (C) towards CH_4 from 35.7 ($AD_{(101)} = 7.81$, $p < 0.05^*$) to 38.8 ($AD_{(101)} = 3.73$, $p < 0.05^*$). The selectivity to CO and CO_2 were consequently reduced from 9.1 ($AD_{(101)} = 4.86$, $p < 0.05$) to 7.5 ($AD_{(96)} = 1.68$, $p < 0.05$) and from 55.2 ($AD_{(101)} = 7.05$, $p < 0.05^*$) to 53.7 ($AD_{(101)} = 1.49$, $p < 0.05^*$) respectively. The sum of the O and C production rates (derived from the production rates of CO, CO_2 and CH_4) increased from 20.5 and 17.1 $\mu\text{mole s}^{-1}$ (3000-3500s) to 23.4 and 20.4 $\mu\text{mole s}^{-1}$ (9500-10000s) respectively. This meant that the ratio of O to C production rate reduced from 1.20 to

1.15. In other words, the molar amounts of both O and C in the products increased with time on stream while the C production rate relative to the O production rate increased. This explained how the feedstock conversion could increase while the water conversion remained stable.

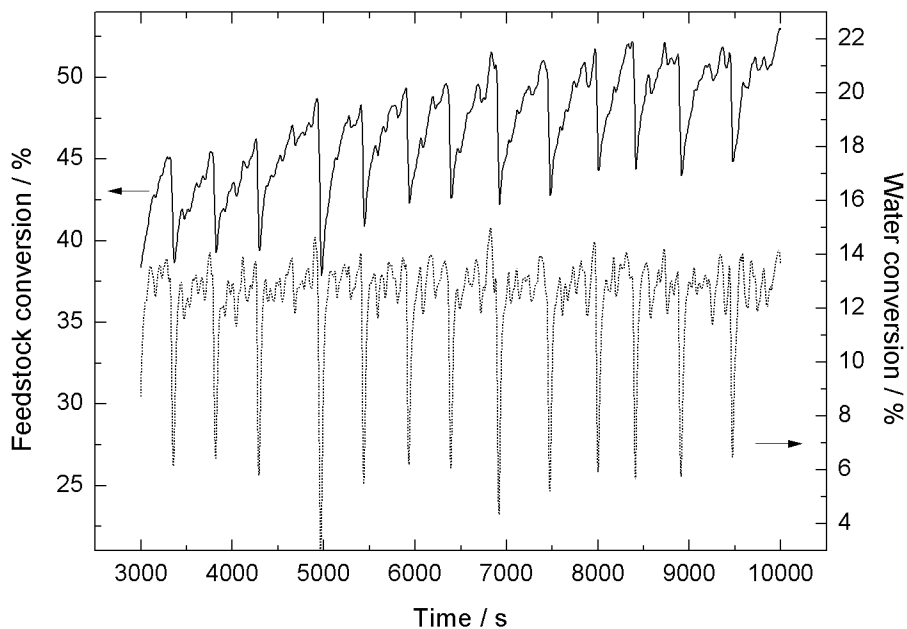


Figure 8. 43. Feedstock and water conversion during Run 9 (Al support impregnation).

The methane production rate at the end of Run 9 (9500-10000s) with alumina support pieces was $8.0 \mu\text{mole s}^{-1}$ ($AD_{(93)} = 0.81$, $p < 0.05$) which was the highest observed throughout all runs (Table 8. 7). The CO methanation reaction is favoured by low temperatures. The nichrome wire was threaded through 26 holes when the monolith was used (Figure 8. 38) while it was threaded through 14 holes when the alumina pieces were used (Figure 8. 39). This meant that a shorter length of wire was used during Run 9. The distance between the holes were also larger than the space between monolith channels, as well as the size of the holes compared to the monolith's channels diameter. These features were hypothesized to have impaired heat transfer in the centre of the reactor, hence favoring CO methanation. The temperatures above the monolith/alumina pieces supported this hypothesis. The temperature above the monolith after monolith coating (Run 7) was $360.4 \text{ }^\circ\text{C}$ ($AD_{(393)} = 0.92$, $p > 0.05$) for the first 2000s time on stream after at steady state (Figure 8. 44). The corresponding temperature above the alumina pieces however was only $284.3 \pm 1.2 \text{ }^\circ\text{C}$ ($AD_{(378)} = 0.34$, $p > 0.05$). CO methanation was further favoured with time on stream as the sorbent was being saturated.

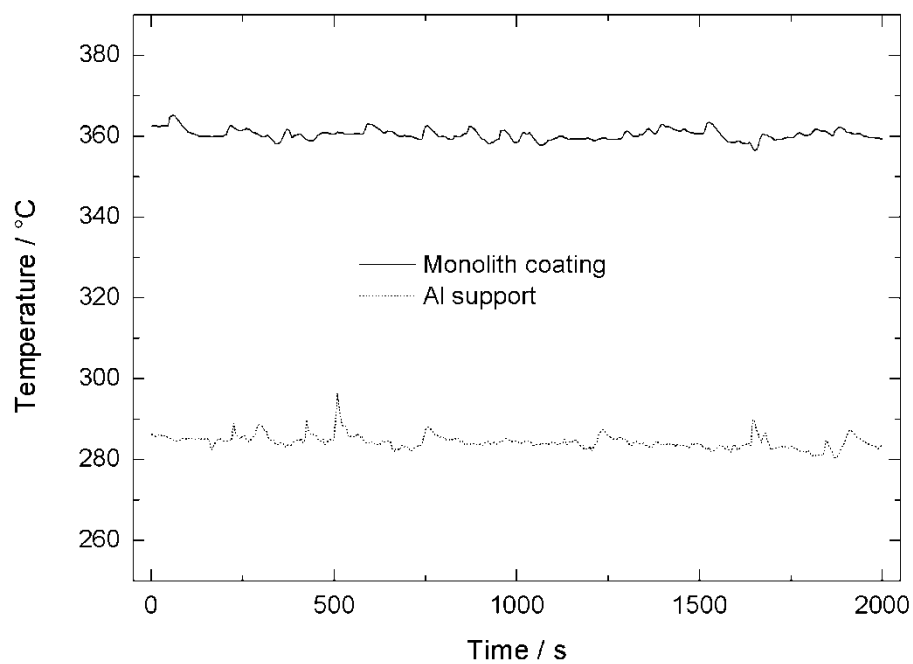


Figure 8. 44. Temperature readings for the first 2000s of steady state recorded by the thermocouple above the monolith after monolith coating (Run 7) and using impregnated Al support pieces (Run 9).

Table 8. 7. Summary of Runs 1-9.

Run	Description	feedstock conversion / %	Water conversion / %	H ₂ yield	H ₂ :CO	Production rates / $\mu\text{mole s}^{-1}$			
						H ₂	CO	CO ₂	CH ₄
1.	Glycerol as feedstock (wire 1)	n/a	n/a	1.4	1.09:1	20.29	18.7	n/a	n/a
2	Ethanol as feedstock (wire 1)	32.7	6.3	1.05	2.20:1	21.35	9.57	0.46	3.18
3	Use of wire 2.	46.7	6.4	1.42	2.03:1	28.78	14.18	1.05*	3.68
4	After pretreatment	44.4	12.6	1.87	4.31:1	37.94	8.76	7.25	2.17
5	Replicate of Run 4	51.1 \pm 7.2	14.0	2.16	4.11:1	43.86	10.72	8.00	2.21 \pm 0.05

*Outliers included, **2500-2600 s (prior to saturation), **5700-6000 s, ****9500-10000 s

Table 8.7 (Continued)

Run	Description	feedstock conversion / %	Water conversion / %	H ₂ yield	H ₂ :CO	Production rates / $\mu\text{mole s}^{-1}$			
6**	Sorbent pellets	n/a	n/a	1.72 ± 0.05	3.87 ± 0.04	34.82 ± 0.99	9.01 ± 0.15	0.33 ± 0.0048	4.26 ± 0.15
7	Monolith coating	48.7*	8.5*	1.69*	2.78:1*	34.38*	12.40*	4.42	2.89
8***	Wire coating	28.6 ± 0.4	7.6% ± 0.4	1.1	5.8:1	21.99	3.80 ± 0.12	5.5 ± 0.02	2.33
9	Al support impregnation	41.9 - 50.8%****	12.8*	1.47*	19.97:1*	29.79*	1.50*	10.4	8.0****

*Outliers included, **2500-2600 s (prior to saturation), **5700-6000 s, ****9500-10000 s

CHAPTER 9: CONCLUSIONS AND FUTURE WORK

“Truth in science can be defined as the working hypothesis best suited to open the way to the next better one”

Konrad Lorenz

9.1 SUMMARY AND CONCLUSIONS

Under thermodynamic equilibrium, the addition of CaO to the SR process results in sorption enhancement which increases H₂ yield and H₂ molar fraction. The H₂ molar fraction can reach 99% because both carbon and oxygen is removed from the gas phase via the formation of CaCO₃. Maximum dry H₂ molar fractions could also be reached at a lower temperature thanks to the exothermicity of the CaO carbonation reaction. It was noted that the CaO competed with CH₄ and water for C and H and that the O content of the feedstock dictated the amount of water needed to convert it to H₂ and CO. This in turn affected water conversion, selectivity and dry molar concentrations. SESR is a viable route to the production of high purity H₂ gas from the feedstocks most commonly used for SR today (methane), today's most ubiquitous biofuel (ethanol) and a waste stream from biodiesel production (glycerol). This demonstrates the possibility to produce renewable H₂ using a well understood method (SR) in combination with CaO used as a CO₂ sorbent.

Ca-D-gluconate can be readily decomposed to CaO with subsequent changes to crystallographic structure, morphology and sample volume. The resulting CaO derived from Ca-D-gluconate had similar surface area and porosity as CaO powder and displayed similar behaviour and capture capacity during carbonation. However, CaO derived from Ca-D-gluconate displayed self-reactivation behaviour over multiple cycles of carbonation and calcination which the CaO powder did not.

A Ca₁₂Al₁₄O₃₃ phase could be successfully incorporated into the CaO powder. The incorporation resulted in a reduction in pores in the 50-100 nm size range and caused self-reactivation behaviour over multiple carbonation and calcination cycles. Ca₁₂Al₁₄O₃₃ sorbent prepared using different CaO precursors displayed the same crystallographic structure but different morphology which could be traced back to the original morphology of the CaO precursor. The capture capacity of the Ca₁₂Al₁₄O₃₃ sorbent was also dependent on the capacity of the precursor. Inclusion of Ca₁₂Al₁₄O₃₃ also allowed for a higher conversion of the CaO in the sorbent through the formation of separated CaO grains.

Pelletisation reduced the capture capacity due to a densification of the sorbent but this reduction could be reversed by compressing hydrated sorbent which was then calcined in situ prior to carbonation. Sorbent morphology possibly affected the severity of the capacity loss.

The results of Rietveld refinement carried out on mixtures of Ca-based sorbents with known composition were in close agreement with the intended composition of the mixtures. The study of Ca(OH)₂ carbonation using conventional TGA made necessary a number of assumptions about the carbonation mechanism and different means of converting TGA data to wt% CaCO₃ depending on the temperature. Both XRD and TGA data showed that a commercial

CaO powder contained Ca(OH)₂ impurities which were successfully removed by heating to 700 °C in N₂ thus leaving a single phase CaO.

There was satisfactory agreement between XRD and TGA data when carbonation of CaO and Ca(OH)₂ was investigated. Discrepancies were attributed to differences between the two setups with regards to conditions of CO₂ contact with the sorbent, sample amount and sample holder dimensions. During carbonation of Ca(OH)₂ no intermediate CaO species were observed, indicating direct conversion to CaCO₃. In partially hydrated CaO, the Ca(OH)₂ phase converted directly to CaCO₃ while the CaO phase remained unaffected up to 500 °C, after which conversion continued through carbonation of CaO. Partial hydration had no impact on capture capacity but caused anisotropic peak broadening in the Ca(OH)₂ phase. High resolution synchrotron diffraction and Rietveld refinement analysis showed that the microstrain in the (100) direction was twice as high in the (001) direction. The results were interpreted as a Ca(OH)₂ shell formed around a CaO core. A combination of refinement and literature data revealed that the stresses in the Ca(OH)₂ phase were much higher its strength which can explain the loss in capacity in Ca-based materials due to hydration.

The Ca₁₂Al₁₄O₃₃ phase in the CaO/Ca₁₂Al₁₄O₃₃ sorbent remained inert during carbonation. Peak overlap was identified as a source of error in the study of CaO/Ca₁₂Al₁₄O₃₃ using XRD. Another source of error was the observed difference in phase peak intensity between scans carried out at different times during a given temperature hold.

There was a trade-off between the quality of the input mixture injection and of the off-gas quantification during SR using a novel wire reactor for SR of liquid feedstock with a nichrome wire acting both as a heating element and a catalyst. A standard operating procedure was developed which included an air purge step and a H₂ reduction step prior to SR. An alumina stack was also included to improve input mixture dispersion and residence time and the position of the Al stack could alter feedstock and water conversion by providing different residence time depending on its position.

Glycerol SR caused gas analyser contamination and so ethanol was used for subsequent investigations. Wire morphology had an impact on feedstock conversion. Redox pretreatment of the wire resulted in the formation of Cr₂O₃ on the wire surface. The pretreatment significantly improved water conversion through a shift in the WGS reaction. The experiments carried out were not long enough to study catalyst deactivation but a reduction in CO₂ production rate was observed which could be an early indicator of coke formation on the nichrome wire surface. The means by which the reactor was heated resulted in 288 W of power being supplied to the reactor for 2-3s at a time followed by a pause for 2-3s. This is the likely to have caused the observed oscillations in reactor off-gas concentrations. In the presence of sorbent the exothermicity of the carbonation reaction caused disruption to the reactor heating with subsequent reduction in

feedstock gasification which highlighted the need for reactor design improvement with regard to heating control.

The addition of sorbent pellets below the monolith removed CO₂ from the reactor off-gas but did not achieve sorption enhancement because the sorbent was not close enough to the catalyst. Monolith coating could not supply enough sorbent to the reactor and the coating hindered WGS possibly due to reduced CO adsorption on the coated surface. Wire coating could supply more sorbent but acted as a material barrier between feedstock and catalyst, hence hindering feedstock conversion. The coverage of the coating eroded with time on stream with subsequent increase in feedstock conversion. Replacing the monolith with sorbent impregnated alumina support pieces impaired heat transfer because the holes were fewer and larger. CO₂ capture occurred without sorption enhancement and as the sorbent became saturated, the CO methanation reaction was favoured in the absence of heat from the CaO carbonation reaction.

9.2 SUGGESTED FUTURE WORK

Further work is needed to understand the effect of pelletisation on carbonation. Such work could include SEM imaging of pellets derived from a range of sorbents with different morphologies. Comparisons between pellets compressed using different pressures could also be made.

More detailed analysis of the synchrotron data is suggested so that a mechanism for hydration of CaO can be suggested.

It is hypothesized based on the work carried out here that there exists a hydration level above which the capture capacity is improved. Investigation of a wide range of sorbents with different levels of hydration is suggested as such work could be used to test this hypothesis.

In situ XRD could be used to investigate the effects of steam on the carbonation process. By comparing XRD data collected with and without the presence of steam, differences with regards to phase composition strain/stress or particle size could be considered.

Suggested future work to be carried out on the wire reactor is divided into three categories. First the reactor design needs to be improved with regards to input mixture injection, residence time and heating control. A higher carrier gas flow would improve input mixture injection as shown in Section 8.5.1, however this would simultaneously reduce residence time so the reactor would need to be longer to compensate for this. The use of gas chromatography would enable off-gas product quantification under high carrier gas flow. In the current setup the thermocouple providing feedback to the power control unit was placed directly underneath the monolith. As the temperature underneath the monolith was being kept at 600 °C the temperature above the monolith was about 200-250 °C lower which was due to the N₂ carrier gas flow and reduced insulation. Consequently the temperature inside the wire reactor was unequally

distributed. Also, the temperature inside the monolith was unknown. Finally, the temperature oscillated heavily over time which was attributed to the on/off temperature control system used. To address these challenges, future work with a focus on enabling temperature measurement in the centre of the reactor as well as enabling reduced periodicity in the power supply is suggested. Alternative temperature control systems such as proportional integral (PI), proportional integral derivative (PID) or pulse width monitoring (PWM) could for example be used to significantly reduce temperature oscillation.

The second category of suggested future work is development of methods for studying the characteristics of the nichrome wire. This work used photography and SEM-EDX out of which the former could supply limited information when combined with a literature review while the latter did not provide useful information. For future work the surface area of the nichrome wires could be determined using a polarographic technique.³⁴⁴

Finally, further investigation of sorbent coatings is suggested. Other Ca-based salts and monolith materials could be tested and the effect of the coatings on for example CO adsorption could be investigated using mass spectrometry.

REFERENCES

1. J.M. Barnola, D. Raynaud, Y.S. Korotkevich and C. Lorius, *Nature* **329**, 408-414 (1987).
2. D.M. Etheridge, L.P. Steele, R.L. Langenfelds, R.J. Francey, J.M. Barnola and V.I. Morgan, *Journal of Geophysical Research-Atmospheres* **101**, 4115-4128 (1996).
3. C. Lorius, J. Jouzel, D. Raynaud, J. Hansen and H. Letreut, *Nature* **347**, 139-145 (1990).
4. D. Luthi, M. Le Floch, B. Bereiter, T. Blunier, J.M. Barnola, U. Siegenthaler, D. Raynaud, J. Jouzel, H. Fischer, K. Kawamura and T.F. Stocker, *Nature* **453**, 379-382 (2008).
5. S.L. Piao, P. Ciais, Y. Huang, Z.H. Shen, S.S. Peng, J.S. Li, L.P. Zhou, H.Y. Liu, Y.C. Ma, Y.H. Ding, P. Friedlingstein, C.Z. Liu, K. Tan, Y.Q. Yu, T.Y. Zhang and J.Y. Fang, *Nature* **467**, 43-51 (2010).
6. D.B. Lobell, W. Schlenker and J. Costa-Roberts, *Science* **333**, 616-620 (2011).
7. S.B. Peng, J.L. Huang, J.E. Sheehy, R.C. Laza, R.M. Visperas, X.H. Zhong, G.S. Centeno, G.S. Khush and K.G. Cassman, *Proceedings of the National Academy of Sciences of the United States of America* **101**, 9971-9975 (2004).
8. M.A. Bender, T.R. Knutson, R.E. Tuleya, J.J. Sirutis, G.A. Vecchi, S.T. Garner and I.M. Held, *Science* **327**, 454-8 (2010).
9. R. Etkins and E.S. Epstein, *Science* **215**, 287-289 (1982).
10. L. Cao, K. Caldeira and A.K. Jain, *Geophysical Research Letters* **34**, L05607 (2007).
11. A.M. Svensson, S. Moller-Holst, R. Glockner and O. Maurstad, *Energy* **32**, 437-445 (2007).
12. J.D. Gifford and R.C. Brown, *Biofuels Bioproducts & Biorefining-Biofpr* **5**, 293-304 (2011).
13. H. Chen, T.N. Cong, W. Yang, C. Tan, Y. Li and Y. Ding, *Progress in Natural Science* **19**, 291-312 (2009).
14. M.P. Hekkert, F.H.J.F. Hendriks, A.P.C. Faaij and M.L. Neelis, *Energy Policy* **33**, 579-594 (2005).
15. E. Heracleous, *International Journal of Hydrogen Energy* **36**, 11501-11511 (2011).
16. D.K. Liguras, D.I. Kondarides and X.E. Verykios, *Applied Catalysis B-Environmental* **43**, 345-354 (2003).
17. C.K. Cheng, S.Y. Foo and A.A. Adesina, *Catalysis Communications* **12**, 292-298 (2010).
18. J.R. Rostrup-Nielsen and T. Rostrup-Nielsen, *Cattech* **6**, 150-159 (2002).

19. G.T. Rochelle, *Science* **325**, 1652-1654 (2009).
20. D.P. Harrison, *Industrial & Engineering Chemistry Research* **47**, 6486-6501 (2008).
21. L. He and D. Chen, *Chemsuschem* **3**, 1169-1171 (2010).
22. B. Balasubramanian, A.L. Ortiz, S. Kaytakoglu and D.P. Harrison, *Chemical Engineering Science* **54**, 3543-3552 (1999).
23. B.L. Dou, V. Dupont, G. Rickett, N. Blakeman, P.T. Williams, H.S. Chen, Y.L. Ding and M. Ghadiri, *Bioresource Technology* **100**, 3540-3547 (2009).
24. A. Charitos, N. Rodriguez, C. Hawthorne, M. Alonso, M. Zieba, B. Arias, G. Kopanakis, G. Scheffknecht and J.C. Abanades, *Industrial & Engineering Chemistry Research* **50**, 9685-9695 (2011).
25. J.C. Abanades, M. Alonso and N. Rodriguez, *International Journal of Greenhouse Gas Control* **5**, 512-520 (2011).
26. M. Alonso, N. Rodriguez, B. Gonzalez, B. Arias and J.C. Abanades, *Industrial & Engineering Chemistry Research* **50**, 6982-6989 (2011).
27. D.P. Schrag, *Science* **325**, 1658-1659 (2009).
28. F.M. Orr, Jr., *Science* **325**, 1656-1658 (2009).
29. F.M. Orr, *Energy & Environmental Science* **2**, 449-458 (2009).
30. J. Blamey, E.J. Anthony, J. Wang and P.S. Fennell, *Progress in Energy and Combustion Science* **36**, 260-279 (2010).
31. N. MacDowell, N. Florin, A. Buchard, J. Hallett, A. Galindo, G. Jackson, C.S. Adjiman, C.K. Williams, N. Shah and P. Fennell, *Energy & Environmental Science* **3**, 1645-1669 (2010).
32. Q. Wang, J. Luo, Z. Zhong and A. Borgna, *Energy & Environmental Science* **4**, 42-55 (2011).
33. C.C. Dean, D. Dugwell and P.S. Fennell, *Energy & Environmental Science* **4**, 2050-2053 (2011).
34. C.C. Dean, J. Blamey, N.H. Florin, M.J. Al-Jeboori and P.S. Fennell, *Chemical Engineering Research & Design* **89**, 836-855 (2011).
35. N. Rodriguez, M. Alonso and J.C. Abanades, *Aiche Journal* **57**, 1356-1366 (2011).
36. J. Blamey, N.P.M. Paterson, D.R. Dugwell and P.S. Fennell, *Energy & Fuels* **24**, 4605-4616 (2010).
37. I. Martínez, G. Grasa, R. Murillo, B. Arias and J.C. Abanades, *Energy & Fuels* **25**, 1294-1301 (2011).

38. G. Xiao, J.R. Grace and C.J. Lim, *Powder Technology* **207**, 183-191 (2011).
39. K. Johnsen and J.R. Grace, *Powder Technology* **173**, 200-202 (2007).
40. P. Sun, J.R. Grace, C.J. Lim and E.J. Anthony, *Aiche Journal* **53**, 2432-2442 (2007).
41. R.M. German, *Sintering: Theory and Practice*. Wiley, New York (1996).
42. P.S. Fennell, R. Pacciani, J.S. Dennis, J.F. Davidson and A.N. Hayhurst, *Energy & Fuels* **21**, 2072-2081 (2007).
43. V. Manovic and E.J. Anthony, *J Phys Chem A* **114**, 3997-4002 (2010).
44. P.S. Fennell, J.F. Davidson, J.S. Dennis and A.N. Hayhurst, *Journal of the Energy Institute* **80**, 116-119 (2007).
45. J. Blamey, N.P.M. Paterson, D.R. Dugwell, P. Stevenson and P.S. Fennel, *Proceedings of the Combustion Institute* **33**, 2673-2681 (2011).
46. V. Manovic and E.J. Anthony, *Environ Sci Technol* **41**, 1420-1425 (2007).
47. V. Manovic and E.J. Anthony, *Fuel* **90**, 233-239 (2011).
48. F. Donat, N.H. Florin, E.J. Anthony and P.S. Fennell, *Environmental Science & Technology* **46**, 1262-1269 (2012).
49. J. Blamey, D.Y. Lu, P.S. Fennell and E.J. Anthony, *Industrial & Engineering Chemistry Research* **50**, 10329-10334 (2011).
50. C.D. Dave and K.K. Pant, *Renewable Energy* **36**, 3195-3202 (2011).
51. F. Pompeo, G. Santori and N.N. Nichio, *International Journal of Hydrogen Energy* **35**, 8912-8920 (2010).
52. C.K. Cheng, S.Y. Foo and A.A. Adesina, *Industrial & Engineering Chemistry Research* **49**, 10804-10817 (2010).
53. Z. Li, N. Cai, Y. Huang and H. Han, *Energy & Fuels* **19**, 1447-1452 (2005).
54. Z.S. Li, N.S. Cai and Y.Y. Huang, *Industrial & Engineering Chemistry Research* **45**, 1911-1917 (2006).
55. V. Dupont, A.B. Ross, E. Knight, I. Hanley and M.V. Twigg, *Chemical Engineering Science* **63**, 2966-2979 (2008).
56. R.J. Hill and C.J. Howard, *Journal of Applied Crystallography* **20**, 467-474 (1987).
57. S. Brunauer, P.H. Emmett and E. Teller, *Journal of the American Chemical Society* **60**, 309-319 (1938).

58. H. Lu, E.P. Reddy and P.G. Smirniotis, *Industrial & Engineering Chemistry Research* **45**, 3944-3949 (2006).
59. H. Lu, P.G. Smirniotis, F.O. Ernst and S.E. Pratsinis, *Chemical Engineering Science* **64**, 1936-1943 (2009).
60. K.B. Yi and D.P. Harrison, *Industrial & Engineering Chemistry Research* **44**, 1665-1669 (2005).
61. C.L. Yaws, *Yaws' Handbook of Properties of the Chemical Elements*. Knovel (2011).
62. C.L. Yaws, *Yaws' Handbook of Thermodynamic Properties for Hydrocarbons and Chemicals*. 2009, Knovel.
63. R.J. Kee, J.A. Miller and T.H. Jefferson, *CHEMKIN: a general purpose problem-independent, transportable, FORTRAN chemical kinetics code package* (1980).
64. S. Himeno, T. Tomita, K. Suzuki and S. Yoshida, *Microporous and Mesoporous Materials* **98**, 62-69 (2007).
65. P. Li, Tezel, F.H., *Microporous & Mesoporous Materials* **98**, 94-101 (2007).
66. L.M. Mulloth and J.E. Finn, *Carbon dioxide adsorption on a 5A zeolite designed for CO₂ removal in spacecraft cabins* (1998).
67. D.S. Lee, D.H. Shin, D.U. Lee, J.C. Kim and H.S. Cheigh, *Journal of Food Engineering* **48**, 183-188 (2001).
68. S. Satyapal, Filburn, T., Trela, J., Strange, J., *Energy & Fuels* **15**, 250-255 (2001).
69. IPCC, *Special Report on Carbon Capture and Storage* (2005).
70. G.X. Wang, B. Feng, J.C. Diniz da Costa and V. Rudolph, *Recent advance of zero emission technologies for coal-based power generations systems, in Asia-Pacific Power and Energy Engineering Conference (APPEEC)*. 2009.
71. R.S. Haszeldine, *Science* **325**, 1647-1652 (2009).
72. V. Dupont, *HELIA* **30**, 103-132 (2007).
73. P. Pimenidou, G. Rickett, V. Dupont and M.V. Twigg, *Bioresource Technology* **101**, 9279-9286 (2010).
74. B. Wang, A.P. Cote, H. Furukawa, M. O'Keeffe and O.M. Yaghi, *Nature* **453**, 207-211 (2008).
75. R. Banerjee, A. Phan, B. Wang, C. Knobler, H. Furukawa, M. O'Keeffe and O.M. Yaghi, *Science* **319**, 939-943 (2008).

76. R.J. Kuppler, D.J. Timmons, Q.R. Fang, J.R. Li, T.A. Makal, M.D. Young, D.Q. Yuan, D. Zhao, W.J. Zhuang and H.C. Zhou, *Coordination Chemistry Reviews* **253**, 3042-3066 (2009).
77. M.R. Othman, N.M. Rasid and W.J.N. Fernando, *Chemical Engineering Science* **61**, 1555-1560 (2006).
78. S.K. Wirawan, Creaser, D., *Separation & Purification Technology* **52**, 224-231 (2006).
79. F.V.S. Lopes, Grande, C.A., Ribeiro, A.M., Loureiro, J.M., Evaggelos, O., Nikolakis, V., Rodrigues, A.E., *Separation Science & Technology* **44**, 1045-1073 (2009).
80. Z.L. Zhao, X.Y. Cui, J.H. Ma and R.F. Li, *International Journal of Greenhouse Gas Control* **1**, 355-359 (2007).
81. F.N. Ridha and P.A. Webley, *Separation & Purification Technology* **67**, 336-343 (2009).
82. R.J. Davis, *Journal of Catalysis* **216**, 396-405 (2003).
83. T. Loiseau, L. Lecroq, C. Volkringer, J. Marrot, G. Ferey, M. Haouas, F. Taulelle, S. Bourrelly, P.L. Llewellyn and M. Latroche, *Journal of the American Chemical Society* **128**, 10223-10230 (2006).
84. S. Surble, Millange, F., Serre, C., Dören, T., Latroche, M., Bourrelly, S., Llewellyn, P.L., Ferey, G., *Journal of the American Chemical Society* **128**, 14889-14896 (2006).
85. Y.S. Bae, O.K. Farha, A.M. Spokoyny, C.A. Mirkin, J.T. Hupp and R.Q. Snurr, *Chemical Communications* 4135-4137 (2008).
86. Y.S. Bae, K.L. Mulfort, H. Frost, P. Ryan, S. Punnathanam, L.J. Broadbelt, J.T. Hupp and R.Q. Snurr, *Langmuir* **24**, 8592-8598 (2008).
87. P. Chowdhury, C. Bikkina, D. Meister, F. Dreisbach and S. Gumma, *Microporous and Mesoporous Materials* **117**, 406-413 (2009).
88. G. Ferey, C. Mellot-Draznieks, C. Serre, F. Millange, J. Dutour, S. Surble and I. Margiolaki, *Science* **309**, 2040-2042 (2005).
89. H.C. Zhou, S.Q. Ma, X.S. Wang and D.Q. Yuan, *Angewandte Chemie-International Edition* **47**, 4130-4133 (2008).
90. T.B. Lee, D. Kim, D.H. Jung, S.B. Choi, J.H. Yoon, J. Kim, K. Choi and S.H. Choi, *Catalysis Today* **120**, 330-335 (2007).
91. E.M. Hampe and D.M. Rudkevich, *Tetrahedron* **59**, 9619-9625 (2003).
92. X.C. Xu, C.S. Song, J.M. Andresen, B.G. Miller and A.W. Scaroni, *Energy & Fuels* **16**, 1463-1469 (2002).

93. X.C. Xu, C.S. Song, J.M. Andresen, B.G. Miller and A.W. Scaroni, *Microporous and Mesoporous Materials* **62**, 29-45 (2003).
94. R.R. Bottoms, *Separation acid gases*, Office, U.S.P., Editor. 1930: United States.
95. D.J. Fauth, E.A. Frommell, J.S. Hoffman, R.P. Reasbeck and H.W. Pennline, *Fuel Processing Technology* **86**, 1503-1521 (2005).
96. B. Ficicilar and T. Dogu, *Catalysis Today* **115**, 274-278 (2006).
97. A.I. Lysikov, A.N. Salanov and A.G. Okunev, *Industrial & Engineering Chemistry Research* **46**, 4633-4638 (2007).
98. J.C. Abanades and D. Alvarez, *Energy & Fuels* **17**, 308-315 (2003).
99. A.D. Ebner, S.P. Reynolds and J.A. Ritter, *Industrial & Engineering Chemistry Research* **46**, 1737-1744 (2007).
100. J. Ida and Y.S. Lin, *Environmental Science & Technology* **37**, 1999-2004 (2003).
101. C.S. Martavaltzi and A.A. Lemonidou, *Microporous and Mesoporous Materials* **110**, 119-127 (2008).
102. H.A. Mosqueda, C. Vazquez, P. Bosch and H. Pfeiffer, *Chemistry of Materials* **18**, 2307-2310 (2006).
103. USGS, *Mineral Commodity Summaries* (2009).
104. USGS, *Minerals Yearbook* (2007).
105. M. Kato, S. Yoshikawa and K. Nakagawa, *Journal of Materials Science Letters* **21**, 485-487 (2002).
106. K. Nakagawa and T. Ohashi, *Journal of the Electrochemical Society* **145**, 1344-1346 (1998).
107. L.M. Palacios-Romero and H. Pfeiffer, *Chemistry Letters* **37**, 862-863 (2008).
108. T. Avalos-Rendon, J. Casa-Madrid and H. Pfeiffer, *Journal of Physical Chemistry A* **113**, 6919-23 (2009).
109. J. Ida, R.T. Xiong and Y.S. Lin, *Separation and Purification Technology* **36**, 41-51 (2004).
110. M. Kato and K. Nakagawa, *Journal of the Ceramic Society of Japan* **109**, 911-914 (2001).
111. K.B. Yi and D.O. Eriksen, *Separation Science and Technology* **41**, 283-296 (2006).
112. R.T. Xiong, J. Ida and Y.S. Lin, *Chemical Engineering Science* **58**, 4377-4385 (2003).
113. K. Kim, S.J. Park and J. Hamaguchi, *Journal of the American Ceramic Society* **76**, 2119-2122 (1993).

114. K.H. Choi, Y. Korai and I. Mochida, *Chemistry Letters* **32**, 924-925 (2003).
115. USGS, *Minerals Yearbook* (2008).
116. B.N. Nair, T. Yamaguchi, H. Kawamura, S.I. Nakao and K. Nakagawa, *Journal of the American Ceramic Society* **87**, 68-74 (2004).
117. S.L. Kang, *Sintering: Densification, Grain Growth and Microstructure*. Elsevier Butterworth-Heinemann, Oxford (2005).
118. Z. Yong, V. Mata and A.E. Rodriguez, *Industrial & Engineering Chemistry Research* **40**, 204-209 (2001).
119. Y. Ding and E. Alpay, *Chemical Engineering Science* **55**, 3461-3474 (2000).
120. E.L.G. Oliveira, C.A. Grande and A.E. Rodrigues, *Separation and Purification Technology* **62**, 137-147 (2008).
121. T. Yamamoto, T. Kodama, N. Hasegawa, M. Tsuji and Y. Tamaura, *Energy Conversion and Management* **36**, 637-640 (1995).
122. J.R. Hufton, S. Mayorga and S. Sircar, *Aiche Journal* **45**, 248-256 (1999).
123. DOE, *Sorption enhanced reaction process (SERP) for the production of hydrogen*, in *Proceedings of the US DOE Hydrogen Program Review*. 1999. p. 244-259.
124. Y. Ding and E. Alpay, *Process Safety & Environmental Protection* **79**, 45-51 (2001).
125. M.K.R. Reddy, Z.P. Xu, G.Q. Lu and J.C.D. Da Costa, *Industrial & Engineering Chemistry Research* **45**, 7504-7509 (2006).
126. C.T. Yavuz, B.D. Shinall, A.V. Iretskii, M.G. White, T. Golden, M. Atilhan, P.C. Ford and G.D. Stucky, *Chemistry of Materials* **21**, 3473-3475 (2009).
127. K.B. Lee, Verdooren, H.S., Caram, H.S., Sircar, C.S., *Journal of Colloid and Interface Science* **308**, 30-39 (2007).
128. N.D. Hutson, S.A. Speakman and E.A. Payzant, *Chemistry of Materials* **16**, 4135-4143 (2004).
129. H.T.J. Reijers, S.E.A. Valster-Schiermeier, P.D. Cobden and R.W. van den Brink, *Industrial & Engineering Chemistry Research* **45**, 2522-2530 (2006).
130. USGS, *Mineral Commodity Summary* (2008).
131. E. Bouquet, G. Leysens, C. Schonnenbeck and P. Gilot, *Chemical Engineering Science* **64**, 2136-2146 (2009).
132. R.H. Borgwardt, K.R. Bruce and J. Blake, *Industrial & Engineering Chemistry Research* **26**, 1993-1998 (1987).

133. H. Lu, A. Khan and P.G. Smirniotis, *Industrial & Engineering Chemistry Research* **47**, 6216-6220 (2008).
134. A. Silaban, M. Narcida and D.P. Harrison, *Chemical Engineering Communications* **146**, 149-162 (1996).
135. D. Alvarez and J.C. Abanades, *Energy & Fuels* **19**, 270-278 (2005).
136. R. Pacciani, C.R. Muller, J.F. Davidson, J.S. Dennis and A.N. Hayhurst, *Canadian Journal of Chemical Engineering* **86**, 356-366 (2008).
137. D. Alvarez and J.C. Abanades, *Industrial & Engineering Chemistry Research* **44**, 5608-5615 (2005).
138. D. Beruto, L. Barco and A.W. Searcy, *Journal of the American Ceramic Society* **67**, 512-515 (1984).
139. J.S. Dennis and R. Pacciani, *Chemical Engineering Science* **64**, 2147-2157 (2009).
140. K.B. Yi, C.H. Ko, J. Park and J. Kim, *Catalysis Today* **146**, 241-247 (2009).
141. V. Manovic and E.J. Anthony, *Industrial & Engineering Chemistry Research* **48**, 8906-8912 (2009).
142. H. Lu, A. Khan, S.E. Pratsinis and P.G. Smirniotis, *Energy & Fuels* **23**, 1093-1100 (2009).
143. N.H. Florin and A.T. Harris, *Chemical Engineering Science* **64**, 187-191 (2009).
144. J.C. Abanades, *Chemical Engineering Journal* **90**, 303-306 (2002).
145. J.S. Wang and E.J. Anthony, *Industrial & Engineering Chemistry Research* **44**, 627-629 (2005).
146. G.S. Grasa and J.C. Abanades, *Industrial & Engineering Chemistry Research* **45**, 8846-8851 (2006).
147. P. Fennel, Pacciani, R., Dennis, J.S., Davidsson, J.F., Haryhurst, A.N., *Energy & Fuels* **21**, 2072-2081 (2007).
148. K.O. Albrecht, K.S. Wagenbach, J.A. Satrio, B.H. Shanks and T.D. Wheelock, *Industrial & Engineering Chemistry Research* **47**, 7841-7848 (2008).
149. Y.J. Li, C.S. Zhao, L.B. Duan, C. Liang, Q.Z. Li, W. Zhou and H.C. Chen, *Fuel Processing Technology* **89**, 1461-1469 (2008).
150. Y. Chen, M. Karthik and H. Bai, *Journal of Environmental Engineering* **135**, 459-464 (2009).
151. V. Manovic and E.J. Anthony, *Energy & Fuels* **23**, 4797-4804 (2009).

152. V. Manovic and E.J. Anthony, *Environmental Science & Technology* **43**, 7117-7122 (2009).
153. V. Manovic, E.J. Anthony, G. Grasa and J.C. Abanades, *Energy & Fuels* **22**, 3258-3264 (2008).
154. R. Pacciani, C.R. Müller, J.F. Davidson, J.S. Dennis and A.N. Hayhurst, *AIChE Journal* **54**, 3308-3311 (2008).
155. N. Epstein, *Chemical Engineering Science* **44**, 777-779 (1989).
156. M. Aihara, T. Nagai, J. Matsushita, Y. Negishi and H. Ohya, *Applied Energy* **69**, 225-238 (2001).
157. Y.J. Li, C.S. Zhao, C.R. Qu, L.B. Duan, Q.Z. Li and C. Liang, *Chemical Engineering & Technology* **31**, 237-244 (2008).
158. S.K. Bhatia and D.D. Perlmutter, *Aiche Journal* **29**, 79-86 (1983).
159. R. Barker, *Journal of Applied Chemistry and Biotechnology* **23**, 733-742 (1973).
160. H. Yu, D. Wang and M. Han, *Journal of the American Chemical Society* **129**, 2333-2337 (2007).
161. IEA, *World Energy Outlook 2009* (2009).
162. BP, *BP Energy Outlook 2030* (2011).
163. WHO, *Health risks of particulate matter from long-range transboundary air pollution* (2006).
164. N.N.A.N. Yusuf, S.K. Kamarudin and Z. Yaakub, *Energy Conversion and Management* **52**, 2741-2751 (2011).
165. A. Gog, M. Roman, M. Tosa, C. Paizs and F.D. Irimie, *Renewable Energy* **39**, 10-16 (2012).
166. C.F. Hansen, A. Hernandez, B.P. Mullan, K. Moore, M. Trezona-Murray, R.H. King and J.R. Pluske, *Animal Production Science* **49**, 154-161 (2009).
167. D.J. Pyle, R.A. Garcia and Z.Y. Wen, *Journal of Agricultural and Food Chemistry* **56**, 3933-3939 (2008).
168. T. Kocsisova and J. Cvengos, *Petroleum and Coal* **48**, 1-5 (2006).
169. J.C. Thompson and B.B. He, *Applied Engineering in Agriculture* **22**, 261-265 (2006).
170. S.S. Yazdani and R. Gonzalez, *Current Opinion in Biotechnology* **18**, 213-219 (2007).
171. D.T. Johnson and K.A. Taconi, *Environmental Progress* **26**, 338-348 (2007).

172. IEA, *Energy Technology Essentials: Biofuel Production* (2007).
173. Emerging Markets Online, *Biodiesel 2020: Global Market Survey, Feedstock Trends and Forecasts* (2008).
174. IEA, *Medium-Term Oil and Gas Markets* (2010).
175. IEA, *Technology Roadmap: Biofuels for Transport* (2011).
176. V. Chiodo, S. Freni, A. Galvagno, N. Mondello and F. Frusteri, *Applied Catalysis A-General* **381**, 1-7 (2010).
177. P.N. Sutar, P.D. Vaidya and A.E. Rodrigues, *Chemical Engineering & Technology* **33**, 1645-1649 (2010).
178. S. Adhikari, S.D. Fernando and A. Haryanto, *Renewable Energy* **33**, 1097-1100 (2008).
179. Y. Choi, N.D. Kim, J. Baek, W. Kim, H.J. Lee and J. Yi, *International Journal of Hydrogen Energy* **36**, 3844-3852 (2011).
180. M. Araque, L.M. Martinez, J.C. Vargas and A.C. Roger, *Catalysis Today* **176**, 352-356 (2011).
181. L.P.R. Profeti, E.A. Ticianelli and E.M. Assaf, *International Journal of Hydrogen Energy* **34**, 5049-5060 (2009).
182. D.L. King, L.A. Zhang, G. Xia, A.M. Karim, D.J. Heldebrant, X.Q. Wang, T. Peterson and Y. Wang, *Applied Catalysis B-Environmental* **99**, 206-213 (2010).
183. X. Hu and G.X. Lu, *Energy & Fuels* **23**, 926-933 (2009).
184. M. Slinn, K. Kendall, C. Mallon and J. Andrews, *Bioresource Technology* **99**, 5851-5858 (2008).
185. R.D. Cortright, R.R. Davda and J.A. Dumesic, *Nature* **418**, 964-7 (2002).
186. B. Liu and J. Greeley, *Journal of Physical Chemistry C* **115**, 19702-19709 (2011).
187. S.C. Huang, C.H. Lin and J.H. Wang, *Journal of Physical Chemistry C* **114**, 9826-9834 (2010).
188. V. Dupont, B.L. Dou, P.T. Williams, H.S. Chen and Y.L. Ding, *Bioresource Technology* **100**, 2613-2620 (2009).
189. A. Corma, G.W. Huber, L. Sauvanaud and P. O'Connor, *Journal of Catalysis* **247**, 307-327 (2007).
190. T. Valliyappan, N.N. Bakhshi and A.K. Dalai, *Bioresource Technology* **99**, 4476-4483 (2008).

191. Y.S. Stein, M.J. Antal and M. Jones, *Journal of Analytical and Applied Pyrolysis* **4**, 283-296 (1983).
192. S. Adhikari, S. Fernando, S.R. Gwaltney, S.D.F. To, R.M. Bricka, P.H. Steele and A. Haryanto, *International Journal of Hydrogen Energy* **32**, 2875-2880 (2007).
193. S. Adhikari, S. Fernando and A. Haryanto, *Energy & Fuels* **21**, 2306-2310 (2007).
194. A. Arpornwichanop, S. Authayanun, Y. Patcharauorachot, W. Wiyaratn and S. Assabumrungrat, *International Journal of Hydrogen Energy* **36**, 267-275 (2011).
195. A.L. da Silva and I.L. Muller, *International Journal of Hydrogen Energy* **36**, 2057-2075 (2011).
196. M.L. Dieuzeide and N. Amadeo, *Chemical Engineering & Technology* **33**, 89-96 (2010).
197. C.C.R.S. Rossi, C.G. Alonso, O.A.C. Antunes, R. Guirardello and L. Cardozo, *International Journal of Hydrogen Energy* **34**, 323-332 (2009).
198. X. Wang, S. Li, H. Wang, B. Liu and X. Ma, *Energy & Fuels* **22**, 4285-4291 (2008).
199. X. Wang, M. Li, S. Li, H. Wang, S. Wang and X. Ma, *Fuel Processing Technology* **91**, 1812-1818 (2010).
200. H. Chen, T. Zhang, B. Dou, V. Dupont, P. Williams, M. Ghadiri and Y. Ding, *International Journal of Hydrogen Energy* **34**, 7208-7222 (2009).
201. H.S. Chen, Y.L. Ding, N.T. Cong, B.L. Dou, V. Dupont, M. Ghadiri and P.T. Williams, *Renewable Energy* **36**, 779-788 (2011).
202. Y. Fernandez, A. Arenillas, J.M. Bermudez and J.A. Menendez, *Journal of Analytical and Applied Pyrolysis* **88**, 155-159 (2010).
203. I.N. Buffoni, F. Pompeo, G.F. Santori and N.N. Nichio, *Catalysis Communications* **10**, 1656-1660 (2009).
204. B. Zhang, X. Tang, Y. Li, Y. Xu and W. Shen, *International Journal of Hydrogen Energy* **32**, 2367-2373 (2007).
205. F. Pompeo, G.F. Santori and N.N. Nichio, *Catalysis Today* **172**, 183-188 (2011).
206. A.M.D. Douette, S.Q. Turn, W. Wang and V.I. Keffer, *Energy & Fuels* **21**, 3499-3504 (2007).
207. Y. Fernandez, A. Arenillas, M.A. Diez, J.J. Pis and J.A. Menendez, *Journal of Analytical and Applied Pyrolysis* **84**, 145-150 (2009).
208. R. Holub and P. Vonka, *The Equilibrium of Gaseous Systems*. ed. Hala, E., Reidel Publishing Company, Holland (1976).

209. S. Adhikari, S.D. Fernando, S.D.F. To, R.M. Bricka, P.H. Steele and A. Haryanto, *Energy & Fuels* **22**, 1220-1226 (2008).
210. A. Gallo, C. Pirovano, M. Marelli, R. Psaro and V. Dal Santo, *Chemical Vapor Deposition* **16**, 305-310 (2010).
211. A. Iriondo, J.F. Cambra, V.L. Barrio, M.B. Guemez, P.L. Arias, M.C. Sanchez-Sanchez, R.M. Navarro and J.L.G. Fierro, *Applied Catalysis B-Environmental* **106**, 83-93 (2011).
212. J.A. Farmer and C.T. Campbell, *Science* **329**, 933-6 (2010).
213. V. Nichele, M. Signoreto, F. Menegazzo, A. Gallo, V. dal Santo, G. Cruciani and G. Cerrato, *Applied Catalysis B-Environmental* **111-112**, 225-232 (2012).
214. E.A. Sanchez, M.A. D'Angelo and R.A. Comelli, *International Journal of Hydrogen Energy* **35**, 5902-5907 (2010).
215. C.K. Cheng, S.Y. Foo and A.A. Adesina, *Catalysis Today* **164**, 268-274 (2011).
216. T. Hirai, N. Ikenaga, T. Miyake and T. Suzuki, *Energy & Fuels* **19**, 1761-1762 (2005).
217. A. Iriondo, V.L. Barrio, J.F. Cambra, P.L. Arias, M.B. Guemez, M.C. Sanchez-Sanchez, R.M. Navarro and J.L.G. Fierro, *International Journal of Hydrogen Energy* **35**, 11622-11633 (2010).
218. B.L. Dou, G.L. Rickett, V. Dupont, P.T. Williams, H.S. Chen, Y.L. Ding and M. Ghadiri, *Bioresource Technology* **101**, 2436-2442 (2010).
219. Y. Li, W. Wang, B. Chen and Y. Cao, *International Journal of Hydrogen Energy* **35**, 7768-7777 (2010).
220. L. He, J.M.S. Parra, E.A. Blekkan and D. Chen, *Energy & Environmental Science* **3**, 1046-1056 (2010).
221. A.L. Ortiz and D.P. Harrison, *Industrial & Engineering Chemistry Research* **40**, 5102-5109 (2001).
222. K. Johnsen, H.J. Ryu, J.R. Grace and C.J. Lim, *Chemical Engineering Science* **61**, 1195-1202 (2006).
223. C.S. Martavaltzi, E.P. Pampaka, E.S. Korkakaki and A.A. Lemonidou, *Energy & Fuels* **24**, 2589-2595 (2010).
224. Z.S. Li, N.S. Cai and J.B. Yang, *Industrial & Engineering Chemistry Research* **45**, 8788-8793 (2006).
225. S. Authayanun, A. Arpornwichanop, W. Paengjuntuek and S. Assabumrungrat, *International Journal of Hydrogen Energy* **35**, 6617-6623 (2010).

226. G. Yang, H. Yu, F. Peng, H. Wang, J. Yang and D. Xie, *Renewable Energy* **36**, 2120-2127 (2011).
227. H. Wang, X. Wang, M. Li, S. Li, S. Wang and X. Ma, *International Journal of Hydrogen Energy* **34**, 5683-5690 (2009).
228. E.B. Pereira, P.R. de la Piscina and N. Homs, *Bioresource Technology* **102**, 3419-3423 (2011).
229. S.M. Swami and M.A. Abraham, *Energy & Fuels* **20**, 2616-2622 (2006).
230. N.J. Luo, X.W. Fu, F.H. Cao, T.C. Xiao and P.P. Edwards, *Fuel* **87**, 3483-3489 (2008).
231. A.O. Menezes, M.T. Rodrigues, A. Zimmaro, L.E.P. Borges and M.A. Fraga, *Renewable Energy* **36**, 595-599 (2011).
232. D.O. Ozgur and B.Z. Uysal, *Biomass & Bioenergy* **35**, 822-826 (2011).
233. R.L. Manfro, A.F. da Costa, N.F.P. Ribeiro and M.M.V.M. Souza, *Fuel Processing Technology* **92**, 330-335 (2011).
234. J.W. Shabaker, G.W. Huber and J.A. Dumesic, *Journal of Catalysis* **222**, 180-191 (2004).
235. A. Wawrzetz, B. Peng, A. Hrabar, A. Jentys, A.A. Lemonidou and J.A. Lercher, *Journal of Catalysis* **269**, 411-420 (2010).
236. L. Barelli, G. Bidini, F. Gallorini and S. Servili, *Energy* **33**, 554-570 (2008).
237. K. Lehnert and P. Claus, *Catalysis Communications* **9**, 2543-2546 (2008).
238. G. Wen, Y. Xu, H. Ma, Z. Xu and Z. Tian, *International Journal of Hydrogen Energy* **33**, 6657-6666 (2008).
239. F.A.P. Voll, C.C.R.S. Rossi, C. Silva, R. Guirardello, R.O.M.A. Souza, V.F. Cabral and L. Cardozo, *International Journal of Hydrogen Energy* **34**, 9737-9744 (2009).
240. F.J.G. Ortiz, P. Ollero, A. Serrera and A. Sanz, *International Journal of Hydrogen Energy* **36**, 8994-9013 (2011).
241. J.G. van Bennekom, R.H. Venderbosch, D. Assink and H.J. Heeres, *Journal of Supercritical Fluids* **58**, 99-113 (2011).
242. A.G. Chakinala, D.W.F. Brilman, W.P.M. van Swaaij and S.R.A. Kersten, *Industrial & Engineering Chemistry Research* **49**, 1113-1122 (2010).
243. A.J. Byrd, K.K. Pant and R.B. Gupta, *Fuel* **87**, 2956-2960 (2008).
244. W. Buhler, E. Dinjus, H.J. Ederer, A. Kruse and C. Mas, *Journal of Supercritical Fluids* **22**, 37-53 (2002).

245. D. Xu, S. Wang, X. Hu, C. Chen, Q. Zhang and Y. Gong, *International Journal of Hydrogen Energy* **34**, 5357-5364 (2009).
246. X. Xu, Y. Matsumura, J. Stenberg and M.J. Antal, *Industrial & Engineering Chemistry Research* **35**, 2522-2530 (1996).
247. A. May, J. Salvado, C. Torras and D. Montane, *Chemical Engineering Journal* **160**, 751-759 (2010).
248. J.A. Onwudili and P.T. Williams, *Fuel* **89**, 501-509 (2010).
249. S.J. Yoon, Y.C. Choi, Y.I. Son, S.H. Lee and J.G. Lee, *Bioresource Technology* **101**, 1227-1232 (2010).
250. D. Atong, S. Ausadasuk and V. Sricharoenchaikul, *International Journal of Chemical Reactor Engineering* **8**, A49 (2010).
251. D. Atong, C. Pechyen, D. Aht-Ong and V. Sricharoenchaikul, *Applied Clay Science* **53**, 244-253 (2011).
252. Y. Fernandez and J.A. Menendez, *Journal of Analytical and Applied Pyrolysis* **91**, 316-322 (2011).
253. Y. Hawangchu, D. Atong and V. Sricharoenchaikul, *International Journal of Chemical Reactor Engineering* **8**, 1-16 (2010).
254. V. Dupont, A.B. Ross, I. Hanley and M.V. Twigg, *International Journal of Hydrogen Energy* **32**, 67-79 (2007).
255. A. Haryanto, S. Fernando, N. Murali and S. Adhikari, *Energy & Fuels* **19**, 2098-2106 (2005).
256. T. Rostrup-Nielsen, *Catalysis Today* **106**, 293-296 (2005).
257. N. Williamson, *Principle mechanical engineer at ITM Power Plc*, 27 April (2012)
258. B. Dou, V. Dupont, P.T. Williams, H. Chen and Y. Ding, *Bioresource Technology* **100**, 2613-2620 (2009).
259. S. Cavallaro, *Energy & Fuels* **14**, 1195-1199 (2000).
260. R.W. Stevens, A. Shamsi, S. Carpenter and R. Siriwardane, *Fuel* **89**, 1280-1286 (2010).
261. C. Han and D.P. Harrison, *Chemical Engineering Science* **49**, 5875-5883 (1994).
262. S. Ramkumar and L.S. Fan, *Industrial & Engineering Chemistry Research* **49**, 7563-7573 (2010).
263. C.R. Müller, R. Pacciani, C.D. Bohn, S.A. Scott and J.S. Dennis, *Industrial & Engineering Chemistry Research* **48**, 10284-10291 (2009).

264. M.A.E. Bretado, M.D.D. Vigil, J.S. Gutierrez, A.L. Ortiz and V. Collins-Martinez, *International Journal of Hydrogen Energy* **35**, 12083-12090 (2010).
265. L. He, H. Berntsen and D. Chen, *Journal of Physical Chemistry A* **114**, 3834-3844 (2010).
266. S.J. Lee, S. Mukerjee, E.A. Ticianelli and J. McBreen, *Electrochimica Acta* **44**, 3283-3293 (1999).
267. M.C. Stewart, V. Manovic, E.J. Anthony and A. Macchi, *Environmental Science & Technology* **44**, 8781-8786 (2010).
268. C.B. Wang, L.F. Jia, Y.W. Tan and E.J. Anthony, *Fuel* **89**, 2628-2632 (2010).
269. A. MacKenzie, D.L. Granatstein, E.J. Anthony and J.C. Abanades, *Energy & Fuels* **21**, 920-926 (2007).
270. A. Baysal and S. Akman, *Talanta* **85**, 2662-2665 (2011).
271. P. Pimenidou and V. Dupont, *Bioresource Technology* **109**, 198-205 (2012).
272. W. Liu, N.W. Low, B. Feng, G. Wang and J.C. Diniz da Costa, *Environmental Science & Technology* **44**, 841-847 (2010).
273. L. Li, D.L. King, Z. Nie and C. Howard, *Industrial & Engineering Chemistry Research* **48**, 10604-10613 (2009).
274. W. Liu, B. Feng, Y. Wu, G. Wang, J. Barry and J.C. da Costa, *Environ Sci Technol* **44**, 3093-3097 (2010).
275. C.S. Martavaltzi and A.A. Lemonidou, *Industrial & Engineering Chemistry Research* **47**, 9537-9543 (2008).
276. C.S. Martavaltzi and A.A. Lemonidou, *Chemical Engineering Science* **65**, 4134-4140 (2010).
277. V. Manovic and E.J. Anthony, *Industrial & Engineering Chemistry Research* **49**, 6916-6922 (2010).
278. V.S. Chew, C.H. Cheh and R.W. Glass. *Mechanism of the CO₂-Ca(OH)₂ reaction*. in 17th DOE Nuclear Air Cleaning Conference (Conf-820833). 1982. Denver, Colorado.
279. P. Liu, T. Kendelewicz, G.E. Brown, G.A. Parks and P. Pianetta, *Surface Science* **416**, 326-340 (1998).
280. S.F. Wu, T.H. Beum, J.I. Yang and J.N. Kim, *Industrial & Engineering Chemistry Research* **46**, 7896-7899 (2007).
281. J. Fernández, F. González, C. Pesquera, C. Blanco and M.J. Renedo, *Industrial & Engineering Chemistry Research* **49**, 2986-2991 (2010).

282. R.W. Hughes, D. Lu, E.J. Anthony and Y.H. Wu, *Industrial & Engineering Chemistry Research* **43**, 5529-5539 (2004).
283. S.M. Shih, C.S. Ho, Y.S. Song and J.P. Lin, *Industrial & Engineering Chemistry Research* **38**, 1316-1322 (1999).
284. B. Arias, J.C. Abanades and G.S. Grasa, *Chemical Engineering Journal* **167**, 255-261 (2011).
285. G.S. Grasa and J.C. Abanades, *Industrial & Engineering Chemistry Research* **45**, 8846-8851 (2006).
286. S.Y. Lin, Y. Wang and Y. Suzuki, *Energy & Fuels* **23**, 2855-2861 (2009).
287. V. Materic, S. Edwards, S.I. Smedley and R. Holt, *Industrial & Engineering Chemistry Research* **49**, 12429-12434 (2010).
288. S.F. Wu, Q.H. Li, J.N. Kim and K.B. Yi, *Industrial & Engineering Chemistry Research* **47**, 180-184 (2008).
289. I. Martinez, G. Grasa, R. Murillo, B. Arias and J.C. Abanades, *Energy & Fuels* **26**, 1432-1440 (2012).
290. Y. Wang, S. Lin and Y. Suzuki, *Energy & Fuels* **21**, 3317-3321 (2007).
291. T. Darroudi and A.W. Searcy, *Journal of Physical Chemistry* **85**, 3971-3974 (1981).
292. Y. Wang, S.Y. Lin and Y. Suzuki, *Energy & Fuels* **22**, 2326-2331 (2008).
293. N.Y. Hu and A.W. Scaroni, *Fuel* **75**, 177-186 (1996).
294. Y. Li, C. Zhao, H. Chen, L. Duan and X. Chen, *Fuel* **89**, 642-649 (2010).
295. L. Li, D.L. King, Z. Nie, X.S. Li and C. Howard, *Energy & Fuels* **24**, 3698-3703 (2010).
296. V. Manovic and E.J. Anthony, *Environmental Science & Technology* **42**, 4170-4174 (2008).
297. V. Manovic and E.J. Anthony, *Thermal Science* **13**, 89-104 (2009).
298. Z. Chen, H.S. Song, N. Portillo, C.J. Lim, J.R. Grace and E.J. Anthony, *Energy & Fuels* **23**, 1437-1444 (2009).
299. N.R. Rodriguez, N., M. Alonso and J.C. Abanades, *Aiche Journal* **57**, 1356-1366 (2011).
300. J.S. Dennis and A.N. Hayhurst, *Chemical Engineering Science* **42**, 2361-2372 (1987).
301. N. Hildenbrand, J. Readman, I.M. Dahl and R. Blom, *Applied Catalysis a-General* **303**, 131-137 (2006).

302. G. Montes-Hernandez, A. Pommerol, F. Renard, P. Beck, E. Quirico and O. Brissaud, *Chemical Engineering Journal* **161**, 250-256 (2010).
303. R. Koirala, K.R. Gunugunuri, S.E. Pratsinis and P.G. Smirniotis, *Journal of Physical Chemistry C* **115**, 24804-24812 (2011).
304. S.L. Xu, F.Z. Zhang, Z.R. Chen, J.H. Yu, D.G. Evans and B.W. Zhang, *Industrial & Engineering Chemistry Research* **50**, 6567-6572 (2011).
305. B.D. Cullity and S.R. Stock, *Elements of X-Ray Diffraction*. ed. Edition, T., Prentice Hall, New Jersey (2001).
306. C. Rodriguez-Navarro, K. Kudlacz and E. Ruiz-Agudo, *American Mineralogist* **97**, 38-51 (2012).
307. K. Efimov, O. Czuprat and A. Feldhoff, *Journal of Solid State Chemistry* **184**, 1085-1089 (2011).
308. A. Lucas, M. Mouallem-Bahout, C. Carel, J. Gaude and M. Matecki, *Journal of Solid State Chemistry* **146**, 73-78 (1999).
309. W. Liu, J.S. Dennis, D.S. Sultan, S.A.T. Redfern and S. Scott, *Chemical Engineering Science* **69**, 644-658 (2012).
310. P. Engler, M.W. Santana, M.L. Mittleman and D. Balazs, *Thermochimica Acta* **140**, 67-76 (1989).
311. L. Vielle, I. Rousselot, F. Leroux, J.-P. Besse and C. Taviot-Guého, *Chemistry of Materials* **15**, 4361-4368 (2003).
312. J. Garcia-Martinez, A. Bueno-Lopez, A. Garcia-Garcia and A. Linares-Solano, *Fuel* **81**, 305-313 (2002).
313. M. Fernandez-Garcia, X.Q. Wang, C. Belver, A. Iglesias-Juez, J.C. Hanson and J.A. Rodriguez, *Chemistry of Materials* **17**, 4181-4193 (2005).
314. J.A. Rodriguez, X. Wang, J.C. Hanson, G. Liu, A. Iglesias-Juez and M. Fernández-García, *Journal of Chemical Physics* **119**, 5659-5669 (2003).
315. D.L. Bish and J.E. Post, *American Mineralogist* **78**, 932-940 (1993).
316. C.G. Kontoyannis and N.V. Vagenas, *Analyst* **125**, 251-255 (2000).
317. R.J. Hill and R.X. Fischer, *Journal of Applied Crystallography* **23**, 462-468 (1990).
318. E. Jansen, W. Schafer and G. Will, *Journal of Applied Crystallography* **27**, 492-496 (1994).

319. L.B. McCusker, R.B. Von Dreele, D.E. Cox, D. Louer and P. Scardi, *Journal of Applied Crystallography* **32**, 36-50 (1999).
320. S. Walspurger, P.D. Cobden, W.G. Haije, R. Westerwaal, G.D. Elzinga and O.V. Safonova, *European Journal of Inorganic Chemistry* 2461-2464 (2010).
321. S. Walspurger, P.D. Cobden, O.V. Safonova, Y. Wu and E.J. Anthony, *Chemistry - A European Journal* **16**, 12694-12700 (2010).
322. R. Barker, *Journal of Applied Chemistry and Biotechnology* **24**, 221-227 (1974).
323. R.H. Borgwardt and K.R. Bruce, *Aiche Journal* **32**, 239-246 (1986).
324. P.S. Fennell, *Senior lecturer in clean energy, Imperial College London*, (2012)
325. O. Chaixpluchery, J. Bouillot, D. Ciosmak, J.C. Niepce and F. Freund, *Journal of Solid State Chemistry* **50**, 247-255 (1983).
326. V. Manovic and E.J. Anthony, *Energy & Fuels* **24**, 5790-5796 (2010).
327. R.W. Cheary and A.A. Coelho, *Journal of Applied Crystallography* **31**, 851-861 (1998).
328. S.P. Thompson, J.E. Parker, J. Potter, T.P. Hill, A. Birt, T.M. Cobb, F. Yuan and C.C. Tang, *Review of Scientific Instruments* **80**, (2009).
329. A.C. Larson and R.B. Von Dreele, *General structure analysis system, GSAS* (2004).
330. G.K. Williamson and W.H. Hall, *Acta Metallurgica* **1**, 22-31 (1953).
331. J.J. Beaudoin, *Cement and Concrete Research* **13**, 319-324 (1983).
332. C.S. Martavaltzi, T.D. Pefkos and A.A. Lemonidou, *Industrial & Engineering Chemistry Research* **50**, 539-545 (2011).
333. K. Essaki, T. Muramatsu and M. Kato, *International Journal of Hydrogen Energy* **33**, 6612-6618 (2008).
334. A.N. Fatsikostas and X.E. Verykios, *Journal of Catalysis* **225**, 439-452 (2004).
335. W. Wang and Y.Q. Wang, *International Journal of Energy Research* **32**, 1432-1443 (2008).
336. S.V. Kumari, M. Natarajan, V.K. Vaidyan and P. Koshy, *Journal of Materials Science Letters* **11**, 761-762 (1992).
337. J.T. Richardson and M.V. Twigg, *Applied Catalysis A-General* **167**, 57-64 (1998).
338. F.A. Cotton, G. Wilkinson, C.A. Murillo and M. Bochmann, *Advanced inorganic chemistry*. Wiley (1999).

339. N.N. Greenwood and A. Earnshaw, *Chemistry of the elements*. Butterworth-Heinemann (1997).
340. T. Rosenqvist, *Principles of extractive metallurgy*. ed. Rosenqvist, T., Tapir Academic Press, Norway (2004).
341. O.M. Cintho, C.P. De Lazzari and J.D.T. Capocchi, *Isij International* **44**, 781-784 (2004).
342. J.F.E. Gootzen, A.H. Wonders, W. Visscher and J.A.R. vanVeen, *Langmuir* **13**, 1659-1667 (1997).
343. J.F.E. Gootzen, W. Visscher and J.A.R. vanVeen, *Langmuir* **12**, 5076-5082 (1996).
344. R.J. Lutz, A. Menawat and J.I. Peterson, *Aiche Journal* **28**, 1027-1030 (1982).

I want to live my life taking the risk all the time that I don't know anything like enough yet; that I haven't understood enough; that I can't know enough; that I'm always hungrily operating on the margins of a potentially great harvest of future knowledge and wisdom, I wouldn't have it any other way

Christopher Hitchens